Cyprus University of Technology

Faculty of Engineering and Technology

Doctoral Dissertation

MAGNETIC RESONANCE IMAGING GUIDED FOCUSED ULTRASOUND IN THE TREATMENT OF NEUROLOGICAL DISORDERS

Anastasia Antoniou

Limassol, September 2023

CYPRUS UNIVERSITY OF TECHNOLOGY

FACULTY OF ENGINEERING AND TECHNOLOGY

DEPARTMENT OF ELECTRICAL ENGINEERING, COMPUTER ENGINEERING AND INFORMATICS

Doctoral Dissertation

MAGNETIC RESONANCE IMAGING GUIDED FOCUSED ULTRASOUND IN THE TREATMENT OF NEUROLOGICAL DISORDERS

Anastasia Antoniou

Limassol, September 2023

Approval Form

Doctoral Dissertation

MAGNETIC RESONANCE IMAGING GUIDED FOCUSED ULTRASOUND IN THE TREATMENT OF NEUROLOGICAL DISORDERS

Presented by

Anastasia Antoniou

Supervisor: Faculty of Engineering and Technology, Dr. Christakis Damianou, Professor

Signature _____

Member of the committee: Dr. Constantinos S. Pattichis, Professor

Signature _____

Member of the committee: Dr. Andreas Anayiotos, Professor

Signature _____

Cyprus University of Technology

Limassol, September 2023

Approval Form of Advisory Committee

Doctoral Dissertation

MAGNETIC RESONANCE IMAGING GUIDED FOCUSED ULTRASOUND IN THE TREATMENT OF NEUROLOGICAL DISORDERS

Presented by

Anastasia Antoniou

Supervisor: Faculty of Engineering and Technology, Dr. Christakis Damianou, Professor

Signature _____

Member of the Committee: Dr. Constantinos S. Pattichis, Professor

Signature _____

Member of the Committee: Dr. Andreas Anayiotos, Professor

Signature _____

Cyprus University of Technology

Limassol, September 2023

Copyrights

The approval of the dissertation by the Department of Electrical Engineering, Computer Engineering and Informatics does not imply necessarily the approval by the Department of the views of the writer.

Acknowledgments

The completion of the current dissertation could not have been accomplished without the guidance of my supervisor, Prof. Christakis Damianou. I would like to express to him my sincere gratitude for giving me the opportunity to get involved in his research activities, as well as for his guidance and support in the implementation of my thesis. His expertise and encouragement has been pivotal in shaping my academic growth and achievements.

I would also like to express gratitude to my current and previous lab colleagues for the constructive cooperation and their overall contribution to the reported research activities. Special thanks to Dr. Marinos Giannakou for designing the robotic systems employed in the study, as well as to Mr. Nikolas Evripidou for his significant contributions to the implementation of the mice experiments.

My grateful thanks are also extended to the team of the Cyprus Institute of Neurology and Genetics, especially to Dr. Ioanna Kousiappa, Mr. Marios Stavrou, Dr. Elena Georgiou, and Dr, Alexia Kagiava for their invaluable cooperation in successfully executing the mice experiments. Their expertise has been crucial in achieving the goals of the current thesis.

Finally, I wish to express my sincere gratitude to my family for the unconditional support they have given me throughout my academic journey.

.

ABSTRACT

Magnetic Resonance guided Focused Ultrasound (MRgFUS) has emerged in the field of neurosurgery as a non-invasive modality for the treatment of various brain diseases. Numerous studies involving the use of mouse models have shown that extracorporeal FUS administered with an US contrast agent can transiently disrupt the Blood Brain Barrier (BBB) so that molecules of pharmacologically relevant size can enter the brain parenchyma to impart therapeutic effects. This doctoral study aimed to provide insights on the topic of transcranial FUS (tFUS) through a series of *ex-vivo* and *in-vivo* preclinical experiments. Realistic phantom models were developed to mimic all the critical properties of live tissue and assessed for their feasibility as quality assurance tools for tFUS procedures. The developed tissue mimicking phantoms served as the main tool for evaluating the practicality of using single-element ultrasonic transducers in trans-skull thermal applications. Critical topics of the preclinical assessment of newly developed systems and emerging applications in the context of MRgFUS were also covered. The study further presents the development of a compact single-stage positioning device dedicated to tFUS applications in small animal models, which was evaluated for its ability to cause safe and efficient BBB disruption (BBBD) in Wild Type mice. The next key objective was to examine the capability of specific anti-Aβ antibodies to penetrate the brain tissue following FUS-mediated BBBD and impart therapeutic effects in the 5XFAD mouse model of the Alzheimer's disease (AD), thus potentially holding promise for the development of disease-modifying therapeutics for AD patients. Some preliminary outcomes on the potential feasibility of this technology in the treatment of neurodevelopmental disorders are reported as well.

Keywords: MRgFUS, brain, transcranial, mice, tissue mimicking phantoms

TABLE OF CONTENTS

LIST OF TABLES

LIST OF FIGURES

LIST OF ABBREVIATIONS

MRgFUS:	Magnetic Resonance guided Focused Ultrasound
HIFU:	High Intensity Focused Ultrasound
CNS:	Central Nervous System
BBB:	Blood Brain Barrier
BBBD:	Blood Brain Barrier Disruption
MBs:	Microbubbles
DF:	Duty Factor
TJs:	Tight Junctions
TMPs:	Tissue Mimicking Phantoms
QA:	Quality Assurance
MRI:	Magnetic Resonance Imaging
FSE:	Fast Spin Echo
GRE:	Gradient Echo
FLASH:	Fast Low Angle Shot
T1-W:	T1-Weighted
T2-W:	T2-Weighted
IR:	Inversion Recovery
SPGR:	Spoiled Gradient Recalled Echo
PRFS:	Proton Resonance Frequency Shift
ETL:	Echo Train Length
pBW:	Pixel Bandwidth
FOV:	Field of View
TE:	Echo Time
TR:	Repetition Time

TI:	Inversion Time
NEX:	Number of Excitations
SI:	Signal Intensity
ROI:	Region of Interest
SD:	Standard Deviation
RFA:	Radiofrequency Ablation
MWA:	Microwave Ablation
LITT:	Laser Interstitial Thermal Therapy
PLA:	Polylactic Acid
ASA:	Acrylonitrile Styrene Acrylate
ABS:	Acrylonitrile Butadiene Styrene
PP:	Polypropylene
PVA:	Polyvinyl Alcohol
PVC:	Polyvinyl Chloride
PMMA:	Polymethylmethacrylate
STL:	Stereolithographic
FDA:	Food and Drug Administration
CAD:	Computer-aided Design
HU:	Hounsfield Units
WT:	Wild Type

1 Introduction

1.1 Introduction to the MRgFUS technology

In recent years, a shift has been observed towards minimally invasive and non-invasive therapeutic solutions, with the Focused Ultrasound (FUS) technology continuously gaining prevalence as a non-invasive alternative to surgery for many oncological and other applications [1]-[2]. Specifically, the past few decades have been characterized by a shift in research interests from the diagnostic value of US to its therapeutic modality, in which non-ionizing energy is deposited in tissue to induce various biological effects. High Intensity Focused Ultrasound (HIFU) is a non-invasive method, in which a focused transducer produces very high intensities at the focal spot, causing coagulative necrosis of tissue [3]. The ultrasonic energy is delivered to the target percutaneously to locally generate lethal temperatures (of up to 90 °C within 10 s of sonication) and instantaneous coagulative necrosis of the exposed tissue [4]. The position and dimensions of the spot depend on the sonication frequency, the diameter, and the radius of curvature of the transducer, and it must be carefully moved to ablate a larger volume of tissue. The produced lesion is usually a cigar- or egg-shaped area, known as Biological Focal Region [5]. FUS also induces various mechanical bioeffects, with the most common one known as cavitation [3]. In this phenomenon, administrated contrast agent microbubbles expand and oscillate at the frequency of the acoustic wave during sonication (stable cavitation) until bubble explosion occurs (inertial cavitation) above a pressure threshold [3]. **Figure 1** presents the two main concepts of lesion formation in tissue.

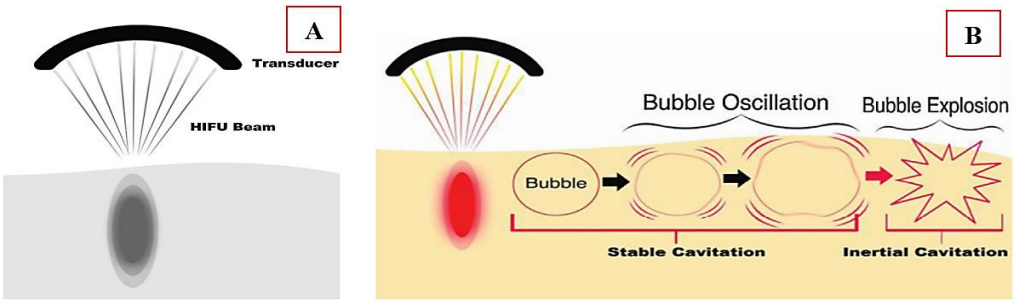

Figure 1: Representation of **(A)** thermal and **(B)** cavitational FUS mechanisms. Figure obtained from Elhelf et al. [6].

Accordingly, FUS is progressively being used in the treatment of several types of benign and malignant solid tumors [7] alternatively to traditional surgery, systemic and radiation therapies. FUS is applied locally, whereas chemotherapy constitutes a systemic therapy. Due to its non-invasive nature, it eliminates all surgery-related side effects and complications. Furthermore, due to its non-ionizing nature, it eliminates all the side effects of radiotherapy, thereby improving the life quality of patients significantly. Additionally, in contrast to other ablative techniques, there is no need of introducing needles into the tissue. The FUS technology was also proven very promising in the treatment of diseases of the Central Nervous System (CNS) [7] due to its ability to disrupt the BBB. FUS-mediated BBB disruption (BBBD) is based on the mechanical effects of FUS (Figure 1B) and involves administering FUS in synergy with microbubbles (MBs).

FUS applications are typically monitored either by US or Magnetic Resonance Imaging (MRI) [6], with the latter one being superior regarding both safety and efficacy. Specifically, MRI offers significantly better contrast between soft tissues and delineation of tumor margins [8]. In addition to the high-quality imaging, MRI also provides accurate monitoring of tissue heating during FUS therapy through the use of MR thermometry [9].

To date, many clinical applications using this modality have been developed, for the treatment of a variety of solid malignant tumors, including those in the pancreas [10], liver [11], kidney [11], bone [12], prostate [13], and breast [14]. It is also utilized for pain palliation of bone metastases. All these applications are briefly reviewed in a recent paper [2], along with other emerging applications, including drug delivery, vessel occlusion, histotripsy, movement disorders treatment, vascular, and psychiatric applications. Currently, among the very wide spectrum of applications of HIFU in clinical medicine, the most common and well-established MRI-guided applications that were granted Food and Drug Administration (FDA) approval are the treatments of uterine fibroids [15], essential tremor [16], and localized prostate cancer [13].

1.2 MRgFUS in neurological applications

1.2.1 Challenges in the field

An obvious challenge in this emerging field was its extension to neurosurgery and brain disorder treatments. The potential of treating disorders of the central nervous system by performing non-invasive procedures is a "holy grail" for researchers. An early experiment performed in the 1940s [17], where ultrasonic energy was deposited in the brain through an impact skull, has underlined the safety issues that should be considered when performing a transcranial sonication. Although brain changes have been achieved, there was evidence of incidental injury to the brain tissue [17]. **Figure 2** shows a schematic representation of FUS application in the brain tissue.

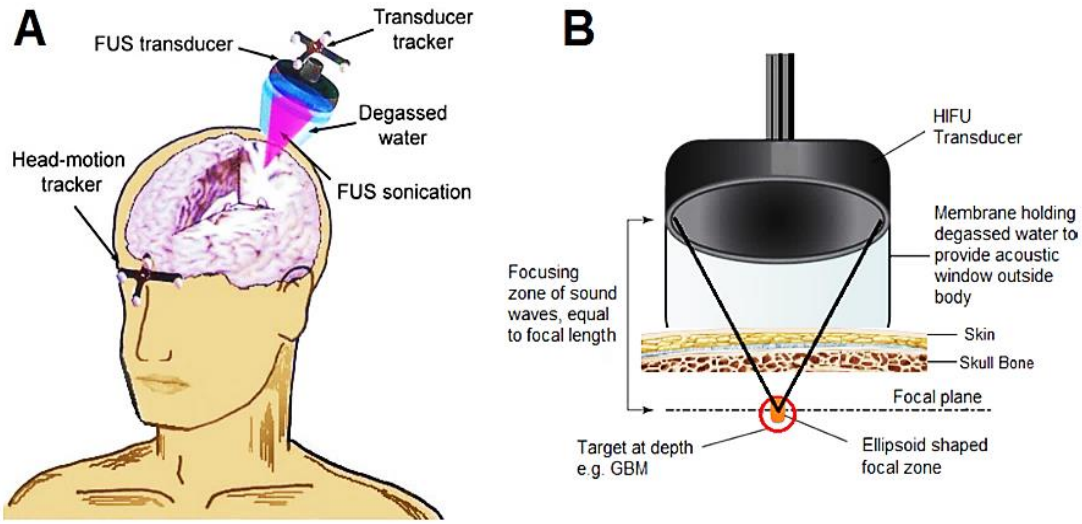

Figure 2: Application of FUS in the brain. Figure obtained from Quadri et al. [7].

Over the years, technological progress enabled efficient ultrasonic delivery through the intact skull and the use of this modality in the treatment of many neurological diseases [18]. The two main innovations that contributed in this regard are the introduction of the *phased-array technology* [19] and the use of *MR thermometry* for real-time temperature monitoring [20]. Automated movement of the transducer using robotic systems has also contributed in this regard by increasing the accuracy and reliability of ultrasonic delivery and the entire procedure [21].

1.2.2 Clinical applications

Some of the transcranial MRgFUS applications that have been translated to the clinical setting include Parkinson's disease [22], obsessive-compulsive disorder [23], major depressive disorder, and essential tremor [16]. Other expanding fields for potential clinical use of MRgFUS, are Alzheimer's disease (AD) [24] and epilepsy [25]. All these applications are presented in a comprehensive review by Quadri *et al.* [7]. Another review by MacDonell *et al.* [26] focused on the use of this modality for brain tumor ablation. The feasibility of ultrasound-mediated BBBD as a safe and efficient method for drug delivery into the brain parenchyma has been quite widely tested in the clinical setting as well [27]. As previously mentioned, the aforementioned applications are based on the ability of MRgFUS to induce various thermal and mechanical effects on brain tissue. Regarding marketed devices, the ExAblate Neuro produced by Insightec [28] for transcranial MRgFUS therapy has gained FDA approval for essential tremor treatment in 2016 [29].

1.3 FUS-mediated drug delivery by BBB disruption

1.3.1 Highly selective nature of BBB

The **BBB** is a **highly selective physical barrier** that separates the lumen of cerebral blood vessels from the brain parenchyma and tightly controls the transfer of molecules from the blood circulation to the brain tissue and vice versa [30]. **Figure 3** shows the cellular constituents of BBB.

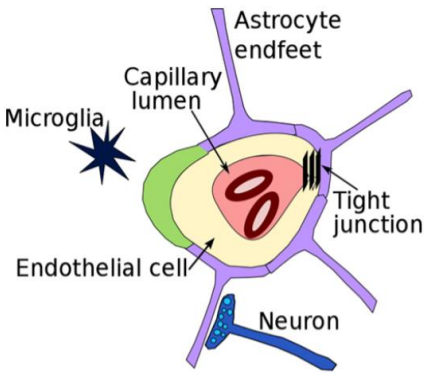

Figure 3: Cellular constituents of BBB. Figure obtained from Burgess et al. [31].

Endothelial cells are tightly linked by robust junctions that limit paracellular permeability to molecules with a weight smaller than 400-500 Da [30]. Due to its highly selective nature, BBB prevents the majority of pharmacological substances from entering the brain parenchyma, thus preventing the treatment of many neurodegenerative diseases [32].

1.3.2 FUS-mediated drug delivery

The available technologies for increasing drug penetration through the BBB include Convection-enhanced delivery (drug injection into the brain parenchyma directly using needles), administration of re-engineered drugs fused to insulin or transferring receptors to cross the BBB via transcellular transport, and hyperosmolar agents such as mannitol to loosen the tight junctions (TJs) of the BBB [33].

In the last decades, FUS has emerged as a novel method to disrupt the BBB temporarily in a completely non-invasive manner [31]. The mechanical effects of FUS, and particularly the previously mentioned cavitational effects, are considered to be the main principle behind this phenomenon [3]. An illustration of the mechanisms of FUS-induced BBBD is shown in **Figure 4**. A comparison of advantages and limitation between FUS and other available methods for BBBD is provided by Burgess et al [31].

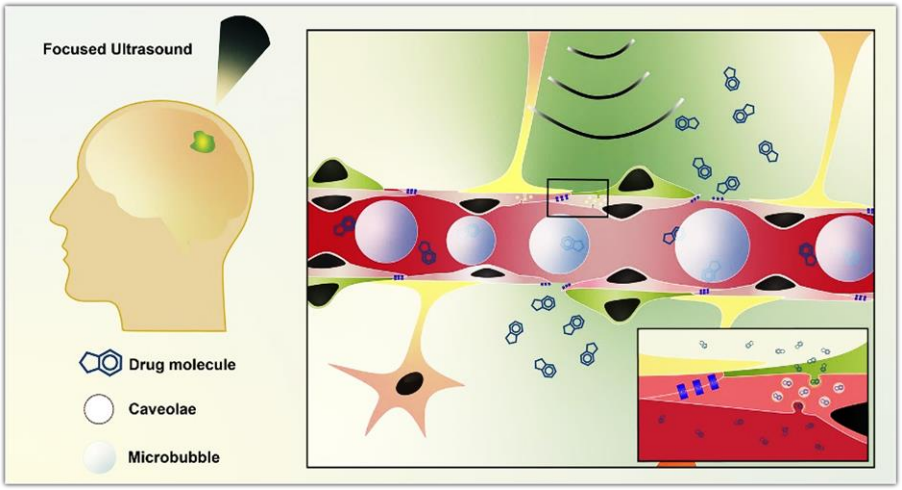

Figure 4: Illustration of mechanisms of FUS-induced blood-brain barrier opening. Figure obtained from Meng et al. [33].

In 2001, Hynynen et al. [34] demonstrated that the acoustic energy (of low intensity US) can be concentrated in the vessels with the use of intravascular contrast agent microbubbles. Reproducible BBBD without long-term damages in brain tissue was proven feasible [34]. Following this early study, the feasibility of FUS-induced BBBD was further investigated by many researchers, with a lot of effort being placed in optimizing the relevant parameters to achieve efficient opening without any associated adverse events [35]. Accordingly, more recent studies proved that FUS-induced BBBD can allow passage of therapeutic drugs into the brain parenchyma [35].

1.3.3 Neurodegenerative diseases

To date, there are not effective treatments to cure most of the neurodegenerative diseases, such as AD, Huntington's disease, Parkinson's disease, and multiple sclerosis. Brain cancer also lacks effective therapeutic regimens that do not compromise the patient's life quality. The biggest obstacle to the treatment of these diseases is the highly selective nature of the BBB, which prevents all large-molecule therapeutics and more than 98 % of small-molecule therapeutics to enter the brain parenchyma [36]. Therefore, extensive research is dedicated in finding ways to temporary and effectively disrupt the BBB, thus enabling delivery of drugs that under normal conditions are blocked by the BBB [30].

1.3.3.1 Alzheimer's Disease

AD normally begins from the hippocampus and spreads across other regions as the disease progresses [37]. The disease is characterized by the development of extracellular amyloid plaques, probably as a result of Amyloid β peptides (Aβ) aggregation, and intracellular neurofibrillary tangles [37]. AD constitutes the most common cause of dementia, accounting for 50-60 % of dementia cases. Notably, a new case of dementia occurs somewhere in the world every 3 seconds, affecting more than 50 million people worldwide [38].

According to Yiannopoulou et al. [39], there are 33 symptomatic treatments in the clinical setting, where agents are administered to improve the clinical (such behavioral and psychological) symptoms of AD, but without any modification of

the pathological steps. Importantly, a main drawback in the use of many agents is their limited penetration through the BBB [39].

1.3.3.2 Hypomyelinating leukodystrophy

Hypomyelinating leukodystrophies are a subset of genetic neurological disorders affecting the white matter, which are characterized by a lack of CNS myelin deposition. [40]. Hypomyelinating leukodystrophy type-2 (HLD2), also known as the Pelizaeus–Merzbacher-like disease (PMLD) is a rare neurological disorder starting in early childhood where the white matter of the brain and spinal cord are progressively degenerated due to genetic mutations, leading to loss of the function of a protein called connexin47 (Cx47) [40]-[41]. This protein is located in oligodendrocytes all over the CNS and has a prominent role in preserving the integrity of brain cells and promoting communication between them. Recessive mutations in the GJC2 gene, which is responsible for encoding Cx47, are associated with the development of HLD2 [41].

MRI is the imaging modality used to monitor myelination activity, visualize myelin deficits in the brain, and quantify the white matter myelin content through quantitative MRI techniques. Accordingly, brain MRI reveals characteristic patterns that are essential in the clinical diagnosis of hypomyelinating disorders [40]. Although significant knowledge advancement on the disease pathology was reported in the past decade, currently, there are no curative treatments for these disorders [40].

1.4 Robotic devices for FUS applications

In modern oncology, robotics has earned a prominent role and been essential in translating new therapeutic modalities to the clinic [42]. Accordingly, robotic devices are continuously being invented for manipulating surgical instruments and energy sources, providing the level of accuracy required for safe clinical applications [42]. The significant benefits of FUS, including its non-invasive and non-ionizing nature, along with the increased accuracy achieved by robotic guidance could minimize all the complications and side effects of standard

therapeutic options (i.e., surgery, radiotherapy, and chemotherapy), thus improving the life quality of patients significantly.

One of the earliest manufacturers of clinical MRgFUS devices with commercialization activities in both Europe, America, and Asia is the Insightec Company, which owns the well-known **ExAblate body system** [43]. Another successful company in the field is the Profound company offering the **Sonalleve system**, which is also intended for body targets [44]. The treatment of uterine fibroids and pain palliation of bone metastasis are two of the most widely applied FDA-approved applications of both systems [45]. Their components are accommodated into an opening of the MRI table offering bottom to top delivery of ultrasonic energy by electronically steering the beam using phased array technology [43]-[44]. Such a therapeutic approach forces the patient in the prone position. Although this constitutes a conventional position in numerous surgical interventions, it is very uncomfortable and tiring for patients, given also that treatment normally last long while patients may be awake (or sedated) depending on the condition being treated. The limited enclosed space of the scanner intensifies this feeling, especially for claustrophobic patients. Notably, FUS instruments [46] and Image Guided Therapy [47] are quite successful companies offering MRgFUS systems for preclinical studies.

Due to the aforementioned disadvantages of prone patient positioning, several manufacturers proceed to the development of systems that use a top to bottom therapeutic approach, thus enabling supine placement of patients [45], [48]–[52]. Most of the available systems use a similar principle of US-guided treatment using a positioning arm dedicated to navigating the diagnostic and therapeutic equipment respective to the target [48]–[51]. This positioning arm is typically integrated into a transportable platform that incorporates the relevant software for therapy monitoring by trained physicians through dedicated computer-based programs [48]–[51]. Other systems use a different approach where one platform is employed for US imaging guidance and another one for controlling the system remotely while the treatment head is positioned above or/and below the patient couch [45],[52]. Typically, multi-element phased array ultrasonic transducers are employed for

precisely focusing the beam and maintaining the acoustic intensity at the skin surface within the safety limits to prevent pain and skin burns [45],[48],[52].

Meanwhile, efforts were being made by the research community with the purpose to develop more advanced systems using the specific approach of top to bottom treatment. Firstly, it is interesting to note that an existing MRgFUS system that in the first place was designed to be placed on the MRI table for bottom to top or lateral approaches was modified by Giannakou et al. [53] to enable access of ultrasonic energy to the region of interest from the top. For this purpose, authors attached an MR-compatible arm to the mechanism in order to raise the transducer at reasonable height from the patient couch.

Tognarelli et al. [54] developed a platform for US-guided robotic-assisted FUS treatment of multiple pathologies. The proposed system comprises a robotic module with two manipulators, each featuring a 6-degrees of freedom (DOF) motion. The first one includes a custom-made phased array transducer, as well as a 2D imaging US probe, whereas a 3D imaging US probe is mounted on the second one.

Another system enabling supine positioning of patient was developed by Price et al. [55] for the purpose of FUS therapy through intact skull in infants. This system is intended for FUS procedures under the guidance of MRI and was classified as MR-conditional. The positioning mechanism includes three prismatic joints that enable translational movement of a 1.2 MHz FUS transducer in three orthogonal axes and two revolute joints for rotation of the robot's wrist about the skull. A major drawback is that the system is placed on the table of the scanner, thus unavoidably constricting the valuable scanner's space.

ExAblate Neuro (Insightec) is the first and till now the only marketed system for MRgFUS treatment of Essential Tremor (FDA approved in 2016) and Parkinson’s Disease (FDA approved in 2021). The system is compatible with some MR scanners of the General Electric (GE) and Siemens Healthineers companies [28]. The system includes a helmet system that is attached on the patient couch and locked into place, a storage transfer cart, an operator console, a stereotactic frame, an equipment cabinet, and a cooling unit. The main component of the helmet system is the helmet-shaped phased array transducer that is consisted of 1024 elements independently operating at 620-720 KHz to efficiently focus the beam to the desired

location into the brain tissue. It has four positioning stages; 3 linear and 1 angular. Pulses of 5-60 s duration are applied for ablating the area by multiple sonications. The ExAblate system can be seen in **Figure 5**.

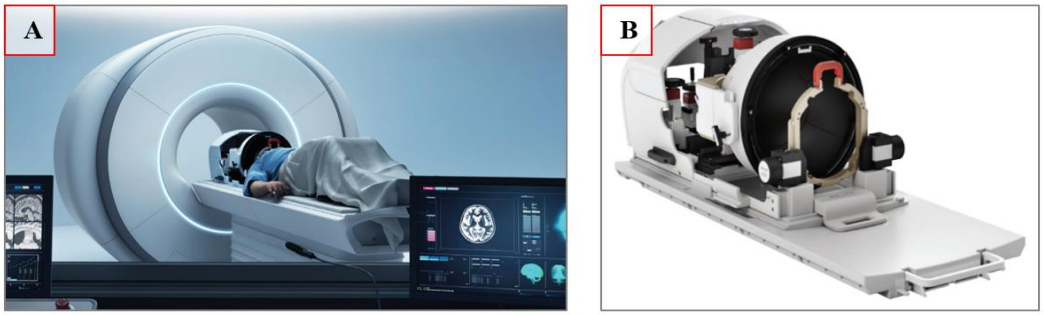

Figure 5: (A) ExAblate Neuro integrated with the MRI scanner during treatment and **(B)** Helmet System; helmet-shaped transducer on a mechanical positioning unit [28].

1.5 Treatment planning software

Safe and efficient clinical practices require the use of high-quality methods for treatment planning and real-time monitoring of heating during FUS. Briefly, the first step in the planning process is pretherapy imaging, and then, tumor segmentation followed by administration of sonication points throughout the marked region of interest (ROI) [56]. These points are sequentially visited by the transducer according to the selected scanning pathway. The planned sonication protocol is executed typically under the guidance of US or MRI [57]. As previously explained, although both are well-established non-invasive imaging modalities, MRI is superior in that it produces anatomical images of significantly higher resolution regardless of depth and intervening structures, thus enabling positioning the beam focus with very high precision [8]. Most importantly, MRI has the unique ability of enabling selective tissue ablation through intraoperative temperature monitoring with MR-based thermometry [9].

The first step in the process of treatment planning is to localize the ROI on MR images of the subject [56]. Currently, the segmentation process requires the involvement of a trained physician, which unavoidably introduces human errors and decreases the accuracy of the procedure [58]. Therefore, there is a need for new computer-based algorithms for automatic segmentation and path planning for complete coverage of the segmented ROI so as to enhance the clinical efficacy [56].

This is expected to impact the overall treatment duration positively. In fact, Loeve et al. [56] collected a series of MRgFUS interventions in the uterine and estimated an average time of 18 min for ROI segmentation. Authors suggested that the total treatment duration could be decreased by automated segmentation, especially when multiple segmentation adjustments are needed for motion compensation [56].

MRI is routinely employed in the detection of brain diseases [59]. Therefore, numerous techniques for brain lesion segmentation in MR images are available literally and may be useful considering the wide adaption of the MRgFUS technology as a neurotherapeutic tool [60]. The existing methods were classified by Zhang et al. [61] into the following categories: 1) conventional methods; i.e., threshold, region, fuzzy theory, and edge detection, 2) classical machine learning-based methods; i.e., K Nearest Neighbor - KNN, random forest, Contingent Valuation Method - CVM, and dictionary learning, and 3) deep learning-based methods; i.e., Convolutional Neural Network - CNN, Fully Convolutional Network - FCN, and encoder-decoder. Notably, a review study by Wadhwa et al. [62] suggests that the combination of a fully CNN and a Conditional Random Field (CRF) statistical method can improve the accuracy of tumor segmentation.

The wide adaption of FUS in the clinical management of uterine fibroids has led scientists to the development of more advanced planning and guiding tools for this specific application. Xu et al. [63] proposed an automatic segmentation method for uterine fibroids on US images. The developed algorithm involves dividing the image into smaller regions called superpixels that are characterized using a texture histogram-based feature representation method and finally merging them again based on their similarities (meaning that the tumor's pixels will be merged together since they have similar texture) [63]. Recently, Ning et al. [58] proposed an image guidance system featuring tools for automatic detection and segmentation of lesions on MR images through a CNN multi-stage segmentation. Notably, the developed system also enables intraoperative lesion tracking on US images [58].

Recently, in the effort to enhance MRgFUS therapy planning, three classical methodology types were assessed for their performance in segmenting ROIs (e.g., tissue, water, and transducer) on MR images of a HIFU setup [64]. The tested methods were the simplest image segmentation method known as the Threshold

method, the Watershed segmentation algorithm with markers (WSAM), and two Level set methods (LSM); the Geodesic Active Contours (GAC) and the Distance Regularized Level Set Evolution (DRLSE) methods. Preliminary results were promising; however, the methods are accompanied by some limitations, such as the need to establish an initial contour for GAC and DRLSE methods and the complex procedure of defining the markers of WSAM, which both require previous intervention by the user for MR image division [64].

The segmentation procedure is followed by path planning for selective ablation of the delineated ROI [56]. Selection of the proper scanning pathway is essential in forming uniform lesions throughout the segmented target and minimizing thermal exposure of normal tissue [65]. A conventional scanning approach in clinical FUS is the Raster scanning where the ultrasonic source sequentially visits spots arranged in horizontal lines that are scanned in the same direction [65]. Thermal diffusion was proven an essential phenomenon reducing the therapeutic outcome of this scanning mode through the formation of asymmetric lesions [65]–[67]. This is attributed to that lesion formation at a specific spot is affected by the thermal energy diffusing from neighboring previously sonicated spots, thereby leading to inadequate treatment of initial spots and extensive heating of the later ones, as well as excess thermal dose deposition in the pre-focal area, a phenomenon known as the near-field heating [68].

Therefore, there are still challenges in achieving ablation of a well-defined area by eliminating thermal diffusion effects while ideally using the minimum energy and treatment time possible. In this effort, researchers have investigated how various scanning paths and the used sonication parameters affect the therapeutic result of FUS therapy [65], [69]–[72]. Zhou et al. [65] investigated how the Spiral scanning from the center to the outside and vice versa affects the formation of lesions by sonicating a gel phantom and bovine liver in a discrete rhombus-shaped grid. The proposed scanning approaches produced more uniform lesions but of a smaller volume than conventional raster scanning when used under the same protocol [65]. Qian et al. [69] also investigated the performance of a Spiral pathway that was executed in a continuous scanning mode covering a square area in acrylamide-based heat-sensitive phantom and bovine liver. The results suggest that uniform lesions

without overheating phenomena can be produced by continuous scanning along the spiral pathway if proper scanning speed to regulate thermal energy diffusion is selected [69].

Typically, discrete scanning modes employ a time delay between successive sonications of equal duration to eliminate intense heating [68]. In accordance, the accumulation of thermal energy should be controlled by selecting not only the proper pathway, but also sufficient cooling periods. A recent study [68] evaluated the effect of increasing time delay on the induced near-field heating and overall treatment time for six different pathway algorithms, including the commonly used Sequential and Spiral algorithms. It is noted that the Sequential algorithm differs from the aforementioned Raster scanning only in that adjacent lines are scanned in opposite directions. Experimental evaluation in a tissue mimicking phantom (TMP) revealed that a minimum time delay of 50–60 s is needed for achieving a safe thermal dose accumulation in the near-field region [68].

At this point, it is interesting to note that the use of different sonication times at the various grid spots was proposed as an alternative method to avoid the introduction of cooling intervals, thus minimizing the overall treatment time [70]. The relevant article compared the performance of the Raster, Spiral, and Skip paths using unequal heating duration with the conventional scanning mode by simulating the ablation of a square area through electronic steering of the beam according to each pathway [70]. The results suggest that the proposed method is robust when used in combination with the Skip scanning path and could lead to a treatment time reduction of more than 50 % [70].

1.6 Evaluation of MRgFUS robotic systems and applications

The introduction of robots in medicine has been critical in establishing minimally invasive therapeutic modalities simultaneously facilitating their translation in the clinical setting [42]. To date, robotic features have extended the benefits of minimally invasive procedures to most surgical specialties [42]. In accordance, robotic systems are constantly being developed to aid in the positioning and manipulation of surgical instruments and energy sources, including ultrasonic sources in the context of MRgFUS.

1.6.1 MRI compatibility

Compatibility with the MRI scanner is required for devices intended to operate in the MRI environment such as in the case of MRgFUS therapy. Electromagnetic interference between the device and scanner can negatively affect not only the imaging quality, but also the device functionality, thus compromising the reliability of the procedure and the patient's safety in highly sensitive procedures. Notably, MR thermometry and thus the efficiency of ultrasonic delivery to the target depend on proper MR imaging.

A common methodology used for MRI compatibility testing makes use of the signal to noise ratio (SNR)'s dependency on the interference between the device and scanner [73]. In fact, it is evaluated whether the presence and operation of the device within the scanner compromises the imaging quality in terms of SNR. Specifically, the SNR of MR images acquired under different activation states of the robotic system is compared. In addition, it is assessed whether any noticeable artifacts appear on images. It should be though clarified that robotic FUS systems are generally classified as MRI-conditional according to American Society for Testing and Materials (ASTM) standards (F2503) since they require electricity to operate.

1.6.2 Accuracy and repeatability of robotic motion

Robotic-assisted procedures require a highly accurate operation to meet the clinical requirement. Therefore, some of the initial tests conducted in the evaluation process concern the accuracy of robotic motion. The accuracy data is also essential for establishing safety guidelines for clinical applications.

All the techniques used to test the mechanical accuracy of a robot are based on the idea of comparing the commanded motion step with the actual displacement as estimated by a distance-measuring technique. Mechanical accuracy refers to both the positioning and repeatability accuracy of motion. Before the procedure is applied in the real environment and *in-vivo*, accuracy assessment is typically carried out in free space; meaning not under real conditions (sometimes referred to as intrinsic system accuracy). Most commonly, after acquiring evidence of sufficient accuracy and repeatability by benchtop testing, the system is evaluated in the

environment that is intended to be clinically used, such as the bore of an MRI system. This is essential for ensuring that the system maintains a high degree of accuracy in real-like scenarios. As mentioned previously, MRI compatibility is required since even a minimal magnetic shift of the system's components in the MRI could affect the accuracy of motion and consequently the accuracy of ultrasonic delivery.

1.6.2.1 Benchtop evaluation

Motion tracking techniques were proposed for assessing the motion accuracy in a free robot workspace [74]–[79]. The targeting accuracy of needle-related interventions, which is estimated by the deviation of the actual tooltip position from its intended location, has been widely evaluated using optical tracking systems [74]–[77]. As an example, the accuracy of a robotic system designed for breast biopsy was evaluated by driving a rigid test tool to various positions through straight and angled paths and monitoring its actual position with an optical tracker [74]. Similarly, Patriciu et al. [75] used an optical tracking system to assess the accuracy of motion of a system for automated brachytherapy seed placement, where an active marker was attached to the end-effector of the robotic arm to enable tracking of its position. Patel et al. [76] also used an optical tracking system to evaluate the performance of a robotic system for shoulder arthrography. In this system, a tracking structure was integrated on the needle guide so that its position can be tracked in relation to a specially-designed reference frame with optical markers [76]. Dou et al. [77] selected a quite different tracking method to estimate the positioning accuracy of a brachytherapy system using a 3D laser tracker, as well as an inertial measurement unit [77]. In other studies, the actual displacement of a linear motion stage [78] and an endoscope manipulator [79] after execution of the commended movement was estimated using an optical measuring microscope and two Charge-Coupled Device (CCD) laser micrometers, respectively.

More straightforward methods involving the use of digital calipers and special structures have also been employed in the laboratory environment for accuracy evaluation purposes. A breast biopsy robot was evaluated in terms of accurate needle tip positioning in free air by targeting crosshairs drawn on a board [80], where the error was defined as the distance from each target's center to the

corresponding pierced hole [80]. A similar approach was followed in the framework of assessing the accuracy of motion of a robot intended for transcranial FUS surgery. In fact, a felt-tipped pen was used in the place of the FUS transducer and commanded to reach multiple points distributed on three orthogonal planes developed to demonstrate the entire robot's workplace [55]. The created marks were assigned in resolution circles to facilitate estimation of the targeting error [55]. Other studies used a simplified method that involved digital calipers. To be more specific, calipers were mounted on the motion stages under evaluation in a way that their actual displacement after executing the commanded motion could be directly measured by the incremental distance of the caliper [81], [82].

Robotic devices for non-invasive FUS applications are constantly being developed [83] and extensively evaluated in terms of motion accuracy by performing multiple ablations. Specifically, the separation precision of multiple ablations constitutes an indication of the positioning error. For instance, in a study by Tao Wu et al. [84] the focus positioning accuracy of a FUS system was assessed by performing multiple sonications on a Lucite cart. The transducer was placed in a water tank for efficient ultrasonic transmission to the target. Left-right and superior-inferior movements by specific distance were commanded by a treatment planning software, resulting in numerous sets of melted spots arranged in discrete patterns. The actual distance between adjacent spots was measured with a digital caliper [84]. In the benchtop setting, gel phantoms constitute another cost-effective tool for ablation experiments. In a study by Yiallouras et al [81], the motion stages were commanded to create discrete ablations of specific spacing in a gel phantom. White coagulation lesions were clearly visible, being spaced by the desired step, thus confirming the accuracy of transducer positioning, as shown in **Figure 6**.

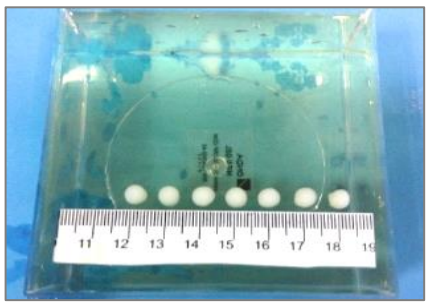

Figure 6: Gel phantom with white coagulation lesions created to assess the motion accuracy of a robotic mechanism [81].

1.6.2.2 MRI evaluation

Experimentation under more realistic conditions is commonly performed after confirming adequate accuracy for needle-related interventions in a free space. Phantoms serve as a common tool for evaluating the accuracy of needle positioning in an imaging environment, where the procedure involves the use of fiducial markers for the visualization and registration of the system in the imaging coordinates. The target locations in the phantom are selected and the insertion parameters are calculated based on a first planning scan [85]–[87]. The estimated coordinates are exported to the motor controller through a dedicated software for motion execution. Follow-up images are collected to assess the accuracy of needle placement relative to the prescribed locations [85]–[87]. Patel et al. [85] performed a phantom study using a needle-based therapeutic ultrasound applicator. The applicator was inserted in various locations (predefined in 3D Slicer) of a gelatin phantom by robotic motion under MRI guidance. Then, the probe tip position as visualized in 3D-Fast Field Echo images was compared with the intended position. Likewise, a system for prostate interventions was assessed in terms of motion accuracy in a TMP [86]. The rectal sheath was aligned with the predefined insertion point automatically and inserted in the phantom manually [86]. The phantom was imaged using Turbo Spin Echo (TSE) proton density sequence, enabling visualization of the void induced by the needle tip, and thus, estimation of the in-plane error of targeting [86]. The accuracy of a robotic mechanism in precisely reaching a target was also assessed in MRI in free space by tracking the position of a gadolinium filled needle on T1-weighted images [87].

Price et al. [55] followed a similar approach but in the context of MRgFUS. An MR conditional robot for transcranial FUS interventions was used to perform multiple sonications in a 2 x 3 pattern in a heat-sensitive gel phantom located in a water tank. The thermal images acquired after each sonication were superimposed onto one image, and the positioning accuracy was defined as the spacing between the centers of adjacent ablated areas [55]. This technique was also selected for evaluating the accuracy of motion of an MR-compatible FUS device intended for brain diseases treatment [21]. A four-point ablation pattern was performed *in vitro*, in lamb brain, with different motion steps of 1 to 10 mm, and the formed lesions were visualized

in T1-weighted Fast Spin Echo (FSE) images. The ablated areas appeared as spots of increased signal intensity (SI), and the distance between neighboring ablations was calculated from the center of each spot. Notably, smaller errors were estimated with increasing step distance [21]. Similarly, Yiallouras et al. [82] performed phantom experiments where T2-weighted FSE images revealed areas of reduced signal being formed in a discrete pattern, as shown in **Figure 7**. It is notable that Sagias et al. [88] developed a motion phantom for evaluating FUS protocols specifically for moving targets in the MRI environment. In another study carried out in a gel phantom [89], the robotic arm of an US-guided FUS ablation system was commanded to move the focal point to ablate the four corners of the phantom, and the targeting accuracy was assessed by visualizing the sonicated areas on US images.

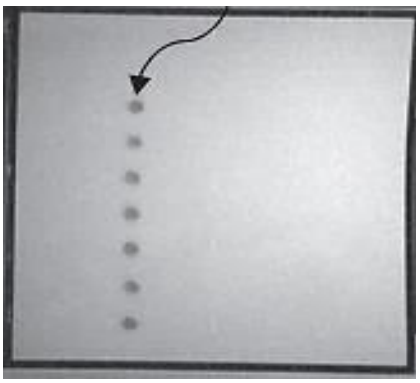

Figure 7: T2-weighted FSE images revealing hypointense spots in discrete pattern [82].

1.6.3 *Ex-vivo* studies - Tissue mimicking phantoms as evaluation tools

Extensive preclinical *ex-vivo* and *in-vivo* evaluation should be carried out in the process to translate new FUS technologies from the lab to the clinical setting. TMPs serve as handy tool in the effort to evaluate emerging FUS applications and optimize therapeutic protocols [90]. For transcranial applications of FUS, both soft tissue and skull phantoms should be developed.

1.6.3.1 Soft-tissue phantoms

So far, various gelling agents have been proposed for the construction of TMPs for multiple purposes, including the evaluation of thermal protocols. Polyacrylamide (PAA) [91]-[92] and agar based phantoms [93]–[96] were shown to be capable of emulating critical thermal, acoustical, and MR relaxation properties of various

tissues [97]. Gelatin-based phantoms were also proven factional in this regard [98]-[99]. However, they lack the capacity to withstand ablative temperatures, and therefore, are only recommended for hyperthermia applications [97]. Other gelling agents identified in the literature are Polyvinyl Alcohol (PVA) [100]–[102], Polyvinyl Chloride (PVC) [103]–[105], silicone [106]**,** [107] and TX-150/ TX-151 [108], [109]. However, adequate information on the efficacy of these materials for thermal applications is lacking.

PAA gels are favorable in that they are characterized by optical transparency, thus allowing for direct visualization of coagulative areas [97]. On the other hand, agar phantoms were proven very promising for use with the MRgFUS technology, with lower preparation costs and without the toxicity issues related to the preparation of PAA gels. **Figure 8** shows an agar-based phantom containing wood powder [110].

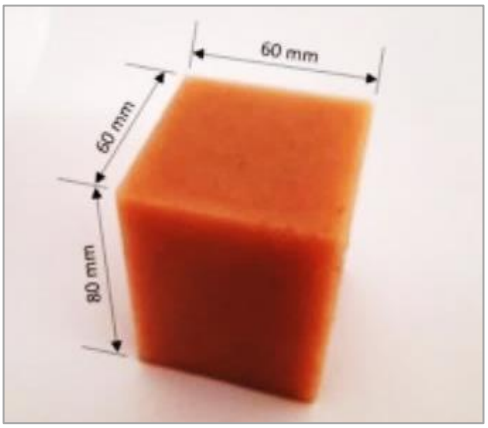

Figure 8: Agar-based wood powder-doped TMP developed by Drakos et al [110].

1.6.3.2 Relaxation properties of soft-tissue phantoms

TMPs designed for FUS studies should have similar acoustic behavior with biological tissue, with the speed of sound in the medium, characteristic acoustic impedance, and attenuation coefficient being the most important properties to be mimicked [96], [111].

Besides the acoustical behavior of TMPs, it is also critical that the thermal characteristics of tissues are replicated. The thermal profile during FUS exposure in a TMP is mainly governed by the three parameters; specific heat capacity, thermal conductivity, and thermal diffusivity [96], [111]. Since the therapeutic result during sonication is evaluated via thermometry based feedback, a tissue like

thermal behavior is of major importance while precise modeling of acoustical properties is not of great importance in this regard. The acoustic and thermal properties of agar-based phantoms have been already assessed in various studies [96].

A suitable TMP for MRgFUS applications should also possess similar MRI properties with tissue. This is attributed to that MR parameters affect the contrast between normal soft tissue and FUS lesions to a great-extend [112]–[114]. Moreover, the contrast in MR images and temperature monitoring during FUS exposures are based on changes in the magnetic relaxation times T1 and T2 of tissues [9]. It is thus ideal for MRgFUS phantoms to produce tissue-like signal in the MRI. Nevertheless, there is a lack of previous studies focusing on the MR relaxation properties of MRgFUS phantoms.

1.6.3.3 Skull phantoms

Without the appropriate knowledge about ultrasonic transmission through the skull, it is extremely difficult to predict the heat deposition and temperature elevation caused by the sonication, and therefore, to prepare an efficient treatment plan. Preclinical studies for evaluating MRgFUS applications using TMPs should involve a skull mimic with well-known properties. Therefore, ultrasonic characterization of materials candidate for the construction of skull phantoms is deemed necessary.

Thermoplastic polymers constitute an appealing solution for fabricating hard tissue phantoms due to their rigidity and high temperature tolerance. Skull phantoms can be constructed by injection molding in patient-specific skull molds [115]-[116]. Polymethylmethacrylate (PMMA) was predominantly selected in this regard, particularly for the production of cranial implants by casting PMMA into customized 3D printed molds [115]-[116].

In the last decade, 3D printing has arisen as a promising manufacturing process providing the ability of cost-effective rapid prototyping [93], [117]. Another major benefit of this emerging technology over molding procedures is the ability to design and develop parts of complex geometries with high accuracy and detail. Accordingly, accurate geometrical replication of a human skull is feasible [93]. Several studies examined the efficacy of 3D printing bone phantoms using

thermoplastic polymers, in terms of thermal and acoustic properties [93], [117]. As an example, **Figure 9** shows the stereolithographic (STL) model of a human skull that was 3D printed for testing transcranial FUS applications [93].

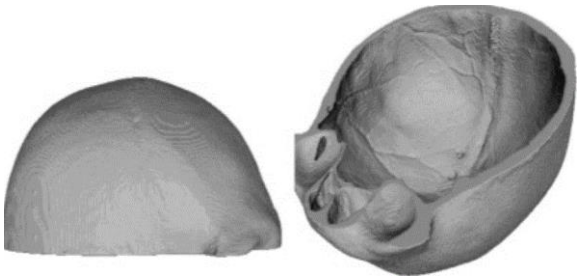

Figure 9: STL model of a **s**kull phantom developed by Menikou et al [93].

1.6.4 *In-vivo* studies

After *ex-vivo* preclinical evaluation in phantoms and excised tissues, a series of animal studies follow. Typically, preclinical validation in animals enables translation of applications to the clinical setting to be applied on humans. A comprehensive search of existing literature regarding FUS studies on BBBD in animals and patients was carried out. The results are presented in **Table I** of the **Appendix**, revealing that mice constitute one of the prominent models for preclinical studies in the field. Other animals used are rabbits, rats, swine, sheep, and rhesus macaques.

1.6.4.1 Mouse models of neurological diseases

Regarding preclinical *in-vivo* studies, genetically modified mice are commonly used for research purposes in the field. Generally, genetic mouse models have been widely used to investigate the physical properties of BBB and enhance the understanding on the mechanisms of the BBB function [118]-[119]. In the last decade, many research studies involving the use of mouse models have shown that FUS administered with an ultrasound contrast agent can sufficiently disrupt the BBB so that molecules of pharmacologically relevant size can enter the brain parenchyma [120]–[124]. Thereby, FUS has emerged in the field of neurosurgery as a non-invasive technology for safe and reversible BBBD.

Choi et al. [120] applied pulsed FUS following administration of MBs to the hippocampus of Wild Type (WT) male C57BL/6 mice transcranially. The induced

BBB opening was sufficient to allow dextrans of 3 and 70 kDa to be diffusely distributed through the treated brain regions. Importantly, this study proved the capability of FUS accompanied with MBs to enable BBB permeability of molecules with a size comparable to that of neurological drugs used in the treatment of major CNS diseases, such as AD, PD, and Huntington's disease [120]. In another study by Wang et al., adeno-associated virus (AAV) vectors were delivered via administration of MBs prior to pulsed FUS at the hippocampus and motor cortex of WT mice, allowing non-invasive neural stimulation [125]. Remarkably, the volume of viral transduction was determined by the volume of BBBD [125].

A large number of studies have focused on the treatment of AD. AD has no established treatment in neurotherapeutics. The current therapeutic approaches improve associated symptoms, but they do not induce considerable disease-modifying effects. In the effort to address this, many studies have examined the feasibility of FUS-induced BBBD as a way of supplying drugs into the brain of mice models [126]–[129]. The transgenic mouse model of AD is extensively selected for such experiments, firstly because it is inexpensive and reproducible, and secondly because it exhibits abundant plaque load. As an example, transgenic AD mice were involved in a study by Burgess et al. [128], in which spatial memory improvement and behavioral changes were observed after repeated MRgFUS, probably resulting from reduced AD-related pathological abnormalities and increased neuronal plasticity of the treated areas. Repeated FUS with MBs was also proven to modulate similar positive therapeutic effects in female triple transgenic AD mice [130].

BBB impermeability also constitutes a major obstacle in brain cancer therapy [131]. In fact, the efficacy of chemotherapy in the treatment of brain tumors is limited by the BBB [131]. Authors in [132] assessed the efficacy of US-mediated BBBD to enhance the anti-tumor activity of a drug called Carboplatin in glioblastoma mouse models. Enhanced efficacy of the chemotherapeutic agent was observed for the mice treated with drug plus US, who showed delayed tumor growth and prolonged survival compared to the drug alone group [132]. Similarly, Ishida et al. [133] showed that MRgFUS is capable of enhancing drug delivery in a mouse model of Diffuse intrinsic pontine glioma (DIPG); a highly aggressive brain tumor in

children [133]. Enhanced drug delivery through the blood–tumor barrier was also evidenced after FUS therapy in combination with MBs in mouse models of brain metastasis from HER2-positive breast cancer [124], thus suggesting that the modality may enhance the transport of chemotherapeutic anticancer agents in breast cancer brain metastases [124]. **Figure 10** shows an example of a typical experimental setup used for FUS-mediated BBBD in mice.

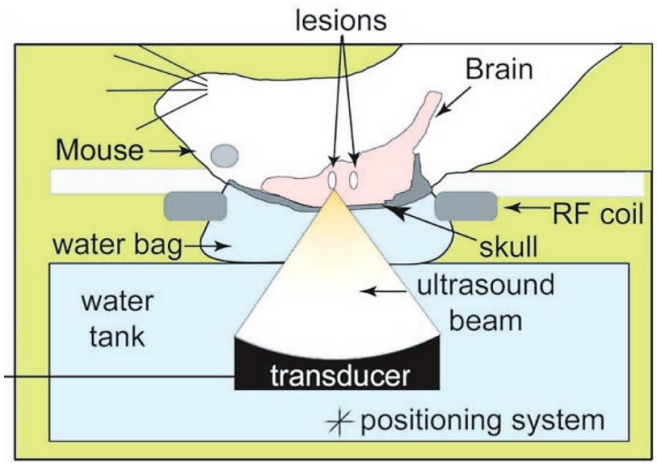

Figure 10: FUS applied in mouse brain. Figure obtained from Raymond et al. [129].

1.7 Study Overview and Research Objectives

MRgFUS was proven a very promising treatment modality. To date, many advances have been reported in medicine due to the use of the specific technology, especially in oncology and neurology. In the area of neurology, this modality has the potential to address the holy grail for researchers of performing completely non-invasive neurosurgery.

The methodology and tools for quality assurance (QA) of MRgFUS devices and emerging applications are still to be standardized. In this regard, there is an increased need for ergonomic and cost-effective TMPs that could mimic all the critical properties of body tissues, including acoustic, thermal, and MR properties, simultaneously contributing towards the minimization of animal testing.

In the framework of the current study, extensive literature search on TMPs, their properties and potential for use with the MRgFUS technology was carried out. Given that a lack of adequate literature on the relaxation properties of TMPs was identified, the study aimed to investigate the T1 and T2 relaxation times of various

agar-based phantom containing different concentration of inclusions. Furthermore, simple and cost-effective methods involving the use of TMPs for the performance assessment of MRgFUS devices and applications were proposed and investigated for their effectiveness.

Another objective was to develop realistic skull phantoms embedding soft tissue mimicking gels, as well as an anatomically accurate mouse model dedicated for testing transcranial FUS applications. The main purpose was to use these phantoms to examine the feasibility of trans-skull ultrasonic delivery using single element transducers.

The previously reported data suggests that FUS-mediated BBBD facilitates the passage of drugs naturally hampered by the BBB. Although the current data are very promising for many neurological conditions, BBB still constitutes a significant limiting factor for the application of therapies in the brain. Furthermore, there are numerous potential applications still to be explored. Thus, the research community underlines the urgent need for extensive research on the subject, which will eventually lead to novel technologies for therapeutic drug delivery across the BBB. Such research activities are essential to accelerating the translation of developed systems/applications from the laboratory to the clinic for the treatment of neurological diseases, especially those with no current effective treatments. Mouse models constitute a powerful tool in this effort.

The current study aimed to contribute in this regard through a series of experiments in mouse models. The study firstly aimed at carrying out an extensive literature search on the specific application of FUS-mediated BBBD and the delivery of therapeutic agents in the brain parenchyma. The next objective was to develop a compact single-stage positioning device dedicated for transcranial applications in small animal models and evaluate its performance in mice. Initially, the therapeutic protocol for safe and efficient BBBD by MBs-enhanced pulsed FUS was established. The next objective was to examine the potential of FUS-induced enhanced therapeutic agent delivery in the treatment of two different brain conditions; AD and HLD2. In the former case, the capability of the Aβ (1-40) antibody to penetrate the brain tissue following FUS-mediated BBBD in the AD 5XFAD mouse model was investigated. In the latter case, FUS-induced BBBD was

examined as a potential non-invasive method to facilitate brain transudation in P30 WT mice by administering different doses of an AAV9 vector and assessing its biodistribution within the CNS.

2 Simple, inexpensive, and ergonomic phantom for quality assurance control of MRgFUS systems

2.1 State of the art

The therapeutic benefits of FUS have been widely exploited in the area of oncology [134]. Malignant cells can be necrotized by concentrating the ultrasonic energy within the target region, thus increasing the temperature to lethal levels non-invasively [134]. The popularity of this technology is increasing substantially while QA tools for FUS devices and protocols remain to be standardized, thus raising the need for dedicated high-quality QA phantoms.

So far, gel-based TMPs have been the main tool for testing FUS hardware in the research and development (R&D) stage, including assessment of the thermal heating abilities of ultrasonic transducers [135]–[137] and the MRI compatibility of devices intended for MRgFUS applications [135]–[139]. To begin with, gel phantoms are considered suitable for thermal studies in that they enable insertion of thermocouples for benchtop temperature measurements [97]. In addition, their tissue-like MRI signal [140] is beneficial in monitoring thermal exposures in the MRI setting through the use of MR thermometry. Accordingly, they serve as a valuable tool for evaluating and optimizing therapeutic protocols before *in-vivo* applications, for example, by examining the impact of various scanning pathways on the off-target heating [68] and the formation of asymmetric lesions owning to thermal diffusion phenomena [65].

PAA gels containing thermosensitive ingredients, such as thermochromic ink that progressively changes colour under heating [92], BSA protein [92], and egg-white [141], were proposed for FUS studies, having the advantage of visualizing the formed lesions due to protein denaturation. Agar gels were also proven effective for FUS studies having the benefit of easy and cost-effective preparation, as well as the ability to simulate the critical thermal, acoustical, and MRI properties of several soft tissues depending on the type and concentration of added complementary ingredients [142]. On the contrary, gelatin-based phantom are only suitable for hyperthermia applications because they cannot withstand ablative temperatures [143]. Notably, the use of 3D printed materials and plastics to mimic bony tissues

is becoming popular in multi-modality phantoms intended for MRI and/or US imaging [93]–[95].

In terms of evaluating the motion accuracy of robotic mechanisms designed to navigate the ultrasonic transducer relative to the subject, the so far proposed R&D techniques include digital caliper-based methods [136], MRI imaging of the ultrasonic transducer or other dedicated MRI visible objects during step motion [144], and visual assessment of lesion formation in transparent thermosensitive phantoms [81], [135].

Regarding clinical use of test phantoms, the basic functionalities of a clinical MRgFUS device can also be tested by mapping the temperature rise during heating in a dedicated phantom. Several studies report on the use of MR thermometry during sonication in US/MRI phantoms as a simple QA method for clinical routine testing [145], [146]. In fact, this method has been the mainstay for clinical QA allowing for testing the acoustic power output, the targeting accuracy, the noise level introduced into the picture, and well as the size and shape of the focal spot. An indicative example is a 4-year retrospective study [146], which was performed to assess the basic functionalities of the first clinical MRgFUS system; ExAblate 2000 (InSightec Inc., Haifa, Israel) before each of 148 uterine fibroid treatment sessions.

The aforementioned QA measures are also employed before clinical deployment since they are extremely essential in the process of a system's technical acceptance [147]. In this regard, the MRgFUS system ExAblate 2000 has been tested by employing MR thermometry in TMPs designed to match the ultrasonic properties of tissue [147]. The focus positioning accuracy was examined by performing grid sonications in coronal and axial planes and comparing the commanded position with the actual position of the focus as defined by the peak temperature location through the controlling software.

Similarly, Vicari et al. [148] proposed a series of radiation force measurements, 3D modelling and geometrical tests for the daily *in-vitro* QA of the InSightec ExAblate 2100 equipment, with emphasis on the delivered power and position of the focus. The authors followed an interesting technique to assess the focus positioning

accuracy and software reliability by sonicating a 96 well plate filled with a thermosensitive BSA-doped PAA gel [148].

While the need for phantoms dedicated to QA of FUS equipment has long been recognized [149], their development was delayed until recently, when two relevant studies were published [150], [151]. The proposed QA phantoms are both based on the concept of placing ultrasonic calibration equipment in a plastic container that is filled with a TMP. To be more specific, Acri et al. [150] developed an ergonomic phantom for clinical routine QA of MRgFUS devices consisting of a hollow PMMA cylinder that can host various movable inserts. These could be PMMA holders specially designed to support instruments, such as a precision balance or a thermometer, or small teflon pieces simulating microcalcifications. According to the authors, it is filled with different fluids depending on the tested parameters, which may be the precision and dimension of the FUS spot, the target temperature, and the linearity of output power.

Ambrogio et al. [151] developed a QA phantom of similar design to evaluate the performance of the Sonalleve commercial MRgFUS system (Philips, Canada) over a 12-month period. The developed phantom is a PMMA cubic structure that embeds a 3D-printed bone-mimic disk made of VeroWhite Plus material and 4 T-type thermocouples within an agar-based soft TMP in clinically relevant places for the specific intended therapeutic modalities of this system.

It becomes clear that gel phantom-based techniques have been essential in both R&D and clinical testing of MRgFUS devices. Although widely accepted, these techniques suffer from many potential sources of error related to human or instrument failures, which may cause the results of assessment to be interpreted incorrectly. For instance, gel phantoms are prone to air or other inhomogeneities that may be introduced during the preparation process, as well as to gradual water loss, which are very possible to influence the formation of uniform lesions and thus the reliability of measurements. Furthermore, since phantoms have limited lifetime, different phantoms will be used at different days, which is not ideal when examining the functionality and loss of precision on a routine basis.

Following the aforementioned unmet needs, in this study, we propose the use of an acrylic thin film as the most cost-effective and ergonomic way of evaluating the

functionality and stability of MRgFUS equipment over time. A robotic device dedicated to MRgFUS preclinical applications, and the relevant treatment planning/ monitoring software were employed in the study. The QA methodology is detailed through a series of experiments designed to assess the performance of this system in terms of targeting accuracy, heating effects of the ultrasonic transducer, software functionality, and proper communication between hardware and software.

2.2 Materials and methods

2.2.1 Quality assurance acrylic film

The QA phantom proposed in this study is a clear film made of acrylic plastic with a thickness of 0.9 mm (FDM400mc print plate, Stratasys, 7665 Commerce Way, Eden Prairie, Minnesota, USA). The ultrasonic attenuation of the film was estimated at 8.5 dB/cm-MHz (at 2 MHz) according to the transmission through technique [152]. The following QA tests take advantage of the almost complete reflection of ultrasonic waves at the plastic–air interface, which results in almost immediate lesion formation on the upper side of the film at a threshold of applied acoustic energy. Accordingly, in all experiments, the upper side of the film involved air while degassed water was used as the coupling media between the transducer and the bottom surface of the film, as shown in **Figure 11**, so lesion formation was mainly based on reflection.

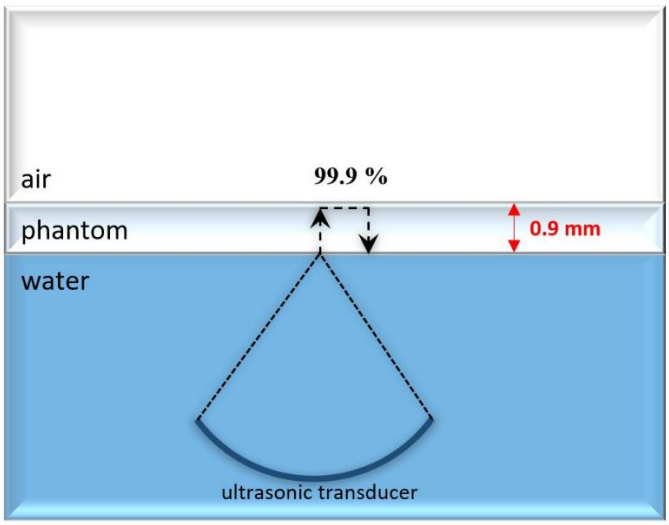

Figure 11: Concept of lesion formation on the plastic film.

2.2.2 MRgFUS robotic device for preclinical use

A preclinical MRgFUS robotic device previously described in detail by Drakos et al. [136] was employed in the study. In brief, the system comprises a mechanism enclosure where all the mechanical and electronic components are hosted and another separate water enclosure where the transducer is actuated. The water enclosure includes an acoustic opening at the top for placing the target.

For the purpose of the current study, the transducer comprised a single element spherically focused ultrasonic piezoelectric (Piezohannas, Wuhan, China) with a nominal frequency of 2.75 MHz (Radius of curvature: 65 mm, Diameter: 50 mm, efficiency: 30 %). The transducer was powered by an RF amplifier (AG1016, AG Series Amplifier, T & C Power Conversion, Rochester, US).

The system was integrated with and controlled by a custom made treatment planning-monitoring software which provided the ability to plan sonications in rectangular grids or complex patterns for full coverage of any segmented area on MRI images, as well as to define the sonication (acoustic power and sonication time) and grid parameters (spatial and temporal step).

2.2.3 Power field assessment

The power field of the 2.75 MHz ultrasonic transducer was evaluated by sonicating the plastic film at varying distance from its surface. The transducer was securely mounted on the bottom part of a plastic holder facing upwards to the plastic film. Careful design of the holder was followed to ensure horizontal placement of the film, thus minimizing sound refraction phenomena. The holder also included a height adjustment mechanism for changing the transducer-film distance with a 10-mm step. The setup was hosted in a tank, which was filled with degassed, deionized water up to the upper surface of the plastic film to achieve the aforementioned “water-plastic-air” configuration. Electrical power of 150 W (acoustic power of 45 W) was applied for 30 s in continuous mode for different transducer-film distances of 40 to 90 mm. The diameter of the formed lesion at each tested distance was measured using a digital caliper.

2.2.4 Assessment of change in lesion size by varying sonication parameters

In this experimental part, the QA film was securely mounted on the acoustic opening of the device using a dedicated holder, as shown in **Figure 12**. The distance from the transducer was adjusted to equal the radius of curvature. Degassed water was used as described above to ensure ultrasonic coupling with the bottom surface of the film. The effect of the power (10-70 W electric power) and duration of sonication (1-11 s) on lesion formation was examined independently by performing sonications spaced by 1 cm.

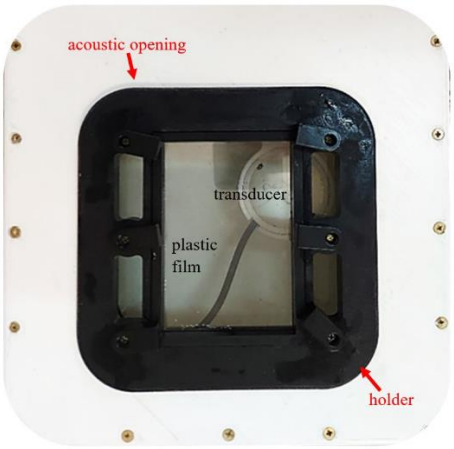

Figure 12: Photo of the experimental setup with the phantom fixed to the acoustic opening of the MRgFUS device above the FUS transducer.

2.2.5 Accuracy and repeatability of motion assessment

This experimental part was carried out to assess the accuracy and repeatability of motion, as well as whether the software commands are properly executed using a similar setup as detailed above. The film was sonicated by robotically moving the transducer along predefined pathways; square or irregular grids using the commands of the relevant software. The planned sonication spots were visited in a Zig-Zag pathway using varying motion step. An acoustical power of 6 W was applied for 5 s to each spot while a waiting time of 60 s was left between successive sonications to ensure adequate heat dissipation in the phantom.

2.3 Results

Lesions of different dimensions were formed by sonicating the acrylic film at varying distance from the transducer surface and served as indicators of the power film distribution. The sonicated films are shown in **Figure 13** with the measured lesion diameter indicated. Among the tested distances, the largest lesion is observed at 40 mm and gradually decreases in size until the distance of 60 mm, whereas at 80 mm it increases again, thus demonstrating heating in the far-field region. This change in lesion size with varying distance gives a good approximation of the power field distribution in that lesion dimensions can be defined as the half width and length of a Gaussian power distribution at each distance.

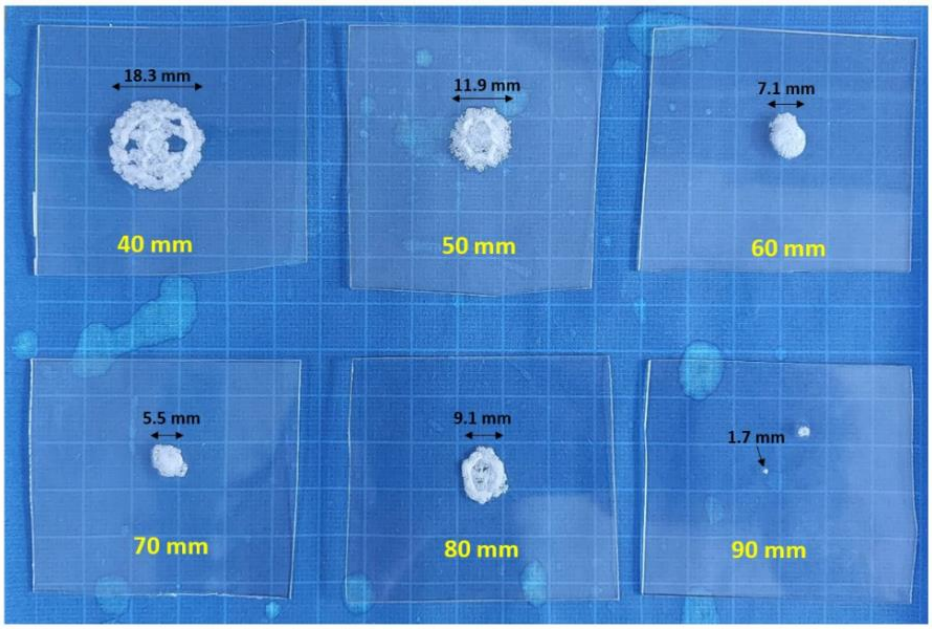

Figure 13: Photo of acrylic films sonicated at increasing distance from the transducer using acoustical power of 45 W for 30 s and the 2.75 MHz transducer (radius of curvature of 65 mm and diameter of 50 mm), indicating the diameter of the formed lesions.

The lesion size at a specific distance from the transducer surface can be controlled by varying the sonication parameters. **Figure 14** shows the change in lesion size by varying the electric power from 10 to 70 W while keeping constant the sonication duration at 6 s at the focal plane. The distance between successive sonications was set at 1 cm.

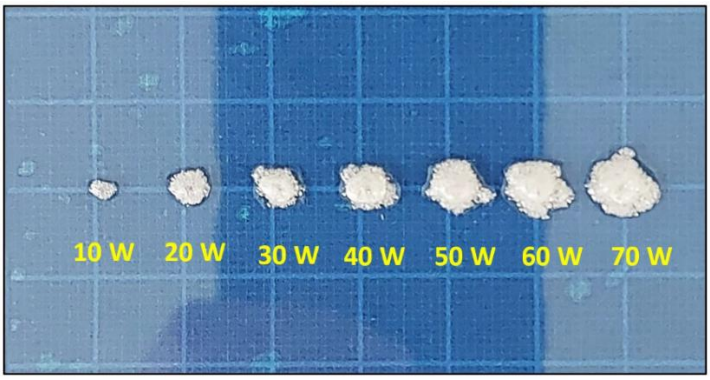

Figure 14: Photo of lesions formed using varying electric power of 10 to 70 W for a constant sonication duration of 6 s.

Figure 15, **Figure 16**, and **Figure 17** show indicative results of multiple lesions formed on the phantom following pathway planning on the dedicated software. **Figure 15** shows discrete lesions formed in a 5 x 5 square grid using a spatial step of 10 mm (each spot exposed to 20 W electric power/ 6 W acoustical power for 5 s). The overlapping lesions shown in **Figure 16** were created after sonication in a 20 x 20 grid using identical ultrasonic parameters but a smaller spatial step of 1 mm. An indicative result of sonication in irregular pattern with similar sonication protocol and a 3-mm step is shown in **Figure 17**. Note that the ablated area matches well the segmented area in the software. The selection of grid step defined the formation of discrete or overlapping lesions. Overall, the lesion patterns demonstrate good motion and alignment accuracy.

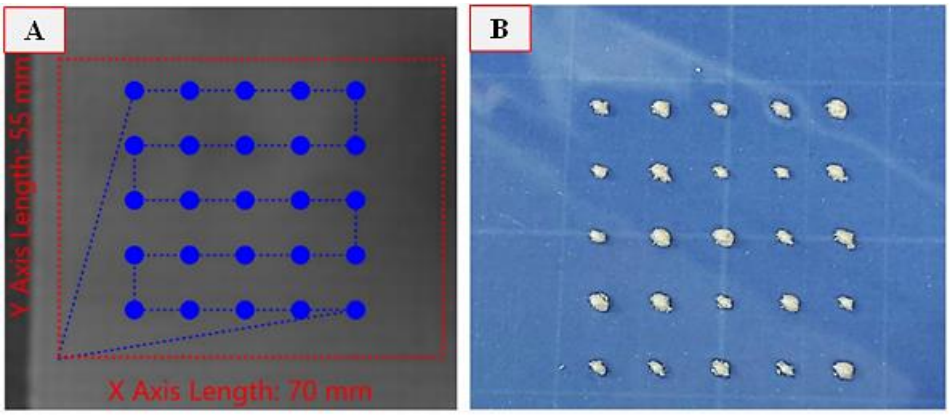

Figure 15: **(A)** Software screenshot showing the sonication spots (5 x 5 grid) and Zig-Zag pathway as planned on an MRI image of an agar phantom. **(B)** The corresponding lesions formed on the plastic film using acoustic power of 6 W for 5 s at each spot, with a spatial step of 10 mm, using the 2.75 MHz transducer (radius of curvature of 65 mm and diameter of 50 mm).

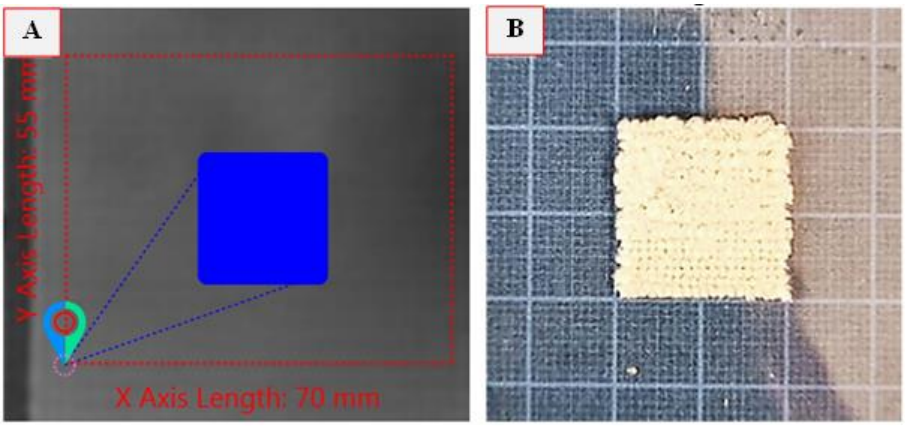

Figure 16: **(A)** Software screenshot showing the sonication area (20 x 20 grid) as planned on an MRI image of an agar phantom. **(B)** The corresponding overlapping lesions formed on the plastic film using acoustic power of 6 W for 5 s at each spot, with a spatial step of 1 mm, using the 2.75 MHz transducer.

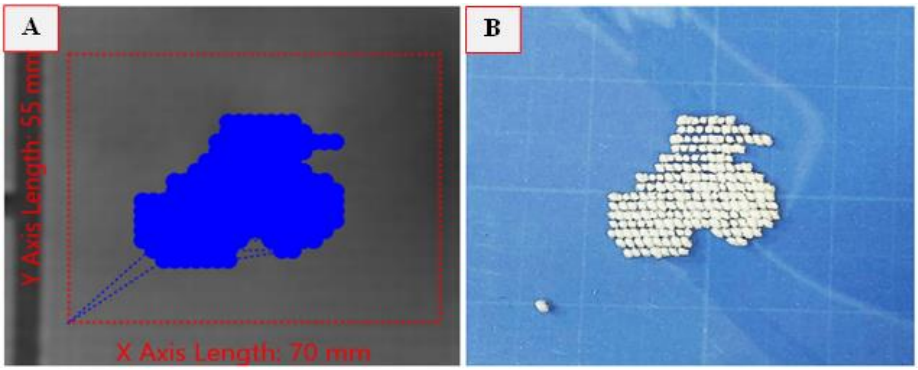

Figure 17: (A) Software screenshot showing the segmented irregular area on an MRI image of an agar phantom. **(B)** The corresponding lesions formed on the plastic film using acoustic power of 6 W for 5 s at each spot, with a spatial step of 3 mm, using the 2.75 MHz transducer.

2.4 Discussion

Through a literature search, it can be easily concluded that while there are well established methods for calibrating FUS equipment, the methods and tools for QA of MRgFUS robotic devices are still far from being standardized. Herein, a thin acrylic film was proposed as the cheapest and most easily accessible QA phantom for assessing the performance of MRgFUS hardware and software. Although, in this study, we used a 0.9 mm-thick print plate obtained from a Stratasys printer, one could simply buy a similar product from a bookstore at a very low price.

Specific methods involving the use of the proposed film were utilized for assessing the functionality of an MRgFUS preclinical robotic device. The setup is extremely simple and is based on the concept of "water-plastic-air" described previously, where lesion formation is mainly the result of sound reflection at the plastic/air boundary.

Regarding quality assurance of the FUS transducer, the phantom provides indication of the beam's cross section. By collecting several slices in cross section, it is possible to get qualitative information on the power field distribution of the FUS transducer in axial direction. In addition, by adjusting the power and time it is possible to control the size of the individual lesions, thus simulating different FUS protocols. Following experiments with varying power and time, an acoustic energy of 18 W was proven sufficient to produce a lesion of easily measurable dimensions (≈ 2 mm in diameter) on the proposed phantom. A limitation of this approach is that evaluation is not possible in the axial direction.

Furthermore, the phantom was proven an efficient tool for assessing the accuracy and repeatability of robotic motion by navigating the robotic system in grid patterns and producing discrete lesions. Note that this was also demonstrated in a previous study [144], but it was further assessed with extensive experimentation of various motion algorithms. It is interesting to note that the formed lesion patterns did not show evidence of thermal diffusion.

By using small spacing during navigation, it is also possible to assess several navigation algorithms as they are used in actual treatments. In this study, complex shapes were sonicated successfully as evidenced by the lesions created on the plastic film, following planning of the sonication sequence on the software. This method helps to assess not only the software performance, but also its communication with the integrated robotic system and whether motion commands are properly executed.

The main limitation of the proposed QA methodology is that it cannot be used as a stand-alone tool to optimize clinical therapeutic protocols since it has different acoustic properties and response to heat than soft tissues. The mechanism of thermal diffusion that affects the formation of uniform lesions and treatment outcome in tissue [65], [66] is less effective in plastics due to the difference in thermal

conductivity. Besides, the mechanism of lesion formation is completely different. This limitation is also considered a benefit in that it allows for reliable assessment of the planning algorithms and robotic motion without phantom-dependent parameters affecting the lesion's size and shape significantly.

So far, tissue-mimicking gel phantoms have been the major tool for characterizing the performance of preclinical and clinical MRgFUS systems. However, they have a limited lifetime and are prone to air or other inhomogeneities, which are very likely to shift or distort the formed lesions. In this regard, they are not ideal for assessing the system's functionality and stability over time or the motion accuracy of robotically positioned MRgFUS devices. Furthermore, in case a thermosensitive TMP is utilized that forms permanent lesions, it should be replaced after each QA test. Notably, two recently published articles report the development of more complex phantoms containing TMPs and FUS measurement tools for QA of clinical MRgFUS devices [150], [151]. In this study, the proposed QA phantom and relevant methodology are simpler and more ergonomic, highly cost-effective, universal, and do not depend on human or instrument-related factors. Although it is not reusable since the formed lesions are permanent, this is not a problem due to its very low cost.

Overall, the obtained results qualify the proposed acrylic phantom as a reliable QA tool for routine testing of MRgFUS robotic devices through a series of simple and quick tests. Accordingly, it could be used for the detection of defects in system's performance and ease maintenance over its lifetime, while concurrently contributing towards developing quality control and calibration guidelines for clinical practices. It is though underlined that state-of-the-art gel-based methods should also be employed when testing therapeutic protocols to optimize the efficiency and safety before *in-vivo* use.

3 Review of MR relaxation properties of tissue-mimicking phantoms

3.1 Methodology

The PubMed database was mainly used since it includes a wide variety of sources in the specific field of biomedical sciences covering all time periods, with 7.1 million articles archived. A systematic search of the PubMed papers was carried out using specific vocabulary. The keywords {T1, MRI, US, phantom} were applied without any year range filter, thus not limiting the amount of data and resulted in a total of 608 results. Additional exclusion criteria were not applied, and all articles were considered to eliminate the possibility of missing articles of irrelevant titles which may actually include useful information. A scientific staff member with experience in therapeutic US and TMPs fabrication evaluated the results to ensure all criteria were applied properly and select the relevant articles for inclusion. A total of 39 articles were considered relevant. Supplementarily, another 5 articles were retrieved from Google Scholar searches of similar keywords.

The search results are organized in three sections. The first one briefly introduces the critical properties of phantoms intended for MRgFUS studies to facilitate the reader's understanding. Next, the included articles are classified into five main categories based on the phantom type (i.e., gelling agent used). Critical tissue mimicking properties and any interesting trend in MR properties of each category are listed. The rest of the paper briefly summarizes and discusses the search results and underlines opportunities for further research in the field that would possibly close gaps identified in existing studies. To the best of our knowledge, this is the first attempt to review the MR properties of TMPs.

3.2 Critical Parameters of MRgFUS phantoms

Firstly, TMPs intended for FUS studies should possess similar acoustic properties with body tissues. The speed of sound in the medium, characteristic acoustic impedance, and attenuation coefficient are probably the most significant properties to be emulated [96], [111]. The thermal characteristics of biological tissues need to

also be replicated by phantoms intended for thermal studies with FUS. The thermal profile of a TMP during FUS exposure is mostly governed by specific parameters, among which the most common are the specific heat capacity, thermal conductivity, and thermal diffusivity [96], [111]. These parameters are particularly crucial in the process of assessing tissue necrosis during ablation under the guidance of MRI. In fact, since the therapeutic result is evaluated via thermometry based feedback, a tissue like thermal behavior is of paramount importance, whereas rigorous modeling of acoustic properties is not required in this regard.

Besides the thermal behavior of TMPs, MR parameters are also critical in determining their suitability for MRgFUS applications. As previously reported, both the contrast in MR images and temperature monitoring during FUS exposures are based on changes in the magnetic relaxation times T1 and T2 of tissues [9]. Most importantly, these parameters greatly affect the contrast between normal soft tissue and FUS lesions [112]–[114]. Accordingly, it is essential for MRgFUS phantoms to produce tissue-like MR signal in the process of evaluating therapeutic protocols.

3.3 Gel phantoms for diagnostic and therapeutic modalities

3.3.1 Agar gels

Agar probably constitutes the most widely used gelling agent for the construction of phantoms for multiple purposes, as confirmed by the current literature search. The widespread use of agar gels may be attributed to several factors, including their ease and low-cost fabrication, as well as their sufficient mechanical strength, which allows them to be formulated in different shapes and layered structures [153]. Another significant benefit of agar as a gelling agent relates to its high melting point of near 78°C [154], which makes it ideal for thermal studies. Additional benefits of these gels will become apparent through the remainder of the paper.

The standard fabrication techniques of agar gels involve heating up degassed/deionized water in an appropriate buffer to about to 50ºC when the agar powder is slowly added, and then gradually heating the mixture to the melting point of agar, while it is continuously stirred to mitigate aggregation of agar in water

[110], [155]. The properties of agar gels can be easily and independently varied by adjusting the concentration of other ingredients added during the manufacturing process [110], [153], [156].

A wide variety of agar-based phantoms simulating thermal and acoustical properties of different types of soft tissue can be found in the literature [93]–[96],[156]–[160]. Ultrasonic attenuation was found to vary with the addition of scattering particles such as silicon dioxide [156], magnesium [157], calcium [157], potassium [157], cellulose [158] and graphite [158] particles, as well as with the addition of glass beads [159]. Evaporated milk was proven a dominant absorber of acoustic energy [153]. Notably, glycerol has been proposed as a modifier of ultrasonic velocity [158].

Agar gels can also provide tissue-like signal (T1 and T2) in MRI [161], and thus, they were predominantly selected for validating new MRI protocols and imaging techniques [155], [161]–[169]. MRI compatible phantoms simulating specific body parts such as brain [170], prostate [171], carotid [161], renal artery [172], and neonatal brain [173] exist in literature. Proper MRI imageability is also required for MRgFUS phantoms since accurate replication of MR relaxation properties is essential for producing tissue-like signal in MRI and more accurately testing and optimizing therapeutic protocols. In this regard, several agar-based TMPs were designed specifically for thermal ablation studies [93], [95], [110], [174].

Literature data clearly indicates that the transverse relaxation time T2 predominantly depends on the agar concentration [155], [162], [163], [175]–[178]. As described in more detail below, agar also served as the main T2 modifier in phantoms containing other types of gelling agents [175], [177]. Furthermore, the addition of MR contrast agents enables better MR visibility while concurrently affecting the magnetic relaxation properties of phantoms [91], [167], [168], [173]. Gadolinium-(Gd) based contrast agents were extensively used allowing adjustment of MR relaxation times, more significantly affecting the longitudinal value T1 [167], [168], [173]. T1 was also varied by incorporating different concentrations of paramagnetic ion salts such as Manganese(II) chloride ($MnCl_2$) [164], Nickel chloride ($NiCl_2$) [165], and Gadolinium(III) chloride ($GdCl_3$) [166]. Moreover, varying concentration of copper (Cu) ions enables changing the T1 values of agar

gels [155]. It is important to note that addition of Cu ions requires the presence of another ingredient called Ethylenediaminetetraacetic acid tetrasodium hydrate (EDTA), which combines to Cu ions forming a stable free molecule; Cu-EDTA. Otherwise, Cu ions will be deposited on agar and loss their T1-modifying capacity [155]. In a representative study by D'Souza et al. [178], the concentration of agar (T2 modifier) and Cu-EDTA (T1 modifier) were properly selected, allowing the creation of phantoms simulating the magnetic relaxation properties of prostate and muscle tissue.

By using preservatives, such as thimerosal [178] and sodium azide (NaN_3) [160], bacterial invasion is prevented, thus extending the phantom lifetime. It is also noteworthy that several studies proposed the addition of animal hide gelatin in combination with agarose as a way to prevent the expulsion of an aqueous solution that may be produced in agar only gels [179].

Although agar-based phantoms were proven functional in a wide range of applications, they are accompanied by some limitations. Firstly, they have relatively low toughness and thus are easily fragile [90]. Also, they provide limited optical opacity, which prevents direct visualization of lesion formation in cases of thermal exposures [90]. Extensive results of prior research are summarized in **Table II1** of **Appendix II**. The referenced study, purpose of study, phantom recipe, and estimated relaxation times T1 and T2 are listed in this table.

3.3.2 Gelatin gels

Another category of phantoms that are easily fabricated and were proven factional is the gelatin-based phantoms [98], [99], [180]–[182]. Again, the gelation process involves solving gelatin powder in aqueous solutions while several soft tissues can be accurately mimicked by adding a proper concentration of other ingredients to the base recipe [98], [99], [180]–[182]. For instance, evaporated milk [180] and graphite powder [183] can be included to control the acoustic behavior of these gels, whereas the addition of ethanediol and polyethylene powder allows modification of electrical properties [184]. These phantoms can be manufactured in a low cost and easy way, with proper mechanical stiffness by incorporating cross-linkers during the phantom-making process [99].

Similar to agar phantoms, gelatin-based gels doped with an MRI contrast agent, most commonly a Gd-based agent, constitute a handy tool for MRI applications [56]**.** In cases where US compatibility is desired, acoustic modifiers should also be added in these phantoms. Farrer et al. [99] used porcine gelatin powders with three different bloom values (125, 175, and 250) for the construction of MRgFUS phantoms of different mechanical stiffness, in which evaporated milk was the main attenuation component. The estimated T1 and T2 values varied for the different bloom types of gelatin [99]. An interesting trend was also observed by Hofstetter et al. [180], who developed a gelatin-based MRI/US compatible phantom containing psyllium husk as the ultrasonic scattering agent. Interestingly, both relaxation times were found to be decreasing with increasing concentration of psyllium husk. Again, evaporated milk was included replacing a percentage of the water component to enhance ultrasonic absorption [180].

Another typical material found in gelatin phantoms is oil [98], [181]. These phantoms are commonly referred to as oil-in-gelatin phantoms and are mainly involved in elastography studies, in which the elastic modulus depends on the volume percentage of oil [181]. Remarkably, the oil concentration was shown to have a noticeable effect on the MR relaxation properties of oil-in-gelatin dispersions [98], [181]. In a study by Madsen et al. [181], the use of safflower oil was proven suitable particularly for US elastography [181]; however, the resultant relaxation properties of phantoms differed considerably from those of soft tissue [181]. Advantageously, Yuan et al. [98] selected pure vegetable oil to develop an oil-in gelatin human thigh phantom intended for radiofrequency heating because its thermal and MR properties are comparable to that of human fat. In this category of phantoms, thimerosal served as the preservative component [181].

Typically, gelatin phantoms possess a relatively low mechanical strength, as well as a low melting temperature making them impractical for thermal regimes exceeding 50°C [185]. These limitations can be fairly addressed with the addition of a bonding agent such as formaldehyde [186] or glutaraldehyde [187]. These chemicals act as cross-linkers of gelatin [54], thus increasing the stiffness and temperature tolerance during thermal exposures in gelatin phantoms [188]. In fact, the typical melting point of gelatin of about 32 ºC [143] can be increased to more

than 60 ºC when using a cross-linking agent [188], [143]. Though this technique has essential benefits, it may cause unfavorable changes in other critical parameters [99].

Phantoms composed of mixtures of agar and gelatin have emerged as alternative candidates for elastography [143] and MRI [179], [188] applications. Employment of agar results in stiffer phantoms (i.e., higher Young's modulus) with increased geometrical stability while at the same time enabling the embedment of inclusions to gelatin gels [143]. To be more specific, a different dry-weight gelatin concentration between background and inclusions could result in over-time size changes of inclusions due to osmotic effects [143]. This phenomenon does not occur in the case of agar, and thus, a phantom of proper stability can be produced by incorporating different agar concentrations between background and inclusions [143]. It is also noteworthy that several studies proposed the addition of animal hide gelatin in combination with agarose as a way to prevent the expulsion of aqueous solution which may be produced in agar only gels [179].

Cu ions have the capacity to lower T1 values of agar/gelatin phantoms [179], [143]. They are usually added in the form of ionic salts such as Cupric chloride ($CuCl_2$). As previously described for the agar gels, addition of EDTA is required for preventing the arrestment of ions to gelatin molecules [179], [143]. A representative example is a study by Madsen et al. [143], who developed an agar/gelatin elastography phantom consisting of agar as the stiffness agent, Cu-EDTA as the T1 modifier, formaldehyde as the cross-linking agent, and glass beads as the attenuation and backscatter component. Sodium chloride (NaCl) was also included to offer tissue-like NMR coil loading. Alternatively, Blechinger et al. [188] selected glycerol instead of paramagnetic ions to attain the desired T1 in an animal hide gel/agar phantom. Variations in glycerol concentration significantly varied T1 values, whereas T2 was minimally affected. In fact, T2 was strongly affected by the animal hide gel concentration [188], confirming that the relaxation times can be varied independently. In line with the previously reported data, the resultant phantom showed durable stability, without any fluid extrusions, most probably due to the addition of formaldehyde and n-propanol offering antibacterial activity, also

given the agar-enhanced rigidity. The proposed gelatin-based phantoms and their T1 and T2 relaxation times are summarized in **Table II2** of **Appendix II**.

3.3.3 Polyacrylamide gels

Another candidate material for fabrication of stable TMPs is PAA [91], [92], [141], [189]–[192]. PAA is probably the most popular material for fabricating heat-responsive phantoms, primarily due to its high melting point [189]. It is also of paramount importance that these phantoms offer optical transparency [190], enabling visual confirmation of coagulation in the phantoms. Common catalysts added for activating PPA polymerization are the ammonium persulfate (APS) and tetramethylethylenediamine (TEMED) [91], [92], [141], [193].

Thermoresponsive proteins such as Bovine serum albumin (BSA) were found to enhance acoustic absorption in PAA phantoms [191]. When these proteins are heated at lethal temperatures undergo irreversible changes in MR values and become opaque, thus enabling discrimination of the heated area both visually and via changes in MRI signal intensity [191], [192]. Specifically, white-opaque lesions are formed when BSA is coagulated at temperatures between 60°C and 70°C. Additional ingredients such as evaporated milk, corn syrup [194], glass beads [195], and silica particles [92] can be used to adjust the acoustical properties of PAA-BSA phantoms in the range of human tissues.

Bazrafshan et al. [193] developed an MR visible liver mimicking phantom intended specifically for Laser interstitial thermal therapy (LITT) applications. The PAA gel was doped with BSA protein for visualization of thermal effects. PVA microspheres were also incorporated to enhance photon scattering. The addition of two different MR contrast agents; Magnevist and Lumirem, allowed modification of the T1 and T2 relaxation times, respectively [193]. NaN_3 was used to prevent microbial growth [193]. Notably, a PAA-based phantom for LITT applications may also contain bovine hemoglobin as a photon absorber [91].

TMPs containing thermochromic ink that exhibits progressive colour change upon heating can also be used for visual monitoring of thermal ablation [92]. Eranki et al. [92] developed a PAA-based thermochromic TMP intended for HIFU applications. Both BSA protein and a thermochromic ink that under heating

changes colour from white to magenta were added. Proper concentration of these inclusions allowed visualization of well-defined regions of permanent colour change upon heating, which correlated well with MRI thermometry data and regions of hypointensity on T2-weighted images [92]. Similar to agar-based phantoms, silicon dioxide served as the attenuation component [92]. In this category of phantoms, NaCl is usually included to adjust electrical conductivity [92], [193]; however, the relaxation values of PAA gels were found independent of the NaCl concentration [196].

Egg-white is another heat-responsive material that was proposed for irradiation studies with FUS as a less expensive alternative to BSA [141]. Careful selection of egg white concentration is critical to maintaining adequate optical clarity in phantoms. A suitable egg white (my mass) concentration of 10 to 40% was proposed by Takegami et al. [141] for sufficient visualization during HIFU exposures. Although the acoustic properties of the proposed phantom were found to be similar to those of soft tissues, MR relaxation properties were not investigated.

Toxic materials are typically employed complicating the preparation of PAA gels and generating safety concerns [197]. Specifically, the procedure involves polymerization of acrylamide, a toxic monomer, which requires proper care and may be hazardous when PAA-gels are not stored under proper environmental conditions [197]. Another limitation relates to the use of BSA or egg white, which undergo permanent changes when coagulated, thus making the phantoms unsuitable for repeated use. The relevant studies are listed in **Table II3** of **Appendix II**.

3.3.4 Carrageenan gels

Carrageenan constitutes a common additive that can be used as a bonding material for phantom fabrication [177]. Although, as a poly-saccharide, it generally presents similar characteristics with agar, carrageenan gels were proven less fragile than agar-based gels [177]. They are elastic and can be easily shaped to form strong phantoms of any configuration without the addition of other reinforcing materials [177]. It should though be noted that carrageenan phantoms are not suitable for HIFU exposures since they can only withstand temperatures of up to about 60°C before liquefaction [177].

The addition of carrageenan in agar gels seems to solve the problem of low toughness in agar-only gels [97], [175]–[177]. Yoshida et al. [177] developed an MRI phantom using carrageenan as a solidifier and agarose as the T2-modifying component. T1 values were adjusted by addition of proper $GdCl_3$ concentration. Furthermore, inclusion of NaCl affected both T1 and T2 values, with T1 being affected in a slightly larger degree [177]. Accordingly, in a study by Yoshimura et al. [175], both relaxation times T1 and T2 were found to be increasing, respectively, upon increasing concentration of $GdCl_3$ and agarose at a fixed concentration of carrageenan. Again, carrageenan served as the solidifying agent allowing the creation of a robust phantom, while agarose served as the T2 modifier [175]. Neumann et al. [176] have proposed a carrageenan phantom mimicking thorax tissue, in which T1 was adjusted by adding proper amount of gadoterate meglumine. Again, NaN_3 may be added in this phantom type acting as an antiseptic [176], [177]. The proposed carrageenan phantoms are summarized in **Table II4** of **Appendix II**.

3.3.5 Other gelling agents

Other former candidates that were identified include PVA [100]–[102], PVC [103]–[105], silicone [106], [107] and TX-150/151 [108], [109]. These materials served as gelling agents in phantoms intended for imaging applications. Detailed results can be found in **Table II5** of **Appendix II**.

PVA is a water-soluble rubbery synthetic polymer with which cryogels can be formed through a repeated freeze-thaw method [100]–[102]. PVA cryogels doped with Gd-based contrast agents were proposed for MR imaging studies [100]. It should be noted that different types of contrast agents can be used to offer compatibility with multiple imaging modalities. For instance, a PVA-based brain phantom containing Barium sulfate ($BaSO_4$) as computerized tomography (CT) contrast agent, Copper sulfate ($CuSO_4$) as MR contrast agent, and talcum as US contrast agent was recommended by Chen et al. [101] for multimodal imaging. In such cases, the MR contrast agent acts as the main relaxation time modifier. A notable trend observed by Surry et al. [102] is that increasing number of freeze-thaw cycles during phantom preparation results in lower T1 relaxation times.

Another common synthetic chemical polymer is PVC. Soft PVC phantoms are relatively low-cost, with long-term easy storage [104]. The fabrication process involves heating up a mixture of PVC powder and softener until polymerization under constant stirring [103]–[105]. PVC gels mimicking soft tissue are useful in MR and US elasticity imaging [104]. Chatelin et al. [104] found that their MR relaxation properties are slightly influenced by the variation of the mass ratio PVC /plasticizer. In this study, cellulose served as a source of echogenicity without consistent influence on relaxation values [104]. Another study [105] confirmed that the MR properties of PVC gels can be regulated to mimic different soft tissues by adjusting the ratio of the softener to polymer [105]. Remarkably, inclusion of glass beads moderately lowered T2. Mineral oil was also incorporated to facilitate needle insertion applications but did not produce any apparent effect on T1 or T2 [105].

More recently, a polysaccharide material called TX-150 has been introduced as a candidate gelling agent for the construction of water-based TMPs for MRI applications [108], [109]. Groch et al. [109] prepared a lesion phantom for MRI, in which increasing weight % concentration of TX-150 in degassed water shortened both relaxation times. This study suggests that T1 and T2 can be altered independently by incorporating metal phthalocyanines and 2-2-diphenyl-1 picrylhydrazyl, respectively [109]. A modified form of this polysaccharide; TX-151 was used in the development of an MRI compatible breast phantom by Mazzara et al. [108]. The amount of gelling agent had a weak influence on relaxation times. Aluminum powder served as the dielectric component having insignificant effect on T1 values. On the other hand, T2 was significantly shortened upon addition of aluminum and largely affected by varying aluminum (Al) concentration [108]. The relaxation time T1 was found to be decreasing with increasing Gd-DTPA concentration. Authors concluded that variation of these additives allows the creation of phantoms with a wide range of tissue-comparable MR relaxation times [108].

3.4 Discussion on literature search outcomes

Due to the increasing popularity of the MRgFUS technology, there is a critical need for TMPs that can replicate all the critical characteristics of human tissues,

including acoustical, thermal, and MR properties. So far, TMPs have been widely characterized in terms of thermal and acoustical properties; however, more limited data is available about their MR properties. Thereby, this study aimed to review the MR relaxation properties of different phantom types through a systematic search of the literature. Although various physical properties of the referenced phantoms were discussed through the article, particular focus was placed on their T1 and T2 relaxation values.

In this article, the several phantoms previously proposed for a wide range of applications were briefly reviewed by category of gelling agent. However, the included studies could also be classified according to the intended application of the proposed phantom. Some studies were designed to investigate the physical parameters of phantoms intended specifically for thermal therapy studies, whereas the vast majority of included articles have proposed TMPs for imaging or QA purposes.

As confirmed by the search results, agar is probably the most common gelling agent for widespread applications. In fact, the majority of identified studies reporting MR properties of phantoms (~43%) involve the use of agar-based gels [93], [110], [155], [161–174], [178]. Agar has been quite extensively used as a gelling agent in FUS phantoms simulating different soft tissues, with additional materials added to adjust their thermal and acoustical properties [93]–[96]. In this regard, critical properties that have been sufficiently investigated include the speed of sound, acoustic attenuation, acoustic impedance, thermal diffusivity, specific heat capacity, and thermal conductivity [93], [96], [110]. In addition, their tissue-like MR signal makes them the material of choice for validating new MRI protocols and imaging techniques [155], [161]–[169]. In such cases, modifiers of acoustic properties such as glycerol [161], [172], cellulose particles [161], milk [178], and glass beads [178], are also added and adjusted to provide tissue-like US visibility.

Regarding thermal studies, PAA [91], [92], agar [93]–[96], and gelatin [98], [99] constitute the preferable gelling agents, each one having its own benefits and limitations. The ability of all three to accurately simulate physical properties of various biological tissues upon addition of proper concentration of inclusions has been demonstrated [90], [97]. Both agar and PAA materials are characterized by

temperature tolerance sufficiently high to maintain their physical and mechanical properties during HIFU exposures [154], [189]. On the other hand, gelatin phantoms lack the capacity to withstand ablation temperatures. Their low melting temperature makes them unsuitable for thermal studies in which temperatures exceed 50°C, and thus, are only recommended for hyperthermia applications [185].

Upon proper use and storage, gelatin gels can maintain long-term stability; however, they generally possess relatively low mechanical strength, which is strongly dependent on temperature variations [180]. Although their insufficient mechanical stability and temperature tolerance can be improved with the addition of a bonding agent such as formaldehyde [186] and glutaraldehyde [187], this may negatively affect their physical properties. Likewise, agar has been employed in gelatin phantoms to provide geometrical stability and allow the creation of inclusions without undesirable osmotic phenomena [143]. Thereby, the synergy of agar and gelatin seems to provide essential benefits related to long term stability and increased shelf life [143].

Except from being tissue equivalent and temperature resistant, phantoms intended for thermal ablation studies should ideally offer visualization of the coagulative regions, thus facilitating evaluation of therapeutic protocols. Visual capacity is also of great importance for visual assessment of the motion accuracy in robotic applications [81], [144]. Therefore, the optical transparency of PAA gels makes them favorable over agar gels [190]. However, synthesis of PAA gels is generally considered more complicated since it requires special care due to the use neurotoxic ingredients [197].

On the other hand, agar phantoms are easily prepared and stored, cost-effective, harmless, and with durable stability [97], [110], [155]. At this point, it should be noted that carrageenan can be used as a mechanical stabilizer in agar gels, enabling even more robust anatomical models [175], [177]. It should though be pointed out that carrageenan cannot withstand ablation temperatures, and thus, it is unsuitable for FUS ablation therapies [177].

Other mimicking materials identified in the literature are the PVA [100]–[102], PVC [103]–[105], silicone [106], [107], and TX-150/ TX-151 gels [108], [109]. Although various studies report some very promising results, the physical

properties of these materials have not been sufficiently investigated, and their efficacy in thermal studies is yet to be established. This would of course require further evaluation of those characteristics critical for thermal applications, and particularly MRgFUS. In addition, proper gelation and solidification of such materials typically require m ultiple steps [100]–[102] leading to more complicated fabrication processes and sometimes to increased costs. Regarding TX-150, its gelation parameters are not well defined, thus causing difficulties in the fabrication process [108]. Moreover, TX-150 gels normally undergo bacterial degradation in just a few days. It is though notable that the addition of metal phthalocyanines was shown to create more stable and durable phantoms [109].

Potential modifiers of MR relaxation times become apparent through the collected data. T2 relaxation time was predominantly tailored by varying the gelling agent concentration. In fact, agarose served as the predominant T2 modifier in all the proposed agar-based phantoms [155], [162], [163], [175]–[177], as well in phantoms containing other types of gelling agents [175]–[177]. Varying animal hide gel concentration also provides T2-modifying capacity [188], whereas both T1 and T2 of gelatin phantoms were found to vary for different types of gelatin [99]. This does not imply in the case of TX-151 gels, for which the amount of gelling agent seems to cause insignificant influence on relaxation times [108]. Regarding synthetic polymers, the MR properties of PVC gels can be adjusted to mimic different soft tissues by adjusting the ratio of the softener to polymer [105], whereas for PVA phantoms, smaller T1 values were observed with increasing number of freeze-thaw cycles [102].

Ingredients added as modifiers of acoustical properties also have a significant effect on the MR behavior of TMPs. Firstly, inclusion of glass beads was proven to slightly lower T2 of PVC phantoms [105]. A similar trend was reported in a study by Huber et al. [198], wherein the inclusion of glass beads lowered both T1 and T2 relaxation times of an agar/gelatin-based phantom. Another interesting trend observed is the decrease of T2 with increasing concentration of psyllium husk in gelatin-based phantoms [180]. Regarding the longitudinal relaxation time T1, it can be varied by incorporating different concentrations of paramagnetic ion salts, such as $MnCl_2$ [164], $NiCl_2$ [165], and $GdCl_3$ [166], or copper ions [155]. Finally, both

T1 and T2 can be modified with the addition of proper type and concentration of MRI contrast agents [91].

Another remark emerging from the gathered data is that the same phantom ingredient may act differently on the MR relaxation properties when companied with different gelling agents. For instance, addition of NaCl in agar-based phantoms markedly affected T1 and T2 values [177]. On the contrary, the relaxation values of a PAA phantom were found independent of the NaCl concentration [196]. Therefore, the previously reported trends should be considered with caution, considering synergic components and how they may interrelate. Additionally, preservatives are required to prevent bacterial invention and offer long-term use. NaN_3 is maybe the most widely used preservative since it was selected to lengthen the lifetime of various phantom types, including agar [160], PAA [193], and Carrageenan [176], [177] phantoms.

Even though an ideal phantom would possess all the characteristics of the simulated tissue, this is extremely difficult. Thus, phantom recipes are adjusted to simulate only the critical properties of tissue depending on the intended phantom application. In the current study, focus was placed on the MR properties of a wide range of TMPs. In synergy with other studies reviewing acoustical and thermal properties, the reported data is expected to facilitate the selection of appropriate materials for the construction of high-quality MRgFUS phantoms.

4 MR relaxation times of agar-based tissue mimicking phantoms

4.1 State of the art

Gel phantoms constitute a more economical and ergonomic solution for preclinical research compared to experimental animals, also given that their lifespan can be simply lengthened by adding preservatives [90], [97]. As concluded from the previously presented literature study, several categories of gelling agents, including agar [110], gelatin [180], PAA [92], PVA [102], PVC [105], silicone [106], and TX-151 [108] have been used in the construction of gel phantoms for quality assessment purposes in medicine and biomedical research. Accurate replication of tissue properties is of great importance for the efficacy of such procedures, especially when evaluating therapeutic applications with clinical potential.

The current increasing application of FUS in medicine [134] requires the development of high quality TMPs specially designed for use with this specific technology to accelerate its clinical translation. The FUS-induced thermal effects were proven to be essential in many oncological applications, thereby serving as an alternative therapeutic solution over surgical and systemic approaches [1]. Therefore, TMPs intended for FUS studies should be capable of accurately replicating both the acoustical and thermal characteristics of biological tissue.

FUS treatment is typically applied under US or Magnetic Resonance Imaging (MRI) guidance [1], with MRI being the method of choice because of its superior imaging resolution and its ability to acquire temperature data by intraoperative MR thermometry [8], [9]. The contrast in MR images emerges from changes in the proton density and the magnetic relaxation times T1 and T2 of tissues [9]. Several animal studies have shown that the MR parameters of tissue greatly affect the contrast between normal untreated tissue and FUS-ablated areas [112], [113]. In fact, the MR relaxation times of FUS lesions were found to vary depending on the tissue type, suggesting that the MR properties of the host tissue define the MR appearance of lesions [112]. More importantly, the temperature dependence of tissue relaxation times allows for noninvasive temperature monitoring during thermal applications [9], [199]. Therefore, precise replication of MR relaxation parameters is essential for producing tissue-like MR signal and more realistic

temperature maps in the process of evaluating thermal protocols. It is thus of paramount importance that TMPs are both US and MR imageable and possess tissue-like MR properties in order to be qualified for use with the MRgFUS technology.

As shown from the above literature study, PAA, gelatin, and agar-based phantoms were proven efficient to properly mimic biological tissues in thermal studies by replicating critical acoustical, thermal, and MR properties [92], [97], [110], [180]. Agar and PAA gels are favorable in that they possess melting points sufficiently high for ablative FUS [97]. Nevertheless, agar gels serve as a more natural alternative having easier and more cost-effective preparation and storage compared to PAA gels [110]. They can be easily shaped to any configuration to form phantoms of durable stability. Furthermore, their tissue-like MR signal makes them the material of choice for MRI studies [155], [161], [164]–[166], [170], [171].

Agar-based phantoms has been quite widely used for thermal studies with FUS [93], [95], [110], [156], [174] where agar served as the gelling agent, and proper concentration of other materials was added to modify mainly the thermal and acoustical properties depending on the tissue to be mimicked. Notably, a quite large data on the acoustical properties of agar phantoms exist in the literature. Silicon dioxide [156], cellulose [158] and graphite particles [158] are examples of ingredients that served as attenuation modifiers enhancing ultrasonic scattering.

Although more limited research has been applied in the investigation of MR parameters of agar-based phantoms, some interesting trends become apparent through the literature. Agar turned out to be the prominent T2 modifier even in the case where another material serves as the gelling agent [155], [163], whereas T1 was predominantly tailored by varying the concentration of paramagnetic ion salts [164], [165] and copper ions [155].

Our group has previously proposed and characterized several agar-based phantoms by estimating critical tissue properties, including the mass density, speed of sound, acoustic attenuation, acoustic impedance, thermal diffusivity, specific heat, and thermal conductivity [93], [96], [110]. Given the current need for TMPs that can also replicate critical MR parameters, as well as the lack of targeted research on trends between added ingredients and resultant MR properties of agar phantoms,

the current study investigates the MR relaxation times of different mixtures of agar-based phantoms previously proposed by our group.

4.2 Materials and methods

4.2.1 Phantoms' development

Ten agar-based phantoms with different concentrations of additives were prepared and contained in a rectangular container. The container was specially developed having 12 compartments to accommodate the TMPs and two reference liquids (water, oil), as shown in **Figure 18A**. **Figure 18B** shows the composition of materials used in each insert.

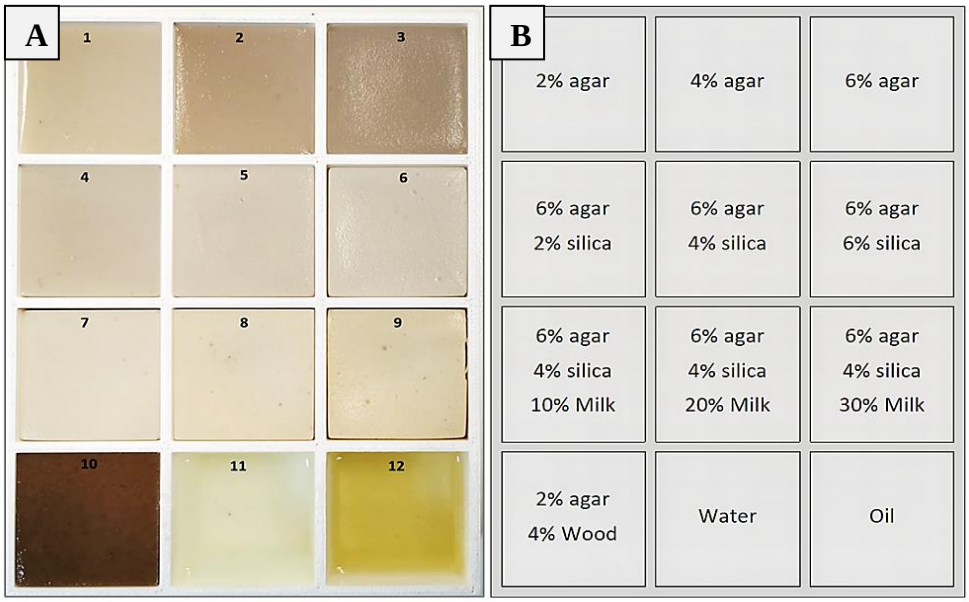

Figure 18: (A) Photo of the phantoms in the container. **(B)** Recipe used for each one.

Three phantoms with varying agarose (Merck KGaA, EMD Millipore Corporation, Darmstadt, Germany) concentrations of 2 – 6 % weight per volume (w/v) were prepared to assess the role of agar as a modifier of the relaxation times. The effect of varying silicon dioxide (Sigma-Aldrich, St. Louis, Missouri, United States) concentration (2 – 6 % w/v) on the relaxation times was then investigated using a certain amount of 6 % w/v agar. Finally, various amounts of evaporated milk (Nounou, Friesland Campina, Marousi, Greece) were added in phantoms with fixed concentrations of 6 % w/v agar and 4 % w/v silicon dioxide. The volume per volume (v/v) concentration of evaporated milk varied from 10 to 30 %.

Agar-based phantoms doped with wood powder were previously found to possess lower thermal conductivity compared to the silica/evaporated milk doped phantoms and an acoustic absorption coefficient closer to that of soft tissue [110]. Thereby, another phantom containing 2 % w/v agar and 4 % w/v wood powder was constructed according to the procedure previously described by our group [110].

4.2.2 MR properties of phantoms

4.2.2.1 Physical Principle of MR relaxation times

Tissues are characterized by two relaxation times, which describe the rate at which protons return to equilibrium following a radiofrequency pulse. The maximum transverse magnetization M_{xy0} after a radiofrequency pulse is lost with time as the spinning protons interact with each other and lose phase coherence. T2 is the transverse relaxation time, which by default equals to the time needed for the transverse magnetization (M_{xy}) to fall to approximately 37% of its maximum value (M_{xy0}) and mathematically is defined by the following equation [200]:

$$M_{xy} = M_{0xy} e^{-\frac{TE}{T2}} \quad [1]$$

where TE is the echo time.

Accordingly, T1 relates to the realignment of spinning protons with the external magnetic field and is defined as the time required for the longitudinal magnetization (M_z) to recover to approximately 63% of its maximum value (M_{0z}). Mathematically, this recovery is described as follows [200]:

$$M_z = M_{0z}(1 - 2e^{-\frac{TI}{T1}}) \quad [2]$$

where TI represents the inversion time. It is noted that this expression assumes that the repetition time (TR) is sufficiently longer than the T1 to be estimated.

4.2.2.2 Estimation of MR relaxation parameters

The developed phantoms were imaged in a 1.5 T MRI scanner (GE Signa HD16, GE Healthcare, Chicago, Illinois, United States) to demonstrate the effect of the various additives on their MR properties. The container was covered by the posterior head and face part of a head/neck/spine coil (Signa 1.5T, 16 channel, GE Medical Systems, Milwaukee, Wisconsin, USA) as shown in **Figure 19**.

Figure 19: The phantom container positioned on the MRI table within the posterior head and face part of the head/neck/spine coil.

A 2D MultiEcho imaging sequence was used for assessing the transverse relaxation time. Multiple coronal scans were obtained at variable TE values, thus demonstrating the transverse magnetization exponential decay. T2 was estimated by fitting the measured SI over TE to the exponential function of equation 1. The images were acquired with the following parameters: TR = 200 ms, TE = 12.0 – 250.0 ms, flip angle (FA) = 90º, echo train length (ETL) = 4, pixel bandwidth (pBW) = 122.1 kHz, matrix size = 160 x 128, field of view (FOV) = 260 × 260 mm^2, slice thickness = 7 mm, and number of averages (NEX) = 0.75.

Accordingly, T1-weighted (T1W) inversion recovery (IR) FSE images of the phantoms were obtained at variable TIs for T1 mapping. The data were fitted into equation 2 to estimate the longitudinal relaxation time (T1). 2D axial images were acquired with the following parameters: TR = 7000 ms, TE = 9.94 ms, TI = 50 - 3000 ms, FA = 90º, ETL = 9, pBW = 27.10 kHz, matrix size = 192 x 128, FOV = 260 × 260 mm^2, slice thickness = 7 mm, and NEX = 1.

The methodology for estimating the MR relaxation times of each phantom included both ROI and voxel-by-voxel analysis. The ROI approach for T1 and T2 mapping involved measurement of the SI in specific predefined ROI in the phantom for each TI and TE, respectively. The mean values of the SI were fitted to equations 1 and 2. Similarly, in the voxel-based approach, parametric maps were derived from the

series of images by fitting the mathematic models to the acquired data for each individual voxel through automated algorithmic processing.

4.3 Results

The phantoms were initially scanned in coronal plane using a MultiEcho sequence with TE values ranging from 12 to 250 ms. **Figure 20** shows indicative MR images acquired at various TEs within this range.

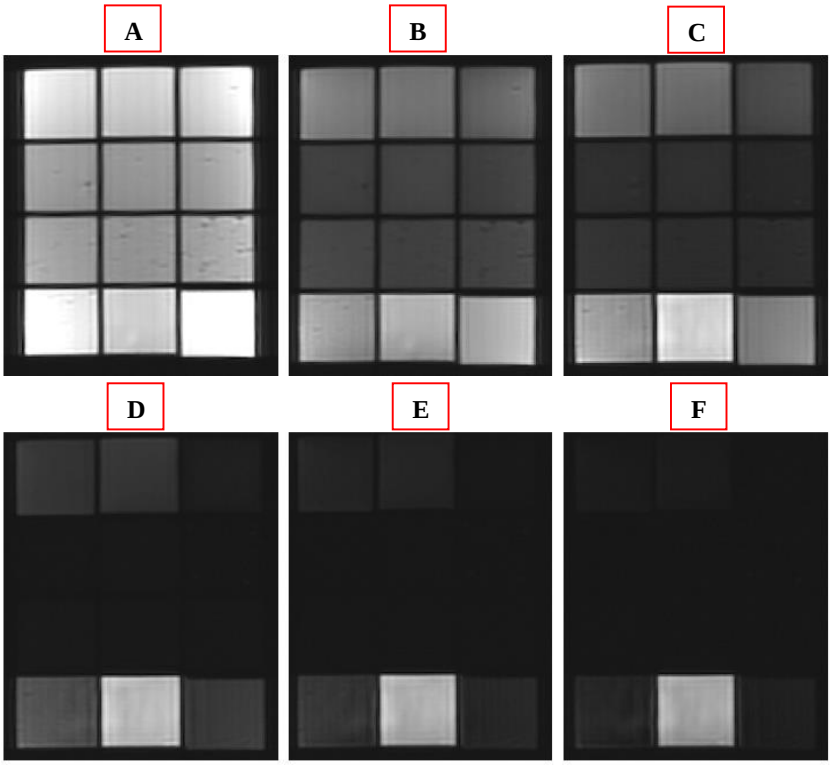

Figure 20: Coronal slices acquired using a 2D MultiEcho sequence at TE values of **(A)** 12 ms, **(B)** 36 ms, **(C)** 50 ms, **(D)** 100 ms, **(E)** 150 ms and **(F)** 200 ms.

Figure 21 shows an indicative graph of the estimated mean SI in a predefined ROI of the phantom in insert 7 (6 % w/v agar, 4 % w/v silica, and 10 % v/v milk) plotted against the TE, demonstrating the rate of transverse magnetization decay. The T2 parametric map of the phantoms as generated by the voxel-by-voxel analysis is presented in **Figure 22**.

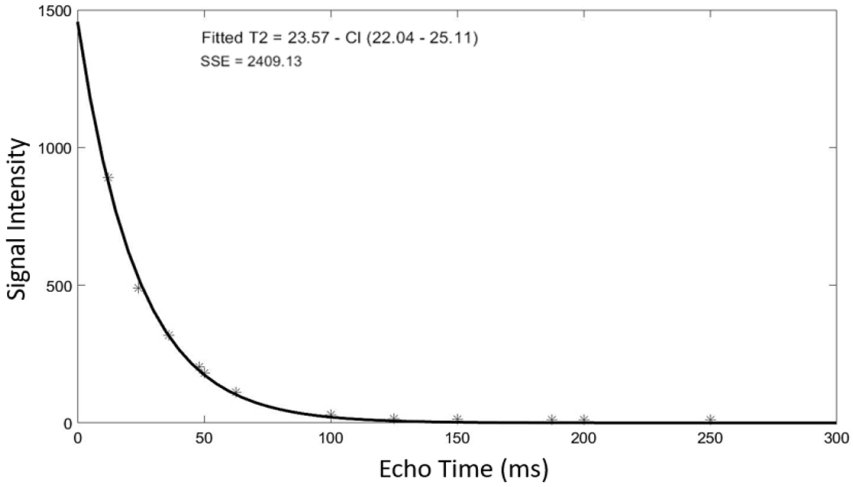

Figure 21: Plot of the mean SI measured from the MultiEcho images using the region of interest approach against TE for phantom 7 (6% w/v agar, 4% w/v silica, and 10% v/v milk). SSE corresponds to sum of square errors. CI corresponds to 95% confidence intervals for the estimated values.

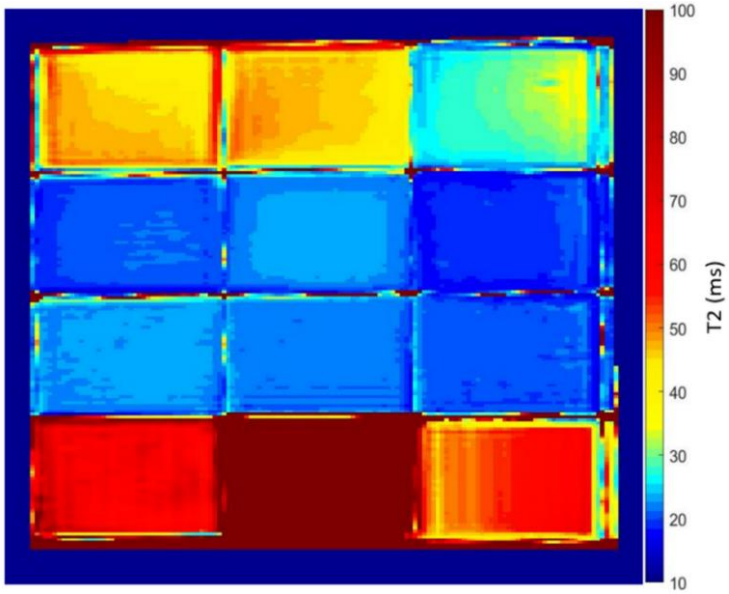

Figure 22: T2 parametric map of phantoms. The map was generated by voxel-based analysis of a series of 2D MultiEcho images with different TE values (12 - 250 ms).

Imaging of phantoms was then done in axial plane using a T1W IR FSE sequence at various TI values in the range of 50 to 3000 ms. Indicative results are presented in **Figure 23**, where the yellow dotted circles indicate the phantoms with the lowest SI for each TI. A typical graph of the change in SI with increasing TI value as estimated by the ROI approach is shown in **Figure 24**, which demonstrates the mean SI versus TI for the phantom in insert 9 (6 % w/v agar, 4 % w/v silica, and 30

% v/v evaporated milk). The T1 parametric map generated by the voxel-by-voxel analysis is presented in **Figure 25**.

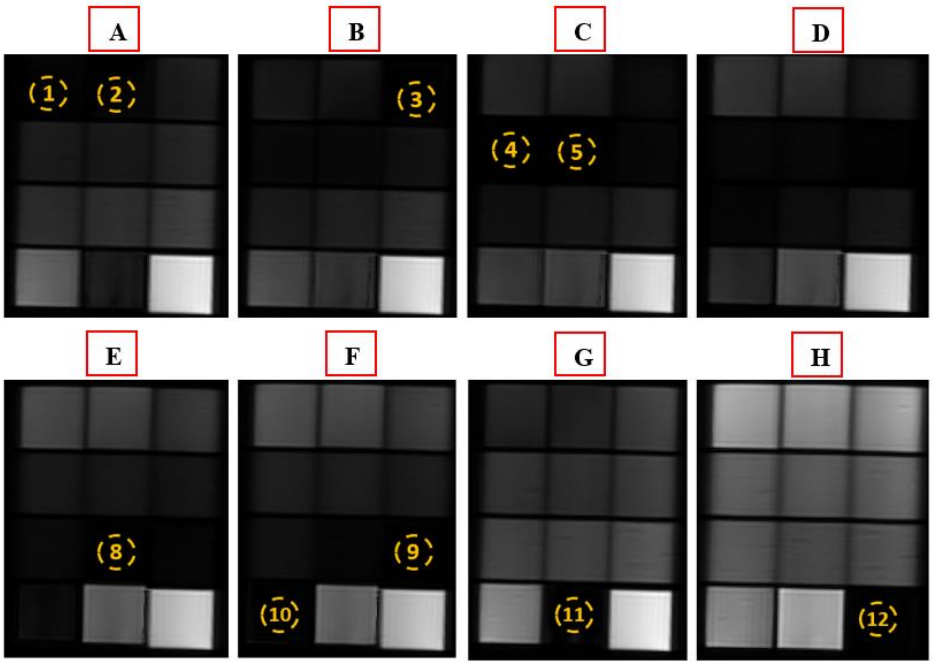

Figure 23: Axial slices of the phantoms acquired using a 2D T1W IR FSE sequence at TI values of **(A)** 1200 ms, **(B)** 1000 ms, **(C)** 900 ms, **(D)** 800 ms, **(E)** 650 ms, **(F)** 600 ms, **(G)** 1500 ms and **(H)** 125 ms. The material shown in the yellow dotted circle has the lowest SI.

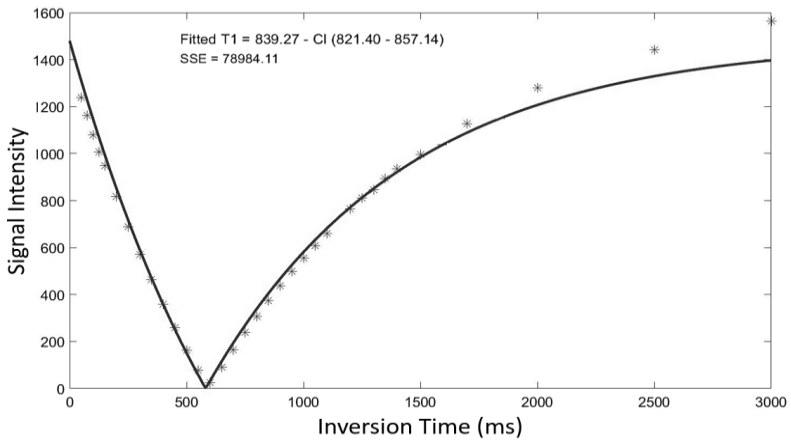

Figure 24: Plot of the mean SI measured from the T1W IR FSE images using the region of interest approach against TI for phantom 9 (6% w/v agar, 4% w/v silica, and 30% v/v evaporated milk). SSE corresponds to sum of square errors. CI corresponds to 95% confidence intervals for the estimated values.

The mean value of the T1 and T2 relaxation times and the corresponding standard deviation (SD) for each phantom as estimated by the voxel-based approach are listed in **Table 1**.

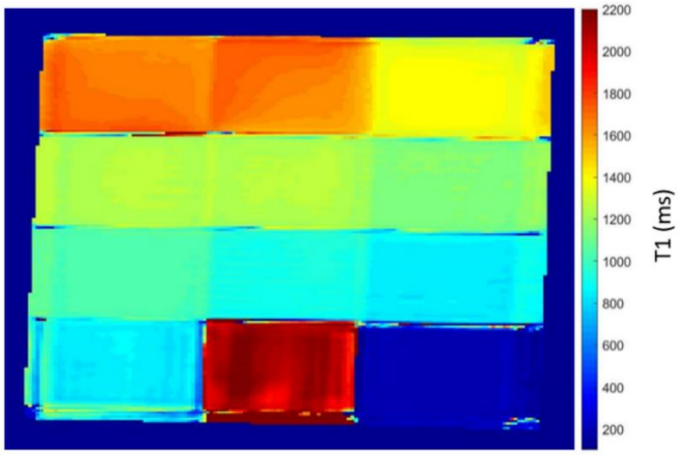

Figure 25: T1 parametric map of phantoms, generated by voxel-based analysis of a series of 2D axial T1-W IR FSE images with different TI values (50 - 3000 ms).

Table 1: Mean T1 and T2 and SD of phantoms estimated by voxel-based analysis.

Phantom #	Recipe	T2 (ms)	SD (ms)	T1 (ms)	SD (ms)
1	2 % agar	46.2	1.1	1669.5	13.3
2	4 % agar	46.7	1.0	1662.7	27.6
3	6 % agar	29.4	1.7	1394.9	3.8
4	6 % agar, 2% silica	20.9	0.4	1249.8	6.4
5	6 % agar, 4% silica	23.4	0.2	1251	3.0
6	6 % agar, 6% silica	19.0	0.3	1147.7	7.3
7	6 % agar, 4% silica, 10% milk	23.0	0.2	1038.8	4.7
8	6 % agar, 4% silica, 20% milk	21.8	0.2	916.8	6.4
9	6 % agar, 4% silica, 30% milk	20.1	0.23	841.3	8.1
10	2% agar, 4% wood	65.2	2.7	837.5	12.0
11	Water	-	-	2125.6	42.1
12	oil	55.2	3.4	193.3	1.8

Figure 26A and **Figure 26B** show the estimated T1 and T2 values plotted against the agar concentration, respectively, where the data points were fitted to a 2nd order polynomial (R^2=1) using non-linear least square regression. Accordingly, the effect of varying amount of silicon dioxide and evaporated milk on T1 is presented in **Figure 27**, in which the graphs also represent 2nd order polynomials (R^2=0.899 and R^2=0.999, respectively).

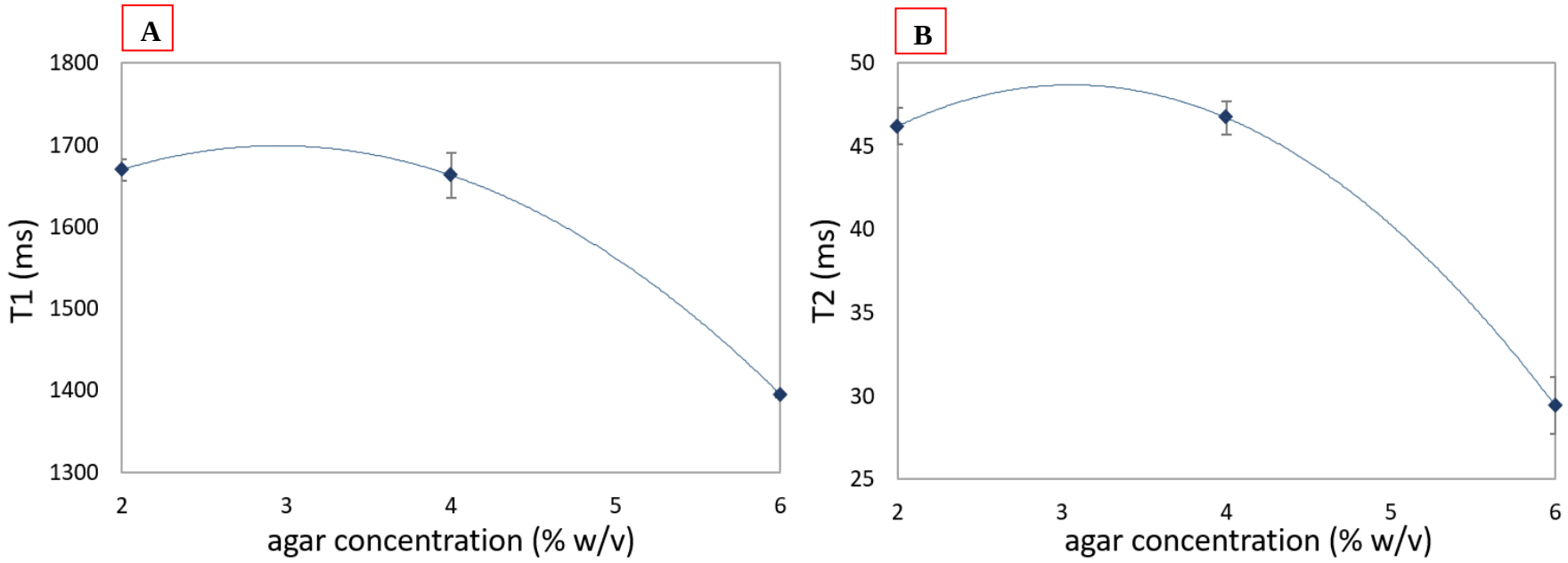

Figure 26: The mean **(A)** T1 and **(B)** T2 values plotted against the agar concentration. The data points are fitted by polynomial regression where the error bars correspond to the standard deviation as estimated by voxel-based analysis.

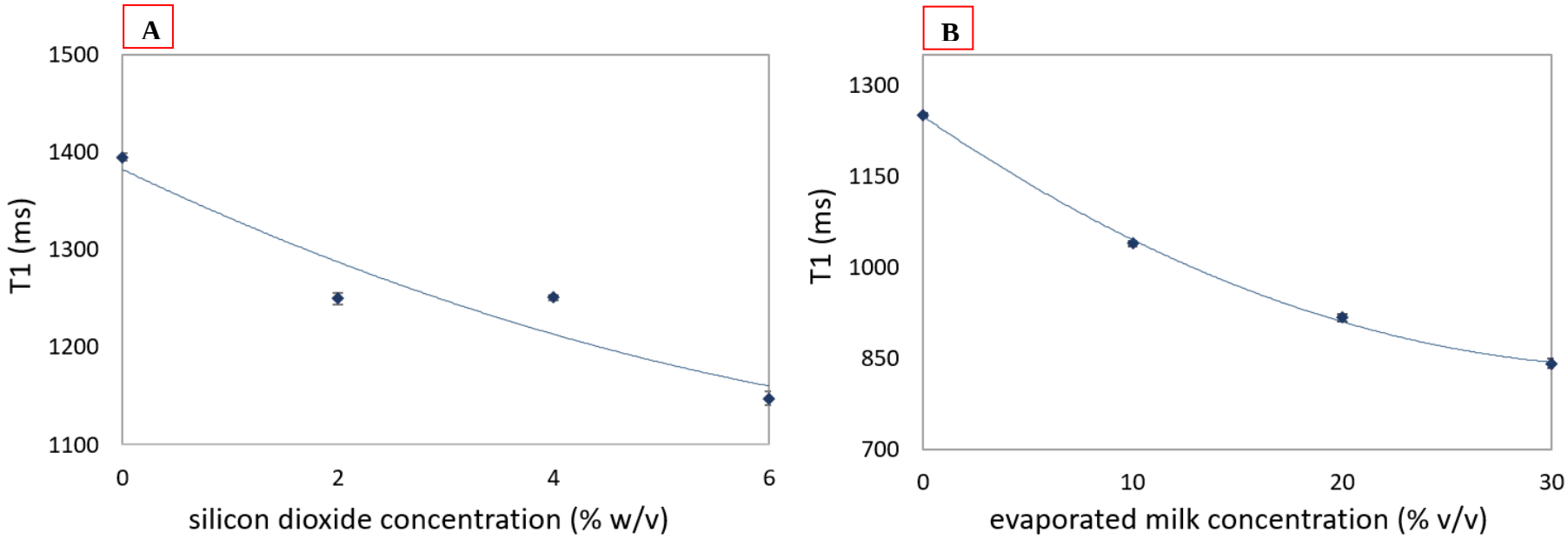

Figure 27: The mean T1 value plotted against **(A)** the silica concentration for a fixed amount of 6 % w/v agar and **(B)** the evaporated milk concentration for fixed amounts of 6 % w/v agar and 4 % w/v silica. The data points are fitted by polynomial regression where the error bars correspond to the standard deviation as estimated by voxel-based analysis.

4.4 Discussion

Ten different agar-based TMPs were prepared and imaged in a 1.5 T MRI scanner to assess their suitability to match the MR properties of real tissue. It is widely known that the MR SI depends on the characteristic relaxation times of the imaged object [9]. A typical methodology that makes use of this dependency was followed for T1 and T2 mapping. A series of MultiEcho images were acquired at different TE values for T2 mapping. Accordingly, T1 mapping was performed by acquiring T1W IR images at different TIs after applying the inversion pulse (180°). The relaxation times were estimated by fitting the acquired data to the signal decay and recovery curves, respectively, through both ROI and voxel-based approaches.

Pure agarose phantoms were initially scanned to demonstrate the effect of agar concentration on the relaxation times. Both relaxation parameters showed similar behavior. Increment of the agar concentration from 2 to 4 % w/v had no impact on the resultant relaxation times, whereas both T1 and T2 showed a noticeable decrease as agar concentration increased to 6 % w/v. It is notable that the relation between both relaxation times and the agar concentration can be perfectly modeled as a 2nd degree polynomial function (R^2=1). Although the present results are in line with previous studies [155], [163] proposing agarose as a T2 modifier, they suggest that this only applies for agar concentrations of 4 % w/v and above.

The change in MR properties of agar gels upon addition of various amounts of silicon dioxide and evaporated milk was then assessed. The addition of silica particles further lowered the relaxation times. However, no specific trend became apparent with increasing silicon dioxide concentration for none of the relaxation times. The results further suggest that the addition of evaporated milk has no specific impact on T2, whereas a noticeable decrease is observed in the case of the longitudinal relaxation time (T1). In fact, the T2 relaxation time of milk-doped agar gels (6 % w/v agar and 4 % w/v silicon dioxide) remained similar to those containing only silicon dioxide. On the contrary, milk-doped agar-silica gels exhibit noticeably shorter T1 relaxation times, with increasing evaporated milk concentration (0 – 30 % v/v) resulting in a gradual reduction of T1 in a 2nd order polynomial manner (R^2=0.999). This implies that T1 and T2 may be changed

independently; however, this should be further investigated. It is also noted that milk concentrations higher than 30 %, which would probably lower T1 even more, were not attempted because they would result in loose phantoms [201].

Our results further demonstrated that agarose could also serve as a T1 modifier. However, it seems that T2 depends more strongly on the amount of agarose and is not remarkably affected by the concentration of other additives. Note that with increasing agar concentration at TEs of 36-200 ms the signal drops (Figure 20). On the contrary, with a fixed agar concentration of 6 % w/v and increasing silica, the signal does not change much. Note also that the same holds by increasing the milk concentration. This result ties well with previous studies wherein T2 was mostly defined by the gelling agent concentration, whereas T1 was mainly varied by incorporating different concentrations of paramagnetic ion salts [164]–[166].

The MR parameters of TMPs have been previously shown to be dependent on the concentration of scatterers [180], [198]. In a study by Hofstetter et al. [180], a decrease of T2 occurred with increasing concentration of psyllium husk in gelatin-based phantoms. A similar trend was reported in a study by Huber et al. [198], wherein the inclusion of glass beads shortened T1 of an agar/gelatin-based phantom. Herein, the addition of wood scatterers also lowered T1 of the pure agar gel (2 % w/v). The phantoms doped with silicon dioxide appeared with lower relaxation times compared to agar only gels as well. However, it should be emphasized that the trend with increasing silica may not be reliable as the distribution of silica in the material might be random.

Overall, the MR relaxation times of the proposed agar-based phantoms are comparable with the values reported for body tissues. A review article by Bottomley et al. [202] reports T2 relaxation times of soft tissues ranging roughly between 40 to 80 ms. Herein, the estimated T2 values ranged from a minimum value of 19.0 (±0.3) ms for the phantom in insert 6 (6% agar, 6% silica) to a maximum value of 65.2 (±2.7) ms for the phantom in insert 10 (2% agar and 4% wood). Authors also report a mean T2 in adisope tissue of 84 (±36) ms [202], which compares well with the value of 55.2 (±3.4) ms found by the current study for oil. At this point, it should be noted that the T2 measurement of water is not reported because of insufficiently high echo times due to machine limitations. Regarding the longitudinal relaxation

time, the estimated T1 values range from 837.5 (±12) ms to 1669.5 (±13.3) ms for the phantoms in inserts 10 and 1, respectively. These estimates are partly consistent with the literature documenting T1 values for soft tissues harshly between 500 – 1000 ms [203].

The several phantom recipes can be matched with specific tissue types through a more detailed comparison with the cited literature. For instance, by using concentrations of 2 % w/v agar and 4 % w/v wood (phantom in insert 10), a T2 value of 65.2 (±2.7) ms was found, which agrees with the value of 61 (±11) ms reported by prior research for the kidney tissue [203]. Regarding the T1 relaxation time, the value of 837.5 (±12.0) ms estimated by the current study is quite higher than the value of 709 (±60) reported literally for the kidney [203]. Accordingly, the silica/milk doped phantom in insert 7 was found to possess MR properties close to that of skeletal muscle and heart tissue (at 1.5 T) [203]. Note that the high T1 values estimated for the agar only phantoms can be well correlated only with the T1 relaxation times of human blood [203].

5 Tumor phantom model for MRgFUS ablation studies

5.1 State of the art

Ex-vivo tumor models have an essential role in early stage experimentation and validation of imaging and therapeutic modalities and protocols in the context of oncology, provided that the use of animal tumor models is not only costly and resource-intensive, but also against the minimization of animal testing [90]. Accordingly, as part of the effort to enable cost-effective and easily implemented research methods to optimize such modalities and identify beneficial advancements prior to *in-vivo* application, there exist numerous tumor models mainly involving the use of gel phantoms proposed in the literature.

One category of tumor-bearing tissue phantoms concerns imaging applications. High quality test objects are needed for examining the performance of newly developed imaging applications or even routine testing of well-established imaging systems and techniques [90], [204]–[206]. Recently, the 3D printing technology allowed the development of more realistic tumor phantoms for x-ray radiographic imaging [207], [208]. Phantoms simulating tumor heterogeneity in imaging have been employed in radiomic studies as well [209]–[211]. Besides their usefulness for imaging applications, tumor phantom models constitute a critical asset for the training and experimentation on interventional procedures including needle biopsies, and the assessment of relevant robotic-assisted equipment [80], [212]–[214].

Image guided thermal ablation has arisen as a feasible alternative to invasive surgery for patients with malignancies [215], and it may be minimally invasive with the use of percutaneous radiofrequency ablation (RFA) and microwave ablation (MWA) applicators [216], or completely non-invasive with the extracorporeal use of FUS [57]. Although a wide variety of gel-based phantom models have been proposed as ergonomic tools for preclinical thermal therapy studies [97], only some of them incorporate tumor simulators. Thermally sensitive PAA phantoms are considered advantageous in that they offer visualization of thermal damage owing to the inclusion of heat-responsive materials, such as BSA protein [191], egg white [141], and thermochromic ink [92]. As an example, Zhou et al. [217] proposed a

tumor model for testing ablation protocols that consists of a 3-cm spherical tumor mimic embedded in a PAA gel loaded with thermochromic ink.

Driven by the increasing utilization of RFA and MWA as the prevalent non-invasive modalities for the management of hepatocellular carcinoma (HCC), gel phantom models intended for RFA and MWA of the liver were quite widely described in the literature [218], but with only few of them involving thermal heating of a tumor model. In a relevant study [219], authors constructed a 5 % agar cylindrical phantom featuring a cylindrical hole of 2 cm in diameter, which was filled with an agar solution of smaller agar concentration of 0.25 % to represent a tumor. The outer section also included an oil-based solute, the amount of which was varied to achieve different thermal conductivities. According to thermocouple measurements, changes in RF heating occurred as a result of this difference, with the authors concluding that lower values of thermal conductivity in the background material can increase the temperatures produced within the tumor target significantly [219].

A two-section phantom was also utilized by Haemmerich et al. [220] for the purpose of evaluating the functionality of low frequency RFA in tumor destruction by thermocouple thermometry. The tumor phantom was a thin layer of 5 % agar gel laid on the top of a piece of *ex-vivo* bovine liver tissue. In a similar study regarding MWA, thermocouple measurements were performed in an agar-based breast tumor phantom to evaluate the thermal effects of three types of microwave antennas [221]. The breast tissue was mimicked by a mixture of detergent, oil, and agarose in water having embedded 1-cm and 1.5-cm spherical tumor inserts made of Sodium chloride (NaCl), ethanol, and agarose, which served as modifiers of the conductivity, permittivity, and solidity, respectively [221].

Tumor-bearing phantom models for interventional and thermal studies should ideally combine both tissue-like imaging and therapeutic features provided the apparent need for image guidance of such procedures. An indicative phantom model featuring a tumor was presented by Zhong et al. [222] for the purpose of performing thermal ablations and tumor puncture studies under US, CT or MRI guidance. The phantom was formed by embedding a PAA-based 3-cm spherical tumor mimic in a PAA gel loaded with thermochromic ink. Iohexol and psyllium husk were added in

the tumor mimic serving as the CT and US/MR contrast agents, respectively. Another example is a study by Ki Soo et al. [223], who developed a two-compartment phantom for RF studies, where normal and tumor tissues were mimicked by agar gels doped with $CuSO_4$ solution serving as the electrical conductivity controller. The tumor compartment was differentiated from the surrounding with the inclusion of a Fe_3O_4 nanoparticle suspension and 4% sodium carboxymethyl cellulose. Temperature changes were intermittently recorded during RF heating by performing MR thermometry in a 3T scanner, demonstrating that nanoparticle-doped regions developed higher temperatures than the background. Carrageenan was also used as the gelling agent for developing a tumor-bearing phantom as a tool for evaluating RF ablation margins in HCC by contrast-enhanced ultrasound-CT/MR image fusion [224]. Notably, while carrageenan gels possess proper physical properties, they are not considered the material of choice for evaluating thermal ablation protocols [140], [224].

Among the thermal ablation techniques, the rapidly evolving technology of FUS has proven a promising non-invasive alternative to traditional cancer therapy [1], [57]. In this process, tissue mimicking phantoms provided a test environment for preliminary evaluation of equipment and protocols. Hassanuddin et al. [225] investigated the impact of obstacles such as bone and metallic implants on FUS thermal therapy in a novel tumor-bearing phantom. This phantom was a mixture of PAA gel and BSA protein containing several metallic and plastic objects, as well as a water-filled rubber balloon mimicking a cyst [226]. In another study [227], an agar-based tumor model was utilized to evaluate the effectiveness of a newly proposed dual modality combining magnetic and FUS heating for cancer therapy.

Numerous gelling agents have been proposed so far for the development of phantoms for diagnostic and therapeutic ultrasound applications, with agar being one of the most widely used. Although the use of agar-based phantoms in FUS ablation studies is widespread [93]–[95], [97], [110], [174], [228], there is an identified need for more realistic tissue-mimicking phantoms embedding tumor simulators. Despite that agar gels don’t possess optical transparency, they are considered ideal in mimicking biological tissues by replicating their most critical thermal, acoustic, and MR properties when mixed with proper concentration of

other ingredients [96], [110], [142], [153], as well as withstanding ablative temperatures while maintaining their integrity [229]. They can be easily created in any size and shape with inexpensive non-toxic materials and tailored to suit different applications. Accordingly, we herein present the development and evaluation of an agar-based single-tumor phantom model with tissue-like US, CT, and MR visibility for MRgFUS ablation studies and the performance assessment of relevant equipment and protocols. The proposed two-section phantom is based on two inexpensive ingredients; agar and silicon dioxide, whose concentration was selected to impart tissue-like properties and good US, CT, and MRI contrast of the tumor simulator. The most critical acoustic, thermal, and MRI properties of the phantom were investigated. High power single and grid FUS sonications were performed in selected ROIs in and out of the tumor simulator and the temperature evolution was recorded using MR thermometry to assess the suitability of the proposed phantom model for the evaluation of FUS thermal protocols. The phantom was sonicated using an MRgFUS robotic system featuring a 2.4 MHz single element FUS transducer.

5.2 Materials and methods

5.2.1 Tumor phantom model design

The tumor phantom model was developed in the laboratory following a simple procedure. The main ingredient was agar in granular form (particle size of 1400 μm, Merck KGaA). This ingredient acts as a solidifier, but also by varying its concentration it's possible to adjust the MR relaxation properties of the gel [140]. The second ingredient was silicon dioxide (Sigma-Aldrich, St. Louis, Missouri, USA) that was previously proven an effective modifier of ultrasonic attenuation [140], [153].

The two-compartment phantom model was developed with the assistance of dedicated molds that were 3D printed using Polylactic acid (PLA) plastic on a rapid prototyping machine (FDM400, Stratasys). The background material was prepared by dissolving proper amount of agar grounded into powder in degassed/deionized water previously heated to 50 ˚C so as to achieve the desired w/v concentration of 6 %. A mixture containing similar amount of 6 % w/v agar and 4 % w/v silicon

dioxide was selected as the tumor material. Silicon dioxide was slowly added a few minutes after agar was poured while continuously stirring to avoid aggregation of ingredients [110]. The tumor material was poured into the mold shown in **Figure 28A** and left to solidify to form a 3-cm spherical tumor mimic (volume of about 14 cm^3) having a thread running through it. Following demolding, the tumor mimic was fixed in the center of the rectangular mold shown in **Figure 28B** by mounting the thread at opposite sides of the mold and finally the background material was poured in the container to form the final phantom, which is shown in **Figure 28C**.

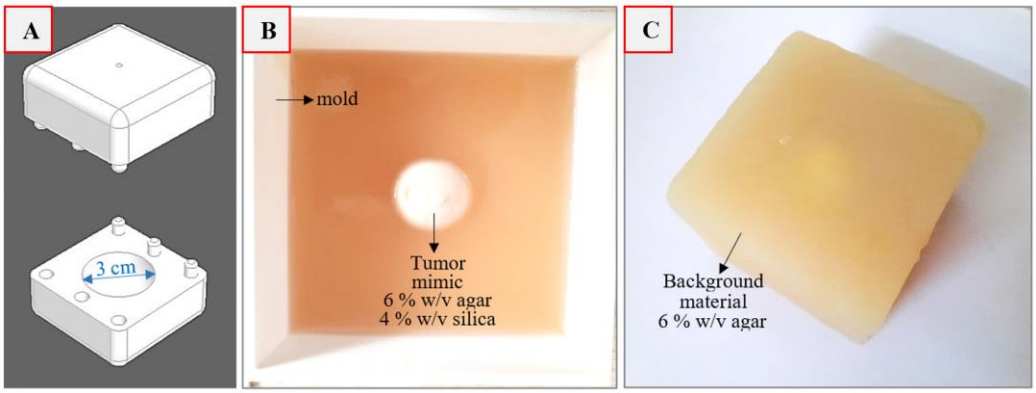

Figure 28: **(A)** The mold used for tumor mimic development. **(B)** Photo during phantom development showing the tumor mimic within the rectangular mold. **(C)** Photo of the developed agar-based tumor phantom model.

5.2.2 Characterization of tumor phantom model

5.2.2.1 Acoustical properties

The ultrasonic attenuation in the tumor and background materials was investigated using the transmission-through variable thickness technique [153]. The specific method is based on comparing the ultrasonic signals acquired through samples of different thickness (2 cm and 4 cm). Planar transducers of 30-mm diameter and operating frequency of 1.1 MHz (CeramTec, Plochingen, Germany) were employed; one as the transmitter and one for receiving the attenuated signals, which were displaced on a digital oscilloscope (TDS 2012, Tektronix, Inc., Beaverton, Oregon, USA).

The well-established pulse-echo methodology was employed for estimating the ultrasonic velocity in the two phantom compartments [152]. Samples of 2-cm

thickness were fixed between a planar transducer (diameter of 10 mm, central frequency of 2.7 MHz) and a reflector. The transducer was connected to a pulser/receiver (model 500 PR, GE Panametrics, Waltham, MA; 25 MHz bandwidth) and the reflection signals returning from the samples were recorded on the oscilloscope. The characteristic acoustic impedance was then determined by multiplying the density of each sample with the corresponding estimated speed of sound.

The absorption coefficient was estimated according to the procedure described by Drakos et al. [201]. The rate of temperature change (dT/dt) during phantom sonication was recorded using a thermocouple (type K insulated beaded wire, Omega Thermometer, HH806AU, Omega engineering, USA) for a short time so that the effect of conduction is minimized, and a liner increase of temperature with time can be assumed. This is a reasonable approach also given the low conductivity of the phantom (estimated in section 5.2.2.2). Finally, the ultrasonic backscatter coefficient was extracted from previous work of the group [230].

5.2.2.2 Thermal properties

The thermal properties (thermal conductivity, thermal diffusivity, and specific heat capacity) of both phantom compartments were measured using a portable heat transfer analyzer (Isomet model 2104, Applied Precision, Bratislava, Slovakia). A dedicated needle sensor (S/N 09030019, Applied Precision) with a measurement range of 0.2–1 W/m K was used for the measurements. The detailed description of the employed methodology can be found in the study by Filippou et al. [231].

5.2.2.3 MR relaxation properties

The MR relaxation properties of the phantom were investigated as well. For this purpose, the phantom was imaged in a 3T MRI scanner (Magnetom Vida, Siemens Healthineers, Erlangen, Germany) using a multichannel body coil (Body18, Siemens Healthineers) that was securely positioned at a small distance above its top surface.

Variable Echo Time T2 Mapping was employed for estimating the T2 relaxation times of the tumor and background materials using a T2-W TSE sequence with TR

= 250 ms, FA = 180º, FOV = 260 × 260 mm^2, Slice thickness =10 mm, matrix size =128 × 128, NEX = 2, ETL = 12, and varying TE values in the range of 8 to 69 ms. Similarly, for T2* mapping, the TE value was varied from 4 to 67 ms and the parameters were as follows: TR = 445 ms, FA = 60º, FOV = 220 × 220 mm^2, Slice thickness = 5 mm, matrix size = 384 × 384, NEX = 1, and ETL = 10. The measured SI in the ROI plotted against the TE value was fitted to the exponential decay function describing the gradual decrease in the transverse magnetization and measured signal strength for T2 relaxation time estimation [200].

Accordingly, for T1 relaxation time mapping, images were obtained using a Gradient Echo (GRE) sequence at variable FA values in the range of 3 to 15º using the following parameters: TR = 15 ms, TE = 1.93 ms, slice thickness = 5 mm, FOV = 250 x 250 mm^2, matrix size = 256 x 256, ETL = 1, and NEX = 1. The obtained data were fitted into the formula describing the recovery of the longitudinal magnetization to its equilibrium value for calculating the relevant T1 relaxation time values [200].

5.2.2.4 Imaging features

The sonographic appearance of the developed tumor phantom model was evaluated using a portable ultrasound machine (UMT-150, Shenzhen Mindray Bio- Medical Electronics Co., Ltd., Shenzhen, P.R. China). The phantom was then scanned in a high-resolution CT system (Optima CT580, General Electric (GE) Medical Systems, Wisconsin, United States) to examine its radiographic appearance. The employed parameters were: tube voltage = 100 kVp, tube current = 300 mA, exposure time = 2.0 s, and slice thickness = 1.25 mm. The radiographic properties of the phantom were also extracted from a previous study of the group. Finally, MR images of the phantom were acquired in a 3T scanner (Magnetom Vida, Siemens Healthineers) using a T2-Weighted (T2-W) Turbo Spin Echo (TSE) sequence with the following parameters: TR = 2500 ms, TE = 52 ms, FA =180 º, ETL =12, slice thickness = 10 mm, FOV = 260 x 260 mm^2, matrix size = 128 x 128, and NEX = 2, to assess the MR contrast between the tumor mimic and surrounding material.

5.2.3 Phantom response to thermal heating

The phantom was sonicated with a FUS transducer incorporating a single spherically focused piezoelectric element (Piezo Hannas Tech Co. Ltd, Wuhan, China) with a nominal frequency of 2.4 MHz, a diameter of 50 mm, and a radius of curvature of 65 mm. The transducer's acoustic efficiency was 30 %. An MRI compatible positioning device featuring 4 degrees of freedom was employed in the study allowing for robotic movement and placement of the transducer relative to the tumor location [136]. A dedicated software was interfaced with the system enabling remote control of the FUS transducer and positioning mechanism, as well as with the MR scanner enabling sonication planning on preoperative MR images and the use of MR thermometry for thermal ablation monitoring.

The robotic device was positioned on the MRI couch (Magnetom Vida, Siemens Healthineers) with the phantom securely placed on the acoustic opening above the transducer, which was supplied by an RF amplifier (AG1016, T & C Power Conversion). Communication between the robotic device and software was achieved through an electronic driving system placed outside of the MRI room. The phantom was scanned using the 18-channel body coil (Siemens Healthineers) that was securely fixed a few mm above its surface with the assistance of a rigid supporting structure, as illustrated in the experimental setup of **Figure 29**.

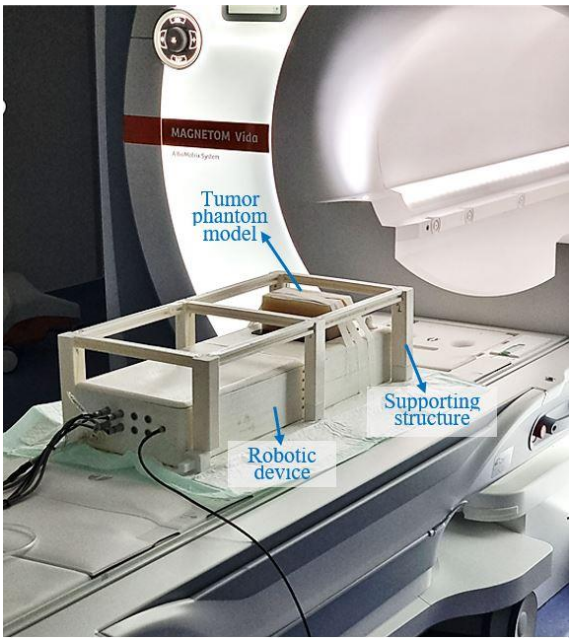

Figure 29: The experimental setup arranged on the MRI table for phantom sonications.

The distance between the phantom surface and the transducer was set at 30 mm resulting in a focal depth of 35 mm. Single and grid ultrasonic sonications were performed, where an electric power of 150-200 W (corresponding to focal intensities of 8,000 -11,000 W/cm^2) was applied for 60 s to each sonication spot.

The temperature change in the ROI during and after heating was calculated using the well-known proton resonance frequency shift (PRFS) method [9]. This technique makes use of the PRF change that occurs upon temperature change in the subject. This PRF change is proportional to the difference in phase between an initial image acquired at a specific baseline temperature (φ_0) and images obtained at various pre- and post-sonication time spots (φ), making it simple to translate phase differences ($\varphi - \varphi_0$) into temperature changes (ΔT) through the following relation [9]:

$$\Delta T = \frac{\varphi - \varphi_0}{\gamma \, \alpha \, B_0 \, TE} \quad [3]$$

where γ is the gyromagnetic ratio, α is the PRF change coefficient, B_0 is the magnetic field strength, and TE is the echo time. The magnitude of α was set at 0.0094 ppm/ºC [232]–[234].

Accordingly, a pixel-by-pixel analysis of phase differences was followed to determine the temperature change in a given ROI in the tumor mimic or surrounding material. Coronal and axial thermal maps were derived from Fast Low Angle Shot (FLASH) images acquired with the following parameters: TR = 25 ms, TE = 10 ms, FOV = 280×280 mm^2, Slice thickness = 3 mm, NEX = 1, FA = 30º, ETL = 1, matrix size = 96 x 96, and Acquisition time/slice = 2.4 s. Colour maps were produced by colour-coding the measured temperatures from the minimum to the maximum value from yellow to red.

5.3 Results

5.3.1 Characterization of tumor phantom model

Table 2 summarizes the acoustic, thermal, MRI, and CT properties of both the tumor mimic and surrounding materials, as measured in the current study or extracted from previous studies of the group, along with indicative literature values for biological tissues. Data are presented as mean ± standard deviation (n=10).

Note that the tumor-mimicking material was found to attenuate ultrasonic waves to a greater extent. Similarly, it possesses higher ultrasonic velocity and acoustic impedance. The results of relaxation time mapping in the 3T scanner revealed lower relaxation times in the tumor material. The estimated thermal properties suggest that the tumor mimic heats up more quickly owing to the addition of silicon dioxide.

Table 2: The acoustic, thermal, MRI, and CT properties of the phantom as measured in this study or extracted from previous studies of the group, compared with literature values for soft tissues.

Property	6 % agar	6 % agar + 4 % silica	Source	Soft tissues
Attenuation coefficient (dB/cm-MHz) at 1.1 MHz	0.63 ± 0.05	0.75 ± 0.06	Self-measured	0.54 ± 0.37 [235]
Absorption coefficient (dB/cm-MHz) at 1 MHz	0.10	0.15	Self-measured	0.16 - 0.34 (brain, liver, kidney) [236]
Group velocity (m/s) at 2.7 MHz	1512 ± 16	1535 ± 17	Self-measured	1561 ± 51 [235]
Mass density (kg/m^3)	945.5 ± 17.7	1020.0 ± 20.2	Self-measured	1043 ± 42 [235]
Acoustic impedance (MRayls)	1.45 ± 0.03	1.61 ± 0.03	Self-measured	≈ 1.6 [237]
Backscatter coefficient (dB/cm-MHz) at 1.1 MHz	–	0.078 ± 0.014	[230]	–
Thermal conductivity (W/m-K)	0.520 ± 0.002	0.543 ± 0.002	Self-measured	0.545 – 0.587 [238]
Thermal diffusivity (10^{-6} m^2/s)	0.296 ± 0.001	0.306 ± 0.001	Self-measured	0.13 – 0.15 [238]
Specific heat capacity (J/kg-K)	1859 ± 40	1738 ± 39	Self-measured	3590 – 3890 [238]
T1 (ms)	2135.8	2099.2	Self-measured	500 – 1000 [202], [203]
T2 (ms)	40.0	35.7	Self-measured	40 – 80 [202], [203]
T2*(ms)	21.7	18.5	Self-measured	–
CT number (HU)	24.4	54.3	[239]	20 – 80 [240]

The US, CT, and MR images of the developed tumor phantom model are shown in **Figure 30**. The inclusion of silicon dioxide in the tumor material provided sufficient contrast for clear tumor delineation in all three imaging modalities. Note that the tumor mimic appears more echogenic (**Figure 30B**) than the surrounding due to the property of silicon dioxide to scatter ultrasound waves. Note also in the CT image (**Figure 30**C) that some air spaces were created within the tumor mimic due to insufficient stirring. The case shown was the worst case that was encountered. The tumor mimic appeared with decreased intensity compared to the surrounding in the T2-W MR image (**Figure 30D**) due to its lower water concentration.

5.3.2 Phantom response to thermal heating

Figure 31 and **Figure 32** present indicative thermal maps for a single sonication within the tumor mimic acquired in coronal and axial planes, respectively. The phantom was exposed at 60 W acoustic power for 60 s at a focal depth of 35 mm. The specific sonication parameters yielded ablative temperatures in the tumor. In fact, peak temperatures of 75ºC and 70ºC were estimated in coronal and axial planes, respectively, each starting from a baseline temperature of 37ºC. The corresponding results for single sonication outside of the tumor are shown in **Figure 33**, which is a collection of coronal thermal maps acquired at specific time spots during and after sonication. In this case, a smaller peak temperature of 65 ºC was recorded. Note that some artifacts occur in these maps due to phantom vibration caused by the ultrasound waves.

Typical results for a 3 x 3 grid sonication with a spatial step of 10 mm and a time delay of 60 s between adjacent sonications are shown in **Figure 34**. In this case, an acoustic power of 45 W was applied for 60 s at each sonication spot. **Figure 34A** shows the sonication points overlaid on the thermal map acquired 4 s post-sonication. The temperature evolution over time recorded for the 9 grid points is shown in **Figure 34B**. Note that the recorded temperature changes were smaller compared to the single sonication due to the use of a smaller acoustic power. Note also that a progressive temperature increase occurred due to near-field heating while during heating the largest temperature changes were observed within the tumor material.

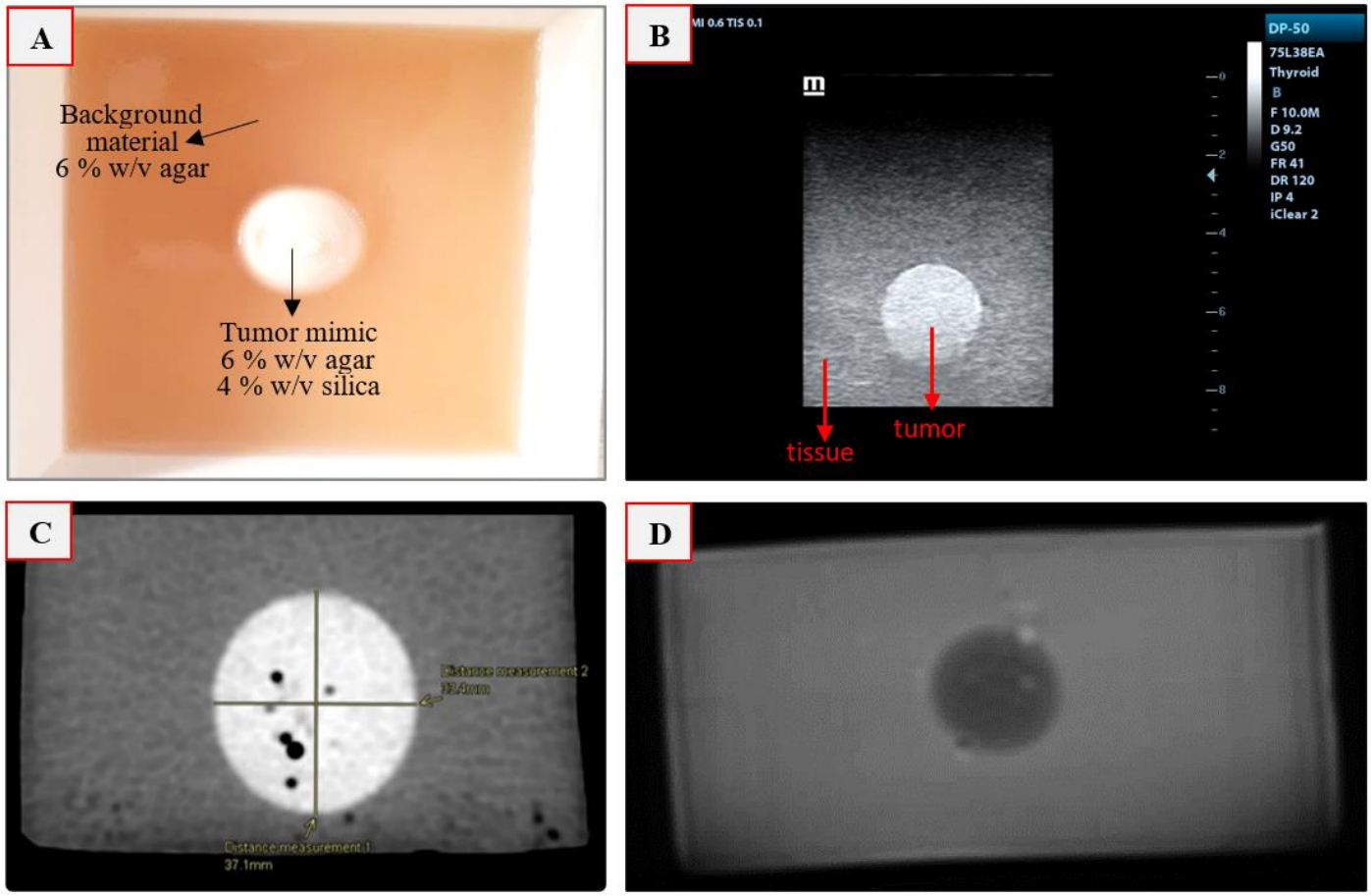

Figure 30: (A) The proposed tumor phantom model. **(B)** US, **(C)** CT (tube voltage = 100 kVp, tube current = 300 mA, exposure time = 2.0 s, and slice thickness = 1.25 mm), and **(D)** T2-W TSE coronal (TR = 2500 ms, TE = 52 ms, FA =180 °, ETL =12, slice thickness = 10 mm, FOV = 260 x 260 mm^2, matrix size = 128 x 128, and NEX = 2) images of the developed tumor phantom model.

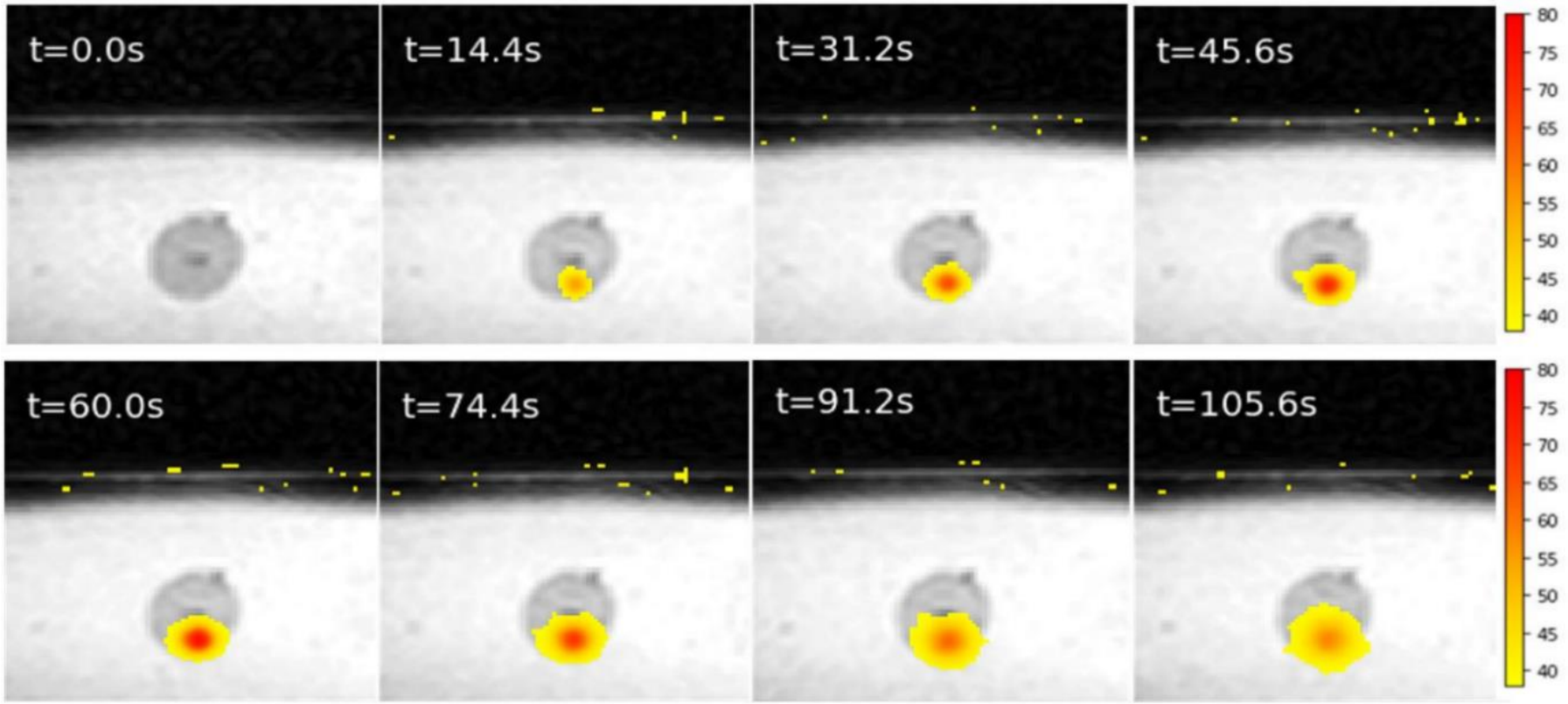

Figure 31: Coronal thermal maps extracted from FLASH images (TR=25 ms, TE=10 ms, FOV= 280×280 mm^2, slice thickness = 3 mm, NEX = 1, FA = 30^o, ETL = 1, matrix size = 96 x 96, and acquisition time/slice = 2.4 s) during and after sonication within the tumor mimic with acoustic power of 60 W, sonication duration of 60 s, and focal depth of 35 mm at 2.4 MHz.

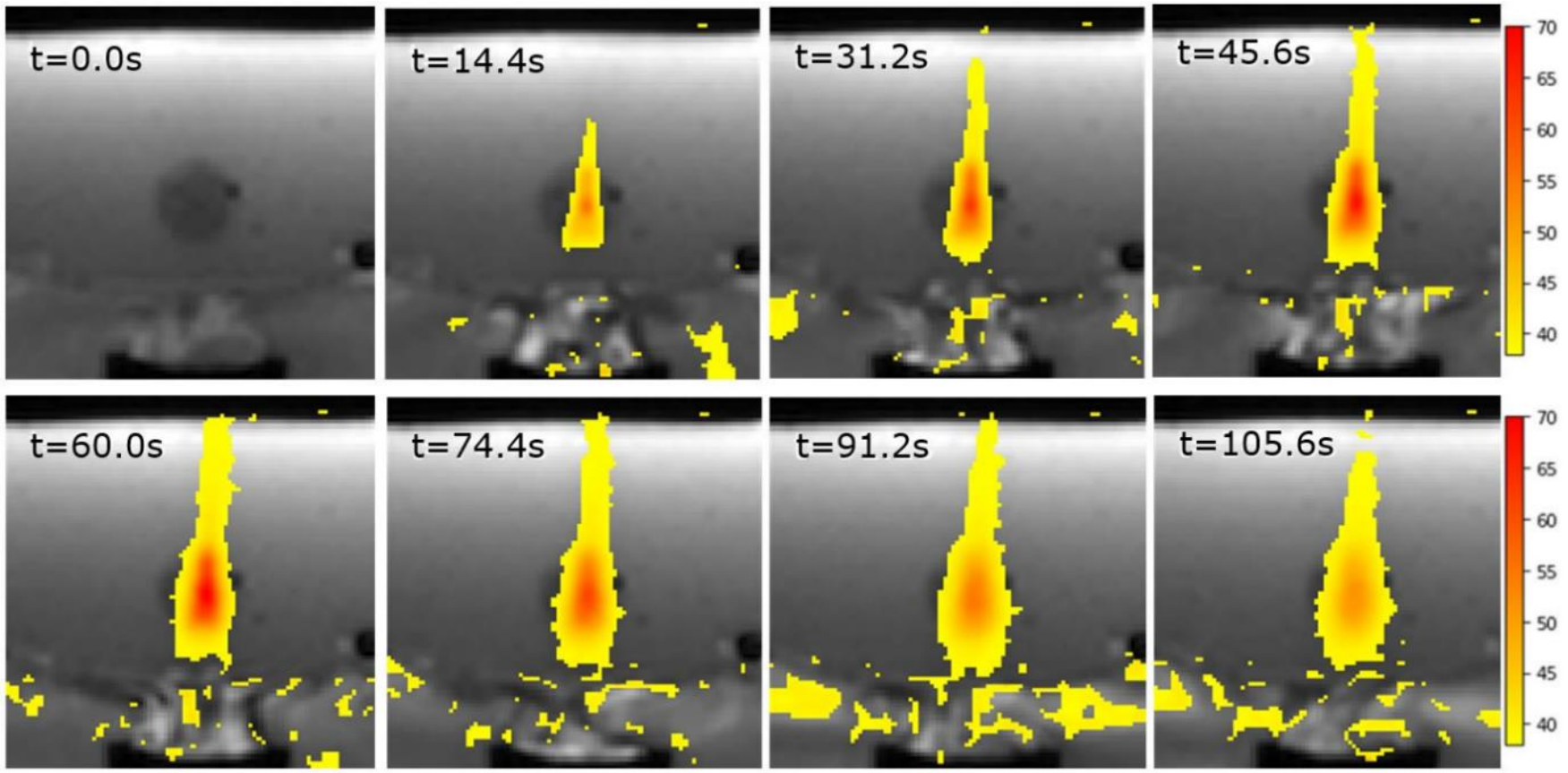

Figure 32: Axial thermal maps extracted from FLASH images (TR=25 ms, TE=10 ms, FOV= 280×280 mm^2, slice thickness = 3 mm, NEX = 1, FA = 30^o, ETL = 1, matrix size = 96 x 96, and acquisition time/slice = 2.4 s) during and after sonication within the tumor mimic with acoustic power of 60 W, sonication duration of 60 s, and focal depth of 35 mm at 2.4 MHz.

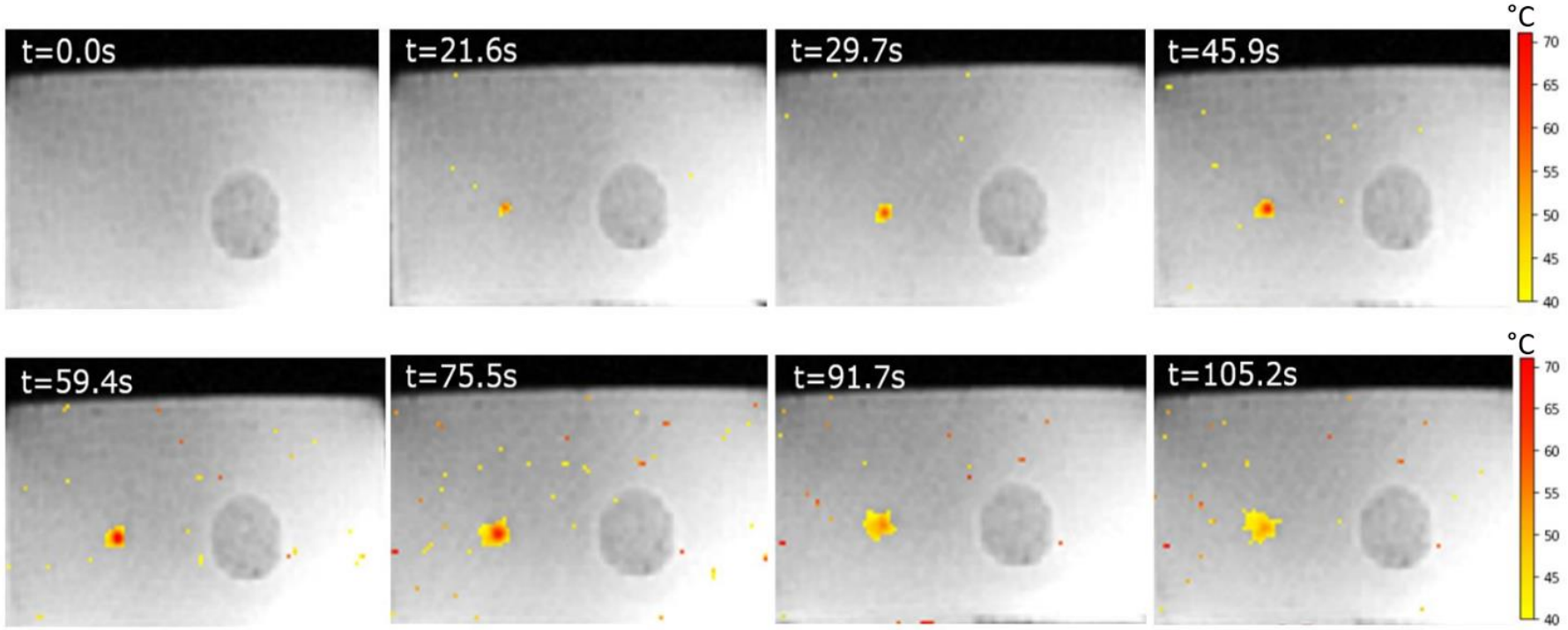

Figure 33: Coronal thermal maps extracted from FLASH images (TR=25 ms, TE=10 ms, FOV= 280×280 mm^2, slice thickness = 3 mm, NEX = 1, FA = 30^o, ETL = 1, matrix size = 96 x 96, and acquisition time/slice = 2.4 s) during and after sonication outside of the tumor mimic with acoustic power of 60 W, sonication duration of 60 s, and focal depth of 35 mm at 2.4 MHz.

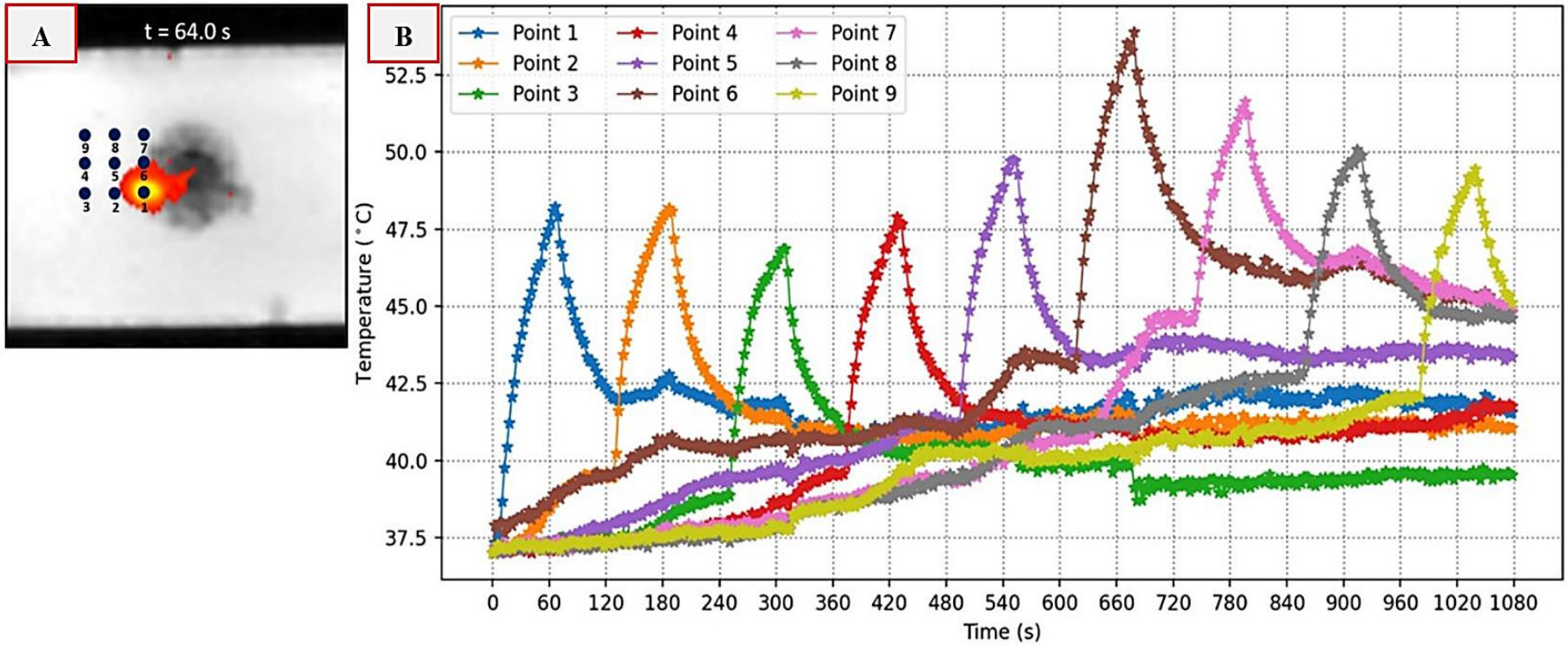

Figure 34: (A) The 9 sonication points (3x3) overlaid on the thermal map acquired 4 s post-sonication. **(B)** The recorded thermal profiles for the 9 spots sequentially exposed at 45 W acoustic power for 60 s, at 35 mm focal depth with the 2.4 MHz transducer

5.4 Discussion

This section presents the development and assessment of an US/CT/MRI compatible tumor-bearing TMP model for MRgFUS ablation studies. The selection of phantom materials and their concentration was based on knowledge acquired through previous experimentation and published work of the group [142], [153], [230]. While previous studies were focused on assessing how specific properties of agar-based gels are affected by varying the concentration of inclusions, the current study aimed to design a phantom not only replicating a wider range of properties (acoustic, thermal, and MRI) but also embedding a tumor simulator with different response to FUS heating from the surrounding material mimicking normal tissue.

The developed two-compartment phantom model consists of a 3-cm spherical tumor simulator embedded in a square tissue mimicking phantom. Agar was selected as the main ingredient for both compartments. The properties of the tumor mimic were differentiated from those of the surrounding material mimicking normal tissue by adding silicon dioxide. Although in this study a simplistic tumor model was adopted to obtain proof of concept of the proposed phantom, one could create patient-specific tumors, which may also be embedded in organ-specific phantoms to enable more realistic conditions. This could be achieved by 3D-printing dedicated molds having a cavity with the unique shape of the body part/ tumor to be mimicked, as extracted from CT data, and filling them with tissue-mimicking agar-based gels.

The estimated ultrasonic attenuation coefficient and velocity of the proposed phantom fall well within the range of literature-reported values for soft tissues (**Table 2**). The acoustic impedance was also found to be consistent between the phantom and live tissue, whereas both phantom compartments were found to possess an absorption coefficient quite below the reported range for soft tissues. Notably, it was shown that inclusion of a proper amount of milk in this phantom type can increase absorption to the level observed in tissue [153]; however, milk addition reduces the phantom robustness and shelf life. Note also that the tumor-mimicking material was found to attenuate ultrasonic waves to a greater extent verifying that silicon dioxide is an effective modifier of ultrasonic attenuation, as

also demonstrated by previous research [140], [153]. Similarly, it possesses higher ultrasonic velocity and acoustic impedance than the background material. Regarding thermal properties, while the phantom's thermal conductivity matches well that of soft tissues, the thermal diffusivity and specific heat capacity are roughly two-fold higher and smaller, respectively, than those reported by Giering et al. [238] for the kidney, heart, spleen, and liver (**Table 2**).

The imaging contrast between the two compartments should be sufficiently high to enable ease identification of the tumor mimic so that treatment planning and navigation of the ultrasonic beam relative to the target (using the motion commands of the relevant software) can be performed accurately. In the case of MRI monitoring, good contrast further enables monitoring whether thermal energy is delivered within the tumor with the required precision and as planned by intraprocedural MR imaging and thermometry. Herein, the selected concentration of 4 % w/v silicon dioxide resulted in shorter relaxation times and good delineation of the tumor in MRI. This result ties well with the results of section 4, wherein increasing silicon dioxide concentration in agar gels resulted in gradual decrease of both relaxation times, with a greater effect on T1 [142]. Notably, the estimated T2 relaxation times fall within the range of values reported literally for biological tissues, whereas the T1 relaxation times are longer than those observed in live tissues (**Table 2**).

The proposed phantom further demonstrated excellent tumor visualization in CT and US imaging. The silicon dioxide-doped tumor mimic has larger stiffness and appeared with increased radiographic density on CT images. It is also characterized by increased echogenicity due to the property of silicon dioxide to scatter ultrasound waves. Previous studies have also demonstrated that the inclusion of a metal or metalloid powder imparts noticeable ultrasonic attenuation [140].

The phantom's response to thermal heating was investigated by performing high power sonications with a 2.4 MHz single element spherically focused ultrasonic transducer in a 3T MRI scanner. An acoustic power of 60 W applied for a duration of 60 s inside the tumor mimic yielded sufficient temperature elevation (> 30 ºC) resulting in maximum focal temperatures over 70 ºC, which fall within the ablative range. In fact, most human soft tissues undergo coagulative necrosis promptly when

exposed at temperatures over 56 ºC [241], [242]. Sonication in the background material with similar parameters resulted in a smaller focal temperature of 65 ºC, which is though sufficiently high for ablation purposes. Therefore, the selected recipes were deemed suitable in terms of achieving a different thermal response to heating between the tumor (6 % agar and 4 % silicon dioxide) and normal tissue (6 % agar) phantoms. In fact, the tumor material is characterized by a higher ultrasonic absorption coefficient and a lower specific heat capacity, thus heating up more rapidly and being a better heat reservoir than the surrounding normal tissue. It is worth noting that the effect of silicon dioxide on ultrasonic absorption has also been explored in a prior study [201], which found that the absorption coefficient increases at low silicon dioxide concentrations of up to 4%. It seems that the scattering effect of this material becomes prominent decreasing ultrasonic absorption at silicon dioxide concentrations higher than 4% [201]. Therefore, the higher temperatures recorded in the tumor mimic can be attributed to the silicon dioxide-induced increase in ultrasonic absorption and reduction in specific heat capacity. At this point, it should be mentioned that the overall ultrasonic attenuation is higher in the tumor material while simultaneously ultrasonic waves encounter additional attenuation at the tumor borders due to beam reflection and scattering, which unavoidably reduces the ultrasonic energy reaching the tumor interior to some extent. Refraction and diffraction phenomena may also affect the energy deposition by causing distortion of the penetrating beam. In this example, the beam incidence was perpendicular to the tumor surface and transducer diameter was short, thus minimizing such energy losses. Although further investigation is needed to determine the significance of these energy losses, they do not seem to affect the thermal deposition to an extent that would reverse the effect of increased heat accumulation observed in the silica-doped material.

For grid sonications, the transducer was robotically moved in a horizontal plane to sequentially visit adjacent sonication spots using the relevant software commands. The thermal profiles obtained by MR thermometry (**Figure 34**) reveal a rapid temperature increase within the 60 s of sonication followed by exponential decrease at a lower rate after transducer deactivation due to dissipation of heat through conduction mechanisms. Notably, smaller temperature changes (≅10 ºC) were

recorded compared to the single sonication (≅30 ºC), resulting in smaller ablation areas, due to the use of a smaller acoustic power of 45 W. Generally, the ablation area can be easily increased by increasing the sonication time or applied power similarly to what is observed in biological tissue.

The various sonications points were visited in a sequential manner leaving a 60 s cooling period, which was previously suggested as the minimum required delay to reduce pre-focal heating for the specific sequential pattern [68]. However, the recorded temperature evolution at the 9 sonication points (**Figure 34B**) provides clear evidence of heat dissipation. Generally, the baseline temperature at each point increased over time due to heat dissipation from adjacent previously sonicated regions. Notably, by increasing the time between grid points and adjusting the movement pattern it is possible to reduce the phenomenon of heat deposition in the near field region [68]. Furthermore, although all the recorded thermal profiles show similar trend in the rate of temperature increase and post-sonication decrease, bigger temperature changes occurred at the sonication points located within the tumor mimic (1 and 6) owing to the previously discussed silicon dioxide effects. Note for example that while the grid points 6 and 8 (**Figure 34**), respectively located inside and outside the tumor, show similar thermal accumulation prior to sonication, the recorded temperature change at point 6 within the tumor was more than 50 % larger.

The proposed phantom provides triple-modal imaging characteristics (US/CT/MR), which may provide the basis for other image-guided procedures involving tumor targeting. In fact, given the proven realistic haptic feedback of agar gels [243], the phantom could also serve as a tool for tumor puncture training. Based on previous literature, the phantom could be further optimized for other thermal applications very easily by including additional ingredients during the preparation process. For instance, sodium chloride can be included to modify the electrical conductivity of the phantom for RFA and MWA studies [221], [224].

One limitation of our implementation is that no specific values of acoustic, thermal, and MRI properties were considered for the tumor model. However, since each tumor has its own specific characteristics, it’s not practicable to create a model that mimics the specific properties of a single tumor type. Furthermore, it’s not feasible to develop a model that sufficiently mimics all the critical properties of a specific

tumor type given the wide variability of tumor features among subjects. Of course, individual researchers may modify the proposed recipes to fit their tumor of interest and create patient-specific tumor models. Furthermore, it could be argued that since the ultrasonic absorption and specific heat capacity of the phantom model differ from those of soft tissues, it's response to thermal heating is not realistic and not adequately representative of the clinical scenario. Furthermore, in real tissue, a quicker focal temperature drop is expected due to the presence of blood flow. However, the phantom could be used as a QA tool to assess the functionality of MRgFUS hardware (i.e., robotic devices and transducers) and relevant software. Given the comprehensive characterization of phantom properties, it is also possible that precise dosimetry measurements and assessment of FUS ablation protocols before *in-vivo* application can be accomplished by calibrating the relation between the phantom's and soft tissues' response to thermal heating using mathematical modelling and simulations. Good tumor visualization on US, MRI, and CT images could also provide the basis for more applications, such as, image-guided tumor puncture and ablation using thermal applicators.

Being in agreement with previous studies [96], [142], [153], the current results provide sufficient evidence that the presented agar-based tumor phantom model possesses acoustic, thermal, and MRI properties well comparable with those of soft tissues. The low cost, ease handling, and the capacity to withstand ablative temperatures and produce tissue-like US and MRI signal constitute additional benefits of this phantom type. The phantom model is also capable of generating multi-modality imaging contrast. MR thermometry revealed clear elevations of temperature to ablation levels in and out of the silicon dioxide-doped tumor simulator, with clear evidence of larger heat accumulation within the tumor. It was therefore concluded that the difference in materials between the tumor and surrounding is suitable to impart noticeable change in the thermal response of the two compartments. This simple and inexpensive tumor phantom model could facilitate preclinical MRgFUS studies, and potentially other image-guided thermal ablation techniques upon minimal modifications. It may also allow for reliable monitoring of thermal heating and assessment of ablation outcome through MR thermometry or thermocouple measurements for routine laboratory testing.

6 Development of an US, MRI, and CT imaging compatible realistic mouse phantom for thermal ablation and FUS evaluation

6.1 Introduction

As made clear from the previous chapters, preclinical evaluation of new diagnostic and therapeutic systems and protocols is initially carried out in TMPs [95], [173] or/and excised animal tissue [139], followed by in-vivo evaluation, which may involve rodents [244], large animal models [138], [245], and non-human primates [246]. Realistic TMPs could serve as a valuable tool in this process, offering advanced ergonomics while contributing towards reducing animal experimentation [247]. The phantom design and composition is determined by its specific intended task, such as the assessment of dose accuracy, image quality, geometric accuracy, etc. [248]. Water-based gel phantoms representing the human body constitute a cost effective tool in biomedical research both for evaluation purposes and the training of medical students, provided that low cost supplementary ingredients can be included to adjust their properties [90], [140], [248].

Over the last decades, there has been a lot of research on the development of MRI [108], [175] and US [249] imaging phantoms, which are typically based on hydrogels, such as agar, gelatin, and polymeric materials [90]. Except from a wide variety of in-house made phantoms, there are standards available by the International Electrotechnical Commission (IEC) regarding imaging phantoms and methods for quality assurance of medical ultrasound systems [250]–[252].

The application of FUS in the brain ranging from thermal ablation to drug delivery is currently of intense clinical interest [18]. In the last decade, MBs-enhanced FUS has emerged as a novel modality enabling safe and transient disruption of the BBB so that molecules of pharmacologically relevant size can enter the brain parenchyma [120]–[124]. Both WT and genetically-modified mice serving as models of various neurological diseases have been widely used in the evaluation process and have allowed for a greater understanding of the mechanisms underlying the effects of FUS [120]–[124]. There is thus an urgent need for further research on

this topic, so that clinical translation of transcranial FUS applications is accelerated. Accordingly, realistic mouse phantoms would constitute a powerful tool in this effort, given that they are inexpensive, easily accessible, and ergonomic.

3D printing has become a popular means of creating 3D phantoms for multiple purposes. This emerging technology offers the ability for cost-effective rapid prototyping of complex geometries with high precision and has been extensively employed in the development of bone substitutes [93], [95], [117]. As an example in the context of FUS, 3D-printed parts mimicking the skull [93], femur bone [95], and ribs [94] were developed for FUS exposures, all replicating the ultrasonic attenuation property of human bones.

The use of 3D-printed real-size replicas of mice has already been suggested by numerous studies as an efficient and cost-effective way to replace live mice in a wide range of applications. The 3D printing of both hard and soft tissue anatomical structures is based on data collection from CT scans followed by surface rendering and smoothing techniques [253]. Doney et al. [253] described in detail the process of constructing plastic models of a full rat skeleton as derived from CT scans on three different 3D printers using different printing plastics (acrylic, nylon, and Acrylonitrile butadiene styrene (ABS)) and compared their performance in terms of cost-effectiveness and manufacturing resolution.

Current literature suggest that 3D printed small animal models could be of great value in preclinical medical imaging. Zhang et al. [254] developed an anthropomorphic mouse phantom intended for CT, MRI, and PET imaging. The bone part was manufactured by 3D printing on a Polyjet printer using VERO-WHITE Resin. The skin shell was manufactured on a Fused Deposition Modeling (FDM) printer using ABS thermoplastic and filled with an in-house made agar gel. Micro-pearl powder and magnevist solution were included in the gel serving as the X-ray attenuation and T1 relaxation time modifiers, respectively [254].

Dann et al. [255] proposed the use of PA2200; a commercial polyamide powder, as a novel substrate for 3D printing optical imaging phantoms using a different additive manufacturing technique called selective laser sintering. The authors discovered that this 3D printing material exhibited photoluminescent properties

owing to the anatase derivative of TiO2 and proceed to the development of a PA2200 rat skeleton phantom to be used as a training/teaching tool.

Anthropomorphic mouse models are also gaining popularity as radiation dosimetry tools. Welch et al [256] developed a realistic model mimicking the bone, lung, and tissue of a mouse, in which radiographic films were included to establish dose mapping capabilities. The bone parts were made of an epoxy resin-based material, whereas a tissue equivalent urethane-based mixture containing polystyrene microbeads was used to develop the lung tissue equivalent part. Similarly, Esplen et al. [257] proposed a real-size heterogeneous mouse phantom containing a radiochromic film and a plastic scintillating detector, thus enabling radiation dose measurements. The phantom was constructed on a Stratasys Polyjet printing machine using low-density photopolymer materials, which were chosen to simulate PMMA as closely as possible. A Polyester-filled void served as the lung model. Notably, authors clarified that a careful dosimetric characterization of the phantom is required since the employed materials are not tissue equivalent. It is also interesting to note that in a study by Price et al. [258], a bone-equivalent material composed of ABS and CaTiO3 powder has been proposed as a novel substrate for FDM printing. Authors developed a bone/soft tissue mouse phantom for preclinical radiation dosimetry, in which the soft-tissue mimic was made of ABS and the lungs were represented by air-filled voids.

Notably, Bainier et al. [259] explored the utility of 3D printed rodent phantoms for neurosurgical training. The rodent models consisted of a 3D printed skull mimic that was filled with Polyurethane expanding foam to simulate the brain tissue while a thin silicone sheet was added to simulate the skin [259].

The use of 3D printed hard-tissue mimics filled with TMPs in preclinical therapeutic applications is still under investigation and development. In this regard, the in-house construction of high quality multipurpose phantoms with anthropomorphic characteristics and tissue-equivalent properties remains a challenge. For thermal ablation studies, phantoms should possess similar thermal and acoustic properties with living tissues [96], [111] while concurrently being compatible with the relevant imaging modalities used for guidance, which may be US [260], MRI [261], or, more rarely, CT [262]. The T1 and T2 relaxation

properties are considered the critical MR properties since they greatly affect the contrast between normal tissue and thermal lesions [112]. Monitoring of thermal heating is also based on changes in these properties [9]. Although less common, CT was also employed for planning and guiding thermal ablation procedures, and thus, phantom compatibility with CT scanners constitute an additional advantage for phantoms enabling their wider use [262].

Previously proposed 3D-printed rodent-morphic phantoms matched only imaging properties [254], [255] or they were specifically designed for radiation dosimetry purposes [256], [257]. This may be partly attributed to the difficulty in simultaneously mimicking a wider range of properties. In the effort to contribute in this regard, we herein present the development and evaluation of an US, MRI, and CT imaging compatible and anatomically accurate mouse phantom intended for image-guided thermal ablation and FUS applications, which can mimic all the aforementioned critical properties.

The proposed mouse model consists of skeletal and soft tissue mimics, both being manufactured according to the CT scans data of a male mouse. The skeletal structure was constructed by 3D printing on a Stratasys printer using Acrylonitrile styrene acrylate (ASA) material, whereas the mouse body was mimicked by an in-house made agar-based phantom doped with silicon dioxide. The specific materials and their composition were selected to best approximate the critical properties of the mouse tissue for the intended applications. Note that the thermal, acoustical, and MRI properties of agar-based phantoms have already been investigated in previous studies of our group [96], [142], and were taken into consideration in this study. The candidate 3D printing thermoplastics were also proven suitable for MRI and FUS studies [93], [95], [117]. Therefore, in this study, material characterization was focused on the radiographic properties of the candidate materials. The developed phantom was evaluated to assess whether it provides tissue-like signal in MRI and CT. Trans-skull sonications with a single-element ultrasonic transducer were performed to assess its feasibility for transcranial FUS studies.

6.2 Materials and methods

6.2.1 Selection of materials

The mouse skeleton was developed using 3D printing, which was proven a cost-effective rapid prototyping method that offers the ability to develop complex, high resolution parts [257], [263], given also that there is literature data proving that 3D printed thermoplastics can match the acoustical properties of the human skull and other bony structures sufficiently [93], [95], [117], [152]. Polylactic Acid – PLA (3DJ, Essex, UK), polypropylene – PP (ULTIMAKER, Utrecht, Netherlands), ASA (Stratasys), and VeroWhite Resin (RGD835, Stratasys) served as the candidate materials for manufacturing the skeleton bones.

Agar (Merck KGaA) was selected as the gelling agent for the construction of the soft tissue mimicking phantom for the reasons explained previously in this thesis. Silicon dioxide was included as a modifier of the attenuation property. The concentration of inclusions in the agar-based soft-tissue mimic was selected so as to replicate as closely as possible the aforementioned critical properties for the intended uses of the phantom. Selection was based both on results from the current study, as well as previous studies of the group, where the acoustical, thermal, and MRI properties of agar gels doped with silicon dioxide and evaporated milk were investigated [96], [142], [153].

There is though limited literature on the radiological properties of these candidate materials, and thus, their suitability for imaging with CT remains to be demonstrated. Therefore, in the framework of selecting proper materials that will enable the development of a multimodality phantom, the radiological behavior of candidate materials was examined by measuring their x-ray linear attenuation coefficient using CT scans.

Overall, the current work aimed to combine previous knowledge on the acoustical, thermal, and MRI properties of candidate materials with the current fundings regarding the x-ray attenuation properties, along with the recent advances of the 3D printing technology, to produce a more realistic and accurate model suitable for multimodality imaging and thermal ablation studies, including transcranial FUS applications.

6.2.2 X-ray attenuation in candidate materials

Samples of the candidate soft-tissue and bone mimicking materials were prepared as shown in **Figure 35**. Four agar-based mixtures were prepared and contained in rectangular plastic containers of 64 mm^3 inner volume. **Figure 35** shows the composition of the corresponding materials used in each phantom. Three phantoms contained different agar concentrations of 2 – 6 % w/v to assess the role of agar as a modifier of radiographic attenuation. A fourth phantom was prepared with 6 % w/v agar and 4 % w/v silicon dioxide (Sigma-Aldrich). Agar is a plant-originated substance that can be easily formed into a gel when mixed with water and heated to a temperature of around 85 ºC and left to cool down naturally. The preparation process of agar-based phantoms can be found in detail in the literature [110]. It is important that during heating the mixture should be continuously agitated in order to achieve proper image homogeneity [140].

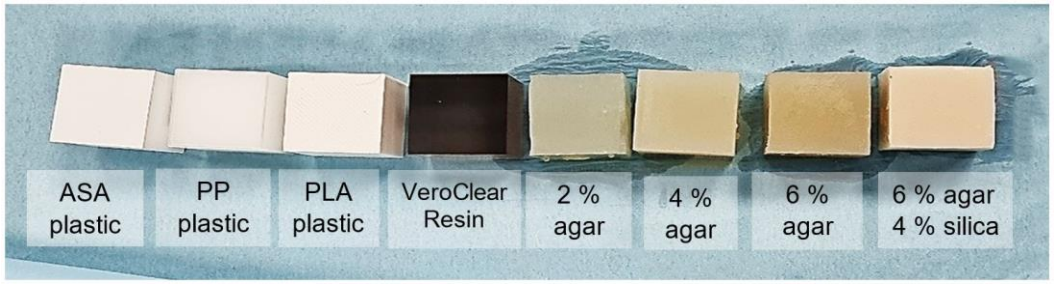

Figure 35: 3D-printed thermoplastics samples (ASA, PP, PLA, and VeroClear resin) and agar-based samples prepared for X-ray imaging.

The candidate thermoplastic materials were 3D printed into cubes with 4 cm side length using 100 % infill. The ASA (Stratasys) sample was manufactured on the F270 Stratasys printer using the FDM technique. The same technique was used for 3D printing the PP (Ultimaker) and PLA (3DJ) samples. The former was manufactured on an Ultimaker printer (3 Extended, Ultimaker, Utrecht, Netherlands) and the latter on a Creality printer (CR10, Shenzhen, China). The fourth phantom was manufacturing using VeroWhite Resin (Stratasys) on a Polyjet 3D printing machine (Object30 pro, Stratasys).

The x-ray attenuation coefficient of the candidate materials was measured using CT scans and compared with that of body tissues. The samples were imaged with a GE CT scanner (Optima CT580, GE Medical Systems) using a tube voltage of 120 kV

and a tube current of 300 mA. The CT number (expressed in Hounsfield Units - HU) for each sample was converted into linear attenuation coefficient ($\boldsymbol{\mu}$) using equation 4 [264]:

$$\mu = \frac{HU * \mu_{water}}{1000} + \mu_{water} \quad [4]$$

where $\boldsymbol{\mu_{water}}$ represents the linear attenuation coefficient of water (0,16 cm^{-1}).

6.2.3 Mouse phantom fabrication

The phantom was designed to resemble the skeletal bone and main body of a mouse. CT images of a healthy mouse provided by the Cyprus Institute of Neurology and Genetics (CING) under the study license CY/EXP/PR.L05/2021 were acquired on the GE Optima CT scanner using the following parameters: tube voltage = 120 kV, tube current = 80 mA, exposure time = 2.26 s, and slice thickness = 1.25 mm. **Figure 36** shows indicative CT images of the mouse. The acquired images were processed in an open source software (3D slicer) [265] to isolate the bone and soft-tissue volumes. Specifically, thresholds were applied to separately delineate the mouse body and skeleton. The extracted geometries were converted into STL format and further processed by an open-source 3D modelling software (Blender, Blender Foundation, Amsterdam, the Netherland) to achieve a continuous and smooth surface and improve feature resolution. The smoothed STL model of the skeletal bone shown in **Figure 37** was imported in the printer's software for final processing and printing.

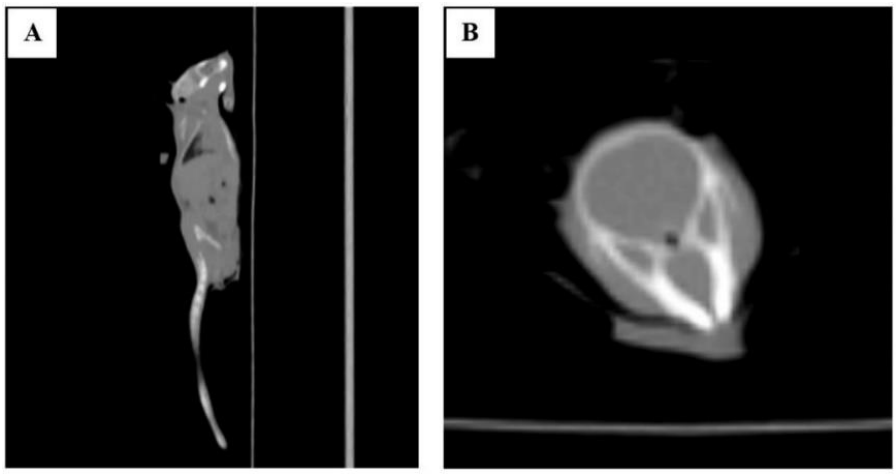

Figure 36: CT images of the mouse **(A)** Sagittal plane, **(B)** Axial plane at the skull level (tube voltage: 120 kV, tube current: 80 mA, exposure time: 2.26 s, slice = 1.25 mm).

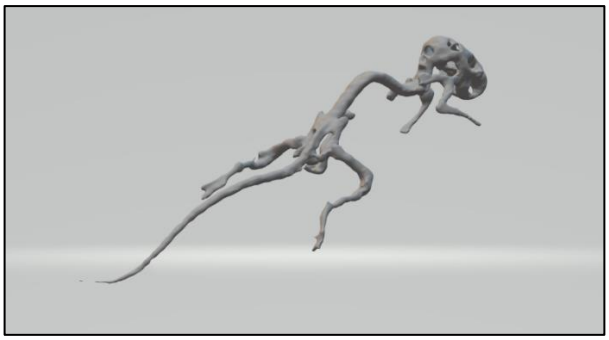

Figure 37: STL model of the segmented mouse skeletal structure after rendering and smoothing.

The mouse body was modelled using an agar-based recipe. The fabrication process was carried out in two steps. Initially, a multi-part mold was 3D printed using PLA having a cavity with the unique shape of the mouse body as extracted from the CT data. **Figure 38A** shows a computer-aided design (CAD) drawing of the mold in exploited view revealing the multiple layers, each one consisting of multiple parts. This quite complex design was required so that the mold can be easily dissembled, thus enabling proper demolding of the mouse model, and avoiding any deformation or other surface defects. The assembled 3D printed mouse mold is shown in **Figure 38B**. Prior to the molding procedure, the 3D printed skeletal bone was placed inside the mold cavity. The agar mixture was poured into the mold and left to solidify overnight. Note that the concentration of included materials was selected based on previous literature and the experimental work performed on the X-ray properties of candidate materials.

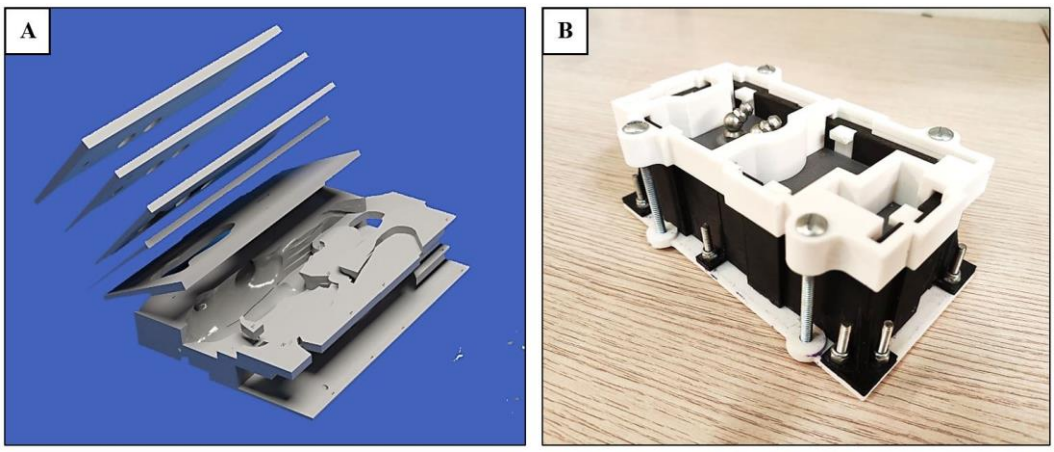

Figure 38: (A) Exploited view of the mouse mold showing the multiple structure layers. **(B)** Assembled 3D printed mouse model.

6.2.4 Phantom Imaging

The mouse phantom was imaged in a 1.5 T MRI scanner (GE Signa HD16, GE Healthcare) using the quad knee/foot/ankle coil (Signa 1.5T Transmitter/Receiver, GE Medical Systems). The coil was sited on the MRI table and the phantom was placed inside the coil cavity. For image acquisition, a proton density Cube 3D sequence was used with the following parameters: TR = 2000 ms, TE = 30, 6 ms, FA = 90°, ETL = 64, pBW = 244 kHz, FOV = 160 x 160 x 1.6 mm^3, matrix size = 224 x 224, NEX = 0.5, acquisition time/ slice = 58.6 s. Image acquisition was then performed on the GE CT scanner with the following parameters: tube voltage = 120 kVp, tube current = 440 mA, exposure time = 2.34 s, and slice thickness = 1.25 mm.

6.2.5 Trans-skull sonication in the mouse phantom

This experimental part was focused on investigating the utility of the mouse phantom in FUS applications. The phantom was mounted on a dedicated holder inside a tank filled with degassed, deionized water. An in-house manufactured transducer comprising a single element spherically focused piezoelectric (Piezohannas, Wuhan, China) of 1 MHz (diameter of 50 mm and radius of curvature of 100 mm) was fixed to the bottom part of the holder facing upwards to the phantom, as shown in **Figure 39**. The distance between the transducer and the phantom was adjusted so that the focal point is located 2 cm deep in the head part. Sonications were performed at electric power of 30 W using continuous FUS and pulsed FUS with duty factor (DF) of 1 % for a total duration of 60 s, and the temperature changes at the focus were recorded using a thermocouple (HH806AU, HH806 Series, OMEGA, CT, USA). The transducer was powered by an AG1016 RF amplifier (T & C Power Conversion). Note that the experimental setup used in this study was not designed to simulate a real scenario of a live mouse study, but to facilitate trans-skull sonication and thermocouple measurements. However, the phantom could be used in any scenario relevant to a live rodent study due to its rodent-morphic shape.

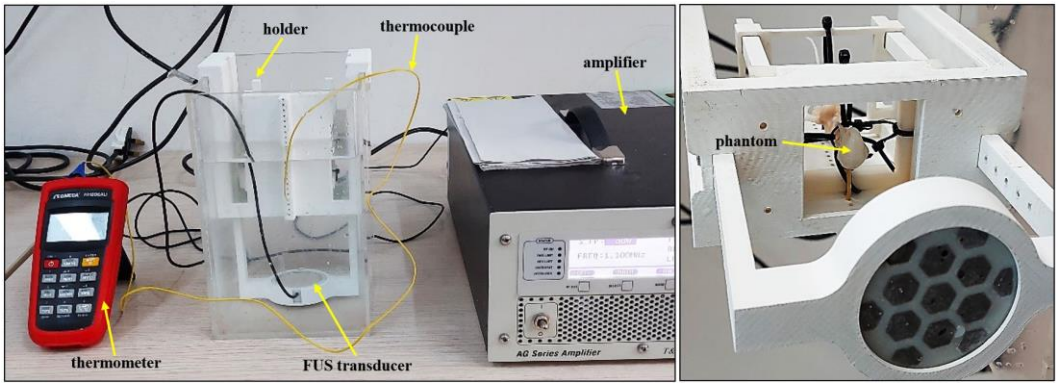

Figure 39: Experimental setup used for performing FUS sonications in the mouse phantom showing the location of each compartment.

6.3 Results

6.3.1 X-ray attenuation in candidate materials

Table 3 lists the estimated CT numbers (expressed in HU) for each sample and the corresponding linear attenuation coefficient, as well the CT numbers of mouse and human tissues for comparison purposes [254], [266]–[269]. **Figure 40** shows indicative CT images for selected samples. The estimated HU values for the ASA, PLA, and VeroClear Resin samples were in the range of 100 to 200, whereas the PP sample was found to possess a negative HU value. Regarding the agar samples, increasing agar concentration from 2 to 6 % w/v, resulted in a gradual small increase of the CT number, which translated to a minimal increase of the linear attenuation coefficient. Further increase of the CT number occurred when silica was added, yielding a slightly higher x-ray attenuation coefficient.

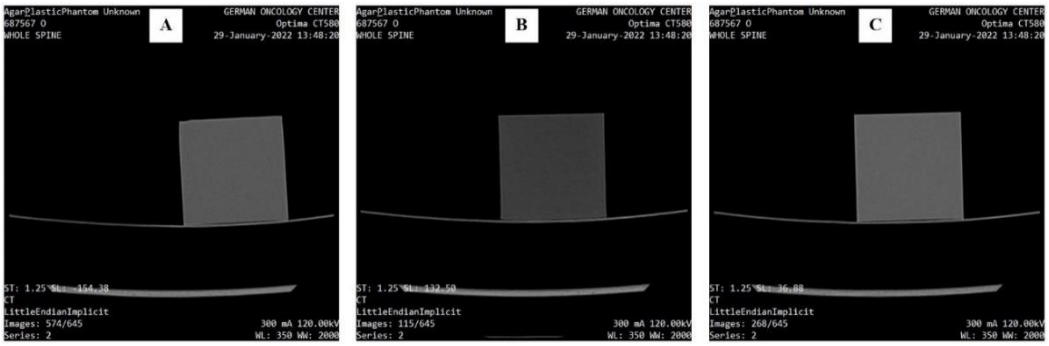

Figure 40: CT images of the **(A)** sample containing 6 % w/v agar and 4 % w/v silica, **(B)** PP sample, and **(C)** Vero Clear Resin sample (120 kV tube voltage and 300 mA tube current).

Table 3: The estimated CT number of each sample expressed in Hounsfield units (HU) and the corresponding x-ray linear attenuation coefficient (μ) for 120 kV tube voltage and 300 mA tube current, along with the CT numbers of mouse and human tissues as extracted from the literature.

Material	CT number (HU)	μ (cm^{-1})	Source
ASA plastic	191.4	0.1906	Self-measured
PP plastic	-171.0	0.1326	
PLA plastic	154.1	0.1847	
VeroClear resin	111.9	0.1779	
VERO-WHITE	130 ± 10	-	[254]
Cortical bone	1524	-	[266]
Cancellous bone	265 ± 135	-	[267]
Mouse skeleton **Rabbit skeleton**	108 ± 20 146 ± 20	-	[254]
2 % agar	10.2	0.1616	Self-measured
4 % agar	16.9	0.1627	
6 % agar	24.4	0.1639	
6 % agar & 4 % silica	54.3	0.1687	
Human muscle	45 ± 5	-	[266]
Brain tissue	20 - 40 28 ± 19	-	[268] [269]

6.3.2 Mouse phantom fabrication

The mouse skeleton was 3D printed to actual scale having a length of approximately 13 cm using ASA thermoplastic. Since none of the tested thermoplastic materials were shown to have the proper radiographic behavior in terms of mimicking bone, selection was based on other criteria. Firstly, ASA was found to possess the highest HU value, which was essential for achieving good radiographic contrast in the final phantom. In addition, it was previously proven to possess bone tissue-like ultrasonic properties. It is also a benefit that ASA models have higher durability and high

temperature resistance [270], and they are 3D printed using the FDM method that is considered more cost-effective than Polyjet printing due to the use of minimal support material [270], thus enabling lower cost production.

The mouse body consisted of 6 % w/v agar and 4 w/v silica. The specific composition of inclusions resulted in a CT number similar to that reported in the literature for soft tissues [254], [266]. The ultrasonic and MR relaxation properties of the soft tissue mimic as estimated in previous studies were also taken into consideration for the recipe selection. **Table 4** summarizes the critical properties of the proposed phantom by combining results of the current and previous studies and compares them with literature values of live tissue. **Figure 41A** shows the 3D printed skeleton as placed inside the mouse mold cavity before pouring the agar mixture. **Figure 41B** shows the mouse skeleton model and the whole mouse phantom side by side.

Table 4: The critical properties of the mouse phantom compared to literature values for live human/mouse tissue.

Property	**Agar-based phantom**	**Live tissue**	**ASA skeleton**	**Live tissue**
Hounsfield Units	54.3	Human muscle: 45 ± 5 [266] Mouse muscle: 41 ± 5 [254]	191.4	Mouse skeleton: 107.91 ± 20 [254]
Attenuation coefficient (dB/cm)	1.1 ± 0.09 (1 MHz) [153]	Rabbit Muscle: 1.18 ± 0.46 [153]	16.8 ± 1.8 (1 MHz) [152]	Skull bone: 13–24 (1 MHz) [271]
Ultrasonic velocity (m/s)	-	-	3041 ± 27 (2.7 MHz) [152]	Skull bone: 2840 ± 158 [271]
T1 relaxation time at 1.5 T (ms)	1251 ± 3 [142]	Human muscle: 1060 ± 155 [203]	-	-
T2 relaxation time at 1.5 T (ms)	23.4 ± 0.2 [142]	Human muscle: 35 ± 4 [203]	-	-
Thermal conductivity (W/m-K)	Agar gel: 0.59 [272]	Human muscle: 0.5–0.6 [273]		

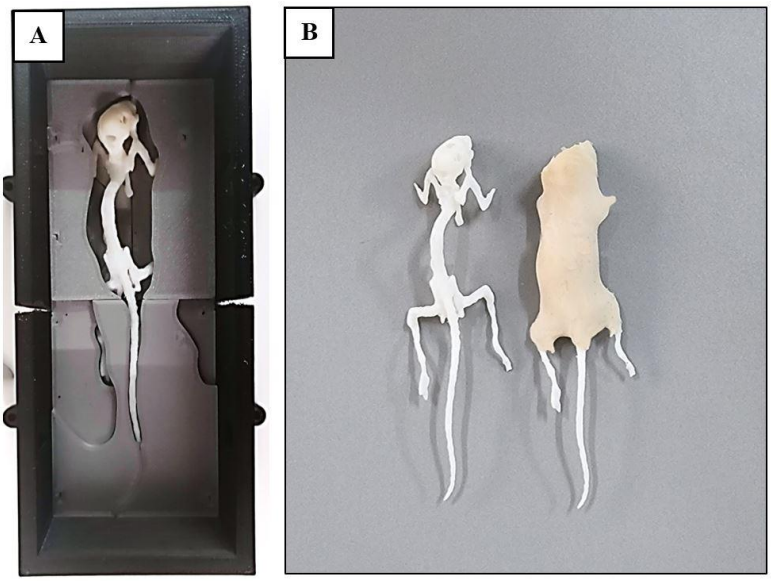

Figure 41: Photos of the **(A)** 3D printed skeleton as placed inside the mouse mold cavity, **(B)** 3D printed mouse skeleton and whole mouse phantom.

6.3.3 Phantom Imaging

Figure 42 shows Proton Density Cube images of the phantom from a 1.5 T MRI scanner. Note that the brightness in Proton Density images is determined by the hydrogen content of the imaging object. Thereby, the 3D printed mouse skeleton appears black due to the lack of protons. On the contrary, the agar-based mouse body phantom is rich in protons due to its large water component, thus producing stronger signal and appearing brighter in the image. CT scans of the phantom are shown in **Figure 43**. Note that there is a good radiological contrast between the mouse skeletal bone and body.

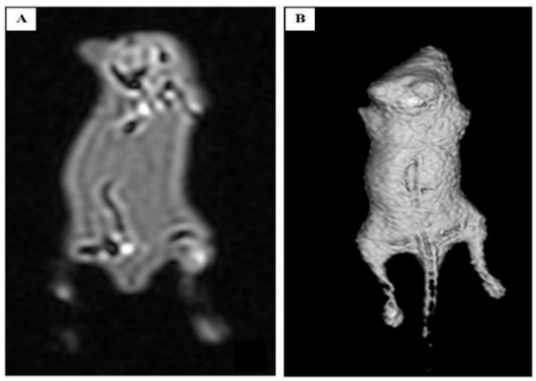

Figure 42: MRI image of the mouse phantom acquired using Proton Density 3D FSE Cube sequence: **(A)** coronal plane with TE = 60 ms, and **(B)** 3D reconstruction with TE = 30 ms.

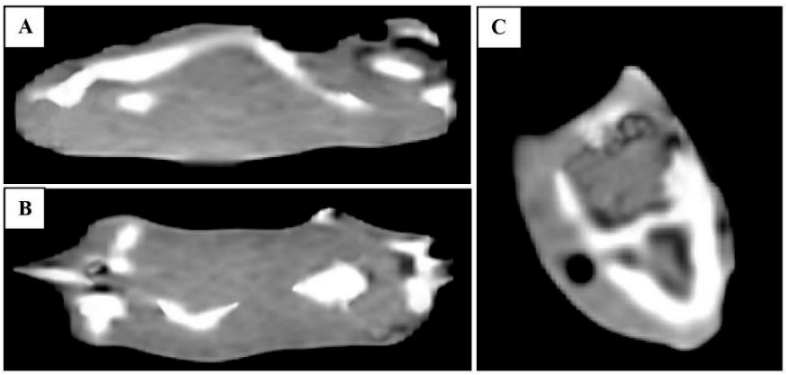

Figure 43: CT image of the whole mouse phantom (tube voltage = 120 kV, tube current = 440 mA, exposure time = 2.34 s, slice thickness = 1.25 mm): **(A)** Side view center slice, **(B)** Top view slice, and **(C)** Front view slice of mouse head.

6.3.4 Trans-skull sonication in the mouse phantom

Sonication with continuous FUS at 30 W (for 60 s) resulted in a total temperature increase of 11.2 ºC at the focus, whereas pulsed FUS (DF=1% for 60 s) caused a temperature rise of 2.9 ºC. The corresponding temperature profiles (focal temperature versus time) can be seen in **Figure 44**. Note that a substantial (about 4-fold) decrease in temperature change is observed when using pulsed FUS (compared to continuous FUS) owing to the very low acoustic intensities produced in the phantom. Also, note that the thermal profile presents plateaus where the temperature remains constant for several seconds indicating a very slow rate of heat deposition.

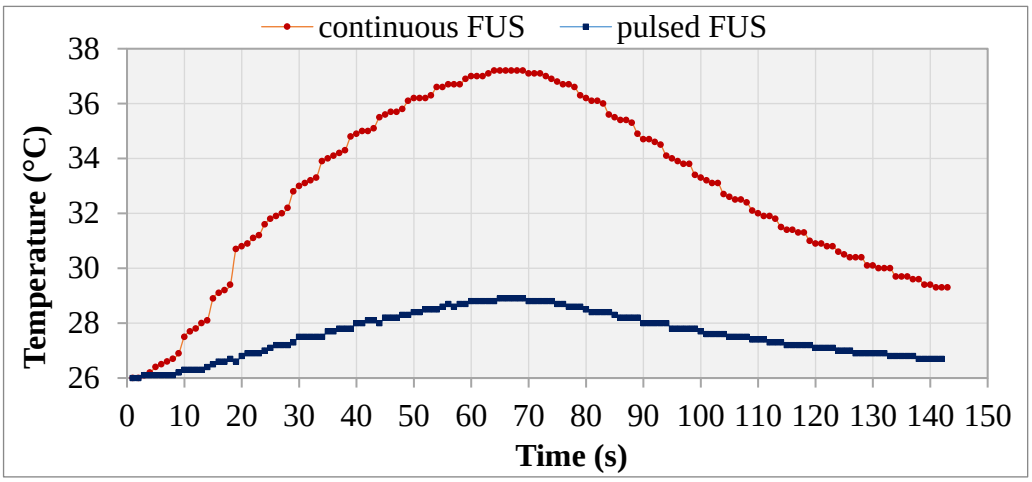

Figure 44: Temperature change versus time recorded in the phantom at focal depth of 20 mm during continuous and pulsed (DF of 1%) sonication at acoustic power of 30 W for 60 s using the 1 MHz transducer.

6.4 Discussion

An US, MRI, and CT imaging compatible realistic mouse phantom for thermal ablation and FUS studies has been developed. The thermal ablation modalities could be RFA, MWA, and laser thermal ablation [215]. The mouse model consists of the mouse body and skeletal bone (excluding the ribs) and was developed according to the segmentation data derived from CT scans of a mouse. The skeletal structure was isolated by thresholding and manufactured by 3D printing with ASA material following further smoothing on a dedicated software. Similarly, the mouse body was constructed by molding an agar-based gel in a 3D printed mold, which was specially-designed having a cavity with the unique shape of the imaged mouse. Careful mold design with multiple layers was followed to allow the mouse model to freely separate from the cavity, thus creating a smooth phantom surface, which is essential for achieving proper ultrasonic transmission.

The selection of an agar-based phantom to mimic soft tissue was based on numerous criteria, including its ability to replicate critical properties of living tissues (**Table 4**). Our results further demonstrated the ability of agar gels to induce similar radiographic attenuation with soft tissues. The x-ray attenuation coefficient of the four candidate soft-tissue mimicking materials was measured using CT scans and compared with that of living tissues. The results suggest that increasing agar concentration (2 to 6 % w/v) increases the CT number at a low rate (10 to 24 HU). The addition of silicon dioxide (4 % silica, 6 % agar) resulted in a more than 2-fold increase of the CT number (54 HU), which is slightly higher than the value of 45 ± 5 HU reported for human muscle [266]. The silica doped phantom also matches sufficiently the value of 41 ± 5 HU reported by Zhang et al [254] for mouse muscle.

The methodology used for manufacturing the skeleton mimic including bone segmentation by thresholding, image processing, and 3D printing resulted in a smooth and detailed model, which matched the size and accurately reproduced the shape of the imaged mouse skeleton. Advantageously, several studies have demonstrated the efficacy of 3D printed thermoplastics to mimic bone in terms of acoustic properties and have suggested their use with the FUS technology [93], [95], [117].

Ideally, bone-mimicking materials should also be x-ray attenuation equivalent to bone in order to be suitable for radiographic imaging. According to the evaluation results, none of the tested thermoplastic samples was found to be radiographically representative of human bones [274], which have significantly higher CT numbers in the range of 300-2000 HU depending on whether they are cancellous or cortical [274]. However, the estimated CT numbers are close to the value of 107.91 ± 20 HU reported by Zhang et al. [254] for mouse bone (at 120 kVp and 100 mAs).

The developed phantom was evaluated by MRI and CT imaging to assess whether it provides tissue-like signal. The agar-based mouse body mimic demonstrated tissue-like MRI signal as expected. In addition, the mouse skeleton was delineated well by MRI imaging (**Figure 42**). Accordingly, the CT images (**Figure 43**) reveal good radiological contrast between the mouse skeletal bone and body, which is similar to that observed for the live mouse (**Figure 36**).

Finally, the mouse phantom was able to reproduce realistic behavior during trans-skull sonication as proved by thermometry measurements with a thermocouple. As demonstrated in **Figure 44**, the temperature increased due to heat absorption and then decreased gradually after transducer deactivation due to heat dissipation through conduction mechanisms. As expected, heat dissipation is a slower process, and its rate decreases with time. In this regard, the phantom demonstrated realistic response to heat, except from the absence of blood flood, which contributes to post-sonication heat loss and would result in steeper drop of the focal temperature. The obtained preliminary results further suggest that the phantom can develop high temperatures during heating, and thus, it can be used for assessing thermal protocols, given also that it possess tissue-like acoustic, thermal, and MRI properties (**Table 4**).

However, further investigation is required to comprehensively assess the phantom's response to thermal heating. Regarding pulsed FUS, the recorded temperature change is important in the sense that it was maintained below the safety threshold where thermal effects can be considered negligible [275]. It is also essential that the phantom enabled the insertion of thermocouples without losing its structural integrity. As expected, the presence of the ASA skull affected the results by decreasing the rate of heat deposition through beam spreading and focal shifting

[152]. Note also that although single element transducers cannot compensate these energy losses, they were proven suitable for trans-skull applications in mice due to their thin skull bone [120], [276]–[278].

The phantom offers realistic visualization in US, MRI, and CT, which constitute the modalities that have been used so far for the positioning of thermal applicators, as well as for therapy guidance or/and determination of tissue destruction [260]–[262]. In the context of transcranial FUS, although the proposed phantom is not physiologically accurate, replication of the main acoustic, thermal, and MRI properties is considered adequate in terms of assessing the spatial accuracy of ultrasound delivery and how it is affected by the skull-induced beam aberration, the dimensions of the FUS spot, thermal effects at the ROI and potential off-target effects, such as thermal deposition near to the skull, as well as the focal acoustic pressure in the case of pulsed FUS. Such information are required for adjusting the setup and/or sonication parameters so as to correct beam shifting, avoid off-target bioeffects, and compensate for energy losses, thus achieving the desired thermal or mechanical effects at the desired location. In terms of equipment testing, examples of particular applications we anticipate the phantom being useful for are the testing of the trans-skull heating abilities of newly-developed FUS transducers or the steering abilities of phased array ones, the linearity of output power, the response to increasing power and the limit for safe operation, as well as the assessment of shelf-heating effects and identification of malfunctions in equipment's operation.

The feasibility experiments performed in this study demonstrated the functionality of the phantom for the evaluation of thermal protocols. Future studies are though needed to further assess the thermal response of the phantom when exposed to continuous FUS at increasing ultrasonic power, as well as the acoustic pressure field generated by pulsed FUS with varying ultrasonic parameters. In this regard, its MRI compatibility will enable temperature monitoring in real-time through MR thermometry. It is clarified that the phantom is not intended to replace mouse studies but rather to minimize the required number of studies by allowing optimization of experimental features and parameters before *in-vivo* experimentation.

7 Simple methods to test the accuracy of MRgFUS robotic systems

7.1 State of the art

All the techniques used to test the mechanical accuracy of a robot are based on the idea of comparing the commanded motion step with the actual displacement as estimated by a distance-measuring technique. Mechanical accuracy refers to both the positioning and repeatability accuracy of motion. Before the procedure is applied and evaluated *in vivo*, accuracy assessment is typically carried out in free space, sometimes referred to as intrinsic system accuracy, meaning not under real conditions. Most commonly, after acquiring evidence of sufficient accuracy and repeatability by benchtop testing, the system is evaluated in the environment that is intended to be clinically used, such as the bore of an MRI system.

Regarding benchtop evaluation, several motion tracking techniques were proposed for assessing the accuracy of motion in a free robot workspace [74]–[79]. Optical tracking systems have been widely used for confirming adequate targeting accuracy for needle-related interventions, where the placement error is defined by the deviation of the actual tooltip position from the desired location [74]–[77]. The accuracy of an automated robot intended for breast biopsy in precisely reaching a target was evaluated using a rigid test tool, which was driven to target positions through straight and angled paths and monitored with an optical tracker [74]. Similarly, other studies [75]-[76] investigated the motion accuracy of robotic systems using optical tracking systems. A different tracking method was chosen by Dou et al. [77], who measured the positioning accuracy of a brachytherapy system using a 3D laser tracker, as well as an inertial measurement unit [77]. An optical measuring microscope has also been proposed for estimating the actual displacement of a linear motion stage after the execution of commanded movements [78].

More straightforward methods involving the use of digital calipers and special structures have also been carried out in the laboratory environment for accuracy evaluation purposes. The needle tip accuracy of a breast biopsy robot was evaluated in free air by targeting crosshairs drawn on a board [80]. The needle tip was

commanded to puncture these targets and the error was estimated by the distance from the center of each target to the corresponding pierced hole [80]. Similarly, in the framework of evaluating the motion accuracy of a robot intended for transcranial FUS surgery, the transducer was replaced by a felt-tipped pen, which was commanded to touch multiple resolution points distributed on three perpendicular planes demonstrating the entire robot's workplace [55]. Each created mark was assigned in resolution circles having radial and angular approximation zones for facilitating targeting error measurement [55]. Another simplified method involves mounting digital calipers on the motion stages of a robot such that their actual displacement after motion execution can be directly measured by the incremental distance of the caliper [81], [82].

Robotic devices intended for non-invasive FUS applications are constantly being developed [83] and extensively evaluated by performing ablation studies, in which the separation precision of multiple ablations constitutes an indication of the positioning error. Tao Wu et al. [84] performed quality control of a FUS system, where the focus positioning accuracy was tested by performing multiple sonications on a Lucite cart. Left-right and superior-inferior movements by specific distance were commanded by a treatment planning software, resulting in numerous sets of melted spots arranged in discrete patterns. The actual distance between adjacent spots was measured with a digital caliper [84]. In other phantom experiments conducted in a benchtop setting [81], the linear motion stages were commanded to create discrete ablations of specific spacing in a gel phantom. White coagulation lesions were clearly visible, being spaced by the desired step, thus confirming the accuracy of positioning.

Price et al. [55] followed a similar approach but in an MRI setting. An MR conditional robot for transcranial FUS interventions was used to perform multiple sonications in a 2 x 3 pattern in a heat-sensitive gel phantom located in a water tank. The thermal images acquired after each sonication were superimposed onto one image, and the positioning accuracy was defined as the spacing between the centers of adjacent ablated areas [55]. This technique was also selected for evaluating the accuracy of motion of an MR-compatible FUS device intended for brain diseases treatment [21]. A four-point ablation pattern was performed *in vitro*, in lamb brain,

with different motion steps of 1 to 10 mm, and the formed lesions were visualized in T1-weighted FSE images. The ablated areas appeared as spots of increased signal intensity, and the distance between neighboring ablations was calculated from the center of each spot. Notably, smaller errors were estimated with increasing step distance [21]. Similarly, Yiallouras et al. [82] performed phantom experiments where T2-weighted FSE images revealed areas of reduced signal formed in a discrete pattern. It is notable that Sagias et al. [88] developed a motion phantom for evaluating FUS protocols specifically for moving targets in the MRI environment.

Herein, we present three simple methods that can be used to assess the accuracy of motion of an MRgFUS robotic system in both benchtop and MRI environments. In the first method, a digital caliper is mounted on the motion stage under evaluation with the assistance of specially designed 3D printed parts, having its one edge fixed on a stationary part and the other on a movable part. In that way, a specific step movement of the stage results in an analogous increment in the caliper. The second evaluation procedure relates to accuracy assessment in the MRI setting. The robotic device is sited on the MRI couch, and a plastic marker is mounted on the top of the FUS transducer so that it can be visualized in MR images. The third method involves performing multiple ablations in a transparent plastic film by robotic movement of the transducer.

7.2 Materials and methods

7.2.1 Robotic system

A robotic system featuring 4 DOF that was developed for preclinical *ex vivo* and *in vivo* applications of the MRgFUS technology was employed in the study. It is particularly intended to treat cancer in small and large companion animals. The positioning device was 3D-printed (F270, Stratasys) with ABS thermoplastic material. The positioning mechanism features motion in 4 DOF, which is adequate to ablate a tissue volume of any shape and size. Specifically, the device allows the user to linearly navigate the focused transducer in three axes (X, Y, and Z), whereas angular rotation about a single axis is also available. All motion stages are computer-controlled through a customized software. Due to the spatial limitations of the bore, there are some motion restrictions. The maximum travel of the

transducer is 60 mm in the X axis (forward and reverse), 75 mm in the Y axis (left and right), and 26 mm in the Z axis (up and down). The rotation limit is 90 degrees. Piezoelectric motors (USR60-S3, Shinsei Corporation, Tokyo, Japan) and dual digital encoders (US Digital Corporation, Vancouver, WA, USA) were incorporated in all motion stages, thus providing a highly accurate motion. The CAD drawing of the fully assembled robotic device is shown in **Figure 63**.

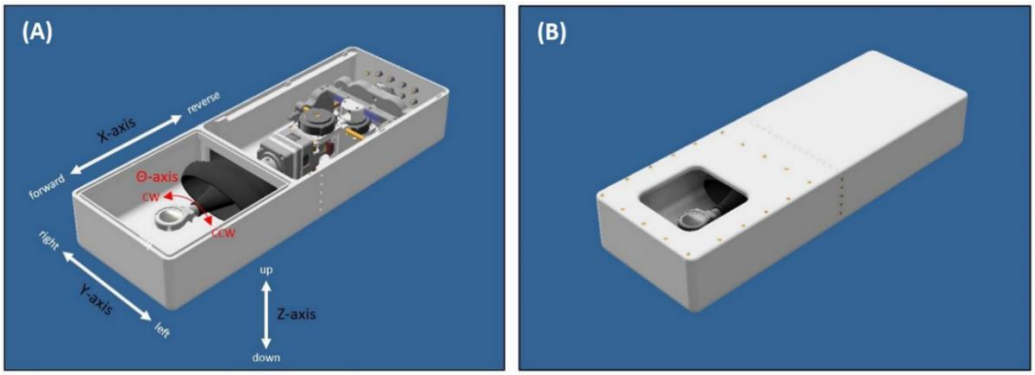

Figure 45: CAD drawing of the 4 DOF robotic system **(A)** without the cover (components are visualized), and **(B)** with the cover.

7.2.2 Digital calipers method

The motion accuracy of the positioning mechanism was evaluated using digital calipers with a measuring accuracy of 0.01 mm. The digital calipers (one for the linear stages and one for the angular stage) were mounted and stabilized on 3D-printed structures. The structures were easily attached to the robotic device as illustrated in **Figure 64**. The one edge of the caliper was securely mounted on a stationary part of the device, while the other part was attached on the movable part. In that way, the caliper was perfectly aligned with the axis under evaluation, thus providing accurate distance estimation. A different structure was used for the measurement of the angular motion as shown in **Figure 65**. Note that this stage was evaluated separately, outside of the mechanism enclosure.

In each case, the motion stage was moved through the designed software at a certain distance (or degrees) and the actual displacement was measured by the incremental distance in the caliper. Both directions of each linear axis were evaluated at step movements of 1, 5, and 10 mm. Accordingly, the angular motion accuracy was

evaluated for clockwise (CW) and counterclockwise (CCW) directions at step angles of 1, 5, and 10°.

Moreover, the speed of motion of the robotic device in all axes (X, Y, Z, and Θ) and directions was calculated by the time required for the stage to cover specific step movements, which was equal to the activation time of the piezoelectric motors as provided by the software.

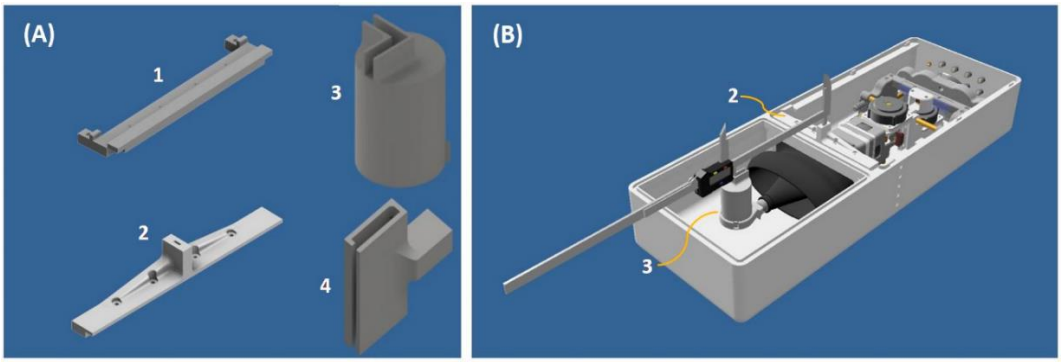

Figure 46: (A) Stationary (1, 2, 4) and moveable (3) 3D-printed structures that were used for the X and Y axes distance measurements. **(B)** CAD drawing of the setup that was used for the X axis motion accuracy estimation.

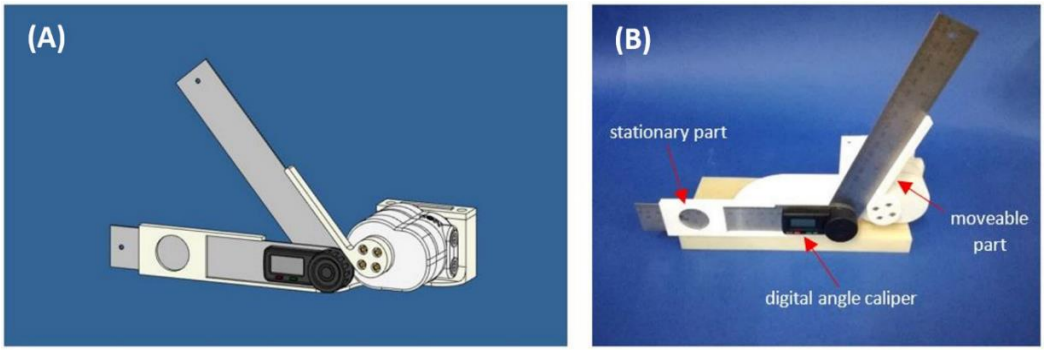

Figure 47: Experimental setup used for estimating the angular motion accuracy using the digital angle caliper: **(A)** CAD drawing, and **(B)** photo.

7.2.3 MRI method

Another simple method for estimating the motion accuracy of a robotic system is through MRI. This method is limited to MR-compatible robotic devices. The concept of the proposed technique is based on the fact that structures without protons appear dark in MR images. The focused transducer was replaced by a 3D-printed plastic structure with a tip of 2 mm thickness, which served as a marker, and the water enclosure was filled with degassed water. The robotic device was

placed inside an MRI scanner (1.5 T, GE Signa HD16, GE Healthcare) and covered with a Signa 1.5 T General Purpose flex surface coil (General Electric Medical Systems, Milwaukee, Wisconsin, USA). **Figure 48A** illustrates the experimental setup as placed on the MRI table, while **Figure 48B** shows a CAD drawing of the plastic marker. MR scanning was performed using an FSE sequence in coronal plane. The main MRI parameters were: TR = 800 ms, TE = 19 ms, FA = 90^{o}, ETL = 3, pBW = 65.1 Hz/pixel, and FOV = 280x280x10 mm^{3}.

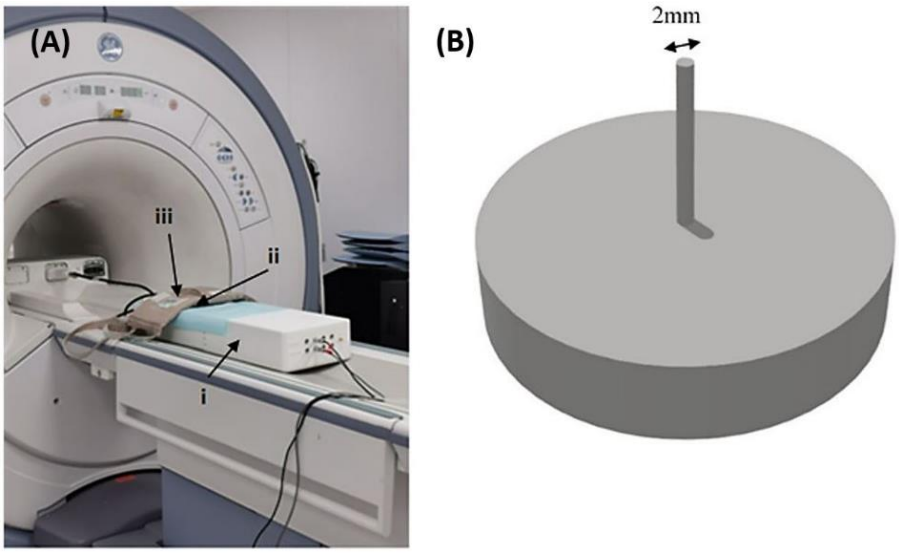

Figure 48: (A) The robotic device (i) as placed on the MRI table, showing the location of the plastic marker (ii) and the flex surface coil (iii). **(B)** CAD drawing of the plastic marker.

The accuracy of linear motion was assessed in the X and Y axes. The initial position of the tip was located, and then the transducer was moved by a certain distance. Bidirectional movements with step of 3 and 5 mm in both axes were tested. An MR image was acquired after each step movement to detect the tip location. A special approach was followed for locating the position of the 2 mm thick tip of the marker. First, the image zoom was enhanced to focus on the plastic marker. Then, the corresponding pixels were scanned to identify the x and y coordinates of the pixel with the lowest SI (assumed to be the center of the marker). The change in pixel number after a step movement reflected the shift in position of the transducer in the tested direction. The pixel difference was then multiplied by the pixel size (0.5469 mm) of the acquisition matrix so as to measure the shift in mm. This technique had an inherent error of ±1 pixel, which translated to ±0.5469 mm. Finally, the series of images were superimposed onto one image for visualizing the motion patterns.

7.2.4 Visual method

The motion accuracy was also assessed through visual observations of multiple ablations produced on a transparent plastic film (0.9 mm thickness, FDM400mc print plate, Stratasys). The acoustic attenuation of the plastic film at the frequency of 2.1 MHz was 8.5 ± 0.2 dB/cm-MHz based on a standard transmission through immersion technique [96]. The water enclosure containing the transducer (spherically focused, frequency: 1.1 MHz, diameter: 50 mm, focal length: 70 mm, Medsonic Ltd., Limassol, Cyprus) was filled with degassed water up to the plastic film. The robotic device was moved to sonicate the film in square grid patterns for evaluating the accuracy of motion, as well as the linear motion alignment in the X and Y axes. An acoustic power of 10 W was applied at each grid point using an RF amplifier (AG1012, T & C Power Conversion). The sonication time varied from 1-4 s so as to control the lesion size. Subsequently, sonications were performed with varying motion step and sonication time, with the time delay between the successive sonications set at 30 s.

Also, the maximum motion range of the positioning mechanism in the horizontal plane was estimated by applying sonications at the extreme points of movement in the X and Y axes. It is noted that lesion formation was a result of reflection from the plastic/air interface.

7.3 Results

The motion accuracy of the robotic device in both linear and angular axes was evaluated using digital calipers. Linear motion steps of 1, 5, and 10 mm and angular steps of 1, 5, and 10^{o} were performed for 20 repetitions in bidirectional movements. **Figure 49** shows a bar chart that displays the actual distance measured at a commanded step movement of 5 mm in both X axis directions for each repetition measurement.

The range of actual displacement measured at each commanded step, as well as the mean motion error and standard deviation for all the axes (X, Y, Z, and Θ) are listed in **Table 5**. Furthermore, the speed of motion of all stages in bidirectional

movements was calculated according to the motors' activation time during movement execution. The corresponding results are also listed in **Table 5**.

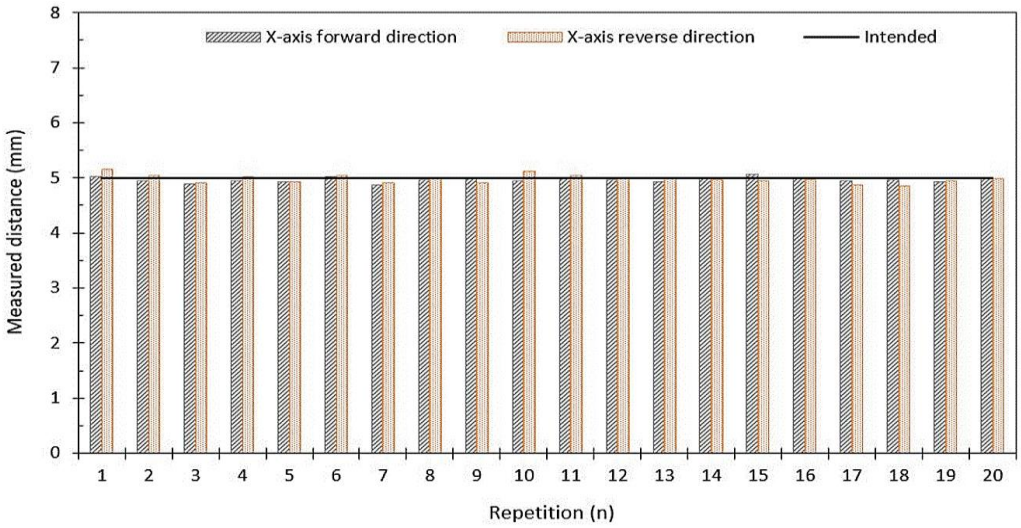

Figure 49: Distance measurements for 20 repetitions in the X axis with step of 5 mm in bidirectional movements. The black straight line indicates the commanded distance.

MRI was also used to examine the accuracy of motion in the X and Y axes. The MR images acquired after execution of each 3 mm motion step in the X axis reverse and Y axis right directions were superimposed onto the images shown in **Figure 50A** and **Figure 50B**, respectively. **Table 6** lists the range of actual distance measured for each commanded motion step (3 and 5 mm) and each direction, as well as the corresponding mean motion error and standard deviation.

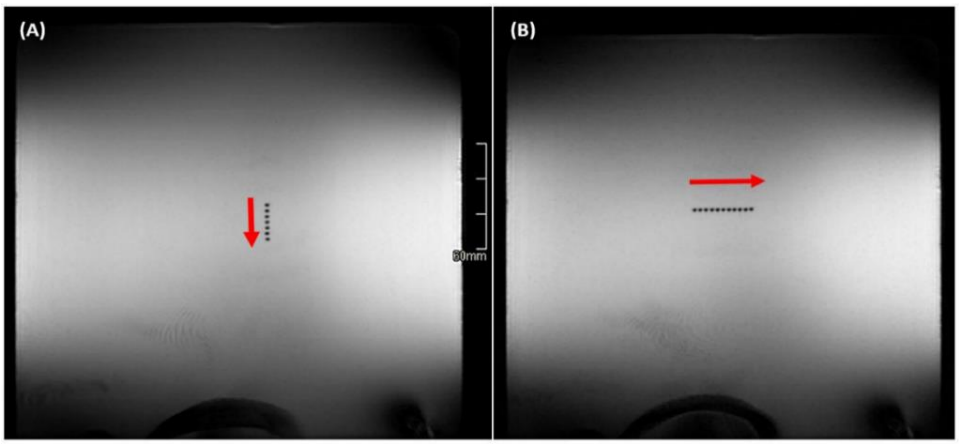

Figure 50: Minimum intensity projection from a combination of FSE coronal images that shows a **(A)** reverse step movement of 3 mm in the X direction, and **(B)** right step movement of 3 mm in the Y direction.

The motion accuracy was visually assessed by sonicating plastic films. Sonications at the extreme points of movement in the horizontal plane revealed a maximum motion range equal to 6 and 7 cm in the X and Y axes, respectively. The effect of lesion formation on the plastic film was originally examined by varying the sonication time while keeping constant the acoustic power as shown in Figure 51.

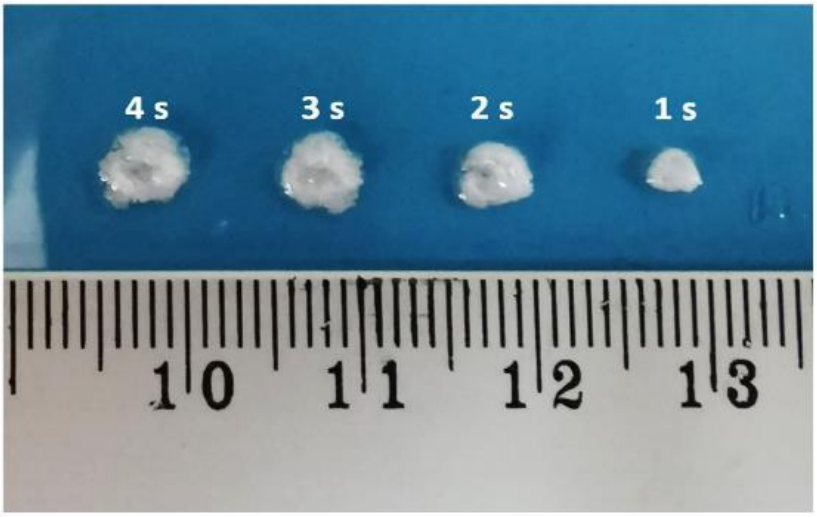

Figure 51: Effect of varying sonication time on lesion formation on the plastic film, using low power and a spatial step of 10 mm (transducer specifications: 1.1 MHz frequency, 50 mm diameter, 70 mm focal length).

The appropriate selection of sonication time and grid step allowed formation of discrete and overlapping lesions, and visual evaluation of the accuracy of motion and alignment. **Figure 52** shows discrete lesions formed after applying sonications at acoustical power of 10 W for 1 s, in a 6x5 grid pattern with a step distance of 5 mm. The formed lesions show satisfactory alignment in both axes.

Sonications at the same acoustical power for a longer time of 3 s in a 15x15 grid pattern with the same time delay of 30 s, but a smaller spatial step of 2 mm, resulted in overlapping lesions as illustrated in **Figure 53**. The ablated area was well defined in a square of about 3.3 x 3.3 cm^2, without any significant protrusions.

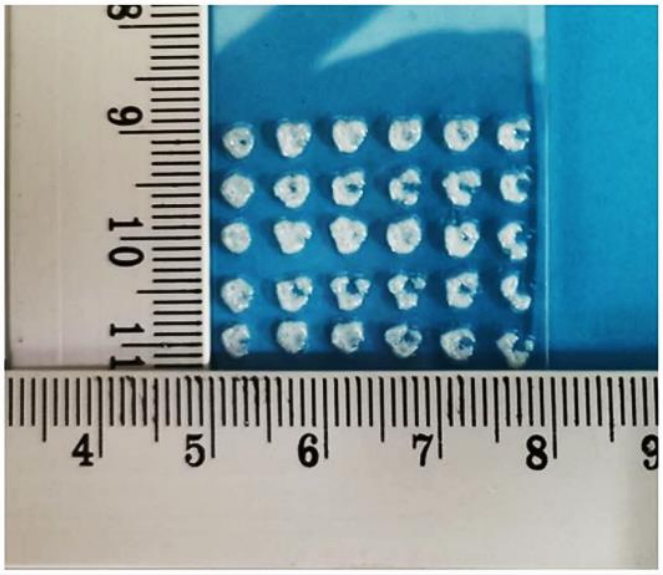

Figure 52: Discrete lesions as formed on the plastic film for sonications in a 6x5 grid pattern, with acoustical power of 10 W for 1 s, and a step distance of 5 mm.

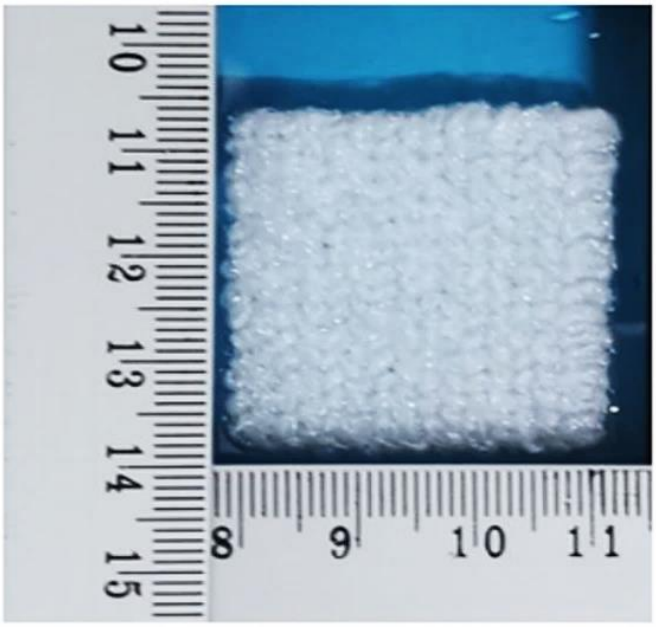

Figure 53: Overlapping lesions as formed on the plastic film for sonications in a 15x15 grid pattern, with acoustical power of 10 W for 3 s, and a step distance of 2 mm.

Table 5: The range of distance measurements at commanded spatial steps of 1, 5, and 10 mm in each linear axis and angular step of 1, 5, and 10º about the rotational axis, the corresponding mean motion error and standard deviation, and the mean speed and standard deviation in each case.

Linear	**Commanded Step (mm)**	**Range of actual displacement (mm)**	**Mean Error ± SD forward (mm)**	**Mean Error ± SD reverse (mm)**	**Mean Speed ± SD forward (mm/s)**	**Mean Speed ± SD reverse (mm/s)**
X	1	0.88 - 1.08	0.042 ± 0.032	0.051 ± 0.032	10.31 ± 0.62	10.05 ± 0.26
	5	4.85 - 5.15	0.047 ± 0.033	0.065 ± 0.044	10.43 ± 0.57	9.80 ± 0.94
	10	9.78 - 10.19	0.081 ± 0.058	0.058 ± 0.057	10.01 ± 0.21	9.98 ± 0.78
Y	**Step (mm)**	**Range (mm)**	**Error right (mm)**	**Error left (mm)**	**Speed right (mm/s)**	**Speed left (mm/s)**
	1	0.88 - 1.09	0.045 ± 0.042	0.042 ± 0.026	14.28 ± 1.40	15.93 ± 0.83
	5	4.89 - 5.19	0.053 ± 0.032	0.084 ± 0.050	13.84 ± 1.02	14.16 ± 0.62
	10	9.85 - 10.29	0.123 ± 0.082	0.086 ± 0.061	14.66 ± 0.29	14.46 ± 0.64
Z	**Step (mm)**	**Range (mm)**	**Error up (mm)**	**Error down (mm)**	**Speed up (mm/s)**	**Speed down (mm/s)**
	1	0.89 - 1.11	0.052 ± 0.029	0.039 ± 0.030	9.90 ± 0.20	10.09 ± 0.21
	5	4.90 - 5.11	0.055 ± 0.037	0.055 ± 0.035	9.90 ± 0.13	9.73 ± 0.30
	10	9.78 - 10.11	0.069 ± 0.060	0.084 ± 0.062	9.78 ± 0.08	9.59 ± 0.38
Angular	**Step (º)**	**Range (º)**	**Error CW (º)**	**Error CCW (º)**	**Speed CW (º/s)**	**Speed CCW (º/s)**
Θ	1	0.8 - 1.3	0.100 ± 0.077	0.155 ± 0.097	132.4 ± 12.2	118.8 ± 16.2
	5	4.7 - 5.7	0.250 ± 0.175	0.245 ± 0.193	144.5 ± 10.8	145.1 ± 10.2
	10	9.9 - 10.7	0.320 ± 0.225	0.290 ± 0.251	148.4 ± 3.74	144.5 ± 3.2

Table 6: The range of distance measurements as estimated by MRI at commanded spatial steps of 3 and 5 mm in X and Y axes bidirectional movements, and the corresponding mean motion error and standard deviation.

Linear	Commanded step (mm)	Range of actual displacement (mm)	Mean Error ± SD forward (mm)	Mean Error ± SD reverse (mm)
X	3	2.73 – 3.83	0.277 ± 0.007	0.342 ± 0.172
	5	4.92 – 5.47	0.339 ± 0.184	0.352 ± 0.179
	Commanded step (mm)	**Range of actual displacement (mm)**	**Mean Error ± SD right (mm)**	**Mean Error ± SD left (mm)**
Y	3	2.73 – 3.83	0.330 ± 0.166	0.278 ± 0.007
	5	4.37 – 5.47	0.171 ± 0.191	0.286 ± 0.239

7.4 Discussion

Three simple and practical methods for assessing the accuracy of motion of a robotic device are described. It is emphasized that the caliper and MRI methods are suitable for evaluating any robotic system, while ablation of the plastic film is intended specifically for FUS systems. It is also noted that the device should be MR-compatible in order to be properly evaluated in an MRI environment. All these methods are based on the idea of evaluating the performance of the device in accurately executing commanded movements.

Firstly, the motion accuracy of an MRgFUS robotic device was evaluated using digital calipers integrated on the motion stages under evaluation using specially designed 3D printed structures. The mean error of linear motion varied from 0.042 ± 0.032 mm for the 1 mm step in the X axis forward direction to 0.123 ± 0.082 mm for the 10 mm step in the Y axis right direction. Accordingly, the mean error of angular motion varied from a minimum value of 0.100 ± 0.077^{o} for the 1^{o} step to a maximum value of 0.320 ± 0.225^{o} for the 10^{o} step (clockwise rotation). Contrary to

the findings of a previous study [21], the mean error was found to be increasing with increasing motion step for all four axes.

The speed of motion was estimated by the time activation of the robot's motors as provided by the controlling software during motion execution. The results revealed no significant difference in the speed of motion for bidirectional movements. A mean motion speed of approximately 10 mm/s was estimated for both the X and Z axes, while a higher value of about 14 mm/s was found for the Y axis.

In comparison with previous designs [21], [81], [82], [279], the principle of movement of the proposed one was significantly improved by the dual encoder positioning control that guarantees a smooth, reliable, and highly accurate motion in all stages. Additionally, the previously observed problem of reduced accuracy for small steps [21] seems to be solved by using faster software commands that makes the encoder's reading more accurate.

The system was then evaluated in the MRI environment that is intended to be used. The accuracy of motion remains satisfactory during full operation of the system in the MRI environment. Additionally, there was no evidence of any magnetically induced shift of the mechanical components that could compromise the accuracy of ultrasound delivery to the target, and therefore the patient's safety. Notably, the spatial positioning errors estimated by the benchtop setting using digital calipers are significantly smaller than those obtained in the MRI setting. This is attributed to the size of voxels of the MR images that determine the finest possible accuracy. Given the MRI resolution of about 0.55 mm per pixel, the estimated motion errors are within a reasonable range. Although this approach suffers from imaging resolution limitations, a smaller pixel could provide more precise distance estimates, but at the cost of increased image acquisition time and reduced SNR.

The high degree of accuracy evidenced by benchtop testing with calipers was also confirmed by multiple ablations on a transparent plastic film. The melted spots formed after grid ablation were arranged in a discrete pattern, in a highly accurate

manner, clearly demonstrating that the linear stages were moved by the commanded step. As observed, the centers of almost all the spots were equally spaced, demonstrating excellent repeatability. Multiple ablations in a grid with a smaller spatial step between adjacent sonications and a three times longer sonication time resulted in a well-defined square area of overlapping lesion. The results suggest that the system can precisely ablate a large tissue volume by overlapping lesions.

The aforementioned ablation method is intended specifically for testing the accuracy of FUS systems and is essential for assessing their ability to precisely deliver heating spots along the desired pattern. It is notable that in such systems the accuracy in free robot workspace is representative of that in more realistic scenarios (phantom and *in vivo* experiments), whereas for instance, in needle-based interventions is not. This is consistent with what has been previously reported by Price et al. [55], who found that the intrinsic accuracy of a FUS system as estimated in the air was similar to that obtained by phantom experiments in the MRI setting.

The proposed methods were greatly improved in terms of accuracy compared to previously used similar methods [81], [82], [280], [281]. The quality of benchtop evaluation was enhanced by using 3D printed structures specially designed for each individual axis, which provided perfect alignment of the caliper with each axis of measurement and reduced systematic errors [81]. Regarding the MRI evaluation, the accuracy of step movement has been previously estimated by locating the transducer on MR images [281]. Advantageously, a more accurate method is proposed herein, involving the use of a 2 mm plastic marker, which is clearly visible on MRI images using the appropriate sequence.

8 Challenges regarding MR compatibility of an MRgFUS robotic system

8.1 State of the art

High intensity FUS is a non-invasive modality for tumor treatment by local thermal ablation [2], [6]. To achieve these localized biological effects, piezoelectric transducers are used to converge ultrasound waves at a pre-selected focal point of interest [2], [6]. Accordingly, precise navigation of the ultrasonic transducer is needed for the ablation of a large tissue volume. FUS can eliminate the risks associated with surgical incisions and exposure to ionizing radiation and allows for multiple treatment repetitions in case of disease recurrence. So far, the most common side effect of FUS thermal therapy is thermal injury (e.g., skin burns), which is caused by energy deposition in the beam pathway [282].

Since Lynn's et al. [283] early studies in 1942 introducing the concept of high intensity FUS and Fry's et al. [284], [285] groundbreaking studies in the 1950s, in which FUS was used for brain surgery in animals and people, this intriguing technology has come a long way in terms of development and maturation. This was made feasible by a number of factors, including improvements in transducer design and particularly the introduction of the phased array technology, as well as in monitoring of ultrasonic delivery, with the major improvement being the development of MR thermometry [19], [286].

When FUS is combined with MRI guidance, precise targeting and real-time temperature monitoring with closed-loop control of energy deposition are achieved with an ideal safety profile [9], [287]. The thermometric data help to adjust the ablation strategy *in situ* through feedback control of the acoustic power, as well as to assess the tissue necrosis and hence define the therapeutic endpoint [288]. Currently, MRI is the only imaging technique that provides quantitative temperature measurements in vivo [9], [287].

Image quality and the accuracy of temperature mapping are largely dependent on the SNR [289]. In conventional MRI, high spatiotemporal resolution is achieved by employing multiple channel coil arrays that are placed in close proximity to the patient [290]. It is well known that phased array coils yield higher SNR compared to single-channel coils for identical parameters of imaging [291]–[294]. An example in the context of FUS is a study by Werner et al. [295], in which a custom built 8-channel head array was proven to offer a 3.5 times higher SNR than that of a standard body coil, thereby providing more anatomical details and better image guidance for MRgFUS neurosurgery. The coil characteristics, such as the number and size of its elements [293], as well as its rigidness [296], have an impact on SNR as well. Random motion of the patient (e.g., due to respiration) and the imaging coil is a common source of image blurring in the MRI and can also impact the measured SNR [297].

Different sources of noise and artifacts may influence the quality of diagnostic and therapeutic information negatively, and may be related to the MRI hardware itself or its interaction with the patient/imaging object or other equipment in the MRI room [298]. In this regard, there are a lot of challenges regarding the development of hardware for robotic assisted MRI-guided therapeutic interventions. The main sources of noise for robotic devices operating within an MRI environment are the employed construction materials, motion actuators and controllers, which are possible to interfere with the static magnetic field, the magnetic field gradients, and RF signals of the scanner depending on their activation condition (passive or active mode).

Materials should be electrically nonconductive, nonmetallic, and nonmagnetic in order to be classified as “MR safe” according to the ASTM standards (F2503) [299]. “MR conditional” devices are anticipated to enter and operate in a specific MRI environment safely (with no hazards) only under specific conditions (e.g., magnetic field strength, spatial gradient, RF fields, etc.). MR unsafe devices are those that

should remain outside the MRI room because they are known to pose hazards in all MRI environments. Generally, electrically active medical devices could be either MR conditional or MR unsafe since they contain electrically conductive components.

Materials are typically classified for MR safety based on their susceptibility property. Materials with very low susceptibility magnitude such as plastics (e.g., ABS, nylon, Polycarbonate, and teflon), rubber, glass, wood, copper, and high-alumina ceramic do not induce detectable image artifacts [300]–[302]. It is interesting to note that in recent years, rapid prototyping with plastic using 3D CAD data offers an ergonomic way to manufacture MR-safe components of any geometry [303], and was widely used for manufacturing motion stages of MR compatible FUS robots [137]–[139], [304]. Easily noticed artifacts can be produced by metals such as titanium, molybdenum, tungsten, tantalum, zirconium, aluminium, as well as by graphite [302], [305]. However, their influence on imaging can be minimized if they are placed at specific locations in the MRI room and at smaller quantities [302], [305]. Since imaging relies on tissue excitation by RF pulses under a strong static magnetic field, ferromagnetic materials such as iron and nickel that are characterized by very high magnetic susceptibility produce significant artifacts and are easily magnetized in the field direction. Therefore, their use should be precluded if possible. Otherwise, in case such materials are to be employed in the MRI room, they should be housed in fixed structures to ensure that they will not be attracted towards the magnet [305].

In robotic devices, magnetic materials are typically found in the mechatronic components (motion actuators and encoders), which are typically arranged in the motion mechanism, thus not raising any safety concerns. However, their presence perturbates the homogeneity of the external field causing errors in the image readout process. Specifically, the magnetic field variations in the presence of magnetic impurities induce variations of the resonance frequency of protons and signal

dephasing, and thus, signal loss [306]. Displacement of signal in the slice selection direction can also cause signal loss in specific regions (black areas) and accumulation of signal in other regions, thus creating another type of artifact known as the “pile-up” artifact [306]. In case the field variations are smooth, the image may exhibit milder artifacts such as geometric distortions [306]. In general, the artifacts originating from magnetic field strength variation at regions with different magnetic susceptibility are commonly known as susceptibility artifacts.

Another concern regarding safe operation of robotic devices in the MRI environment is the use of motion actuators. Piezoelectric motors completely designed with non-ferrous materials are available in the market and are widely incorporated in MR guided robotics [53], [136], [139], [281], [300], [307]. Despite that they are generally considered to be safe for operation in proximity to high field scanners, it was observed that they interfere with the MRI equipment when not used properly [73]. The major issue is the use of electric circuits, which drastically reduce the SNR if not shielded properly [300], [305]. To address this issue, the motors can be placed far away from the scanner’s isocenter [300], [303] so as to function properly, with Larson et al. [308] suggesting a distance of at least 0.5 m. Accordingly, this often creates the need to use mechanical means to transmit the motion to the workspace [300], [309], which unavoidably introduces a source of error since the system is more prone to friction and backlash [300]. Notably, introduction of the motors inside the isocenter of the scanner while maintaining acceptable SNR reduction was proven feasible when placing the electronics into an enclosure acting as a Faraday cage while simultaneously filtering the control lines [310]. Furthermore, accurate motion in robotics requires continuous feedback from sensors. Optical encoders are widely implemented for position sensing, but the generated electric pulses can also introduce noise [305].

Further challenges are faced when employing MRgFUS hardware in the scanner. A technical limitation of an MRgFUS experimental setup relates to the coil position.

It is important that coil arrays do not obstruct the beam's propagation since a clean path is required for proper ultrasonic delivery to the target. It is interesting to note that recently, Corea et al. [290] reported that 3D printed coil arrays exhibit significant transparency to the acoustic energy and proposed their use as a way to enhance image resolution by placing the coil in the beam path.

Caution should also be paid to potential noise that may be introduced by the ultrasonic transducer. Piezoelectric elements are sometimes plated with nickel while backing materials and acoustic matching layers often contain ferromagnetic particles, which are included to increase their density and thus their acoustic impedance [311]. As already mentioned, ferromagnetic components should be avoided since they are known to induce significant susceptibility artifacts [311], [312]. Alternatively, Gerold et al. [312] have suggested the inclusion of other fillers such as Al2O3 or Cu powder. Cu-epoxy composites were shown to offer electromagnetic shielding and proper acoustic impedance for ultrasonic matching with piezocomposite materials [312]. Furthermore, conductive components may develop eddy currents when experiencing magnetic field changes, thereby arising additional safety concerns [311]. Eddy currents can induce not only SNR degradation, but also considerable image distortion [313]. Small components such as wiring and printed circuit boards produce acceptable field disturbance, whereas other bigger conductive structures must be shielded [311]. Finally, it is necessary that the housing of the piezoelectric element is manufactured with proper materials. 3D printed plastic holders were found to be fully compatible with MRI and constitute an ergonomic and cost-effective solution [314].

The experiments described in this section concerned the evaluation of a robotic device dedicated to MRgFUS preclinical use in terms of MR compatibility. The term "MR-compatibility" refers to an MR-conditional device that can be operated in an MRI setting properly without affecting the quality of imaging and diagnostic information significantly. The device used is classified as MRI conditional

according to the ASTM standards because it contains metallic and electronic components. The SNR served as the main metric for evaluating the MR image quality and compatibility of the various system's components (i.e., employed materials, actuators, encoders, and transducer) with a 1.5 T clinical MRI scanner. In addition, various set-up parameters such as the coil stability and its positioning relative to the target, target size and stability, as well as the positioning of electronic components relative to the imaging coil and activation status of encoders (i.e., counting pulses on/off), were examined for optimizing the SNR and imaging quality. Imaging was performed in a TMP and freshly excised pork tissue using common MR sequences. By summarizing all the experimental data, the study aims to contribute to addressing major challenges regarding operation of a robotically positioned MRgFUS system in the MRI environment and raising awareness for potential sources of noise and distortion that may not be obvious to researchers in the field.

8.2 Materials and methods

8.2.1 Robotic Device for MRgFUS applications

The robotic device used in the experiments comprises a mechanism with three linear (X, Y, Z) and one angular (Θ) stages of motion dedicated to positioning a single element spherically focused transducer relative to the target. All the mechanical components are installed in a compact housing, thereby enabling ease integration of the device into the MRI table so that thermal ablation can be accurately performed under the guidance of MRI. The ultrasonic transducer operates in a separate enclosure that includes an acoustic opening at the top for ultrasonic coupling with the target through water. A CAD drawing of the device is shown in **Figure 54A**, whereas **Figure 54B** shows its integration into the MRI table. A dedicated software is used for therapy planning, kinematic control of the positioning mechanism, therapeutic ultrasound control, and monitoring of

ultrasonic delivery through MR thermometry, thereby offering an efficient procedural workflow.

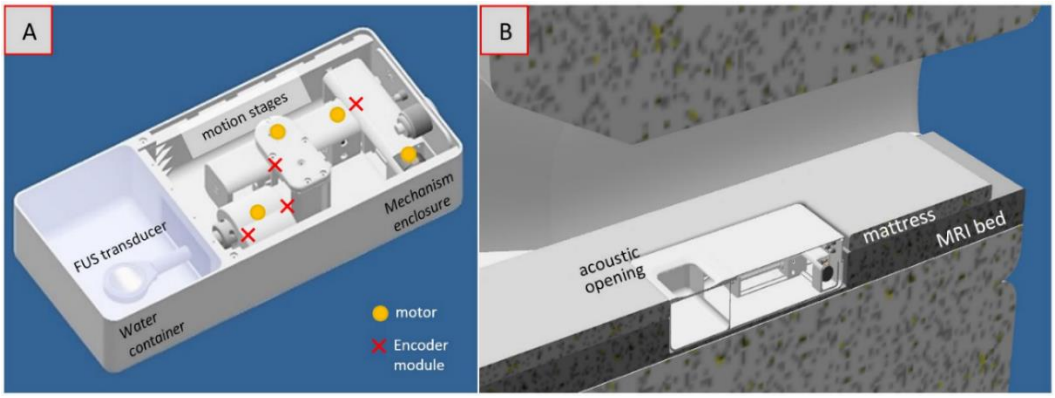

Figure 54: CAD drawings of the robotic device **(A)** without top covers, **(B)** with top covers as integrated in the MRI table, with the main components and location of motors and encoders indicated.

Piezoelectric motors (USR30-S3N, Shinsei Kogyo Corp., Tokyo, Japan) serve as the actuators of motion. The rotational motion of the motors is converted into linear mainly through jackscrew mechanisms, which amplify the motor torque. Motion of each positioning stage is controlled by an optical encoder set up (US Digital Corporation), which increases the motion accuracy and eliminates the possibilities of mechanical problems not being detected. The location of the motors and encoder modules is indicated in **Figure 54A**.

The mechatronic parts (motors and encoders) are wired up to medical non-magnetic connectors (S 103 A053-130+, Fischer Connectors, Saint-prex, Vaud, Switzerland) at the rear of the mechanism enclosure. The driving electronics, i.e., the motor drivers (D6030, Shinsei corporation) and the Microcontroller card (Arduino cc, Ivrea, Italy) used to convert analog signals into digital signals that are recognized by the software, are housed in a compact enclosure located outside of the MRI room. The driving system is powered by a DC supply (24 V, 6A) and is wired up to the device through the grounded MRI penetration panel using rubber-shielded copper cables (Shinsei Kogyo Corp., Tokyo, Japan) for the motors and a copper-

shielded coaxial cable (RJ58, 50 Ω) for transducer supply. Note that each cable has its own shielding layer for reducing electromagnetic emissions. Outside of the MRI room, the transducer is paired to a custom-made low pass RF filter (10 MHz cutoff frequency), which is in turn connected to the amplifier (AG1016, AG Series Amplifier, T & C Power Conversion, Inc., Rochester, US) to block harmonic currents and prevent image distortions effects.

All individual embodiments employed were specially selected to ensure MR compatibility of the system. The structural and moving parts were 3D printed using non-magnetic ABS thermoplastic material on a rapid prototyping machine (FDM400, Stratasys). Regarding the FUS transducer, the element is made of MR-safe piezoceramic material (Piezo Hannas Tech co. Ltd, frequency of 2.45 MHz, radius of curvature of 65 mm, and diameter of 50 mm) and is housed in a plastic case. The conductive surfaces of the piezoelectric element were connected to the electric circuit required for transducer activation through contacts and layered with epoxy (ASonic, Tržaška c. 134, 1000 Ljubljana, Slovenia). The epoxy encapsulant serves as the backing material immobilizing the element inside the housing while providing electrical isolation. The encapsulant is a two-component epoxy adhesive prepared by mixing metal-free resin glue with hardener (1 kg glue to 0.4 kg hardener).

Despite the careful selection of materials and mechatronic parts and the use of cable shielding, the impact of their existence and/or operation in the scanner should be assessed extensively. Evaluation was done as described in the following sections.

8.2.2 Experimental setup in MRI

The MRI experiments took place at the German Oncology Center (GOC) in Cyprus using a 1.5 T MRI scanner (GE Signa HD16, GE Healthcare). For each experiment, the robotic system was sited on the MRI table, with an agar-based phantom or freshly excised pork tissue being positioned at the acoustic opening. The

phantom/excised tissue sample was scanned under different activation conditions and setup parameters. The water container was filled with degassed and deionized water up to the bottom of the phantom/tissue sample so that proper ultrasonic coupling is achieved. The acoustic opening was not covered by a membrane, so the target was in direct contact with water. The phantom was prepared with a 6% w/v concentration of agar (Merck KGaA). The phantom was carefully prepared with constant stirring to achieve MRI homogeneity.

8.2.3 SNR assessment of MR compatibility

To determine the SNR, the ratio of the mean SI of a preselected ROI in the target (SI_{target}) to the standard deviation (σ_{noise}) from a ROI placed in the air (background signal) was simply calculated as follows assuming a gaussian distribution of noise [315]:

$$SNR = {SI_{target}}/{\sigma_{noise}} \quad [5]$$

Specifically, the signal was estimated as the mean intensity and standard deviation of five consecutive measurements in a circular ROI of 5-mm diameter placed in the phantom/excised tissue sample. In all the experiments, the ROI was placed in such a way so that its center coincided with the focus location, i.e., 65 mm above the transducer's surface and 25 mm deep in the phantom. For the SNR measurements, the phantom was centered at the isocenter of the magnet (0,0) using the external laser positioning system so that the ROI is defined at isocenter level. Both the single- and multi-channel coils were centered at constant vertical distance above the phantom/ROI to avoid inhomogeneity due to inconsistent coil placement among the various experiments. Accordingly, the background ROI was also defined at a location with identical offset for all experiments.

With the above-described configuration, the closer motor was located at 24 cm from the isocenter while other mechatronic components were located further away. Connection of motors and encoders with the driving system (located outside of the

MRI room) was achieved through the penetration panel using specially shielded cables.

Image acquisition was mainly performed using an Spoiled gradient recalled echo (SPGR) sequence with the following parameters: TR = 23 ms, TE =16 ms, FA = 35°, ETL = 1, pBW = 45 Hertz/pixel, FOV = 280 x 280 x 10 mm^3, matrix = 128 x 128, and NEX = 2. A FSE sequence was also implemented in a few experiments using TR = 500 ms, TE = 13 ms, FA = 90º, ETL = 13, pBW = 130 Hertz/pixel, FOV = 260 x 260 x 10 mm^3, NEX = 1, and matrix = 256 x 256.

MRI k-space data were used for image reconstruction. Raw data were transferred to MATLAB (MathWorks, Natick, MA, United States) for offline reconstruction using inverse Fourier transform. No filtering was applied. For the multichannel coil, k-space samples were obtained for each coil. The individual coil data was combined using a sum of squares. In all experiments, signal to image conversion was performed using similar scaling, where the recorded signal values were distributed over the gray scale range.

8.2.4 Impact of activation states on SNR

The noise introduced by the presence and operation of the device in the MRI scanner and potential remedies for enhancing compatibility with the scanner were investigated through a series of experiments. Each of the following experiments consisted of a target being imaged with the system in power off and then in power on or moving configuration. Specifically, SNR measurements were performed under different activation states of the robotic mechanism and ultrasonic transducer [81], [138]-[137]. Regarding ultrasonic control, the following states were tested: Ultrasonic RF cable not connected, ultrasonic RF cable connected, amplifier energized (zero ultrasonic power applied), and electrical power applied (50-200 W). Regarding motion control, the following states were tested: motor/encoder cable not connected, motor/encoder cable connected, electronic control system energized

(no motion command initiated, referred to as “DC ON”), and motion command initiated (referred to as “motor moving”). SNR evaluation was mainly carried out in a TMP, but also in freshly excised pork tissue for comparison purposes.

8.2.5 Effect of magnetic impurities in the transducer on image quality

Initially, the potential effect of magnetic impurities contained in the transducer's backing material on image quality was assessed qualitatively. For this purpose, two different transducers were used; the one manufactured with a metal-free epoxy encapsulant and the other one containing ferromagnetic, iron particles. Both transducers were manufactured in house using a similar methodology, where a concave piezoelectric element with central frequency of 2.45 MHz, radius of curvature of 65 mm, and diameter of 50 mm was housed in a 3D printed plastic case which was filled with epoxy (2-part epoxy adhesive, Asonic, Slovenia, Ljubljana). For the “iron-doped” transducer, the epoxy mixture was loaded with iron particles. Specifically, iron filler powder (GF51431240, Sigma-Aldrich) was added during the preparation of the epoxy adhesive.

The transducer was located under the phantom/tissue sample and its location was adjusted so that its focal point was located 2.5 cm deep in the phantom coinciding with the ROI center. The transducer was centered in the horizontal plane with respect to the phantom. Imaging was done with the transducers deactivated using the FSE sequence with identical parameters. Visual assessment was performed by comparing the imaging quality (e.g., signal loss and introduced artifacts) in the presence of each transducer.

At this point, it should be noted that all subsequent experiments were carried out using the transducer containing iron-free epoxy encapsulant that was proven proper for operation in the MRI scanner.

8.2.6 Impact of set-up parameters on SNR

In the effort to eliminate image distortion, several set-up parameters were examined. Initially, the SNR was obtained using a single-channel general-purpose flex surface coil (Signa 1.5T Receiver only, GE Medical Systems), as well as a 12-channel body coil (Signa 1.5T, GE Healthcare Coils, Aurora, Ohio, USA) to confirm the SNR advantage of the multichannel-coil and how significant it is in the context of MRgFUS. Subsequently, the impact of coil stability and positioning in relation to the target was evaluated by comparing the SNR with the multichannel coil being placed in the two different configurations shown in **Figure 55**. In the former case, the coil was placed directly above the phantom using positioning pads and supporting objects (**Figure 55A**), whereas in the latter case it was securely stabilized at sufficient distance above the top of the phantom using a dedicated 3D printed plastic structure with 6 legs (**Figure 55B**).

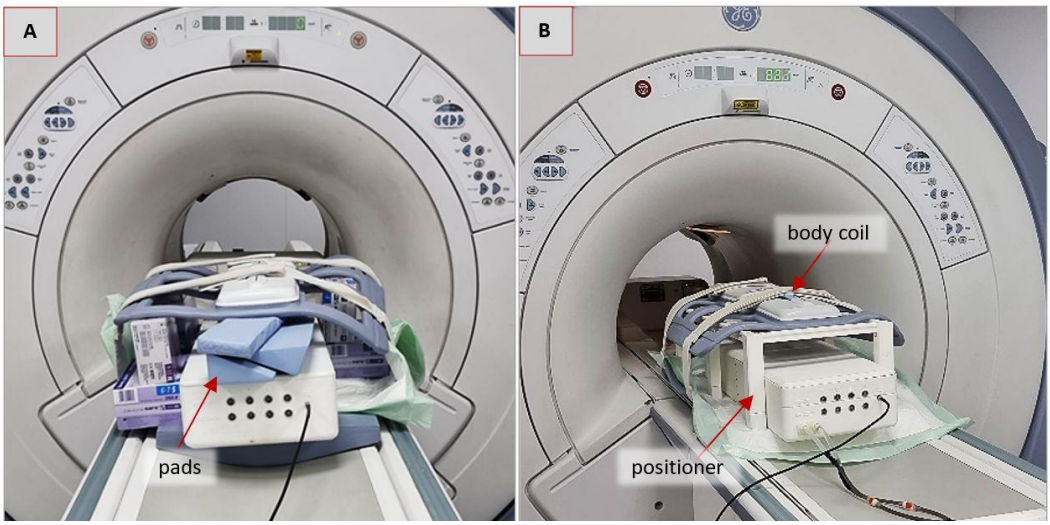

Figure 55: The robotic device positioned on the table of the 1.5 T MRI scanner, with the multi-channel body coil **(A)** placed directly above the phantom using pads and supporting objects and **(B)** securely mounted using a dedicated 3D printed plastic structure.

Similarly, the impact of target stability on image quality was assessed by comparing the SNR estimates in the preselected ROI in a small square phantom and a larger phantom of dedicated shape, as illustrated in **Figure 56A** and **Figure 56B**, respectively.

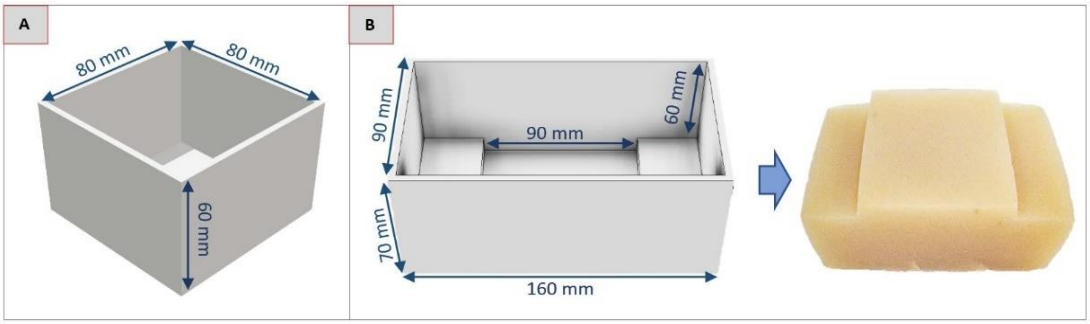

Figure 56: 3D printed molds used for manufacturing the **(A)** small size square phantom and **(B)** the larger phantom of dedicated shape.

In the second case, the phantom's dimensions and shape were modified so that its bottom protruding part was submerged in water through the acoustic opening while its top part was being supported on the plastic top cover, thus improving the phantom's stability during exposures. The phantom's stability was also enhanced by the increased weight. The square phantom had a weight of about 0.8 kg, whereas the bigger dedicated phantom weighted about 1.3 kg.

Other set-up parameters examined in the effort to eliminate electromagnetic interference between the various components and magnet were the positioning of the actuators relative to the imaging coil and encoders' activation status (i.e., counting pulses ON/ OFF). The placement of electronic components relative to the coil is illustrated in **Figure 57**. In **Figure 57A**, the electronic parts are placed within the coil detection area, whereas in **Figure 57B** the electronic parts are placed outside of the coil detection area.

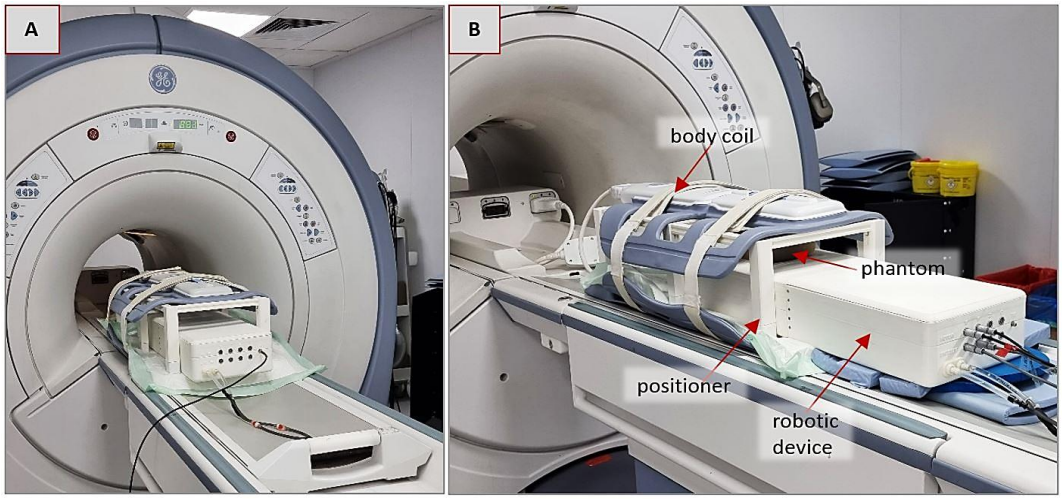

Figure 57: The robotic device positioned on the table of the 1.5 T MRI scanner with the multi-channel body coil securely mounted on the positioner with the electronic parts **(A)** within the coil detection area and **(B)** outside of the coil detection area.

8.3 Results

8.3.1 Effect of magnetic impurities in the transducer on image quality

The effect of transducer material on image quality is revealed by **Figure 58**, in which the FSE images acquired in the presence of the iron-doped (**Figure 58A**) and iron-free (**Figure 58B**) transducers (deactivated) are compared.

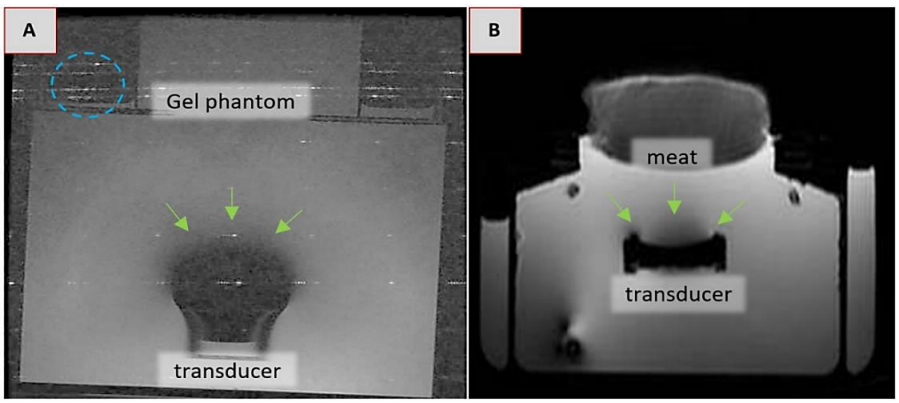

Figure 58: FSE axial images of **(A)** an iron-doped transducer and a gel phantom as the target and **(B)** an iron-free transducer and tissue sample as the target. Green arrows indicate signal loss artifacts around the transducer. The blue dotted circle indicates Zipper artifacts.

It is clearly seen that image quality is compromised in the presence of ferromagnetic impurities due to susceptibility artifacts. Notice that the susceptibility artifacts near the "iron-doped" transducer in **Figure 58A** are more pronounced than the susceptibility artifacts in **Figure 58B**.

8.3.2 Effect of transducer operation on SNR

The impact of the various activation states of the transducer containing iron-free epoxy encapsulant on SNR for the SPGR and FSE sequences is revealed by the bar charts of **Figure 59**. The greatest reduction in SNR occurred during transducer's operation at the highest power level of 200 W for both sequences.

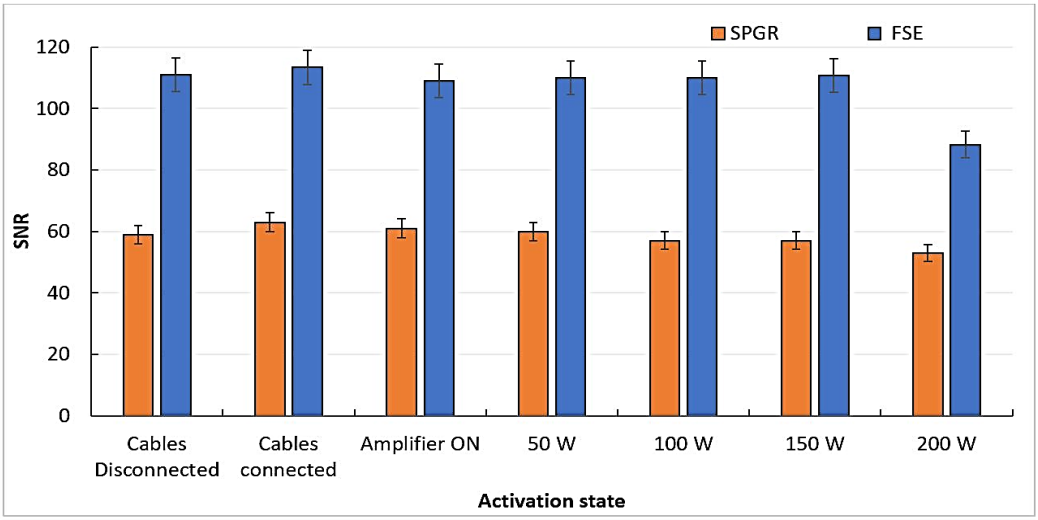

Figure 59: Bar charts of the SNR acquired using the SPGR and FSE pulse sequences under different activation states of the ultrasonic transducer.

Figure 60 compares the SNR values acquired in the (6% w/v) agar phantom and freshly excised pork tissue with the SPGR pulse sequence and the 12-channel coil being properly stabilized above the target. The bar chart shows a slightly higher SNR (approximately 5 on average) in the agar phantom for each tested activation condition of the system. This shows that the developed phantom provides similar SNR with excised tissue. The corresponding SPGR slices of the tissue sample are shown in **Figure 61**.

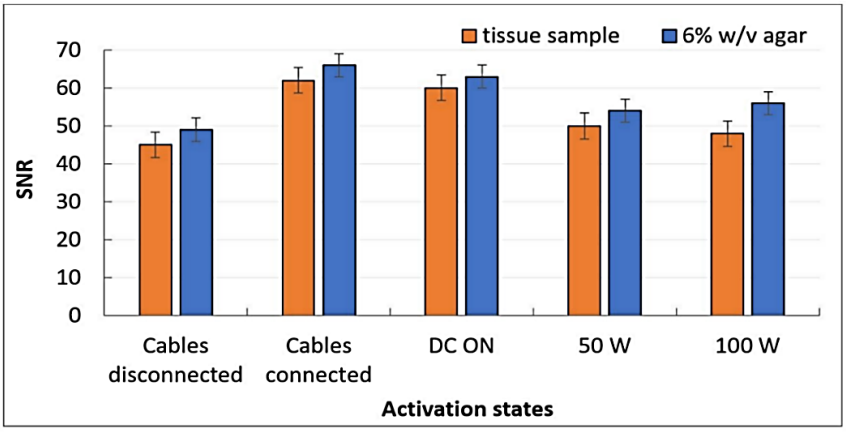

Figure 60: Bar charts of the SNR acquired in excised tissue sample and 6% w/v agar phantom using the SPGR sequence under different activation states of the transducer.

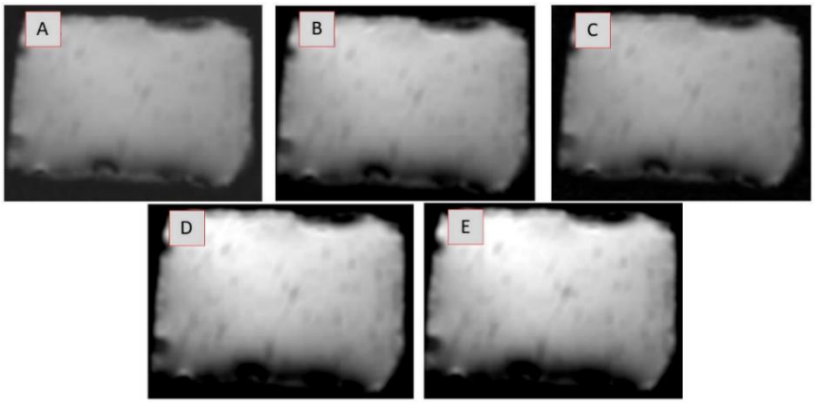

Figure 61: SPGR coronal images of the pork tissue sample acquired with **(A)** disconnected cables, **(B)** connected cables, **(C)** DC ON, and power on at **(D)** 50 W and **(E)** 100 W.

8.3.3 Impact of set-up parameters on SNR

Figure 62 reveals the impact of coil type (single-channel versus multi-channel coil) on SNR for the various activation states of the FUS transducer. Note that the change in SNR among the various conditions follows a similar trend. Also, note that the SNR advantage of the multi-channel coil is more prominent during FUS sonication. Similarly, **Figure 63** shows the SNR evaluation for different transducer activation states for two different positionings of the multi-channel body coil with respect to the phantom. Note that the use of the dedicated supporting structure raises the coil

at sufficient distance above the phantom so that it is not prone to target vibrations during sonication. These results prove that the use of properly stabilized multi-channel coils and their isolation from the target can help towards maintaining sufficiently high SNR during high-power sonications of up to 200 W (electrical power).

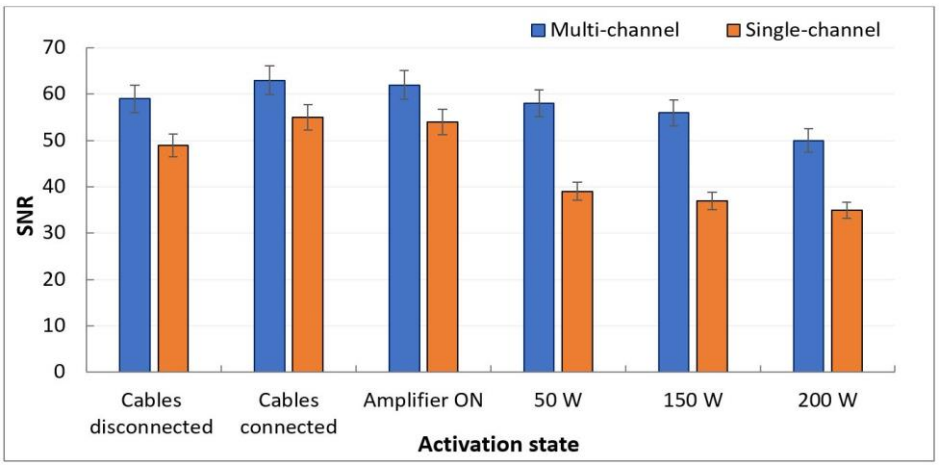

Figure 62: Bar charts of the SNR acquired with the multi-channel and single-channel coils using the SPGR sequence under different activation states of the ultrasonic transducer.

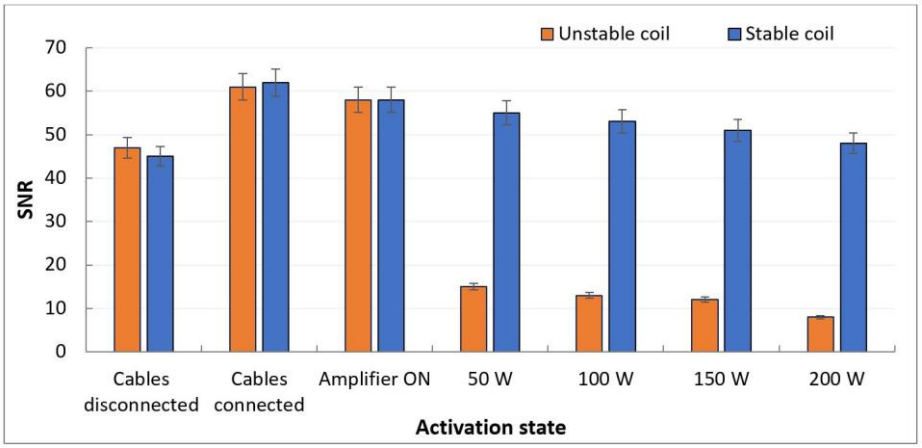

Figure 63: Bar charts of the SNR acquired using the SPGR sequence with the multi-channel body coil being placed without any supporting structure above the phantom (unstable) and securely mounted on a dedicated plastic supporting structure (stable) for different activation states of the ultrasonic transducer.

Further results on the effect of FUS-induced coil vibrations are presented in **Figure 64**. Image acquisition during heating at 200 W electrical power using the SPGR sequence resulted in completely noisy images when the coil was not secured properly at sufficient distance above the phantom. Note that **Figure 64C** was acquired just after deactivation of the transducer. Normal image contrast and detail occurred when the transducer was deactivated.

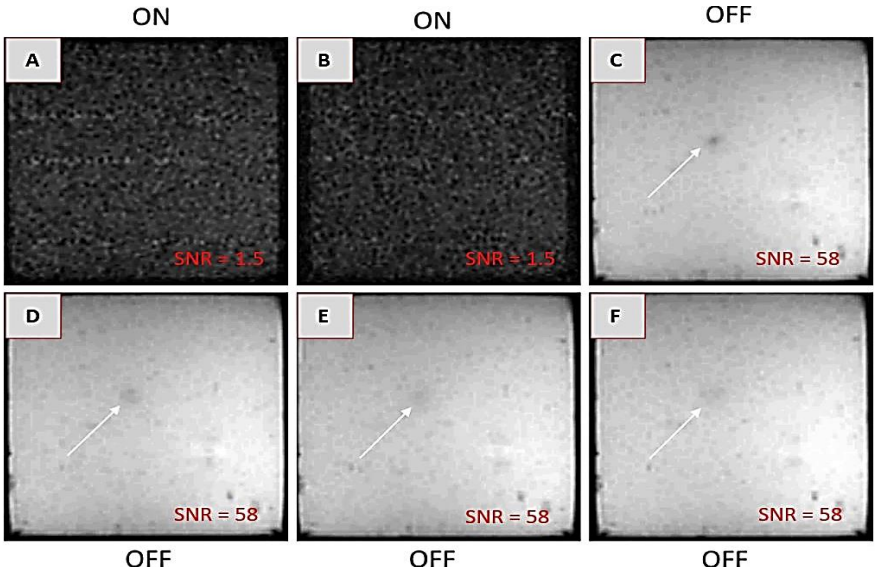

Figure 64: SPGR axial images acquired in a 6% agar phantom with the coil placed directly above the phantom (without supporting structure) during sonication at 200 W for 12 s and after sonication. Images were acquired **(A)** 4 s, **(B)** 8 s, **(C)** 12 s, **(D)** 16 s, **(E)** 20 s, and **(F)** 24 s after the start of sonication. The corresponding SNR is overlaid on each image. White arrows indicate the focal area where temperature increase occurred.

The effect of target size was also evaluated. The bar chart of **Figure 65** reveals a notable SNR improvement owing to the higher stability of the large phantom compared to the small-size phantom. Insights on target size and stability are also given in **Figure 66**, which presents SPGR images of a pork tissue sample obtained with the transducer at different activation states. In this case, image quality during heating is getting degraded as the power is increased from 10 to 100 W, with complete loss of detail and contrast at 100 W owing to the small size of the tissue sample.

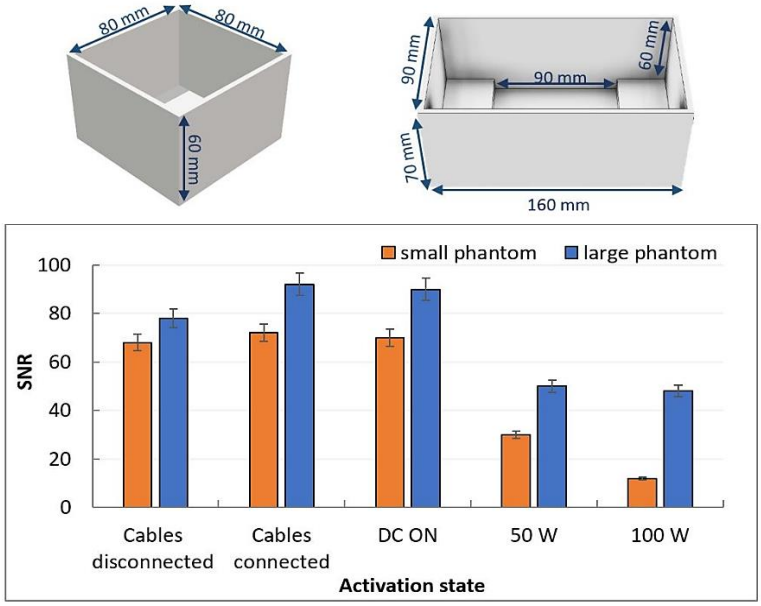

Figure 65: Bar chart of the SNR acquired in the small and large phantom using the SPGR sequence under different activation states of the ultrasonic transducer.

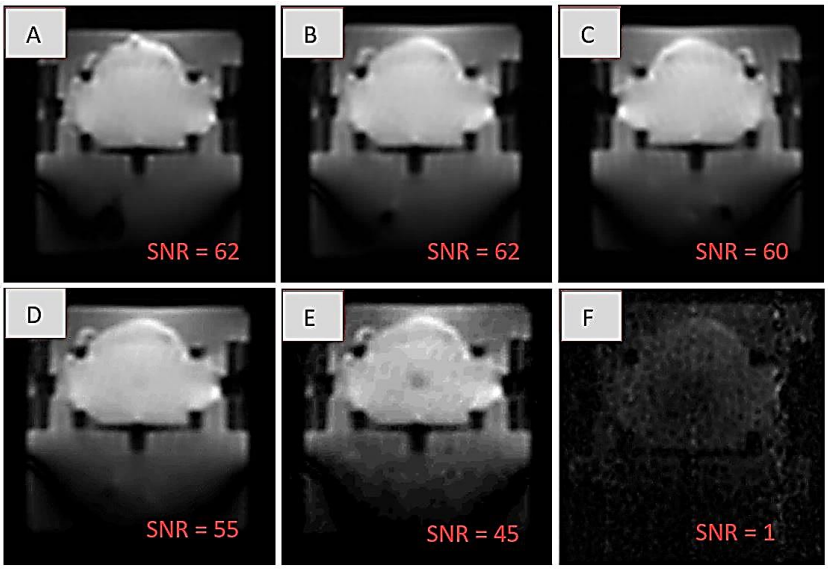

Figure 66: Example of SPGR coronal images acquired in excised tissue sample with the **(A)** Cables disconnected, **(B)** Cables connected, **(C)** DC ON, and power ON at **(D)** 10 W, **(E)** 50 W, and **(F)** 100 W. The corresponding SNR is overlaid on each image.

Finally, the SNR impact of placing the electronic parts outside of the coil detection area is revealed by **Figure 67**, whereas **Figure 68** shows the corresponding SNR improvement occurred after switching off the encoder's counting pulses.

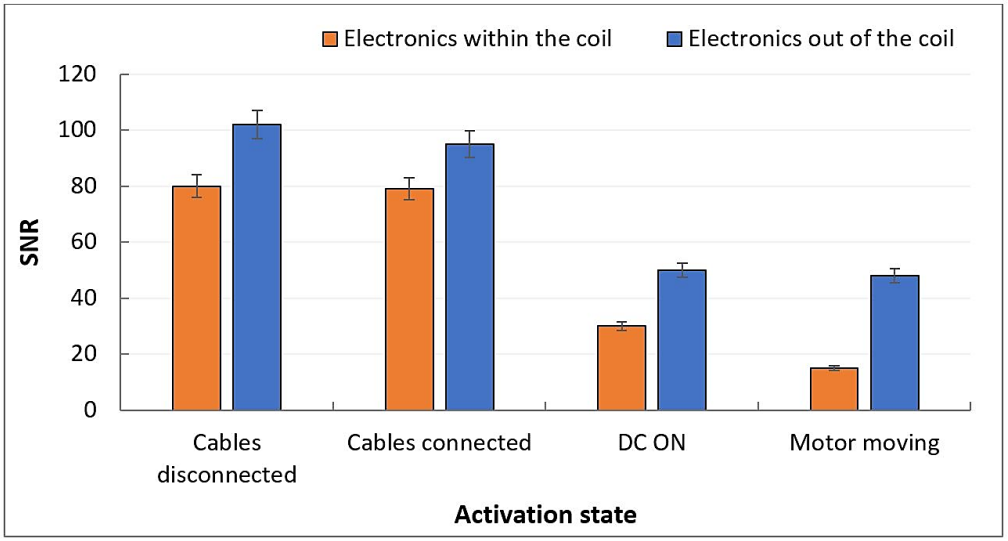

Figure 67: Bar charts of the SNR acquired with the electronic parts inside and outside of the coil detection area using the SPGR sequence under different activation states of the positioning mechanism.

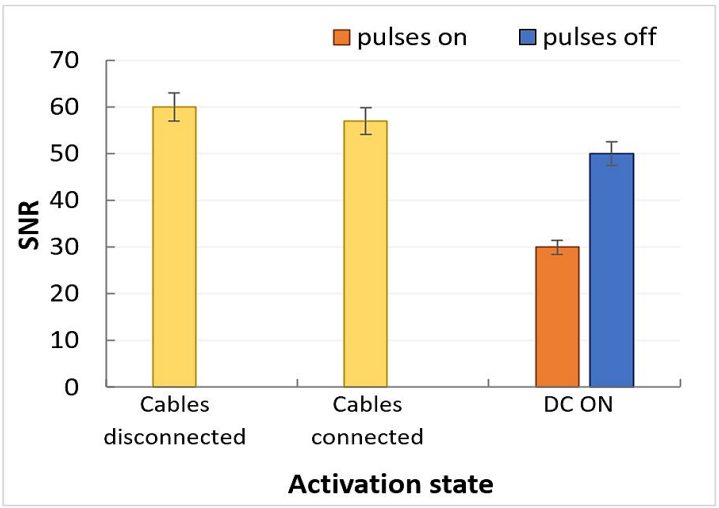

Figure 68: SNR measured using the SPGR sequence with the cables disconnected (reference image), cables connected, and electronic driving system energized (DC ON) for two different cases: encoders' pulses activated and deactivated.

8.4 Discussion

The current section aimed to provide insights on major challenges faced when implementing a FUS robotic system in the MRI by evaluating the compatibility of an MRgFUS robotic device with a 1.5 T scanner. Imaging was performed in tissue mimicking agar-based phantoms (6% w/v agar) and freshly excised pork tissue. The SNR served as the main metric for the quantitative assessment of the MR compatibility of the various system's components. MR compatibility was investigated under different activation states of the system and set-up parameters. Simultaneously, potential sources of SNR degradation and image quality distortion in an MRgFUS system were identified through quantitative and visual examination.

As previously mentioned, there are numerous issues impeding the design of robotic devices for MRI-guided interventions, including the employed construction materials. In the proposed robotic device, metallic components are incorporated in the motion mechanism, which is housed in a plastic enclosure, and thus do not raise any safety concerns. However, their presence perturbates the homogeneity of the external field and may cause susceptibility artifacts. In this study, such artifacts were observed as signal loss and distortion around the transducer, due to the magnetic field inhomogeneity introduced by the iron particles contained in the backing material. In line with previous studies [311], these results highlight that caution should be given not to include ferromagnetic particles during the manufacturing process of ultrasonic transducers, despite that this constitutes a common way for enhancing backing material's density to the desirable level [311].

Note also that some zipper artifacts (appear as white lines) are aligned in phase encode direction for the iron-doped transducer. In the first place, this appears to be a case of RF interference. However, this type of RF artifact is not expected to appear when the transducer is in passive state. We thus speculate that the source of these artifacts is unexpected noise from the amplifier, possibly due to high frequency harmonics that could not be filtered by the low pass filter used. Such kind of RF

artifacts were observed by Shokrollahi et al [316] and were attributed to RF interference caused by electric signals between motors and drivers during imaging with the motors being in active mode. However, since such artifacts can arise for any cable that is not properly installed through the RF waveguides and not related to the MRgFUS setup, further investigation is required to identify their source.

Image acquisition was performed using two standard MR sequences (FSE and SPGR). Both sequences present similar behavior in terms of SNR drop compared to the baseline for the various activation modes. Thermometry maps are typically constructed by PRFS calculation; a method that is typically implemented with an SPGR sequence [9]. Generally, the sensitivity of this sequence type to the PRFS effect makes them ideal for MR thermometry [9]. Therefore, the rest of experiments were carried out using the specific sequence, given also that it produced SNR values sufficiently high for the purposes of the current study.

It is by now widely accepted that multi-channel coils provide substantially higher SNR compared to single-channel coils. In this study, their SNR advantage was examined in the context of MRgFUS, and specifically under different activation states of the FUS transducer. The multi-channel coil increased the SNR compared to the single-channel coil by up to 50%. It is important to note that the SNR improvement differs between activation states, with the highest difference occurring when the transducer is powered on. Therefore, in line with previous studies [295], the use of a multi-channel coil is crucial for proper imaging during MRgFUS.

It is obvious that proper stabilization of the imaging coil is required for proper imaging. The current results go beyond this, showing that the coil placement technique plays a more important role in the context of MRgFUS procedures. When the coil was placed above the phantom without any dedicated supporting fixture was being subject to vibrations of the target during transducer's activation, and consequently the SNR dropped drastically (to about 25%), and imaging was

affected severely (**Figure 63**). To solve this issue, a specially designed positioner was developed using 3D printing in order to securely position the coil a few mm above the phantom. With this arrangement, more than 3-fold improvement in SNR was observed for electric power values of 50-200 W. Although the SNR is slightly affected by increasing the ultrasonic power it remains at sufficiently high levels for high quality imaging. This was true whether a surface or body coil was used.

Visual assessment of SPGR images acquired during and after heating at 200 W yields similar conclusions (**Figure 64**). Specifically, when the transducer was activated, the coil with no support structure caused intense granular noise and resulted in severe image distortion with complete loss of detail. Deactivation of the transducer allowed for proper imaging and visualization of the heated region as a slightly black circular spot that was fading with time due to heat diffusion, thus revealing the coil interaction with the target and instability (and resultant vibration) as the main image polluter in that case.

The weight and shape of the target (phantom/tissue sample) play a very important role as these parameters define its stability under acoustic pressure. It was observed that due to the force exerted by ultrasound on the phantom, the image during a fast MRI pulse sequence was affected severely. In fact, the SNR dropped drastically in the lightweight phantom compared to the heavier phantom. For the highest tested power of 100 W, the SNR during activation with the 0.8 Kg phantom was about 12, whereas for the 1.3 Kg phantom the SNR was increased by 4-fold to 48 (**Figure 65**). Note that the impact of using a stable phantom is more pronounced at higher applied electrical power. Furthermore, it is notable that the SNR for the heavy phantom was not affected by increasing the electrical power from 50 to 100 W. Further results on image degradation arising from small and unstable targets were obtained using an excised pork tissue sample. The details of SPGR images of a ROI including the excised tissue sample placed on a special holder above the transducer (**Figure 66**) were gradually blurred as the electrical power was increased from 10

to 100 W. Note that complete loss of details and contrast occurred at the highest tested power of 100 W.

Although the above experiments do not represent a clinical scenario, it is a possible scenario in the preclinical setting or in the process of QA of clinical MRgFUS equipment. Phantoms are the most commonly used QA tools in this regard [140]. Therefore, the above conclusions may contribute towards optimizing QA methodologies by providing insights on key set-up parameters, given also that methods for QA of MRgFUS devices are still to be established and standardized.

By comparing the SNR among different activation states and experiments, some other interesting observations can be made. Firstly, it was observed that in many cases connected cables provided higher SNR than disconnected cables. This is attributed to that disconnected cables act like antennas and they can easily pick up RF noise, whereas connected cables are grounded and are less likely to cause noise emission. In addition, noise from disconnected cables is somewhat random, and thus, SNR fluctuations are typically observed. It is also worth noting that some SNR variability should be expected among experiments due to FUS electromagnetic noise. When the transducer is in active mode, unexpected noise may be generated from the transducer cable. To be more specific, harmonic components that cannot be eliminated by the filter may fall into the MRI-sensitive frequency band, thus generating noise. Note that this phenomenon is more pronounced at high power operation.

Other main “polluters” of MRI quality existing in an MRgFUS system are the motors and motor control electronics. As explained previously, the presence and operation of the motors can cause susceptibility and RF interference problems, which unavoidable result in signal loss and significant image distortion [316]. Signal voids and pileup artifacts were observed by Shokrollahi et al. [316] and were attributed to inhomogeneities of the external and gradient fields caused by the presence of the motor (deactivated). Herein, a serious SNR degradation occurred

when the electronic control system was energized, and motion command was initiated. In this regard, an important measure for SNR improvement was proven to be the placement of motors and encoder electronics outside of the coil detection area (**Figure 67**). It is interesting to note that the effect of motor orientation and location on image artifacts has already been assessed previously and it was shown that susceptibility artifacts are reduced when the motor's shaft is aligned with the z-axis [316]. In our case, the SNR is affected by the presence of all motors, each one having different location and orientation, since they are all housed in a single enclosure.

According to previous studies, SNR reduction of up to 80% can be caused from harmonic motors, such as the Shinsei motors used in this study, whereas non-harmonic motors cause much less interference [317]. For the specific MRgFUS system proposed herein, it was proven essential to keep the motors and encoders outside of the coil detection area. However, it is possible that other designs allow operation of the electronics within the coil detection area without substantial impact on SNR, maybe through additional shielding or the use of specially designed actuators and encoders. For instance, in a study by Hofstetter et al. [318], imaging remained largely unaffected (in terms of SNR) by the presence and operation of a specially designed electromagnetic servomotor (and the encoder) at 15-cm distance from the object. In comparison with the current study, the closest motor was located 24 cm from the phantom center (ROI location). Generally, the compatibility requirements depend not only on the type, but also on the specific characteristics of motors and encoders.

The tested MRgFUS system incorporates purchased optical encoders, which are considered to be MRI compatible and are widely used in robotic design. Deactivation of the encoders' counting pulses during image acquisition was proven essential for maintaining high SNR (**Figure 68**). Specifically, the acquired SNR with the pulsing system deactivated was increased by about 70% compared to that

obtained with the counting pulses activated. To our knowledge, this aspect was not examined previously.

Overall, among the various activations states of the FUS system, the most significant distortion occurs when the transducer is activated mainly owing to coil and target vibrations and is getting worse as the output power is increased. It is thus crucial to securely stabilize both the coil and imaging object. In this regard, isolation of the imaging coil from the sonicated target is essential to avoid FUS-induced vibrations from being transferred to the coil. The use of a multi-channel coil is also critical for increasing the SNR in the context of MRgFUS. Regarding robotic motion, the current outcomes raise concerns about the proper use of motion actuators and sensors. Piezoelectric motors and optical encoders are extensively employed in MRgFUS devices; nevertheless, the current study suggests that they should be located outside of the coil detection area during imaging, otherwise the image quality may be compromised severely. It is also crucial to have the counting pulses of encoders turned off during image acquisition since this was also proven to increase SNR remarkably. By summarizing all the experimental data, the study contributes towards addressing major challenges regarding operation of an MRgFUS system in the MRI environment and raises awareness for potential sources of noise and distortion to researchers in the field.

9 MRI monitoring of thermal lesions produced by FUS

9.1 Introduction

In the last decades, the adoption of thermal ablation modalities has been rapid, enabling safe and efficient delivery of thermal energy to deep-seated body targets [319], [320]. This is achieved in a minimally invasive manner with the use of radiofrequency ablation (RFA), microwave ablation (MWA), and LITT, or in a non-invasive manner using thermal FUS [319], [320]. While these modalities have been characterized by remarkable developments, such as the introduction of image guidance and robotics [83], [321], the establishment of methods for monitoring ablation lesions has fallen behind.

The superior performance of MRI over other imaging modalities in the acquisition of high resolution anatomical images with excellent contrast among soft tissues and its ability to monitor tissue temperature non-invasively contributed to developing safe and efficient thermal ablation applications that were more easily adopted into clinical practice [60], [322]. Nowadays, there exists a wide range of MRI contrast mechanisms for post-sonication lesion assessment and temperature estimation methods, among which the PRFS thermometry is predominantly utilized for the intraprocedural monitoring of ablation therapy [261], [323].

As early as the 1990s, T2-W MR sequences were proven to provide excellent contrast between FUS lesions and the surrounding intact tissue in excised and *in-vivo* animal tissue [324]–[326], and they are still considered among the standard methods for determining the extent of ablation lesions. In the same period, Hynynen et al. [327] reported that the size of lesions inflicted in rabbit thigh muscle as visualized on T2-W images matched well the size estimated after tissue excision by caliper measurements and histological examination. Another important observation made was that contrast-enhanced T2-W FSE imaging showed signal enhancement only in normal tissue and not in lesions [327]. This phenomenon was also reported

a few years later for rabbit skeletal muscle [328], rabbit brain [329], and synovial tissue [330] and is considered to be attributed to vascular disruption in the ablated tissue. Contrast-enhanced T1-W FSE imaging also allowed accurate lesion assessment following FUS ablation in rabbit skeletal muscle [328] and brain [331], synovial tissue [330], as well as in the clinical setting [332], where the predicted size was well correlated with the histological lesion size.

While both T2-W FSE and contrast-enhanced T1-W FSE sequences are currently considered as gold standard for assessing the extent of FUS damage, it seems that in early studies, T1-W FSE sequences were more frequently employed for MR thermometry rather than lesion assessment due to the superior T2-W FSE contrast between intact and damaged tissues reported in numerous studies at the time [333]. Later, it was clarified that the selection of proper sequence in terms of optimizing lesion contrast and delineation highly depends on the specific tissue characteristics. This has been demonstrated in a study by Damianou et al. [334], who performed FUS ablations below and above the boiling level in freshly excised lamb and *in-vivo* rabbit tissue. Both T1-W and T2-W FSE imaging were suggested by authors for accurately visualizing ablation lesions in the kidney and liver, whereas for boiling lesions, the T2-W sequence was considered optimal. T1-W FSE imaging was proposed as the optimal sequence for detecting brain lesions of either kind. This was supported by another study where T2-W FSE images showed higher anatomical resolution in the brain compared to T1-W FSE images, but the latter ones offered better contrast between lesion and brain tissue [335]. Notably, lesion discrimination can be further optimized by selecting proper imaging parameters. For these two basic sequences; T1-W and T2-W FSE, the effect of the TR and TE on the resultant contrast to noise ratio (CNR) between lesion and normal tissue was investigated in excised lamb brain, with authors suggesting the use of TR values above 500 ms and TE values in the range of 40 to 60 ms for optimized contrast [335].

Intraoperative monitoring of thermal ablation procedures is critical in deciding whether heating should be continued or modified depending on the desired therapeutic outcome. Lesion monitoring is typically carried out utilizing thermosensitive sequences that allow precise monitoring of temperature evolution for controlled coagulative necrosis [9], [261]. There is though a limited literature on the intraprocedural monitoring of signal and contrast changes in the ROI and how these correlate with histological tissue damage and lesion formation.

Bremer et al. [336] investigated the efficacy of non-enhanced MRI to accurately monitor lesion size during LITT in pig liver compared to histological size assessment. For this purpose, T1-W turbo FLASH images were acquired at 1-minute interval, revealing a stable reduction in the standardized SI in the center and periphery of the lesion during LITT, which was partially recovered throughout the cooling period. Furthermore, the SI in the lesion center was found to decrease with increasing deposited laser energy. Another example is a study by Vergara et al. [337], who developed a novel system for navigating electrophysiology catheters to ablate atrial tissue under real-time guidance in a 3T MR scanner with the assistance of dedicated MR sequences [337], whose performance was tested in pigs. In the clinical setting, results on intraprocedural MRI lesion monitoring during MWA of liver malignancies were reported by Lin et al. [338]. Specifically, a series of T2-W fat-suppressed fast-recovery FSE images were acquired every 35 s during ablation to monitor tissue effects, with the results showing a gradual SI decrease in the tumor.

In the context of FUS, T1-W and T2-W FSE imaging was mostly employed before FUS ablation for ROI definition and treatment planning and post-ablation for assessing FUS-induced tissue damage [323], [334], [335]. Furthermore, these sequences were employed in numerous studies involving the use of TMPs and freshly excised animal tissue to investigate the effect of acoustic energy and grid parameters in the formation of discrete and overlapping lesions, as well as how the

selected imaging parameters affect lesion visualization [334], [335]. Despite the widespread use of these sequences in MRgFUS studies, their performance was not well investigated in the context of intraoperative lesion monitoring, which may refer to the visualization and/or quantification of progressive changes in the SI of the exposed ROI over time and also to real-time monitoring of lesions' formation according to the desired pattern.

Therefore, the main goal of this section is to provide insights on the topic of intraoperative lesion monitoring by presenting indicative results of a series of MRI-guided ablation experiments carried out in freshly excised pork tissue. Multiple sonications in sequential patterns were planned on a custom-made dedicated software and executed by an MRI-compatible robotic system featuring a single element spherically FUS transducer with a central frequency of 2.6 MHz [136]. The T1 and T2 relaxation times of the pork tissue and coagulation lesions were estimated in a 3 T MRI scanner. The impact of critical imaging parameters on the resultant CNR between coagulated and intact tissue was then investigated to optimize lesion discrimination on T1-W and T2-W FSE images. Both discrete and overlapping lesions were inflicted in pork tissue samples with simultaneous acquisition of T2-W images at a specific rate to enable visualization of the heated area and assessment of lesion progression with time. Following MRI assessment, the tissue was dissected to confirm successful lesion formation and assess how it is correlated with the CNR changes observed intraoperatively, as well as to obtain quantitative information of the real extent of tissue damage by caliper measurements.

9.2 Materials and methods

9.2.1 FUS ablation of *ex-vivo* porcine tissue

FUS was generated by a spherically focused ultrasonic transducer (Piezo Hannas Tech Co. Ltd) with a nominal frequency of 2.6 MHz, a diameter of 50 mm, a radius

of curvature of 65 mm, and an acoustic efficiency of 30 %, which was utilized over the course of all experiments. The transducer was mounted on an MRI-compatible computer-controlled positioning system with 4 degrees of freedom driven by piezoelectric motors, which is detailed described elsewhere [136], and was supplied by an RF amplifier (AG1016, T & C Power Conversion).

All the experiments were carried out in a GE 1.5 T MRI scanner (GE Signa HD16, GE Healthcare), as well as in a Siemens 3 T scanner (Magnetom Vida, Siemens Healthineers). As shown in the photo of **Figure 69A**, the FUS positioning system was seated on the MRI table and connected to the electronic driving system placed outside of the room through shielded cables. The top cover of the device includes an acoustic opening above the working space of the FUS transducer, to which the porcine tissue sample was fixed. The distance between the bottom surface of the tissue sample and transducer was adjusted at 35 mm, resulting in a focal depth of 30 mm. Degassed, deionized water was poured inside the container until it reached the bottom surface of the tissue sample to achieve efficient ultrasonic coupling. Multichannel body coils (12-channel body coil, Signa 1.5T, GE Healthcare Coils, Aurora, Ohio, USA and 18-channel body coil, Siemens Healthineers) were utilized for image acquisition. In each case, the coil was attached to a rigid plastic structure at some distance from the tissue surface to improve the signal by preventing tissue vibrations due to FUS from being transferred to the coil [339]. **Figure 69B** is an axial T2-W FSE image of the setup showing the concept of tissue sample placement above the FUS transducer and through-water ultrasonic coupling. The imaging parameters were as follows: TR = 2500 ms, TE = 90 ms, FA = 90º, ETL = 60, pBW = 0.50 Hz/pixel, NEX = 2, matrix size = 192×128, and FOV = 260×260×10 mm^3.

A treatment planning/monitoring software was interfaced with the amplifier and electronic driving system enabling remote control of the motion and ultrasonic parameters. The transducer's location was registered relative to the target location based on images obtained at the level of the porcine tissue sample and transducer

as illustrated in the graphic of **Figure 69C**. Specifically, the user segments the transducer (lower image) and the center of the transducer is fused in the tissue image (upper image). Then, the position of the transducer relative to the tissue is easily found.

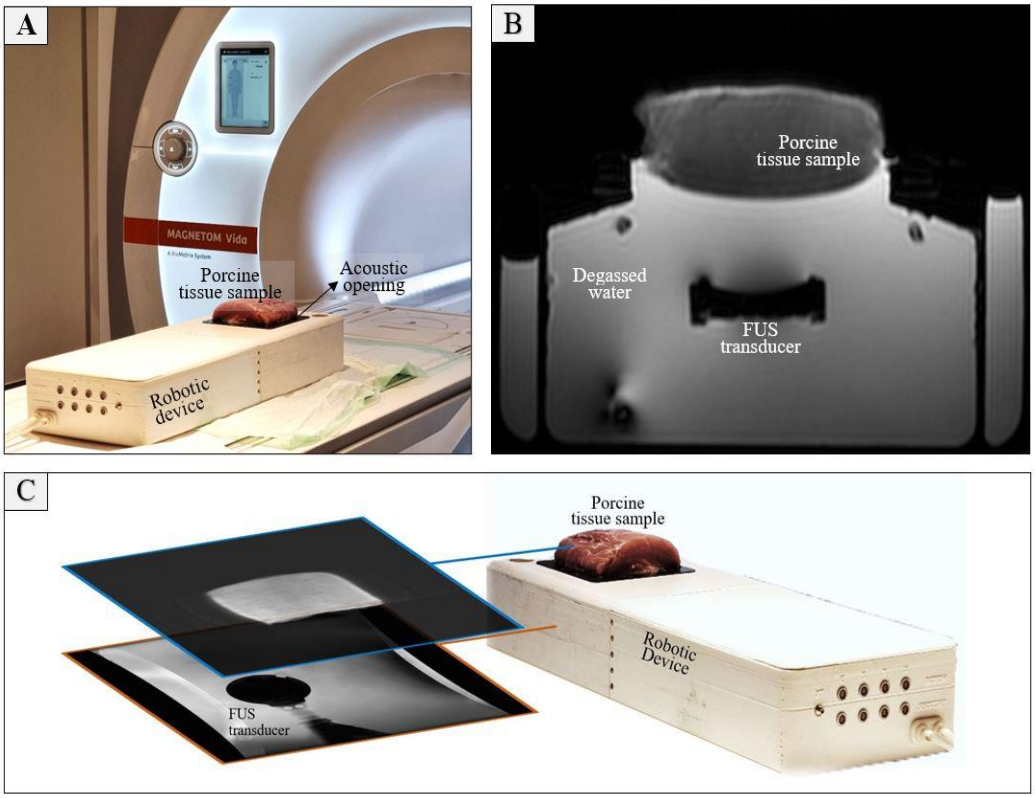

Figure 69: **(A)** The robotic device positioned on the MRI table with the piece of raw porcine meat mounted on the acoustic opening for ablation experiments in the MRI setting. **(B)** Axial T2-W FSE image (TR = 2500 ms, TE = 90 ms, FA = 90º, ETL = 60, pBW = 0.50 Hz/pixel, NEX = 2, matrix size = 192×128, and FOV = 260×260×10 mm^3) of the setup showing the concept of tissue sample placement above the FUS transducer. **(C)** The concept of registering the transducer location relative to the tissue sample by acquiring parallel coronal images at the level of the tissue and transducer.

9.2.2 Estimation of MR relaxation times of lesion and normal porcine tissue

The difference in relaxation times between coagulated and intact porcine tissue was investigated in the 3 T scanner. A piece of raw porcine meat received a single sonication at electrical power of 225 W (corresponding to an acoustic power of nearly 68 W) for 120 s at a focal depth of 30 mm, which resulted in a well-defined lesion. For T1 relaxation time measurements, images of the tissue sample with the inflicted lesion were acquired using a GRE sequence with variable FA. Circular ROIs were defined in the inflicted lesion and surrounding intact tissue. The mean SI measured in each ROI was plotted as a function of FA and the data were fitted to the following formula [340]:

$$M_z = M_{0z}\left(\frac{1-e^{-\frac{TR}{T1}}}{1-\cos a\, e^{-\frac{TR}{T1}}}\right)\sin a \qquad [6]$$

where M_z is the longitudinal magnetization, M_{0z} is the magnetization at thermal equilibrium, a is the excitation flip angle (herein referred to as FA), TR is the repetition time, and T1 is the longitudinal relaxation time. The imaging parameters were as follows: TR = 15 ms, TE = 2.3 ms, pBW = 275 Hz/pixel, matrix size = 256×256, FOV = 160×160×5 mm^3, NEX = 1, ETL = 1, and FA values ranging from 5º to 26 º (step of 3º).

Images were then acquired using a T2-W SE sequence at variable TE for T2 relaxation time mapping. For each ROI, the mean SI was plotted as a function of TE. Following regression analysis, an exponential trendline was fitted to the plotted data to calculate the T2 relaxation time based on the exponential function of equation 1. For image acquisition, the following parameters were employed: TR = 2000 ms, FA = 180º, ETL = 10, pBW = 202 Hz/pixel, matrix size = 192×192, FOV = 220×220×5 mm^3, NEX = 1, and TE values ranging from 10 to 110 ms (step of 10 ms).

9.2.3 Effect of MR parameters on CNR between lesion and normal porcine tissue

In this experimental part, the contrast between the lesion (68 W acoustic power for 120 s) and surrounding intact tissue was calculated as a function of critical MR parameters in the Siemens 3T MRI scanner for optimizing lesion contrast and detectability on FSE sequences; alternatively referred to as TSE by Siemens.

The effect of TE and ETL on the CNR was explored for the T2-W FSE sequence. Specifically, the ETL was varied from 6 to 129 with a TE equal to 51 ms and the TE was varied from 10 to 154 ms for a constant ETL of 60 while in both cases the TR was set at 2000 ms. For the T1-W FSE sequence, variable ETL of 6 to 129 at a constant TR of 2000 ms and variable TR values of 700 to 2500 ms at a constant ETL of 60 were tested using a TE of 10 ms. In all cases, the rest imaging parameters were as follows: FA = 180^{o}, pBW = 150 Hz/pixel, matrix size = 256×256, and FOV = 280×280×5 mm^{3}. For comparison purposes, measurements of the CNR between coagulated and intact porcine tissue as a function of TE were also conducted in the GE 1.5 T MRI scanner (TE = 10 – 150 ms, TR = 2000 ms, FA = 90^{o}, ETL = 12, pBW = 81.4 Hz/pixel, matrix size = 224×192, and FOV = 260×260×4 mm^{3}).

For both sequences, the changes in CNR with varying matrix size and NEX were investigated. Different matrix sizes of 64×64, 96×96, 128×128, 256×256, and 512×512 were tested using a constant NEX of 1. The NEX was varied from 1 to 4 for a contrast matrix size of 256×256. The rest imaging parameters of the T1-W FSE sequence were as follows: TE = 10 ms, TR = 1500 ms, ETL = 60, FA = 180^{o}, pBW = 150 Hz/pixel, and FOV = 280×280×5 mm^{3}. For T2-W FSE imaging, the TE value was changed to 51 ms and the TR value to 2000 ms. Circular ROIs of 3 mm in diameter were initially defined for the lesion, normal tissue, and background noise. These ROIs were consistently placed at the same anterior-posterior location to eliminate signal differences due to the signal drop occurring as one moves away from the coil. For the CNR estimation, the following formula was used [341]:

$$CNR = \frac{SI_{intact\ tissue} - SI_{lesion}}{\sigma_{noise}} \quad [7]$$

The SI was measured as the mean value in the corresponding ROI and the σ_{noise} as the standard deviation from a ROI placed in air/background noise, where the noise was assumed to follow a gaussian distribution.

9.2.4 Lesion monitoring during grid ablation in *ex-vivo* porcine tissue

The transducer's location relative to the target was registered in the MRI coordinates and different sonication patterns were planned on the relevant software as described previously. The sonication patterns were executed by the FUS robotic system under MRI monitoring of lesion formation. Specifically, an image was acquired immediately after each individual sonication to visualize lesion progression in discrete and overlapping patterns.

In the 1.5 T MRI scanner, grid sonications with different spatial step were performed, where an electrical power of 180 W (acoustical power of 54 W) was applied to each individual grid spot for a total duration of 120 s. T2-W FSE images were acquired using TR = 2000 ms, TE = 59 ms, FA = 90º, ETL =60, pBW = 27.1 Hertz/pixel, matrix size = 224×192, and FOV = 260×260×6 mm^3. The time delay between successive sonications was set at 60 s to minimize pre-focal heating [68].

Accordingly, in the 3 T scanner, T2-W FSE images were obtained with TR = 2500 ms, TE = 48 ms, ETL = 60, FA = 180º, pBW = 50 Hz/pixel, matrix size = 256×256, and FOV = 200×200×10 mm^3. Various sonications patterns were tested using a specific electric power of 200 W (acoustic power of 60 W) while the sonication time and spatial step were varied. Again a 60-s cooling time was left between sonications. Post-ablation, the tissue samples were dissected to visualize and quantify the extent of necrosis in planes parallel and perpendicular to the FUS beam direction.

9.3 Results

9.3.1 MR relaxation times of lesion and normal porcine tissue

The T1 and T2 relaxation times calculated for the lesion and normal porcine tissue are summarized in **Table 7**. The FUS lesion is characterized by lower relaxation times than the intact tissue, which is considered to be attributed to changes in the water content of coagulated tissue. The difference in these properties between coagulated and intact tissue allowed assessment of lesion formation by T1-W and T2-W FSE imaging.

Table 7: The mean value and standard deviation (SD) of the T1 and T2 relaxation times of the lesion and normal porcine tissue at 3 T.

Tissue	T1 ± SD (ms)	T2 ± SD (ms)
Lesion	738 ± 46	43 ± 3
Porcine Tissue	1158 ± 58	50 ± 2

9.3.2 Effect of MR parameters on CNR between lesion and normal porcine tissue

Figure 70 shows the T1-W FSE CNR between lesion (created using 68 W acoustic power and 120 s sonication time) and surrounding intact porcine tissue as well as the ratio of the CNR to the acquisition time plotted against the ETL and TR. ETL values up to 60 provided CNR higher than 80 allowing proper lesion discrimination (**Figure 70A**). ETL values in the range of 35 to 60 resulted in the highest CNR/acquisition time. Considering the importance of minimizing imaging time, an ETL value around 60 was considered optimum.

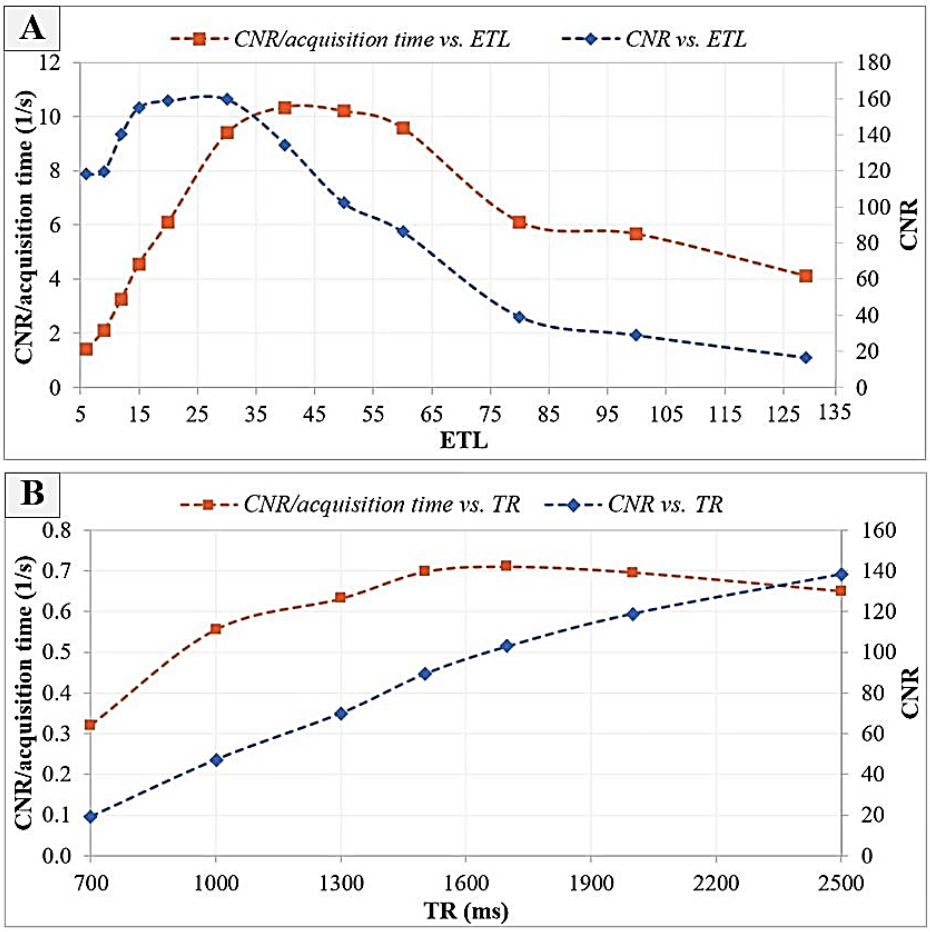

Figure 70: **(A)** Plots of the CNR between lesion and normal tissue and CNR/acquisition time of T1-W FSE images (TR = 2000 ms, TE = 10 ms, FA = 180°, pBW = 150 Hz/pixel, matrix size = 256×256, and FOV = 280×280×5 mm^3) versus ETL (6 – 129) at 3 T. **(B)** Plots of the CNR between lesion and normal tissue and CNR/acquisition time of T1-W FSE images (ETL = 60, TE = 10 ms, FA = 180°, pBW = 150 Hz/pixel, matrix size = 256×256, and FOV = 280×280×5 mm^3) versus TR (700 - 2500 ms) at 3 T.

As seen in the graph of **Figure 70B**, the CNR/acquisition time reached its maximum value and remained almost constant for TR values in the range of 1500 to 2000 while the CNR was increased from 90 to 120. Although the TR of 2500 ms may be considered ideal in terms maximizing contrast, one should alternatively select a value close to 1500 that still provides good CNR (>80) at the minimum time cost possible.

The corresponding results of the ETL and TE effect on lesion contrast of T2-W FSE images are shown in **Figure 71**. From **Figure 71A**, it is observed that ETL values around 90 resulted in the highest values of CNR/acquisition time but in a very poor CNR (< 80), which made lesion detectability difficult. On the contrary, values in the range of 25 to 60 offered both sufficiently high CNR (>80) and CNR/acquisition time, with the ETL of 60 considered the ideal in terms of minimizing the acquisition time.

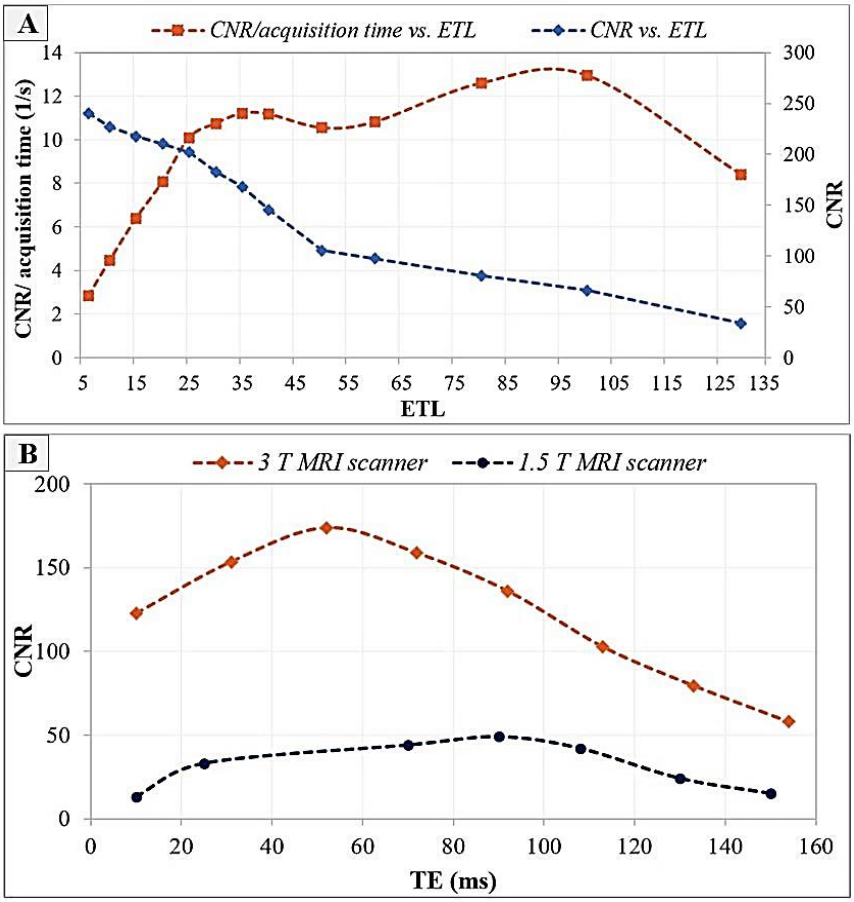

Figure 71: **(A)** Plots of the CNR between lesion and normal tissue and CNR/acquisition time of T2-W FSE images (TR = 2000 ms, TE = 51 ms, FA = 180^{o}, pBW = 150 Hz/pixel, matrix size = 256×256, and FOV = 280×280×5 mm^{3}) versus ETL (6 – 129) at 3 T. **(B)** Plots of the CNR between lesion and normal tissue of T2-W FSE images (TR = 2000 ms, ETL = 60, FA = 180^{o}, pBW = 150 Hz/pixel, matrix size = 256×256, and FOV = 280×280×5 mm^{3}) versus TE (10 - 154 ms) at 1.5 T and 3 T.

In **Figure 71B**, the trend of CNR vs. TE increases until the TE of 50 ms and then gradually decreases, clearly suggesting the TE value of 50 ms as optimum for maximizing CNR. Note that the acquisition time is not considered in that case since it is not affected by TE. The corresponding plot for evaluation at 1.5 T shows a quite similar trend but with a lower increase rate in the TE range of 20 to 90 ms and remarkably smaller CNR values.

The graphs of **Figure 72** show the changes in the CNR and CNR/acquisition time of T2-W FSE images as a function of NEX. The minimum NEX of 1 offered CNR much higher than the minimum suggested value of 80, and thus, the use of a larger NEX is unnecessary provided that it results in longer acquisition times. Similar results were obtained for the T1-W FSE imaging suggesting the NEX of 1 as the optimum.

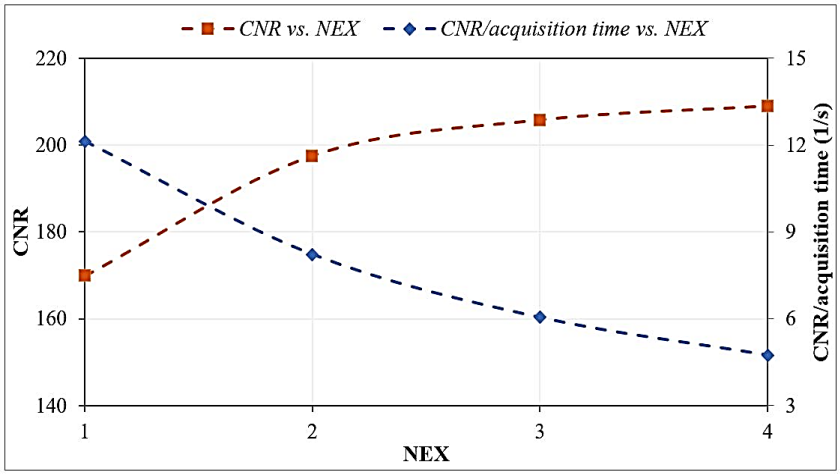

Figure 72: Plots of the CNR between lesion and normal tissue and CNR/acquisition time of T2-W FSE images (TR = 2000 ms, TE = 51 ms, FA = 180^{o}, pBW = 150 Hz/pixel, matrix size = 256×256, and FOV = 280×280×5 mm^{3}) versus NEX (1 – 4) at 3 T.

Finally, concerning the effect of the matrix size, the CNR decreased from about 740 to 95 with increasing matrix size from 64×64 to 512×512 for the T1-W FSE imaging, whereas the CNR in T2-W images decreased from 880 to 140. The smallest matrix size is preferred in terms of minimizing the acquisition time, but it provided poor resolution. On the contrary, the biggest matrix size provided

excellent resolution and sufficiently high CNR (>80), but at the cost of increased acquisition time. By balancing the parameters of CNR and imaging time, the use of a 256×256 matrix size is proposed.

The MR parameters suggested by the current study for optimizing the CNR between FUS lesions and surrounding tissue on T1-W and T2-W FSE images also considering the importance of minimizing the acquisition time are summarized in **Table 8**.

Table 8: Summary of the suggested MR parameters for optimizing CNR between lesion and tissue at the minimum time cost for the specific parameters employed in the study.

MR parameter	T1-W FSE	T2-W FSE
TR (ms)	1500	2000
TE (ms)	10	50
ETL	60	60
NEX	1	1
pBW (Hz/pixel)	150	150
Matrix size	256×256	256×256
FOV (mm^2)	280×280	280×280
Slice thickness (mm)	5	5

9.3.3 Lesion monitoring during grid ablation in *ex-vivo* porcine tissue

An indicative example of lesion monitoring in the 1.5 T MRI scanner is shown in **Figure 73**. **Figure 73A** shows a series of T2-W FSE images acquired during ablation in a 3x3 pattern with a special step of 10 mm, where the coagulated regions appear as spots of reduced SI. The acoustical power of 54 W applied for 120 s was sufficient to induce well-defined easily detectable lesions. Note that the lesion created at the reference location of the transducer is visible on the left side of all images. Note also that a circular area of reduced intensity appears immediately after the first sonication (#1) but not in the next images, thus revealing heat accumulation in the ROI but no evidence of lesion formation.

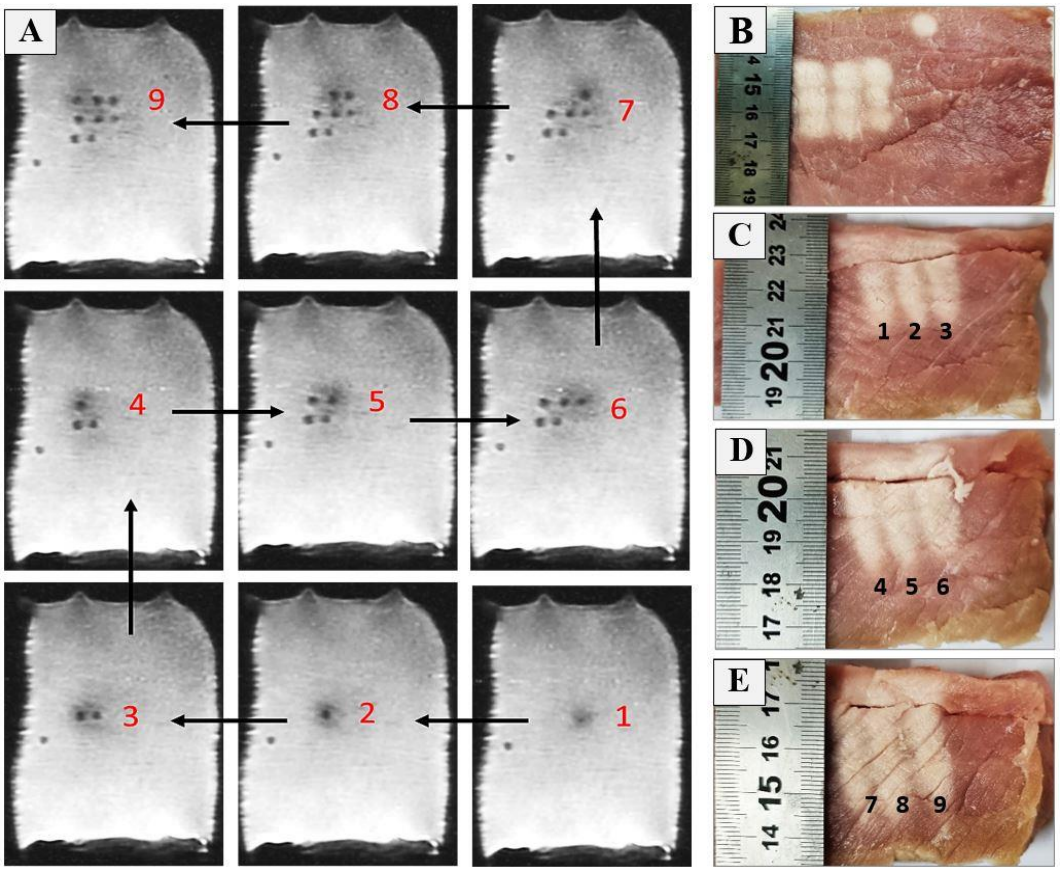

Figure 73: **(A)** 2D Coronal T2-W FSE images (TR = 2000 ms, TE = 59 ms, FA = 90º, ETL =60, pBW = 27.1 Hz/pixel, matrix = 224×192, FOV = 260×260×6 mm^3, and NEX =2) acquired during ablation in a 3×3 pattern (acoustical power of 54 W for 120, 10-mm step, 60-s delay) at 1.5 T. **(B)** The meat sliced (horizontally) at 10 mm from the sonicated side showing the formed lesions and reference lesion. **(C)-(E)** Photos of the tissue sliced vertically: Lesions 1 to 3 had a length of 29 mm, lesions 4 to 6 a length of 30 mm, and lesions 7 to 9 a length of 32 mm.

Figure 73B is a cross section photo of the meat at 10 mm from the sonicated surface. In contrast to the MRI images, all 9 lesions were visible. Tissue was also dissected vertically to visualize the extent of necrosis in a plane parallel to the beam direction. Again, all nine lesions were visible extending 29 to 32 mm from the tissue top surface as shown in **Figure 73C** to **Figure 73E**.

Typical results obtained in the 3T MRI scanner are presented by **Figure 74** to **Figure 76**. All lesions were formed using acoustic power of 60 W. **Figure 74** shows T2-W FSE images of the porcine tissue sample sonicated in a 2×3 grid with varying step of 10 or 15 mm and sonication duration of 10 to 60 s, revealing the effect of sonication time on the resultant lesion size and distance between adjacent lesions.

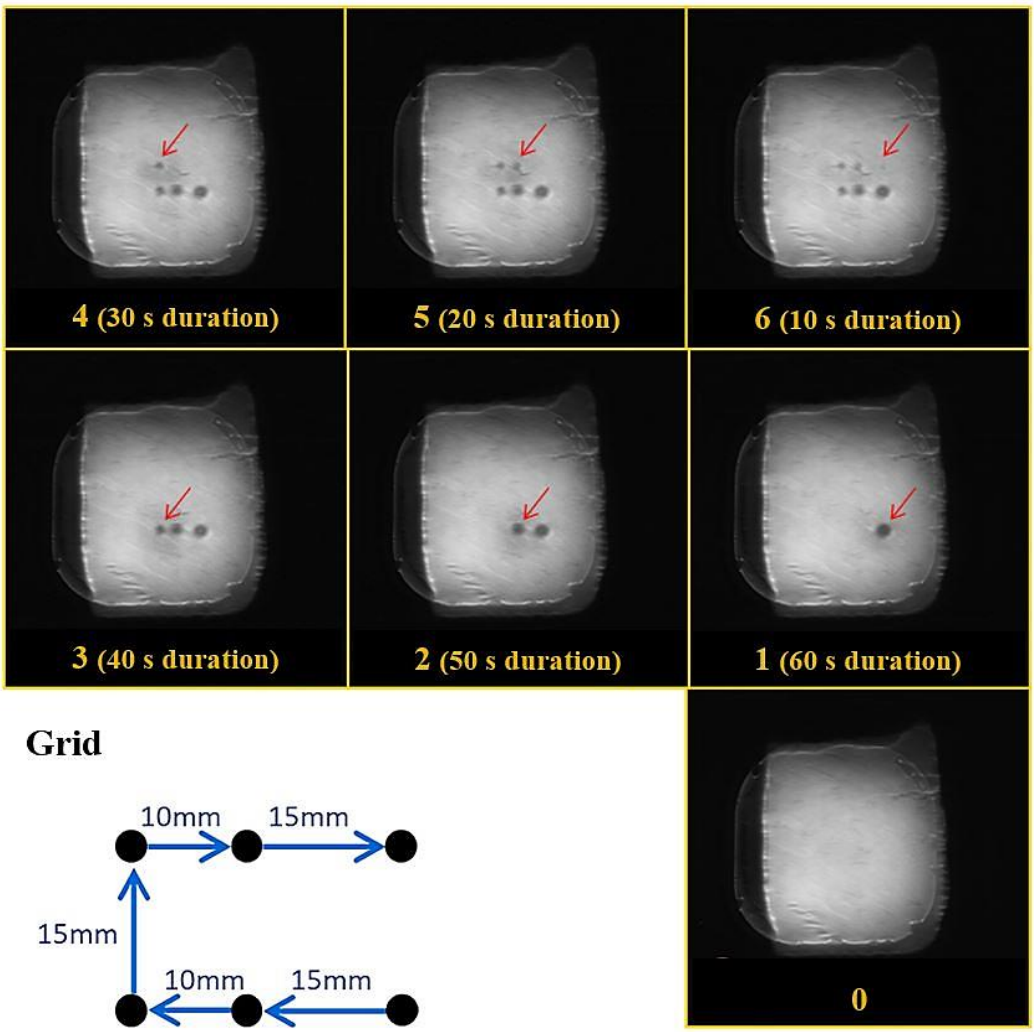

Figure 74: 2D Coronal T2-W FSE images (TR = 2500 ms, TE = 48 ms, FA = 180º, ETL = 60, pBW = 50 Hz/pixel, matrix size = 256×256, and FOV = 200×200×10 mm^3) acquired during sonication in a 2×3 grid (acoustic power of 60 W) using varying sonication time and spatial step in the 3 T MRI scanner. The sonication pattern is presented on the left bottom corner.

The T2-W FSE images of **Figure 75** show the lesion progression for a 3x3 grid with a 10-mm step, where each spot was sonicated for 40 s. With the specific parameters, discrete lesions were inflicted in tissue.

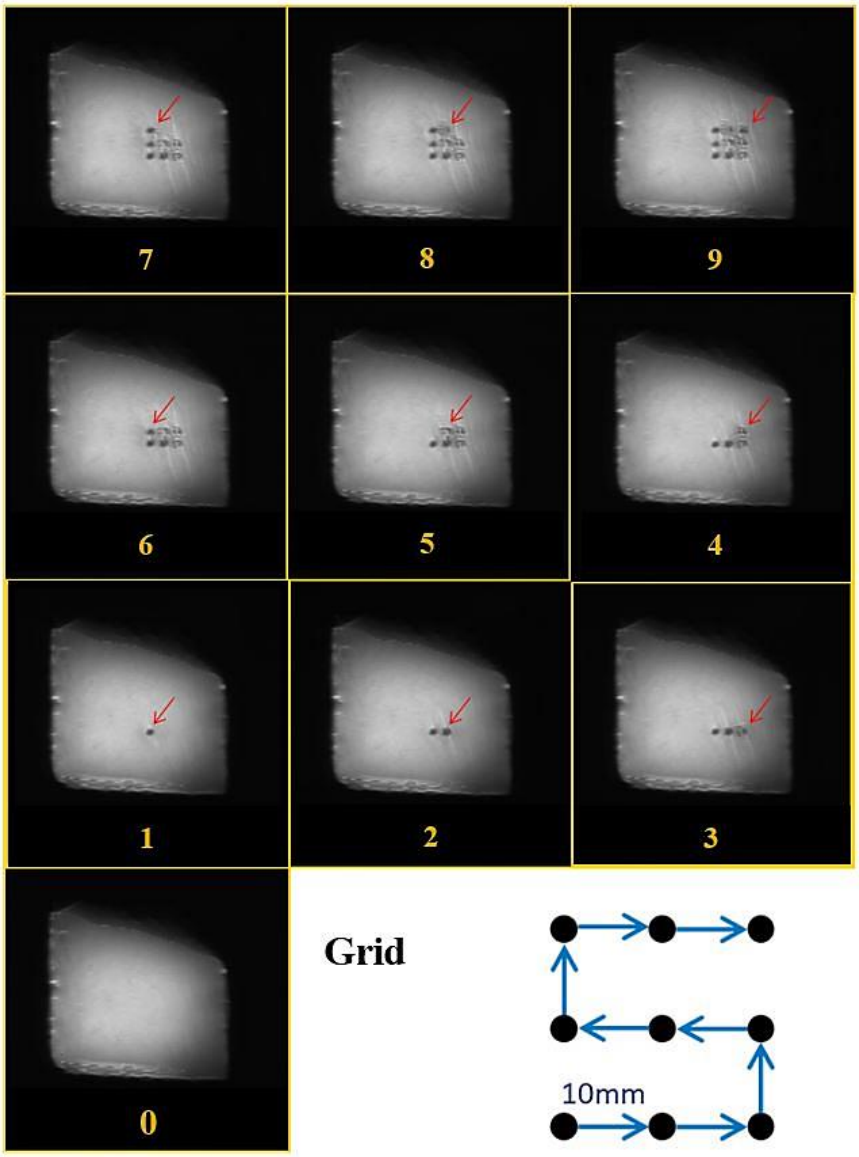

Figure 75: 2D Coronal T2-W FSE images (TR = 2500 ms, TE = 48 ms, FA = 180º, ETL = 60, pBW = 50 Hz/pixel, matrix size = 256×256, and FOV = 200×200×10 mm^3) acquired during sonication in a 3×3 grid (acoustic power of 60 W for 40 s) with a spatial step of 10 mm (time delay of 60 s) in the 3 T MRI scanner. The sonication pattern is presented on the right bottom corner.

The T2-W FSE image of **Figure 76A** shows the overlapping lesion created by reducing the step to 5 mm while keeping the rest parameters identical. **Figure 76B** is a photo of a (horizontal) cross-section of the tissue sample at 10 mm from the top surface, revealing a rectangular necrotic area of about 20×20 mm^2.

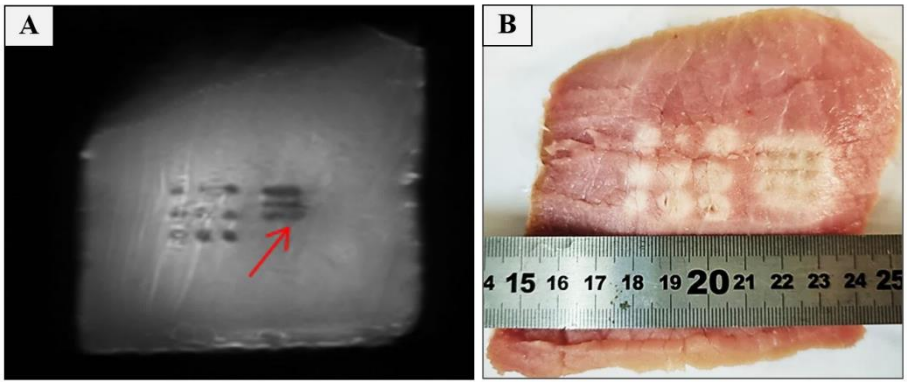

Figure 76: **(A)** 2D Coronal T2-W FSE image (TR = 2500 ms, TE = 48 ms, FA = 180º, ETL = 60, pBW = 50 Hz/pixel, matrix size = 256×256, and FOV = 200×200×10 mm^3) acquired after sonication in a 3×3 grid (acoustic power of 60 W for 40 s) with a spatial step of 5 mm (time delay of 60 s) in the 3 T MRI scanner. The red arrow indicates the formed overlapping lesion. The discrete lesion created with the 10-mm step is also visible on the left side. **(B)** Photo of the tissue sample cut horizontally at 10 mm from the sonicated surface.

9.4 Discussion

The present section focused on parameter optimization for MRI monitoring of lesions produced by FUS using T1-W and T2-W FSE sequences. Such sequences were widely employed for post-sonication lesion assessment, but not for intraprocedural monitoring of lesion progression during multiple ablations in grid patterns. A series of experiments were carried out in freshly excised porcine tissue to provide insights on this topic.

The contrast in T1-W and T2-W FSE images arises from the variation in the relaxation times among tissues [9]. It has been previously demonstrated that the relaxation times of FUS lesions and thus the contrast between healthy tissue and FUS lesions are strongly affected by the specific host tissue characteristic [112]–

[114]. Herein, the FUS lesions were found as expected to possess lower T1 and T2 values than the surrounding non-sonicated porcine tissue at 3 T. This is consistent with what has been found in another study by Hadjisavvas et al. [112], where lower T1 and T2 values were estimated for thermal lesions in *in-vivo* rabbit kidney, liver, heart, and brain compared to the corresponding host tissue. Previous research showed that thermal lesions produced by FUS appear hypointense in T2-W FSE images, whereas hyperintensity is associated with tissue boiling [334]. Opposite behavior is observed in the case of T1-W FSE imaging [334]. Therefore, the hypointense appearance of lesions on T2-W FSE images in the current study provides clear evidence of lesion creation by thermal mechanisms.

The study findings further suggest that the difference in MR relaxation properties between damaged and intact porcine tissue allows excellent lesion discrimination using T1-W and T2-W FSE sequences, provided that appropriate imaging parameters are employed. In this regard, a series of scans with varying parameters were performed to assess how the contrast between ablated and normal tissue is affected. For this purpose, a piece of porcine meat was sonicated using the 2.6 MHz FUS transducer (68 W for 120 s). The ETL, TE, and TR were the sequence parameters tested in terms of the CNR and acquisition time. Overall, higher CNR was achieved with the T2-W FSE sequence. It was thus concluded that T2-W FSE imaging is preferred for lesion monitoring in dead tissue, whereas in the case of live animals T1-W imaging may be preferred due to the use of contrast agents.

CNR values above 80 were deemed sufficient for ease detectability and proper visualization of FUS lesions. With the T1-W FSE sequence, CNR values above 80 were achieved for ETL values of up to 60 (**Figure 70A**), with the value of 60 offering sufficiently high CNR at the minimum time cost (9 s). Therefore, considering both parameters, an ETL of 60 is suggested as the optimum.

The corresponding results on the effect of TR (**Figure 70B**) reveal that the ratio of CNR to the acquisition time in T1-W FSE imaging begins to increase with

increasing TR up to 1500 ms, and then becomes almost flat while at TR longer than 2000 ms it begins to decrease again. On the contrary, the CNR gradually increases from 20 to 140 as TR increases from 700 to 2500 ms, attributing to the increase in the SI difference between lesion and tissue. Notably, this trend is expected to be reversed as the TR is getting longer and the SI of lesion and tissue is reaching its maximum value. Generally, while TR values close to 2500 ms may be considered ideal in terms of maximizing contrast, a value close to 1500 ms constitutes a wiser option in the case of intraoperative monitoring of lesion progression since it still provides good CNR (>80) at smaller acquisition time.

Regarding T2-W FSE imaging, the results (**Figure 71A**) confirm that the use of longer ETL causes CNR decrease. Nevertheless, when the CNR is divided by the acquisition time an increasing trend is observed owing to that the acquisition time and ETL are inversely proportional. By choosing an ETL value in the range of 25 to 60 acceptable CNR (>80) is achieved at a reasonable acquisition time (< 20 s). Further increasing the ETL to reduce the time may result in poor contrast making lesion discrimination difficult or infeasible. Again, the ETL of 60 was deemed ideal for minimizing the acquisition time.

Concerning the effect of TE, the trend of CNR versus TE (**Figure 71B**) begins to increase until it reaches its maximum value of about 170 at TE close to 50 ms and then gradually decreases. Since the imaging time is not affected by the chosen TE, it was concluded that the TE of 50 ms is ideal for lesion monitoring by T2-W FSE imaging and was adopted in follow up experiments. Interestingly, TE values around 50 ms can be considered appropriate for imaging at 1.5 T as well. However, as expected, superior contrast was observed in the 3 T scanner, with almost 4-fold increase in the CNR at the TE of 50 ms. This result ties well with previous studies wherein authors have suggested the use of TE values between 40 and 50 ms to maximize the contrast of thermal lesions on T2-W FSE images following *in-vivo* rabbit experiments [112].

Finally, the effect of the matrix size and NEX on the CNR was investigated using the optimized TR, TE, and ETL values. For both sequences, the minimum NEX of 1 provided excellent CNR and was considered optimum in terms of minimizing the acquisition time. As expected, increasing matrix size resulted in a better resolution and CNR drop simultaneously increasing the imaging time. The matrix size of 256×256 was deemed optimum providing both good CNR (>80) and CNR/acquisition time.

The feasibility of monitoring lesion progression during grid sonications was assessed at both 1.5 T and 3 T using T2-W FSE sequences. The FUS transducer was navigated by a positioning system in the horizontal plane to sonicate porcine tissue samples in grid patterns with varying ultrasonic and grid parameters. Navigation was initiated by registering the transducer's location relative to the target in the MRI coordinates and sonicating the meat at the reference location of the transducer. Lesion formation at the reference point was confirmed by T2-W FSE imaging providing evidence of efficient ultrasonic coupling. The sonication pattern was then executed with intraprocedural acquisition of T2-W FSE images that enabled assessment of lesions progression over time. The lesions appeared as circular black spots with excellent contrast from the surrounding tissue. Notably, immediately after sonication, the tissue surrounding these black spots appeared as a less hypointense area indicating heat accumulation around the coagulated tissue, which returned to its normal intensity during tissue cooling through heat dissipation mechanisms (**Figure 73**, **Figure 74**). Note also that circular focal beams constitute evidence of lesion formation by thermal mechanisms while in the case of boiling lesions the beam was shown to be distorted [334].

An interesting observation made during lesion monitoring in the 1.5 T MRI scanner (**Figure 73**) is that while only eight out of the nine sonicated spots showed clear evidence of lesion formation on the series of T2-W FSE images, nine well-defined lesions were visualized following tissue dissection. In fact, a circular hypo-

enhanced area was observed immediately after the first sonication revealing heat accumulation in the relevant ROI, but it was not present in the next acquisitions. Tissue dissection revealed that the lesion had been shifted from the tissue surface and could only be detected if a deeper slice had been selected. It was also observed that the length of the formed lesions varied from 29 to 32 mm, most probably attributed to heat dissipation from previously sonicated spots.

The excellent lesion contrast from the surrounding hyperintense background also allowed assessment of the lesion size depending on the applied acoustic energy. In **Figure 74**, the spots of a 2x3 grid were sequentially exposed at similar acoustic power while the sonication time was decreased from 60 to 10 s resulting in lesions of decreasing diameter, with the last one receiving the lowest energy being barely visible. Furthermore, by varying the spatial step between sequential sonications the distance between adjacent lesions on the T2-W FSE images was varied accordingly.

Overall, the current section provides insights on the topic of FUS lesion progression monitoring by T1-W and T2-W FSE imaging through a series of ablation experiments in *ex-vivo* porcine tissue. The study findings confirmed that lesion discrimination on T1-W and T2-W FSE images highly depends on the selected MRI parameters while the imaging time should also be considered in the context of intraprocedural lesion monitoring. Thereby, critical MR parameters, i.e., TE, TR, and ETL, should be optimized by balancing between the CNR and acquisition time. In this regard, the use of CNR values above 80 was set as the criterion for proper lesion visualization. Also considering the need to minimize the acquisition time, a TR close to 1500 ms is suggested for T1-W FSE imaging. A TE close to 50 ms was considered optimum for T2-W FSE imaging. For both sequences, an ETL of 60 was proven ideal. During sonications in discrete and overlapping patterns, acute FUS lesions were visualized as spots of reduced intensity on T2-W FSE images with excellent contrast from the surrounding intact tissue.

10 Feasibility of ultrasonic heating through skull phantom using single-element transducer

10.1 State of the art

In the 1950s, revolutionary studies were conducted by Fry et al. [342], [343] to assess the high intensity FUS effects on human brain tissue. However, transcranial focusing was unattainable because of the strong aberrating and attenuating nature of the skull resulting in significant beam defocusing [271]. Thereby, for many years, studies involved craniotomy for precise delivery of ultrasonic energy to the brain tissue through an acoustic window [344].

In the 1990s, the multi-element ultrasonic technology has emerged as a way to actively form the beam compensating for such losses through regulating the phase of each element individually [345], [346]. While this procedure was initially invasive, the introduction of numerical simulations for accurately estimating the resultant phase profile of the beam transmitted though the skull allowed for completely non-invasive transcranial applications [347], [348]. In this regard, MRI was also a significant milestone that accelerated the adoption of this technology mainly through the development of MR thermometry [9], which is currently the only tool for monitoring temperature changes during sonication in almost real-time. Simultaneously, MRI is considered ideal as a guidance modality since it offers non-invasive optimal imaging of brain tumors without exposing patients to ionizing radiation [8]. Overall, these technological advances offered the accuracy required to safely target areas in the CNS without threatening adjacent or intervening tissues.

So far, the transcranial FUS technology has been investigated for its feasibility in treating essential tremor [349], PD [350], obsessive-compulsive disorder [351], major depressive disorder [351], and epilepsy [352]. The last years, a lot of research was devoted in investigating the use of this technology for tumor ablation and drug delivery by selective disruption of the BBB [60].

Currently, the available devices for brain ultrasound therapy in the clinic are limited. The SonoCloud (CarThera, France) [353] and NaviFUS (NaviFUS, Taiwan) [354] systems offer FUS plus MBs-mediated disruption of the BBB. The first one comprises a non-focused transducer that is implanted in the skull, whereas the later one offers neuronavigation-guided extracorporeal therapy. The ExAblate Neuro 4000 system (InSightec, Israel) is considered the leading MRgFUS brain system and the first to be approved by the FDA for targeted thermoablation of brain tissue [355]. Both extracorporeal systems use phased arrays for electronic steering of the beam [354], [355]. The ExAblate system incorporates a helmet with 1024 elements operating at a frequency of 650 KHz, whereas the NaviFUS incorporates a more compact hemispherical transducer of fewer elements.

Though the phased array technology has immense benefits, it requires the use of sophisticated driving electronics that complicate its use and portability. Furthermore, it typically involves the use of a stereotactic frame making the procedure minimally invasive [355]. The high cost of this technology constitutes another shortcoming limiting its wider adaption, especially in the preclinical setting.

The use of a single-element transducer could address these issues, but at the cost of difficulties in ultrasonic penetration through the skull. Successful trans-skull BBBD using a single element FUS transducer was achieved in experimental animals such as rabbits [356] and mice [120], [276]–[278] by administration of MBs-enhanced pulsed FUS of 0.7 and 1.5 MHz, respectively. Single-element FUS transducers driven at a lower frequency of about 0.5 MHz were proven efficient for BBBD in larger animals, and particularly non-human primates [357]–[362]. Even lower frequencies of 0.4 and 0.25 MHz were chosen for similar applications in swine [363] and sheep [364], respectively.

Simplified techniques for compensating for skull-induced energy losses were used in the effort to enable efficient trans-skull delivery of ultrasonic energy by single

element transducers. As an example, a setup incorporating a single element 0.5 MHz spherical transducer for FUS-mediated BBBD was proposed by Marquet et al. [360]. The proposed system is intended for use under stereotactic targeting and real-time monitoring by passive cavitation spectral analysis so as to enable MRI independent treatment sessions. In the framework of the system's evaluation, authors attempted BBBD of deep subcortical structures in macaque monkeys. The amplitude of ultrasonic emission was enhanced to compensate for the scalp and brain-induced attenuation losses as estimated by pressure measurements in vitro, thus leading to successful BBBD.

Pouliopoulos et al. [246] proposed a neuronavigation-guided system incorporating a single-element FUS transducer of 0.25 MHz nominal frequency, as well as a simulation framework for predicting the beam shift. The focusing properties of the transducer were assessed using a capsule hydrophone. The insertion of a human skull fragment in the beam path resulted in a pressure attenuation of about 45% compared to that measured in free field for a normal incidence angle, whereas a focal shift of 0.5 (± 0.4) and 2.1 (± 1.1) mm was observed along the lateral and axial dimensions, respectively [246]. Notably, authors report a successful MBs-enhanced FUS-mediated BBB opening in the thalamus and dorsolateral prefrontal cortex of two non-human primates, which was evidenced by T1-W gadodiamide-enhanced MRI scans [246]. Notably, authors clarify that knowledge of the exact intracranial pressure with the proposed system is infeasible, and thus, the pressure field should be simulated utilizing CT head scans of each subject individually.

More recently, the use of 3D printed holographic acoustic lenses customized to each skull geometry have been proposed as a more comprehensive low-cost way to compensate for skull losses, thereby enabling transcranial therapy with a single-element transducer [365], [366]. Maimbourg et al. [365] demonstrated a 10-fold increase in the accumulated energy in the targeted area using the specific approach of aberration correction with lenses.

This section provides insights on the use of single element FUS transducers with no other means of defocusing corrections for transcranial FUS in humans by preclinical experimentation using a brain-tissue/skull phantom setup. The optimal phantom to mimic brain tissue was selected among twelve agar-based phantoms prepared in house with different concentrations of agar, silicon dioxide, and evaporated milk, based on the ultrasonic attenuation property of these phantoms as estimated by the transmission-through technique. Rapid prototyping was used for the construction of the skull model. The ultrasonic attenuation in three common thermoplastic materials was initially assessed, from which two were deemed suitable to replicate the attenuation observed in the skull bone adequately. Two thermoplastic phantoms with the precise skull bone geometry of a male patient were then 3D printed following segmentation on a CT head scan image. The main part of the study involved performing FUS sonications in the brain-tissue phantom through water (without any obstacle in the beam's path) and then, with each skull phantom intervening the beam under the same experimental conditions. Single element spherically focused transducers of 0.4 and 1.1 MHz central frequency were used. In each case, thermometry during heating was performed at the focal spot using thermocouples.

10.2 Materials and methods

10.2.1 Thermoplastic skull phantom

10.2.1.1 Development of block thermoplastic samples

Three (3) solid blocks (100% infill) were 3D printed using the FDM technique with ABS (Stratasys) and VeroWhite Resin (RGD835, Stratasys) materials on a Stratasys printer (F270), as well as with PLA (3DJ) thermoplastic on an Ultimaker printer (3 Extended). The samples were modeled into flat plates of 5-mm thickness and 63 x 63 mm area as shown in **Figure 77**.

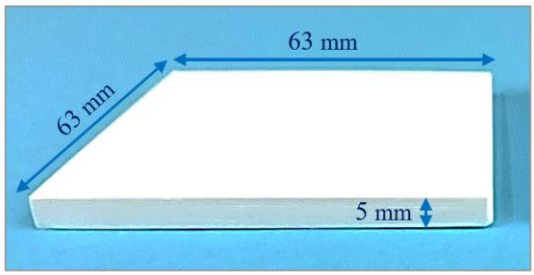

Figure 77: Photo of the 3-D printed ABS flat plate with indicated dimensions.

10.2.1.2 Ultrasonic attenuation in thermoplastic samples

The ultrasonic attenuation in the thermoplastic samples was measured using a transmission-through immersion technique. Two identical transducers (custom-made, central frequency of 2.1 MHz and diameter of 10 mm) and the test-thermoplastic were fixed into a specially designed plastic holder ensuring vertical incidence of the waves on the sample and minimizing energy losses due to refraction. The holder was submerged in degassed water and the first transducer was connected to the signal generator (33220A, Agilent, Santa Clara, CA 95051, United States), whereas the second transducer was connected to a digital oscilloscope (TDS 2012, Tektronix, Inc.) to display the received signal. The corresponding experimental setup is shown in **Figure 78**.

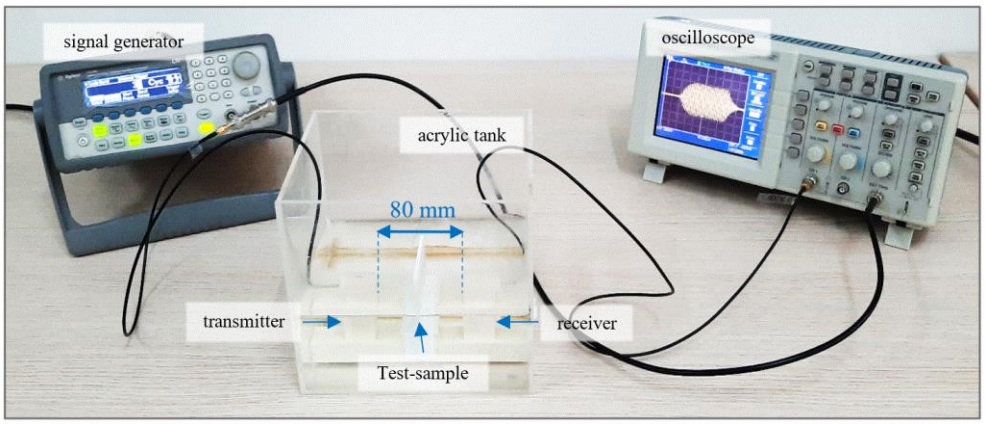

Figure 78: Photo of the experimental setup used to estimate the ultrasonic attenuation by the transmission-through method with indicated components.

Pulsed ultrasound of 2.1 MHz frequency (20-cycle bursts with a period of 10 ms) was transmitted through the layered media. Initially, the peak-to-peak voltage was measured by the oscilloscope without any material between the transducers (reference signal). Then, the signal was recorded with the thermoplastic sample fixed in between the two transducers. The attenuation coefficient a of the sample was estimated by including the reference signal amplitude (A_w) and the one measured in the presence of the sample (A_s), together with the thickness of the sample x, and the transmission coefficient T of the water-sample interface in the following equation [152]:

$$a = a_w + \frac{20\ loge}{x} * ln\left(\frac{A_w}{A_s} T\right) \quad [8]$$

in which α_w represents the attenuation coefficient of water. The transmission coefficient was estimated by the speed of sound in the samples using the widely known pulse-echo technique as previously described by Selfridge et al. [367]. All the measurements were conducted at room temperature (≅ 22 °C).

10.2.1.3 Development of phantoms with skull geometry

The skull bone of an anonymized male patient was isolated following segmentation on CT head scan images. **Figure 79A** shows the STL format of the whole human skull. For the purpose of this study, a circle-shaped part was isolated from the temporal region of the human skull model, and then imported in each printer's software in STL format for further processing. Samples were 3D printed in solid mode having a diameter of approximately 60 mm and a thickness varying from 2.55 to 10.75 mm. The sample made with ABS (Stratasys) material is shown in **Figure 79B**.

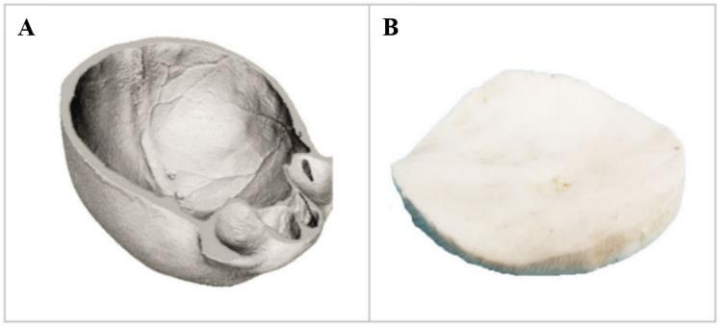

Figure 79: (A) STL format of the whole skull model. **(B)** 3D printed skull phantom.

10.2.2 Brain-tissue phantoms

10.2.2.1 Preparation of agar-based phantoms

Phantoms were prepared according to the procedure previously described by Drakos et al. [110] using agar (Merck KGaA) as the gelling agent while silicon dioxide (Sigma-Aldrich) and evaporated milk (Nounou) were included as modifiers of ultrasonic scattering and absorption, respectively [140]. Agar-only samples were prepared with different agar concentration of 2 %, 4 %, 6 % and 8 % w/v. Silica-doped phantoms were prepared using a silicon dioxide powder concentration of 2 %, 4 %, 6 %, 8 % and 10 % w/v for a constant agar concentration of 6 % w/v. The effect of evaporated milk concentration was assessed by including different v/v concentrations of 10 %, 20 % and 30 % (replacing a percentage of the water component) at solutions with fixed concentrations of 6 % w/v agar and 4 % w/v silicon dioxide. For each recipe, the solution was poured in two molds of different thickness (20 and 40 mm) and left to solidify to form the final phantoms, as shown in the photo of **Figure 80**.

10.2.2.2 Ultrasonic attenuation in agar-based gels

The ultrasonic attenuation coefficient of the developed agar-based phantoms was estimated (at 22 °C) using the previously presented experimental set-up (**Figure 78**), but a quite different procedure known as the variable thickness method [96] to

assess which one matches better the acoustic characteristics of brain tissue. The specific method involves comparison of ultrasonic signals acquired through samples of different thickness for estimating the attenuation coefficient (in units of dB/cm) through the following formula [96]:

$$a = \frac{20}{X_2 - X_1} * log\left(\frac{A_{x2}}{A_{x1}}\right) \quad [9]$$

where A_{x1} and A_{x2} symbolize the peak-to-peak voltages in the presence of the thinner (X_1 = 20 mm) and thicker (X_2 = 40 mm) samples, respectively.

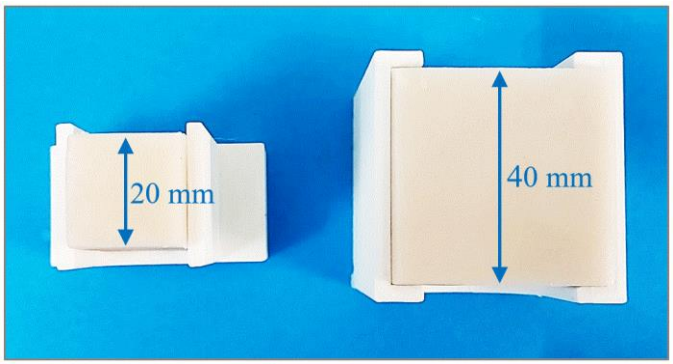

Figure 80: Top view of the thinner and thicker agar-based phantoms.

10.2.3 Thermometry during FUS heating in brain-tissue/skull phantom

The property of the skull phantoms to obstruct the propagation of acoustic waves generated by a single element transducer was evaluated by sonicating the agar-based phantom that was deemed suitable to mimic brain tissue (6 % w/v agar and 4% w/v silicon dioxide). For proper FUS exposures, a special holder was 3D printed to accommodate the focused transducer and the phantom in a water tank, thus ensuring a normal incidence angle. Specifically, the transducer was fixed at the bottom part facing towards the phantom, as shown in **Figure 81**. The holder was geometrically designed to allow horizontal insertion of a thermocouple in the phantom every 5 mm. Therefore, the focal spot was easily located enabling recording of the temperature changes using a thermometer (Omega Engineering).

As illustrated in **Figure 81**, the holder also included a special structure underneath the phantom's location to accommodate the skull sample. Degassed water was poured inside the tank until it reached the top level of the phantom serving as the coupling medium. The transducer was connected to an amplifier (AG1012, AG Series Amplifier, T&G Power Conversion, Inc.) with a build-in signal generator. Sonications were performed with two different single element spherically focused transducers (Sonic concepts, Washington, USA). The first one had a central frequency of 1.1 MHz, radius of curvature of 100 mm, and diameter of 40 mm, whereas the second one had a central frequency of 0.4 MHz, radius of curvature of 70 mm, and diameter of 40 mm. The acoustic efficacy of both transducers was approximately 100 %.

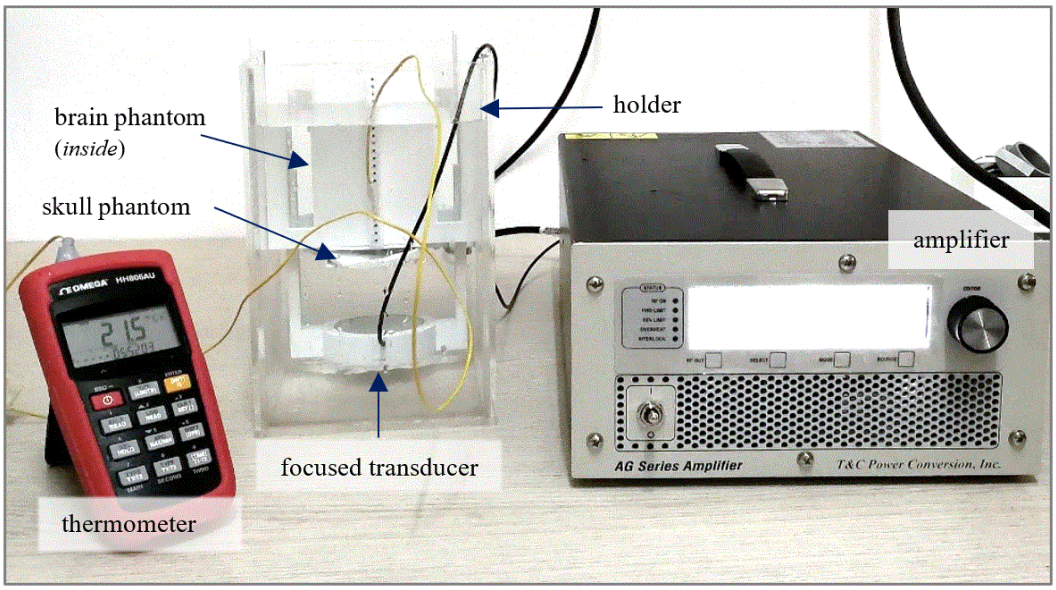

Figure 81: Photo of the experimental setup used to estimate temperature changes in the phantom during heating, showing the designed holder and the location of the compartments.

The distance between the bottom of the phantom and each transducer was properly adjusted so that the focal depth is 2.5 cm for both. Temperature measurements were acquired using a thermometer (HH806AU, Omega Engineering, USA) with a

sampling rate of 1s. Firstly, the temperature evolution during sonication was recorded through water path (without any plastic phantom), and then, in the presence of each skull phantom sequentially. For the sake of comparison, the experiment was also conducted with a 3-mm ABS flat plate inserted in the pathway of the beam.

10.3 Results

10.3.1 Ultrasonic attenuation in thermoplastic samples

The attenuation of ultrasonic waves in the 3D printed thermoplastic samples (5-mm thick solid plates) was estimated using a common transmission-through technique and pulsed ultrasound of 2.1 MHz frequency. The mean attenuation coefficient was estimated at 8.4 ± 0.2 dB/cm for the Resin (Stratasys), at 14.9 ± 0.6 dB/cm for the PLA (3DJ), and at 37.7 ± 1.8 dB/cm for the ABS (Stratasys). The estimated coefficient of the Resin material was considered small compared to the values reported literally for the skull bone [271], [368], [369]. Therefore, the PLA and ABS thermoplastics were used for the construction of phantoms with precise geometry of a human skull, thus more accurately replicating the distortion and attenuation effects of the skull.

10.3.2 Ultrasonic attenuation in agar-based gels

Twelve (12) agar-based phantoms were developed with varying concentrations of agar, silicon dioxide and evaporated milk. The results suggest that the attenuation of ultrasonic waves is enhanced with increasing concentration of each inclusion (agar, silicone dioxide, and evaporated milk). **Figure 82** shows the trend for the gels containing only agar. The corresponding results for the silica- and evaporated milk-doped phantoms are shown in **Figure 83** and **Figure 84**, respectively.

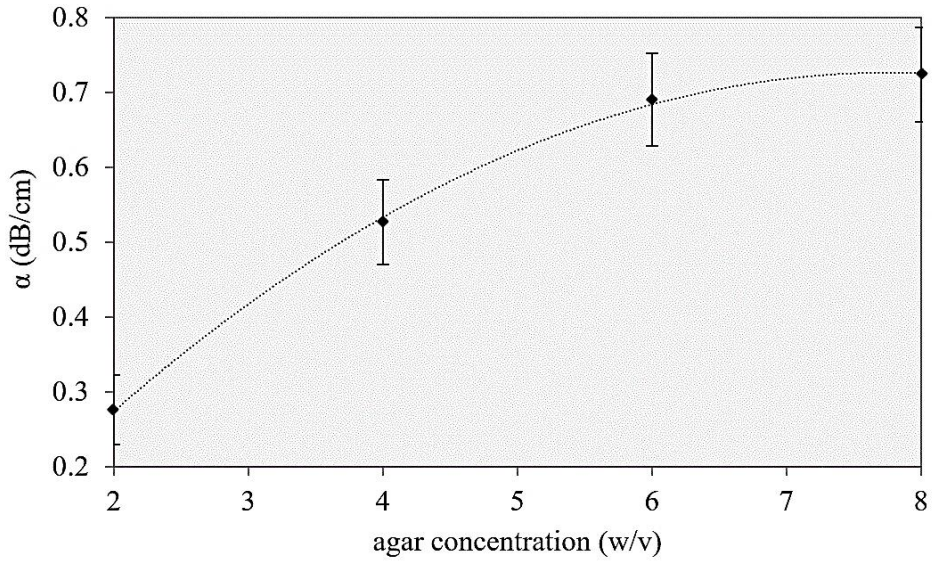

Figure 82: The mean attenuation coefficient (at 1.1 MHz) plotted against the agar concentration. The data points were fitted by polynomial regression. The error bars correspond to the standard deviation.

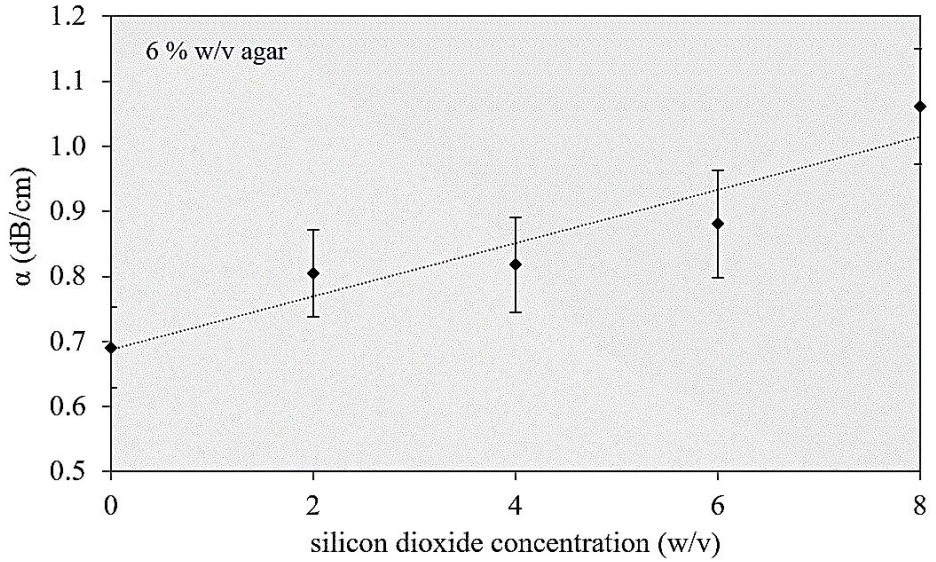

Figure 83: The mean attenuation coefficient (at 1.1 MHz) plotted against the silicon dioxide concentration for a fixed amount of 6 % w/v agar. The data points were fitted by linear regression. The error bars correspond to the standard deviation.

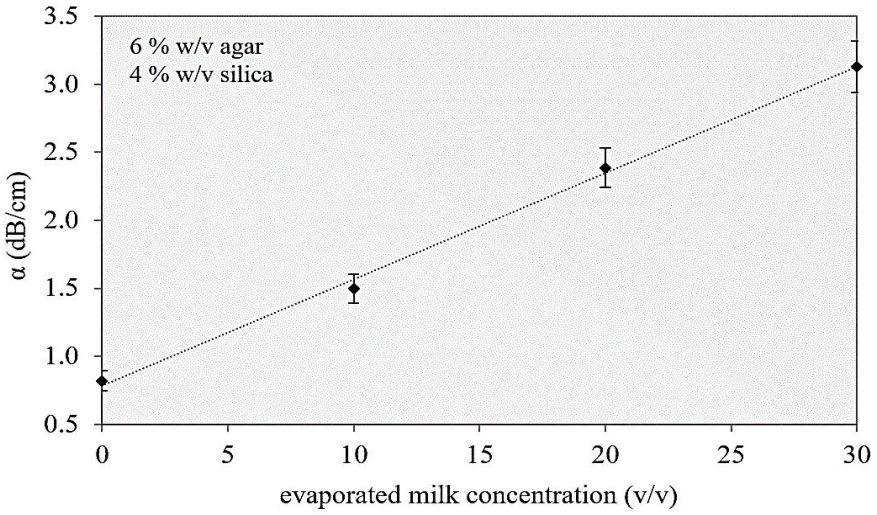

Figure 84: The mean attenuation coefficient (at 1.1 MHz) plotted against the evaporated milk concentration for a fixed amount of 6 % w/v agar and 4 % w/v silicon dioxide. The data points were fitted by linear regression. The error bars correspond to the standard deviation.

The phantom containing 6 % w/v agar and 4 % w/v silicon dioxide was found to possess an attenuation coefficient (0.75 ± 0.06 dB/cm-MHz) in the range of 0.65 - 0.95 dB/cm-MHz reported literally for brain tissues [370] and deemed suitable to mimic brain tissue in subsequent experiments.

10.3.3 Thermometry during FUS heating in brain-tissue/skull phantom

These experiments aimed to assess the feasibility of two single element transducers of different frequency to heat up the soft-tissue phantom through the skull mimics by performing high power sonications. The selected phantom containing 6% agar and 4% silicon dioxide served as the brain tissue mimic. The thermometry data obtained by thermocouple measurements are listed in **Table 9**, including the transducer characteristics and the corresponding temperature changes achieved at the focal depth of 2.5 cm in free field (No skull), as well as in the presence of each skull phantom. The results of sonication through a 3-mm flat sample are also listed for comparison purposes.

Table 9: List of transducer specifications and the corresponding temperature changes recorded using acoustical power of 30 W for 30 s at the focal depth of 2.5 cm with no plastic, as well as with the ABS and PLA phantoms intervening the beam path.

Transducer characteristics			***Thermometry results*** **ΔT (˚C)**			
f (MHz)	**D (mm)**	**R (mm)**	**No Skull**	**PLA skull α ≅ 15 dB/cm**	**ABS skull α ≅ 38 dB/cm**	**ABS flat 3 mm**
0.4	40	70	15.7	1.9	2.7	-
1.1	40	100	24.7	0	0.4	2.2

Figure 85 and **Figure 86** show the corresponding temperature profiles (temperature change versus time) recorded in the phantom using the 0.40 MHz (diameter of 40 mm and radius of curvature of 70 mm) and 1.10 MHz (diameter of 50 mm and radius of curvature of 100 mm) transducers, respectively.

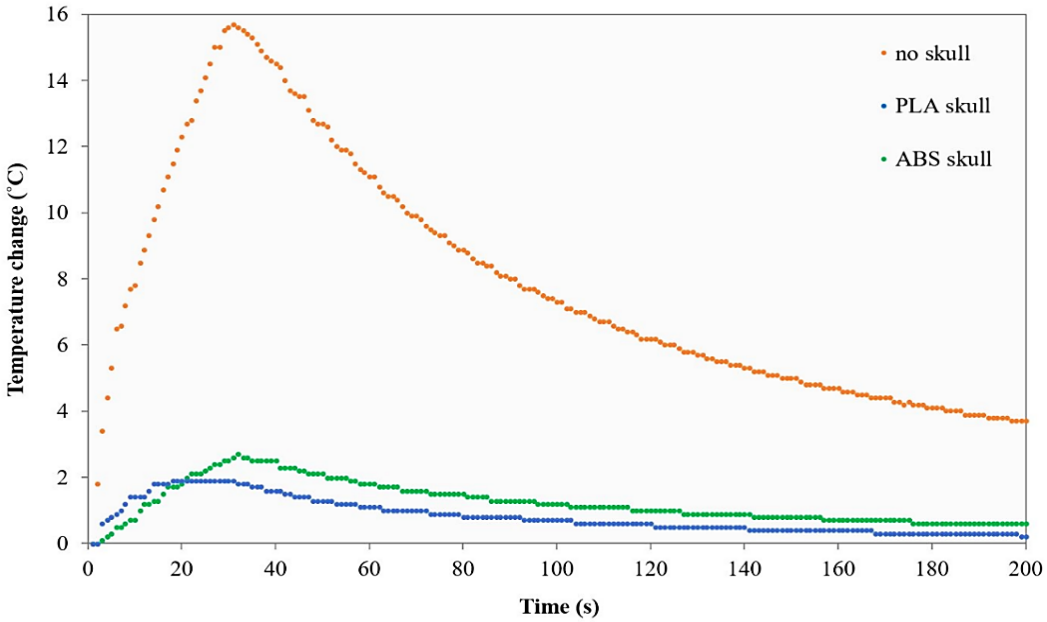

Figure 85: Temperature change versus time recorded in agar-based phantom at focal depth of 2.5 cm during sonication at acoustic power of 30 W for 30 s using the 0.4 MHz transducer (diameter = 40 mm and radius of curvature = 70 mm) with no skull, as well as with the skull phantoms inserted in the beam path.

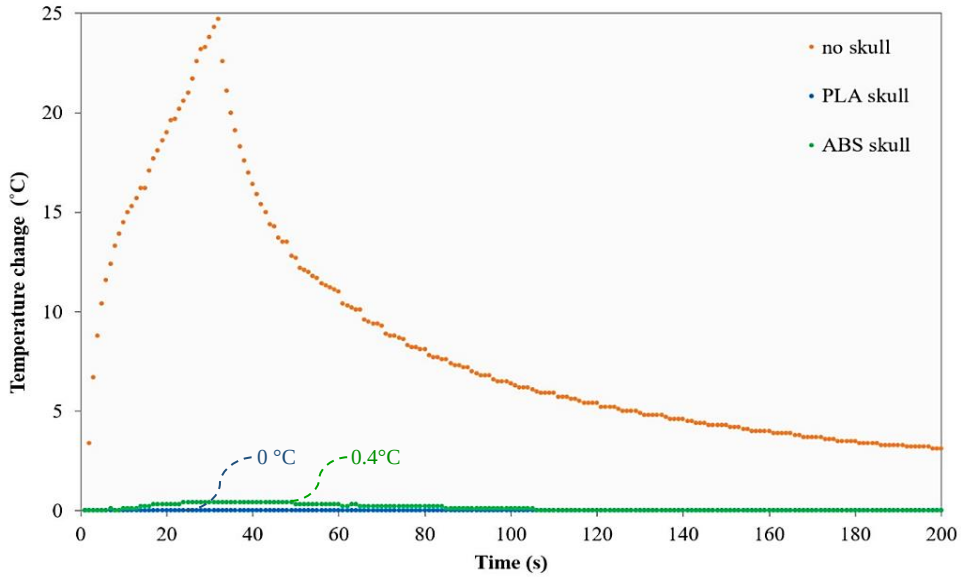

Figure 86: Temperature change versus time recorded in agar-based phantom at focal depth of 2.5 cm during sonication at acoustical power of 30 W for 30 s using the 1.1 MHz transducer (diameter = 40 mm and radius of curvature = 100 mm) with no skull, as well as with the skull phantoms inserted in the beam path.

During sonication, heat absorption was responsible for the temperature rise while conduction decreased the rate of temperature elevation, whereas post-sonication only conduction mechanism remained, thus resulting in temperature reduction. As expected, the temperature change at the focal point is significantly reduced when the ultrasonic waves are obstructed by the skull phantoms.

10.4 Discussion

This section aimed to examine the performance of single element spherically focused transducers in terms of trans-skull heating of tissue. For this purpose, an agar based phantom was prepared to mimic brain tissue, whereas the skull was mimicked by a 3D printed thermoplastic skull model.

The 3D printing technology is continuously gaining popularity as a cost-effective tool for rapid prototyping, offering the ability to design structures of complex

geometry with high precision [94], [371]. In the last decade, it has been increasingly employed for the construction of bone mimicking phantoms using thermoplastic materials [93]–[95], [117], including MRI compatible skull phantoms embedding tissue-mimicking gels or freshly excised tissue [93], [117]. Skull phantoms were initially manufactured with a simplified geometry [117] and later with the precise geometry of a real human skull as extracted from brain CT scans [93]. More recently, a 3D printed skull filled with a phantom mimicking both the vessels and tissue in the cranium has been proposed [249]. These phantoms were designed to match the ultrasonic properties of human skull. Accordingly, in this study, two anthropomorphic skull models were 3D printed using two different thermoplastic materials, which were selected based on transmission-through ultrasonic attenuation measurements.

The longitudinal attenuation coefficient of three common 3D printing thermoplastics was estimated using a transmission-through technique. The estimated attenuation coefficient of the Resin sample (8.4 ± 0.2 dB/cm) was considered small compared to the literature values for skull bone. Ammi et al. [369] report attenuation values in the temporal bone of 13.4 – 22.14 dB/cm at 1 MHz and 34.2 – 48.5 dB/cm at 2 MHz for skulls not presenting temporal bone window insufficiency. Therefore, the PLA and ABS samples with mean attenuation coefficients of 14.9 (± 0.6) and 37.7 (± 1.8) dB/cm were deemed more suitable to replicate the insertion energy loss in human skull bone and used for phantom development. Note that the high ultrasonic attenuation reported for the skull bone is related to the varying thickness, porosity of the cancellous bone and other inhomogeneities, which serve as additional sources of attenuation not existing in thermoplastic samples.

Phantoms were then prepared following accurate geometrical replication of a human skull to account for the defocusing effects induced by the varying thickness of the skull. The skull bone geometry of a male adult was obtained from CT head

scans and a circle shape part was isolated from the temporal region, which constitutes an optimal window for transcranial delivery of ultrasonic energy [369]. Phantoms were 3D printed in solid mode using the selected thermoplastic materials (ABS, Stratasys and PLA, 3DJ).

The approach utilized in this study suffers from the limitation that the candidate thermoplastic materials were only investigated in terms of ultrasonic attenuation. However, thermoplastics were previously proven capable of sufficiently matching the propagation velocity of ultrasonic waves in the human skull as well [152], [249]. Of course, given that in the real scenario ultrasonic waves interact with the complex microstructure of the bone (i.e., multilayer structure including cancellous bone), the proposed phantom constitutes a much simplified model of the human skull. However, since it was 3D printed with the exact geometry of a human skull, beam aberration mechanisms due to the varying skull thickness can be considered consistent between the phantom and real human skull.

Gel phantoms were prepared with varying concentrations of agar, silicone dioxide, and evaporated milk to achieve different levels of ultrasonic attenuation. The attenuation results estimated by the variable thickness methodology suggest that attenuation increases with increasing w/v concentration of agar from 2 to 8% following a second order polynomial (R^2=0.99). The influence of the evaporated milk concentration on the resultant attenuation followed a linear pattern (R^2=0.99). Increasing silicon dioxide concentration also enhanced attenuation, though not in a specific trend. In line with our findings, a positive linear relation between attenuation and concentration of milk was previously reported in the literature [93]. Notably, the role of these inclusions was examined in previous studies, in which silica particles were found to enhance acoustic scattering [156], whereas evaporated milk was proven a key absorber of ultrasonic energy [140].

Phantoms doped with silicon dioxide at concentrations of 2, 4, and 6 % w/v (6 % w/v agar) were found to possess attenuation coefficient values that fall well in the

range of 0.65 - 0.95 dB/cm-MHz reported literally for brain tissues [370]. However, solutions with silica concentrations of more than 4 % undergo rapid solidification and are more likely to contain inhomogeneities. Therefore, the phantoms doped with 2-4 % w/v silicon dioxide were deemed suitable to mimic brain tissue. Since almost equal attenuation coefficient was estimated for both recipes, the one with 4 % w/v silica was selected to be used in subsequent experiments. Moreover, agar/silica phantoms are more stable and durable than milk-doped phantoms.

The heating properties of two single element transducers through the developed skull phantoms were investigated by thermocouple measurements in the brain tissue phantom (6 % w/v agar and 4 % w/v silica). The phantoms were mounted on a specially designed set-up being immersed in degassed water for proper ultrasonic propagation. Thermal profiles at the focus (2.5 cm) were recorded during sonications at acoustic power of 30 W. Absorption was the responsible mechanism for temperature rise in the agar gel, whereas upon deactivation of the transducer conduction-induced heat loss occurred. It is interesting that in the presence of the skull phantoms the thermal profiles presented plateaus where the temperature remained constant for several seconds revealing that the rate of heat deposition was very slow.

Without any sample along the beam's path, the 1.1 MHz sonication caused bigger temperature change (24.7 ˚C) compared to the 0.4 MHz sonication (15.7 ˚C) despite the use of similar acoustic parameters (acoustical power 30 W for 30 s). This is attributed to the fact that the 0.4 MHz beam is wider, and thereby, the produced intensities are lower. In fact, the focusing capability is determined by the transducer characteristics; frequency (f), radius of curvature (R), and diameter (D). Alternatively, when the focal depth and diameter are combined into the f-number ($=R/D$), the focus effect is determined by the f-number and frequency. For single element spherically focused transducers the focal beam diameter (cross section) equals to $\lambda *$ f-number (where λ is the wavelength), thus being proportional to the

f-number and inversely proportional to frequency. For the tested 1.1 and 0.4 MHz transducers, the beam radius at the focal depth equals to about 0.17 cm and 0.33 cm, respectively. Accordingly, the applied acoustic power of 30 W corresponds to focal intensities of 329 W/cm^2 and 89 W/cm^2 for the 1.1 and 0.4 MHz transducers. Therefore, without the skull mimic, the 1.1 MHz transducer results in higher temperature increase at the focus.

Nevertheless, in the presence of the skull phantoms a larger temperature change was recorded using the 0.4 MHz focused transducer. It seems that the phenomenon of scattering is the major factor responsible for this observation. Even though the 0.4 MHz transducer produces a wider beam, it seems that a larger amount of ultrasonic energy propagates through the thermoplastic samples due to the decreased scattering occurring at lower frequencies. Overall, the 0.4 MHz transducer showed better performance in trans-skull transmission. Notably, the use of such low frequencies is widely reported in studies involving non-human primates and large animals [357]–[364] and is driven by the highly aberrating nature of the skull bone. It should be though noted that these studies exploit the mechanical rather than the thermal effects of FUS.

The propagation of ultrasonic waves by single element emissions was blocked to a great degree by the skull phantoms, leading to minimal temperature increase at the focal point. In fact, the focal temperature change in the presence of the skull phantoms was reduced to less than 20 % of that recorded in free filed. This is attributed to the high ultrasonic attenuation occurring in the phantoms, but also to the defocusing effects of the varying thickness that were proven to cause spreading of the beam and focal shifting [246]. Notably, the strong defocusing effects of an ABS skull model were previously demonstrated using MR thermometry in a gel phantom [93] and were associated with a great temperature reduction at the focal region [93]. This is where the phased array approach takes effect.

The specific mechanisms of energy loss through the skull phantoms such as the aforementioned beam defocusing were not explored quantitatively in the current study and may be addressed in a future study. Qualitative assessment was though performed by comparing the temperature evolution during sonication at 1.1 MHz through the ABS skull phantom with that recorded for a flat sample using similar acoustic parameters. With the skull phantom intervening the beam path, a minimal temperature change of 0.4 ˚C was achieved. The flat sample resulted in bigger temperature rise of 2.2 ˚C, confirming that the thickness variability of the skull phantom induced greater energy losses.

Single element transducers were proven efficient for transcranial applications in small experimental animals such as mice [120], [276]–[278] because of their thin skull bone. Furthermore, many studies report successful use of this technology for BBB disruption in non-human primates [357]–[362], whose skull resembles better the human skull. It should be though noted that these applications exploit the mechanical - cavitational effects of FUS rather than the thermal effects. Even in that case, there are many safety concerns, and thus, precise refocusing techniques are needed to compensate for energy losses and focal shifts, thus achieving accurate targeting and sufficient deposition of energy without threatening sensitive brain structures.

Overall, the herein findings confirm the inability of a single element transducer to efficiently steer the beam through the human skull to impart thermal effects to tissue unless a comprehensive correction technique is applied. The phased array technology is still considered the only tool offering optimal deposition of ultrasonic energy in the brain while maintaining the safety levels required in the clinical setting. Recently, the use of 3D printed lenses to compensate beam aberrations while using single element transducers has been proposed [365], [366]; however, further investigation is required to verify these findings and prove the feasibility of this approach.

11 MR thermometry assessment of FUS heating in brain tissue/skull phantom using 1-MHz single-element transducer

11.1 State of the art

As discussed in previous sections, the widespread use of tFUS has been limited for a long period of time by the challenge of accurately delivering the acoustic waves in the brain through the complex skull structure. This issue has been addressed through the development of the phased array technology [19] and the introduction of MRI-based thermometry [9]. Despite the limitations of single-element transducers in terms of beam steering, they remain a valuable tool for neurotherapeutics. In recent years, low intensity tFUS has received significant attention due to its potential as a non-invasive modality for neuromodulation [372]. Successful brain stimulation by delivering low-intensity pulsed ultrasound with single-element transducers has been demonstrated in small animals [373]–[375], non-human primates [376], and humans [377], [378]. Single-element transducers were also proven efficient for BBBD in several animal models, including mice [277], [278], rabbits [356], non-human primates [358], [359], [362]. However, the complex subject-dependent skull geometry makes it difficult to predict the amount of transmitted energy and the exact brain region affected by single-element emissions, thereby raising numerous concerns regarding clinical safety.

Image-guided numerical simulations can be used to predict ultrasonic propagation through the skull and simulate the intracranial field, thus being a valuable tool for correcting the focal point shifting and compensating for energy losses [379]–[382]. Such simulations are typically based on image data from CT or MRI, from which the skull geometry is extracted. Yoon et al. [379] have proposed a finite-difference time domain-based simulation method employing a multi-resolution approach to model the trans-skull propagation of ultrasonic waves from single-element transducers. Performance evaluation in a sheep skull model suggests that the

method can provide on-site feedback on the location, shape, and pressure profile of the focus to the user. This information is possible to allow for adjusting the transducer's location so that the desired pressure levels are achieved at the targeted tissue with sufficient precision. A similar simulation platform was employed by Deffieux et al. [381] in an effort to examine the focalization ability of single-element transducers operating at a low frequency range of 0.3 to 1 MHz through both primate and human skulls in the context of FUS-mediated BBBD. In another study [380], the wave propagation by single-element emissions and the resultant intracranial energy distribution were numerically investigated in a realistic multi-tissue model of the human head to assess the feasibility of low-intensity FUS neuromodulation of the hippocampus. However, it should be noted that simulation-based guidance of tFUS may demand intensive computational resources to enable timely on-site feedback to the user.

Hydrophone-based experimental and numerical measurements were combined by Chen et al. [383], who examined the transmission of FUS from single-element transducers with frequencies of up to 1.5 MHz through human skulls. Interestingly, an exponential reduction in the transmission efficiency occurred with increasing ultrasonic frequency. An innovative virtual brain projection method has been recently proposed as another ergonomic tool for testing the behavior of tFUS beams of single-element transducers and identifying factors that may impact the effectiveness of tFUS therapy in the treatment of neurological conditions [384]. It is also worth mentioning that recently the 3D printing technology was employed in the creation of customized patient-specific holographic acoustic lenses (i.e., 3D printed plastic lenses featuring textured surfaces) to counteract the beam aberration effects induced by the varying skull thickness [365], [366]. Dedicated algorithms and simulation techniques can be used to design the digital model of the lens with the desired textured surface. This method was found to increase the energy accumulation within the targeted region by ten-fold [365], thus holding promise for tFUS thermal therapy using single-element transducers.

Recently, systems incorporating single-element transducers have been proposed for FUS-mediated BBBD under stereotactic targeting and real-time passive cavitation monitoring with the aim of enabling MRI-independent treatment sessions [246], [360]. Pouliopoulos et al. [246] presented a neuronavigation-guided system featuring a 0.25 MHz single-element transducer. Simulation studies and hydrophone-based experiments involving a human skull fragment were performed to assess the transducer's focusing properties. As expected, the insertion of the skull fragment in the beam path resulted in considerable focal shifting and a pressure attenuation of about 45%. A similar approach was followed by Marquet et al. [360], who report successful BBBD of deep subcortical structures in monkeys with a 0.5 MHz transducer. The ultrasonic amplitude of emitted waves was increased based on pressure measurements taken in vitro to compensate for attenuation losses through the scalp and brain [360].

TMPs have been a valuable tool in the early-stage assessment of transcranial FUS applications, in which accurate geometric reconstruction of the skull bone is essential for replicating the defocusing effects caused by the variable thickness and complex structure of the cranium accurately. Experiments were carried out in both simplistic and more-advanced geometrically-accurate skull models using both thermocouple and MR thermometry measurements [93], [117].

Given the recent scientific interest in transcranial FUS therapeutics using single-element transducers and the effort to establish techniques for overcoming their trans-skull steering inability, this sections presents key findings on the feasibility of delivering FUS in a realistic brain tissue/skull phantom using a 1-MHz single-element spherically focused transducer. FUS sonications were performed through 3D-printed geometrically accurate skull phantoms filled with an agar-based gel mimicking the brain tissue without any means of defocusing corrections. The temperature evolution and thermal field distribution during and after heating were monitored using MR thermometry. Skull phantoms made of two different

thermoplastic materials were employed to assess the effect of ultrasonic attenuation on the thermal effects achieved within the soft tissue phantom. Furthermore, the study examined the feasibility of efficiently delivering FUS to heat up the phantom material through a 1-mm skull mimic. This technique is proposed as a potential novel approach to treat unresectable (i.e., multiple, recurrent, deep-seated, etc.) brain tumors by temporarily replacing the skull with a thin biocompatible insert to enable sufficient penetration and heating at ablative temperatures. Through these experiments, the study aims to provide insights on the practicality of using single-element transducers for tFUS in the context of thermal therapy, also given that so far, ultrasonic transmission has been mostly assessed by numerical simulations.

11.2 Materials and methods

11.2.1 Construction of brain tissue/skull phantoms

Two-compartment skull phantoms were manufactured by rapid prototyping. The skull bone model was extracted by segmentation on CT head scan images of an anonymized female volunteer. A circular piece of the temporal-parietal skull region was isolated, resulting in a two-compartment skull model. The skull model was 3D-printed using two common thermoplastic materials; ABS (Stratasys) and Resin (Stratasys), on the F270 and Object30 Prime 3D printers of Stratasys, respectively. Following further processing and smoothing on the dedicated software of each printer, the phantoms were manufactured with 100% infill. The circular insert had a diameter of 60 mm and an average thickness of about 6 mm.

Another thinner skull mimic was created to account for the effect of the skull thickness on ultrasonic transmission. Specifically, the STL format of the circular skull insert was processed to adjust its thickness to 1 mm through its entire surface. The thin skull mimic was 3D-printed with Resin (Stratasys) material only. The rationale behind investigating the use of a 1-mm skull insert is that by temporarily removing a small skull part and replacing it with a thin biocompatible skull insert,

the FUS ablation of unresectable brain tumors by single-element emissions could be feasible. Accordingly, the benefits of single-element transducers in terms of simplicity and cost-effective over phased array transducers could be exploited through this approach.

The brain tissue was mimicked by an agar-based gel containing a 6 % w/v agar (Merck KGaA) and 4 % w/v silicon dioxide (Sigma-Aldrich). The concentration of these inclusions was proven to impart the desired phantom characteristics for the specific application of thermal FUS studies, including acoustical, thermal, and MRI properties comparable to human tissues [96], [142], [153]. The ultrasonic attenuation coefficient of this phantom was previously estimated at 1.10 ± 0.09 dB/cm-MHz [153]. The process for creating the gel phantom, as previously outlined by Drakos et al. [110], involved dissolving the agar and silicon dioxide powders in water. The agar solution was poured into the skull phantom and allowed to solidify, resulting in the final phantom shown in **Figure 87A**. As shown in **Figure 87B**, the circular skull insert can be easily removed to expose the brain-tissue phantom. **Figure 87C** compares the 1-mm Resin insert with that of varying thickness.

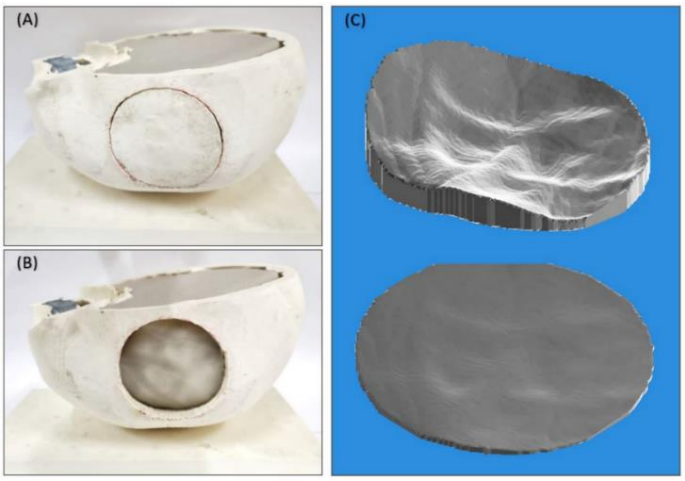

Figure 87: (A) The two-compartment skull phantom filled with the tissue mimicking agar gel. **(B)** The skull phantom with the circular insert being removed from the lateral side exposing the brain tissue phantom. **(C)** Comparison between the 1-mm and varying thickness Resin inserts.

11.2.2 CT imaging of the skull phantoms

Before proceeding to FUS experiments, it was considered essential to investigate the existence of air pores within the phantoms, which may be introduced during 3D printing and affect the propagation of ultrasonic waves considerably. Therefore, the radiographic behavior of the ABS and Resin skull mimics was investigated. CT imaging was performed with a GE CT scanner (Optima 580 RT, GE Medical Systems) using a tube voltage of 120 kV, a tube current of 410 mA, and a slice thickness of 1.25 mm to examine if there were any voids within the Resin and ABS samples.

11.2.3 FUS sonications in the phantom

FUS sonications were performed in the developed phantom with and without the circular skull insert (**Figure 87**) in a 3T MRI scanner (Magnetom Vida, Siemens Healthineers). The FUS transducer employed in the study was made of a spherically focused single-element piezoelectric (Piezohannas, Wuhan, China, f = 1.1 MHz, D = 50 mm, R = 100 mm) with acoustic efficiency of 30 %. The element was hosted in a dedicated MRI-compatible plastic housing. The transducer was supplied by an RF amplifier (AG1016, T & C Power Conversion) located outside of the MRI room through MR shieled cables.

The experimental setup, as arranged on the MRI table, can be seen in **Figure 88**. The brain tissue/skull phantom was submerged in a water tank filled with degassed and deionized water. The FUS transducer was attached to a specially designed 3D-printed holder facing toward the movable part of the phantom (circular insert). The transducer holder was attached on the top edges of the tank. The holder was able to be moved enabling adjustment of the distance between the transducer and phantom. For image acquisition, a multichannel body coil (Body18, Siemens Healthineers) was fixed on a dedicated support structure above the phantom. Caution was given

not to include the transducer within the coil's detection area to avoid interference and signal loss [339].

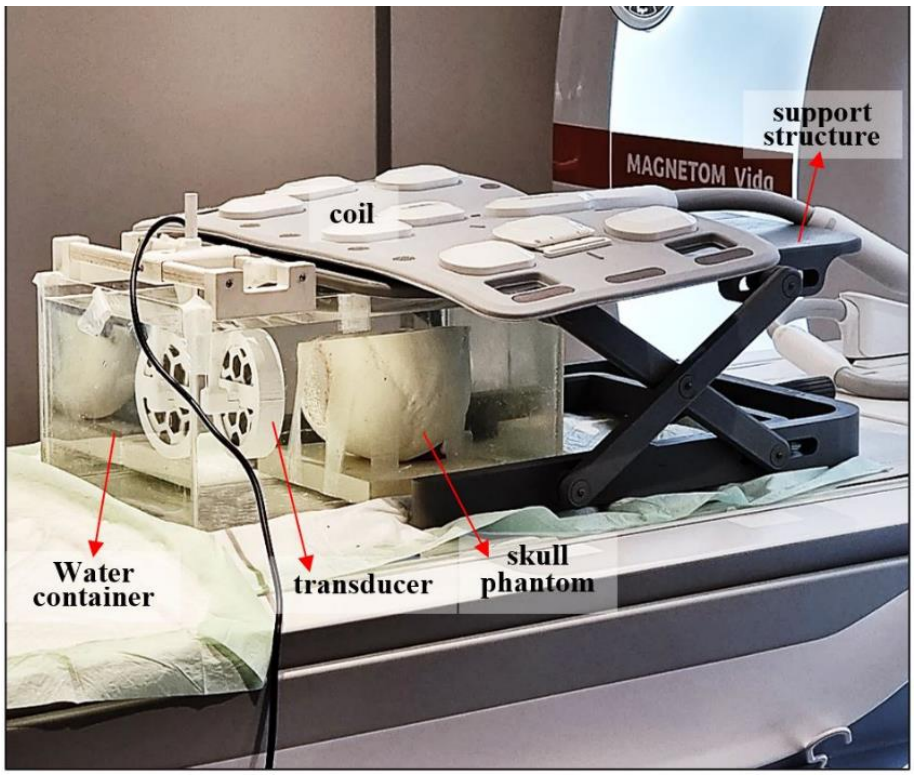

Figure 88: Photo of the experimental setup for FUS sonications in the brain tissue/skull phantom as arranged on the MRI table of the 3T scanner, with the various components indicated.

For all reported experiments, the distance between the transducer and phantom was adjusted so that the focal depth is 40 mm. Continuous FUS was applied at acoustic power of 90 W for 60 s. The corresponding focal intensity was calculated as the acoustic power value divided by the beam area where the ultrasound energy is concentrated (i.e., cross-sectional area at the focal point; πr^2), equalling to 1583 W/cm^2. Notably, the focal beam diameter is typically calculated by the structural characteristics of the transducer, as $\frac{\lambda R}{D}$, where λ is the wavelength (defined by the operating frequency and speed of sound in the medium).

The temperature evolution during sonication and having a 60-s cooling time was monitored using MR thermometry. The PRFS method [9] was used for calculating the temperature changes in a ROI set within the phantom according to **Equation 3**. The magnitude of α was set at 0.0094 ppm/ºC [232], [233].

The temperature changes in the ROI were calculated based on a pixel-by-pixel analysis of the phase differences. Coronal and axial thermal maps were derived from 2D FLASH images acquired with the following parameters: TR = 25 ms, TE = 10 ms, FOV = 280×280 mm^2, slice thickness = 3 mm, NEX = 1, FA = 30º, ETL = 1, matrix size = 96 x 96, pBW = 250 Hz/pixel, and acquisition time/slice = 2.4 s. Colour maps were produced by colour-coding the measured temperatures from the minimum to the maximum value from yellow to red.

11.3 Results

Indicative CT images of the two skull mimics made of ABS and Resin are presented in **Figure 89**, revealing the presence of some air-filled pores within the ABS sample. On the contrary, the Resin sample appears completely solid. This finding was useful in interpreting the results of the follow-up FUS experiments.

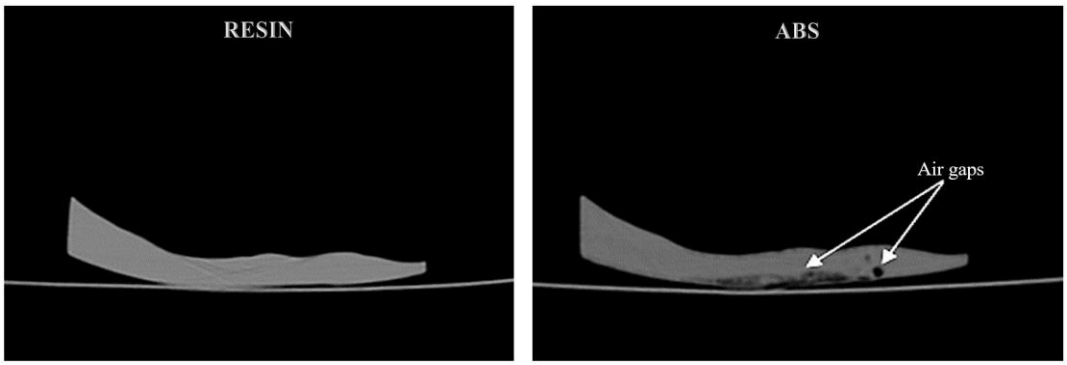

Figure 89: CT images of the Resin and ABS samples acquired with a tube voltage of 120 kV, current of 410 mA, and a slice thickness of 1.25 mm.

The results of FUS sonications are summarized in

Table 10, along with the ultrasonic attenuation coefficients for the Resin and ABS thermoplastics, as measured using a common transmission-through immersion technique [385].

Note that a single 60-s sonication at acoustic power of 90 W, corresponding to a focal intensity of about 1583 W/cm^2, without any obstacle in the beam path (free field), as well as through the 1-mm Resin insert, heated up the agar-based material from room temperature up to ablative temperatures (> 60 ºC). In fact, sonication in free field resulted in a maximum recorded focal temperature of 93 ºC. Indicative thermal maps acquired at various time spots during and after heating without any obstacle intervening in the beam path are shown in **Figure 90**.

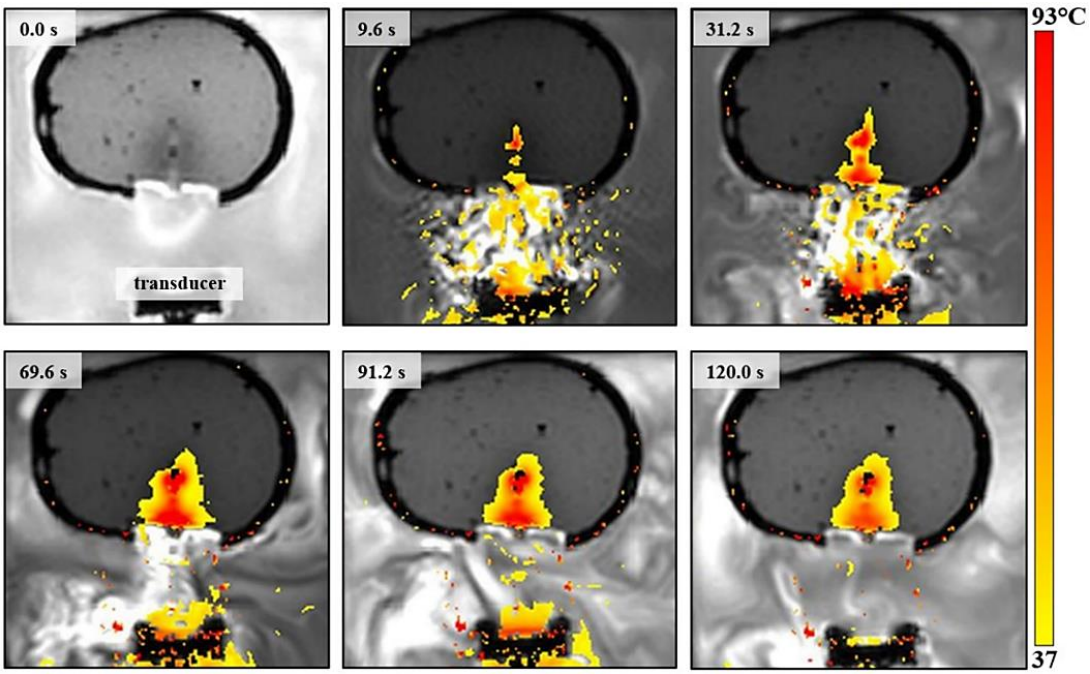

Figure 90: Coronal thermal maps derived from FLASH images during sonication in the phantom at acoustic power of 90 W for 60 s at a focal depth of 40 mm, without any obstacle in the beam path.

Table 10: The focal temperature change (ΔT) recorded in the phantom using acoustical power of 90 W for 60 s at a focal depth of 40 mm with no plastic, as well as with the ABS and RESIN skull mimics intervening the beam.

Skull phantom	Thickness (mm)	ΔT (ºC)	Ultrasonic attenuation (dB/cm)
NO	-	55	-
ABS	6 (average)	1.8	37.7 ± 1.8
Resin	6 (average)	9.7	8.4 ± 0.2
Resin thin	1	33	

The corresponding results for similar sonications through the ABS and Resin skulls (of varying thickness) are shown in **Figure 91**. Note that the ultrasonic waves were strongly blocked by the ABS skull resulting in zero temperature increase within the phantom volume. Conversely, detachable heating was observed in the case of the Resin skull, with the baseline temperature of 37 ºC increasing to almost 47ºC at the focal area but remaining at hyperthermia levels.

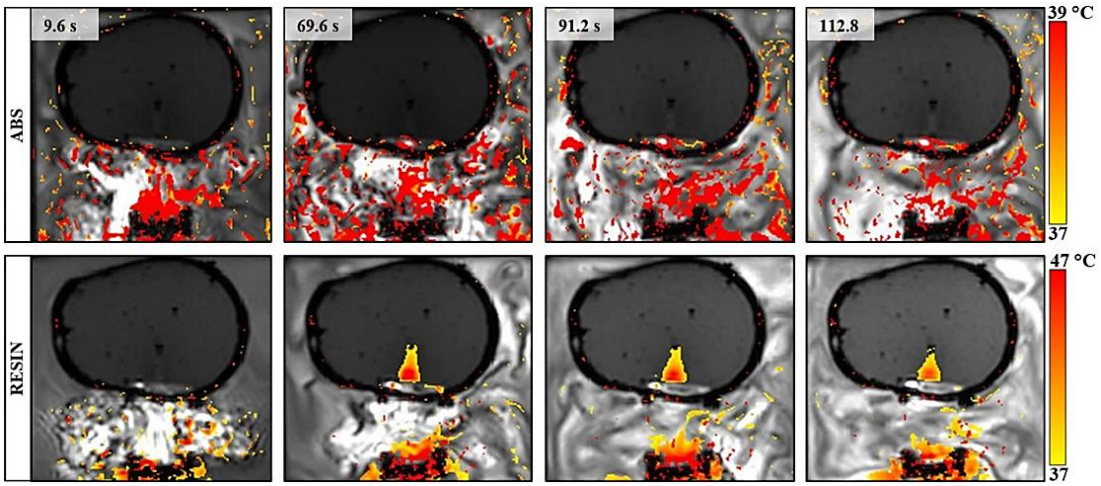

Figure 91: Coronal thermal maps derived from FLASH images during sonication at acoustic power of 90 W for 60 s at a focal depth of 40 mm through the ABS and Resin skull inserts.

Note also that heating through the ABS sample resulted in a slight temperature rise of 1.8 ºC in the phantom adjacent to the skull mimic surface interfering with the beam, revealing a negligible heat accumulation in the region.

The use of a thin skull phantom of 1 mm thickness provided significantly better results in terms of trans-skull ultrasonic transmission and heating of the phantom material compared to the thick one. The temperature profile of **Figure 92A** reveals a maximum focal temperature of 70 ºC, compared to that of 47 ºC achieved by sonication through the varying thickness Resin skull. **Figure 92B** presents indicative thermal maps acquired in both axial and coronal planes, showing efficient beam penetration and heating of the phantom material at ablative temperatures.

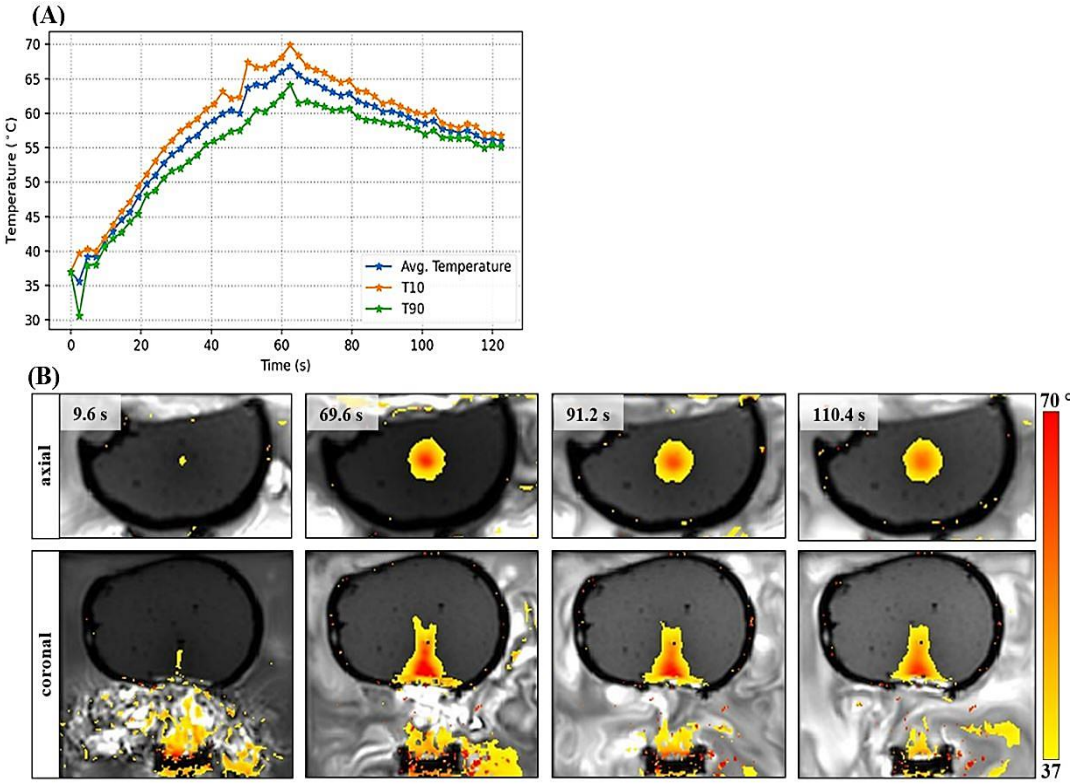

Figure 92: (A) Temperature increase versus time during phantom sonication throught the 1-mm Resin skull at acoustic power of 90 W for 60 s at a focal depth of 40 mm. **(B)** Indicative axial and coronal thermal maps acquired during sonication.

11.4 Discussion

In the current section, the heating capabilities of a custom-made 1-MHz single-element spherically focused transducer through geometrically accurate skull phantoms embedding a brain-tissue mimicking material was examined based on MR thermometry measurements. The study further provides insights on the feasibility of precisely delivering FUS through a skull mimic of 1-mm thickness as a potential method for the treatment of unresectable brain tumors.

A single FUS sonication at focal acoustic intensities close to 1580 W/cm^2 for 60 s in free field heated up the agar phantom to ablative temperatures. Ablative temperatures were also produced in the case of the 1-mm Resin insert, which allowed efficient ultrasonic penetration. The focal temperature change was reduced to 60 % (ΔT = 33 ˚C) of that achieved without any obstacle in the beam path (ΔT = 55 ˚C). These findings are consistent with what has been observed in prior animal research, where tFUS at frequencies close to 1 MHz was established as an efficient modality for applications in small animal models, such as mice and rabbits [278], [356], whose skull thickness is comparable to that of the thin Resin insert. In this regard, single-element transducers may also be effective for therapeutic applications in toddles through the temporal bone, which is in the order of 2 mm in thickness [386], thus potentially constituting an effective acoustic window.

On the contrary, in the presence of the varying thickness Resin insert the temperature change was decreased to about 18 % ($\Delta T \approx 10$ ˚C) of that achieved in free field, whereas no heating was detected in the phantom bulk during sonication through the ABS skull. Being consistent with prior research, these findings validate that single-element transducers are incapable of effectively directing the beam through the human cranium to cause thermal heating of brain tissue unless a thorough correction method is implemented.

The Resin and ABS phantoms showed a completely different response to FUS heating. Since the defocusing effects of the varying skull thickness are considered similar for the two phantoms, this difference can be attributed to the higher ultrasonic attenuation (Table 1) and porosity of the ABS material. In fact, investigation of the radiographic behavior of the two thermoplastic materials revealed air gaps within the ABS sample. The ABS phantom was manufactured using the FDM method, which constitutes a thermal technique that naturally incorporates pores into the manufactured specimens, thus unavoidably enhancing ultrasonic attenuation within the phantom's interior.

There are several energy loss mechanisms affecting the ultrasonic propagation through the real skull. Intense reflections of the propagating waves occur at the interface between the skull bone and outside fluid [271], [387]. Within the skull bone, the acoustic wave is strongly scattered due to its interaction with the internal microstructure of the skull with conversions between longitudinal and shear modes taking place [271], [387]. The bone also absorbs some of the wave energy, which it then transforms into heat. Despite the complexity of quantifying the energy loss induced by each individual attenuation mechanism, it has been shown that the primary causes of attenuation are reflection, scattering, and mode conversion, whereas absorption is responsible for only a small part of the total attenuation [387]. On the contrary, in soft tissues, the wave attenuation is mostly caused by the absorption and conversion of ultrasonic energy into heat. Accordingly, the skull-induced spreading and defocusing of the beam reduces the penetration depth and energy deposited in tissue significantly.

The current study did not investigate the individual energy loss mechanisms occurring during propagation of ultrasonic waves through the skull phantoms. This area of investigation could be the subject of a future study. However, the study did perform a qualitative evaluation on the effect of the varying skull thickness on ultrasonic transmission and intracranial energy distribution. Although both Resin

skulls allowed for sufficient beam focusing within the phantom, FUS sonication through the thin skull insert generated significantly higher temperatures (50 %), heating up a larger phantom area. Furthermore, a reduction in the beam's penetration depth was observed in the presence of the varying thickness insert, confining the heating in a narrower and shallower area of the phantom. These observations can be attributed to the acoustic aberration induced by the varying skull thickness, causing considerable energy losses and focal spot shifting [246].

An important consideration related to the highly aberrating nature of the human skull is the potential for thermal injuries of the skull and adjacent healthy tissues [368], [387]. The PRFS-based MR thermometry method employed in this study does not allow for measuring the skull heating directly [9]. This method relies on the detection of temperature-induced changes in the resonance frequency of water protons, and thus, a large number of protons is needed to create strong MRI signal for high quality imaging and the production of thermal maps [9]. Similarly, temperature monitoring within the thermoplastic materials that do not contain sufficient water protons is not feasible. However, the specific thermometry method can be used for monitoring the heat accumulation adjacent to the skull to assess potential damage of brain tissue [388].

In this study, there was evidence of a slight heat accumulation around the ABS skull insert. Specifically, a marginal temperature change of 1.8 ˚C was produced close to the skull. In the real scenario, it is expected that the complex porous structure of the cranium will more strongly attenuate the acoustic waves, potentially confining them within the skull bone, thus raising the safety concern of unwanted skull heating [389]. In this regard, an apparent limitation of the proposed skull model is its solid infill, which makes it a very simplistic model in comparison to the real cranium consisting of both cortical and cancellous bone compartments. Notably, studies have showed that during trans-skull heating, active cooling of the skull surface is essential to protecting the bone and surrounding tissues from thermal damages

[387]. In addition, the transmission efficacy can be enhanced by selecting a proper transducer frequency, further contributing to the mitigation of such risks [383].

Phased array ultrasonic transducers are predominantly used in the context of clinical tFUS since they allow for targeting deep brain regions with the required precision to produce the desired therapeutic effects without harming healthy tissue, thus meeting the clinical requirements [390]. They also contribute towards delivering the ultrasonic energy over a large skull area, thus reducing the possibility for excessive heat accumulation in the skull [391]. However, it could be argued that their main limitation compared to single-element transducers is their increased complexity and expensiveness, as well as the need to use advanced signal processing algorithms to control the individual array elements [390].

The present findings provide initial evidence on the feasibility of the proposed approach of treating recurrent, multiple, or deep-seated brain tumors that cannot be removed surgically by FUS ablation through a 1-mm biocompatible skull insert. Temporal replacement of a small skull part with a 1-mm skull mimic is expected to allow the development of high temperatures of up to 90 ^{o}C within the tumor and repeated therapies to be performed. This approach exploits the unique advantages of single-element transducers (less expensive, more ergonomic, etc.) over phased arrays, thus addressing the concerns regarding insufficient trans-skull ultrasonic penetration and focal temperature increase. These benefits come at the cost of performing a small craniotomy, which is still far less invasive compared to the standard surgical therapy. Remarkably, the highest temperatures achieved through intact skull with phased arrays have been so far limited to around 60 °C [392]. Overall, a more comprehensive preclinical experimentation is required to demonstrate reproducibility of these promising results and the clinical potential of the proposed approach.

12 Robotic device for transcranial FUS applications in small animal models

12.1 State of the art

Penetration of the BBB to deliver medication into the brain is a subject that has aroused the interest of many research groups. The techniques available so far are not very effective. The BBB, which is the body's defense against toxic substances, also provides resistance to the supply of therapeutic agents. Therefore, the provision of medication to the brain is a main problem to overcome. In this regard, FUS seems to be an alternative completely non-invasive method that can enhance treatment against neurodegenerative diseases [393].

It has been shown that opening of the BBB can be achieved with the use of therapeutic ultrasound and the administration of MBs [394]. This process is reversible, thus maintaining the ability of the brain to stay protected against harmful substances. Specifically, application of pulsed FUS induces various mechanical phenomena in tissue, which in synergy with MBs, loosen the endothelial cell connections allowing medication to reach the brain [395]. This method is targeted since the ultrasonic energy is focused at a specific area of the brain, thus reducing the risk for complications from the process [396]. The relaxation of the endothelial ligaments is completely reversible, with complete recovery occurring within a few hours after the treatment [356]. Since low intensity FUS is used, the temperature remains at safe levels.

The application of this method for disrupting the BBB has been tested in various animal models, mostly mice and rats [397]–[399]. Due to their small size, mice are easier to handle and allow the use of more economical infrastructure, compared to larger animals. However, their small size also appeared to be a challenge in terms of accurate targeting in the laboratory environment, where MRI feedback is not

available. For this reason, various experimental devices have been used by several research groups involved in the field to facilitate studies in small animal models.

The team of Konofagou did a remarkable work in the field using a 3-axis robotic system (Velmex Inc., Lachine, QC, Canada) [120], [276], [400], [401]. The FUS transducer was attached to the positioning system, as well as to a water-filled cone. Another water tank featuring an acoustic opening at the bottom was used [120], [276], [400], [401], and coupled to the mouse head using ultrasound gel [402]. The water tank was stable allowing the transducer as integrated with the water-filled cone to move inside the tank relative to the target, without affecting the coupling with the mouse head. Notably, the team of Hynynen [356] proposed a manual mounting system. The mouse was placed in the supine position above a water container. The transducer was positioned in the container under the mouse head and acoustic coupling was achieved using a bag filled with water. Similar experimental setups as the ones described above with some modifications were used in relevant studies [403]–[406].

There are also systems available in the market that were developed for research activities. An example is the PK50 system offered by the FUS Instruments company (Toronto, Canada). The system has 3 DOF for transducer positioning [407]. This company also offers another mounting device with 3 DOF, which approaches the target from the bottom (LP100, FUS Instruments, Toronto, Canada) [407]. Another company that offers robotic devices for research purposes is Verasonics (Kirkland WA, USA) [408]. The company owns a robotic system with 2 DOF, where ultrasonic coupling is achieved using a water filled bladder. The guidance of the system is achieved with diagnostic ultrasound [408]. Image guided therapy is another company in the field, which manufactures robotic systems compatible with MRI. This company offers 2 different robotic systems featuring 5 DOF [409]. These systems are intended for various therapeutic ultrasound applications. However, they are complex and thus not ergonomic, especially for small animal experiments [409].

The company Sonovol focuses on imaging modalities for preclinical applications [410], but it also offers a preclinical device for FUS applications guided by three-dimensional ultrasound combined with acoustic angiography. The system was designed to assist research with therapeutic ultrasound, given that fusion of ultrasound imaging and angiography can be beneficial for guiding BBBD. Notably, the system offers a wide field of view combining the two imaging modalities.

Robotic-assistance was introduced in many studies to improve the accuracy of ultrasonic targeting [411], [412]. As an example, Kujawska et al. [413], [414] developed a computer-controlled robotic system with 4 DOF for FUS ablation preclinical studies. The 4 DOF positioner is attached on a water-filled tank to maneuver a dedicated platform that carries the target relative to the FUS transducer, which is fixed coaxially with an ultrasound imaging probe on the bottom of the tank facing towards the underside of the target.

There is an increasing demand for preclinical robotic devices, as various FUS applications are continuously being developed and should be investigated to demonstrate the accuracy and repeatability needed for their clinical translation. Preclinical devices are the most cost-effective solution because medical certification is not necessary. Although numerous devices with different functionalities have been developed and tested so far, more simplistic and ergonomic devices dedicated for small experimental animals would be of great usefulness in accelerating research in the field.

In this section, we propose two systems dedicated to maneuvering a single element FUS transducer for preclinical research in small animal models. The first system had the ability to maneuver the transducer in two dimensions. The operation of the system is simplistic since all the moving parts are placed in a single water tank that includes an acoustic window on the top. A target supporting platform was specially designed to securely position rodents above the ultrasonic source. The second system was built to simplify targeting given the very small size of the mouse head

and offer improved ergonomics. In this version, the mouse is placed in the more stable prone position on a flat platform, with the transducer reaching the head with a top to bottom approach. In fact, the transducer is located inside a cone that is acoustically coupled to the mouse head using ultrasound gel. With this design, the administration of anesthesia is more flexible.

Both devices were made MRI compatible. Even though the two devices were primarily developed for laboratory use, MRI compatibility is important since it allows for treatment planning and accurate targeting in the MRI setting, as well as confirmation of BBBD by contrast agent enhanced imaging directly after treatment. Furthermore, the two devices were engineered in a way that ensures ease of use, with adjustment tools to suit the different species. Especially for very small animals such as mice, the accuracy benefits of the proposed experimental setup are of high importance.

12.2 Materials and methods

12.2.1 FUS setup

A custom-made FUS transducer was manufactured in-house using a single piezoceramic element (Piezo Hannas Tech Co. Ltd), with a radius of curvature of 80 mm, an active diameter of 50 mm, and an operating frequency of 1 MHz. A dedicated housing was 3D printed using ASA material on the F270 Stratasys printer having a circle-shaped cavity, wherein the element was soldered. An electric circuit was created and encapsulated with epoxy, which serves as electric isolator and simultaneously as a backing material preventing excessive vibration of the element and improving the acoustic performance of the transducer. The acoustic efficiency of the transducer was experimentally determined at 33 % by the radiation force balance method [415]. Note that the selection of the various transducer components was based on MR-compatibility.

The transducer is tuned to an RF amplifier (T&G Power conversion) and its actuation is controlled via an in house developed software, which allows selection between continuous and pulsed ultrasound sonication. There is also the possibility to set the sonication parameters, such as the electric power, sonication duration, frequency, and duty cycle.

12.2.2 Positioning devices

12.2.2.1 Robotic positioning device V1

A 2 DOF motorized device was manufactured using a 3D printing machine (FDM 270, Stratasys). **Figure 93** shows CAD drawings of the device revealing its components and how they are assembled. The various parts were produced using the FDM technology with ASA thermoplastic. The positioning mechanism maneuveres the proposed transducer in the X and Y linear axes, with a motion range of 60 mm and 130 mm, respectively. Specifically, the rotational motion of two piezoelectric motors (USR30-S3; Shinsei Kogyo Corp.) located outside the water enclosure is converted into linear motion via complex mechanisms located inside the enclosure, as shown in **Figure 93**.

The X axis angular motion is converted into linear motion by a jack screw mechanism. The motor rotates the jack screw that is linked with the X-plate (**Figure 93A**). The rotation of the jack screw in turn causes the X plate to move forward (upon counterclockwise rotation) or back (upon clockwise rotation) along dedicated guides of the X-frame, which has also a supportive role increasing structural rigidity. The pitch of the jack screw is 1.44 cm, meaning that for each complete rotation, the X stage moves 1.44 cm.

The Y axis mechanism involves additional moving parts since the motion has to be delivered at a 90° angle (**Figure 93B**). The motor was placed outside the water container and was connected to a hexagonal drive shaft for transferring the motion to the interior parts. Bevel gears were coupled to the shaft transferring the motion

at 90° (along the Y axis). Bevel gears refers to a type of gears with conically shaped teeth that transmit motion at an angle. The gear rotates the Y axis jackscrew, thus converting rotational motion into linear motion of the Y plate. The angular to linear motion ratio of the X and Y axes is equal, thus establishing uniformity.

The entire mechanism operates within the water container (**Figure 93C**), which is sealed by a cover (**Figure 93D**) having a square acoustic opening on the top. A platform with adjustable plates is fixed to the opening to secure the mouse above the FUS transducer.

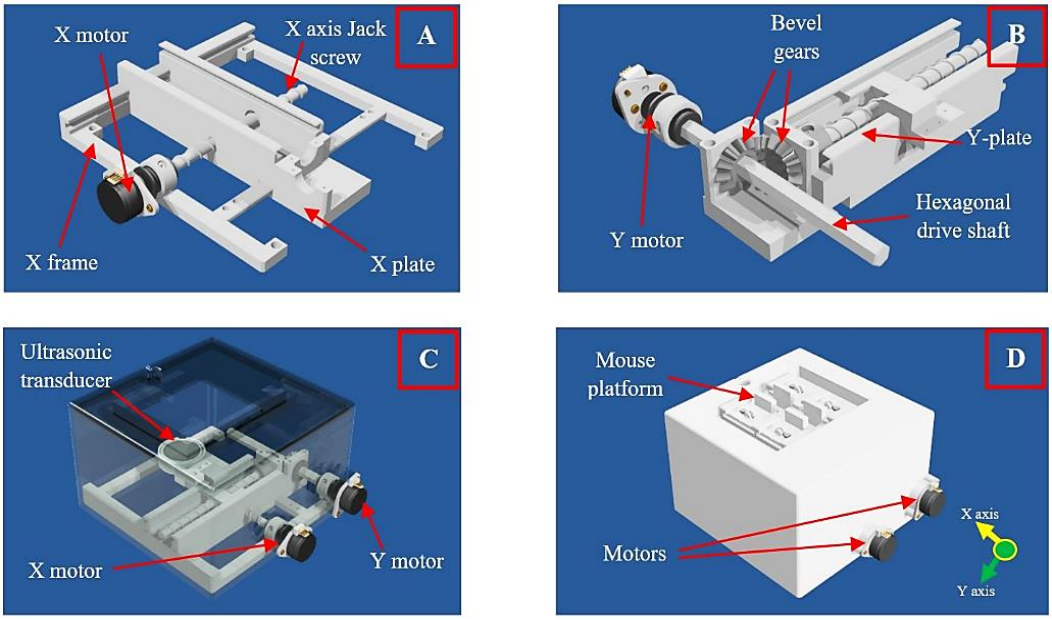

Figure 93: CAD drawings of the **(A)** X-stage, **(B)** Y-stage, **(C)** positioning device with transparent enclosure, and **(D)** positioning device.

12.2.2.2 Robotic positioning device V2

The second version of the device is shown in **Figure 94** and was developed to achieve more efficient ultrasonic delivery in the mouse brain using a top to bottom approach. The main advantage of this approach is the ability to visually confirm proper coupling with the mouse head. Furthermore, this device was made smaller in size, and hence, it is lighter and easier to transport. Another essential benefit of

this version is that intravenous injections and anesthesia administration can be performed without removing the mouse from the device. For these reasons, it is considered more ideal for small animal experiments.

The device was manufactured on a polyjet 3D printing machine (Object30 pro, Stratasys) using resin, which is cured when exposed to ultraviolent radiation. This technology offers high resolution, thus enabling the production of dimensionally accurate parts. The surface finish is also superior compared to the FDM technology where the layer lines are more visible.

This version of the device includes a flat platform where the mouse is positioned. Notably, an absorber was embedded in the center of the platform for minimizing ultrasound reflections. This platform is connected to a frame that includes linear guides for height adjustment via a moving plate (**Figure 94B**). The height adjustment plate carries a conical holder, which was designed to accommodate the FUS transducer (transducer cone in **Figure 94C**).

The height adjustment plate is operated in conjunction with a jack screw having its first side attached to the platform and its second side connected to the top plate. The jackscrew is rotated by an ultrasonic motor (USR30, Shinsei) inducing vertical motion of the height adjustment plate so that the transducer cone can be fixed on targets of different size. Notably, its bottom part is securely sealed with a thin silicone membrane that is held by an O-ring (**Figure 94C**). Upon operation, this cone is filled with degassed-deionized water and is coupled to the target using ultrasound gel for proper ultrasonic transmission.

The transducer was mounted on the upper section of the cone using a special mechanism that enables its manual angulation. Angulation of the transducer is limited by a stop, thus ensuring the alignment of the ultrasonic beam with the acoustic opening (**Figure 94D**). This mechanism allows for easy removal of the air that is usually trapped on the transducer element during filling of the cone with water.

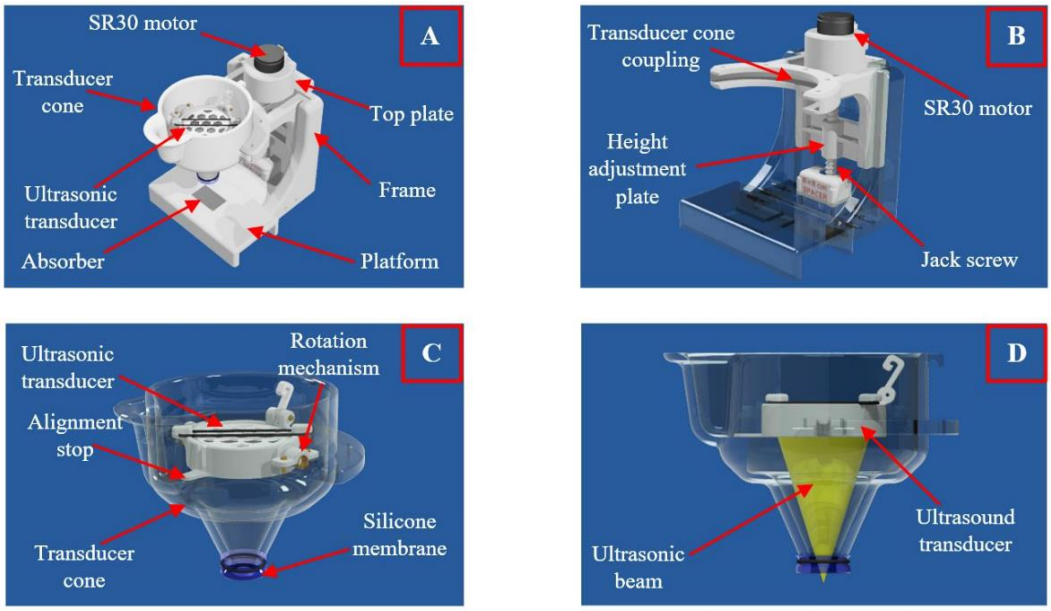

Figure 94: CAD drawings of the **(A)** robotic positioning device V2, **(B)** height adjustment mechanism, **(C)** transducer cone, and **(D)** transducer cone showing the ultrasonic beam.

12.2.3 Power field assessment

The axial and radial power field of the designed transducer operating at its fundamental frequency of 1 MHz was evaluated by FUS field scanning with a hydrophone. A dedicated plastic holder was utilized to accommodate the designed transducer and the needle hydrophone (NH0500, Precision Acoustic, Dorset, UK) in an acrylic tank filled with degassed, deionized water. The transducer was precisely moved along the axial and radial directions by a system of stepping motors (VXM, Velmex Inc, Bloomfield, NY, USA) while the hydrophone was aligned to the beam axis to record the pressure waves at increasing distance from the transducer's surface. The hydrophone signal was displayed on a digital oscilloscope (TDS 2012, Tektronix, Inc.) and the peak to peak voltage recordings were collected. In total, 65 measurements were acquired with 2 mm intervals, in the range of 3 cm to 16 cm from the transducer's surface. At the estimated focal distance, 80

measurements were acquired in radial direction with 0.1 mm intervals. A voltage of 50 mV was applied in each case.

12.2.4 Motion accuracy assessment

The accuracy and repeatability of robotic motion for the two versions of the robot was assessed following a caliper-based method as previously detailed in the literature [144]. Briefly, motion steps of 1, 5, and 10 mm were commanded through the motion commands of the relevant software and compared with the actual displacements as measured with a high-precision digital caliper. Additionally, the speed of motion in each axis was estimated by the activation time of the motion actuators, which is provided by the controlling software and equals to the time needed for the stage to cover the commanded step.

12.2.5 MRI compatibility assessment

The developed robotic devices were then evaluated in terms of proper operation in the MRI environment. Evaluation was carried out in a 1.5 T MRI scanner (GE Signa HD16) by imaging an agar-based TMP (6% w/v agar; Merck KGaA) using the SPGR sequence with the following parameters: TR = 23 ms, TE =16 ms, FA = 35°, ETL = 1, pBW = 45 Hertz/pixel, FOV = 280 x 280 x 10 mm^3, matrix = 128 x 128, NEX = 2, and acquisition time/slice = 7 s. The SNR served as the main tool for assessing compatibility with the scanner and was determined according to **Equation 5**. The following activation states of the positioning mechanism were tested: motor/encoder cable not connected, motor/encoder cable connected, electronic control system energized but no motion command initiated (referred to as: DC ON), and motion command initiated (referred to as: motor moving). Regarding the FUS system, the following states were tested: RF cable not connected, RF cable connected, amplifier energized (zero power applied), and ultrasonic power applied. Electrical power values of 50-200 W were tested.

12.2.6 Feasibility study in mice

Feasibility experiments were conducted in WT mice (1-month old, body weight 10-12 gr) in collaboration with the CING to obtain proof of concept for the first version of the device. All the experimental procedures were approved by the Cyprus Veterinary Service under the protocol number CY/EXP/PR.L05/2021.

Initially, the transducer's location was adjusted to coincide with the circle-shaped opening of the mouse holder (where the mouse head is fixed) through the motion commands of the interfaced software. The mouse head was shaved using hair removal cream. The mouse was then anesthetized with isoflurane (Chanelle Pharm, I-so-vet®, Loughrea, Co Galway, Ireland) following administration of 10 or 20 μL of SonoVue MBs (Bracco Imaging, Turin, Italy) intravenously through the tail vein with a 30G syringe. Once the mouse was sufficiently anesthetized, it was mounted on the device above the FUS transducer in the supine position and immobilized by properly adjusting the holder's handles. The container was filled with degassed-deionized water up to the mouse head to ensure efficient ultrasonic coupling. It is essential to mention that before fixing the mouse to the holder, the transducer was energized enabling visual localization of the beam at the water surface, thus providing an additional reference for mouse positioning. Each mouse received a single sonication using FUS pulses of 10 ms length, applied at a repetition frequency of 1 Hz, for a total duration of 60 s using electrical power of 20 or 30 W.

In total, 6 mice were included in the study. Four (4) mice were treated using MBs-enhanced FUS. The Evans Blue (EB) dye method was used to assess the success of BBBD. Specifically, 5 μl/g of body weight of a 4% EB stain solution (Sigma, St. Louis, MO, USA) was injected intravenously into each mouse immediately after sonication; 30 min before they were sacrificed. One mouse received EB only and another mouse served as the control mouse and received no treatment or EB.

All mice were sacrificed approximately 30 min after the sonication or/and EB administration. Slides containing brain sections were directly visualized using a Nikon eclipse-Ni (Tokyo, Japan) fluorescence microscope to examine the EB extravasation. Furthermore, cryosections from brain were immunostained for fibronectin (DAKO, Glostrup, Denmark, 1:100) and FITC-labeled polyclonal fibrinogen antibody (DAKO, 1:500) to assess the protein leakage into the parenchyma. DAPI staining (Sigma-Aldrich, St. Louis, MO, USA) was used for nuclear localization (blue).

12.3 Results

12.3.1 Power field assessment

Ultrasonic pressure field characterization was performed using a hydrophone. The voltage recordings show a maximum pressure at 7.5 cm indicating that the actual focal spot is slightly shifted towards the transducer's surface. The axial pressure profile approximately followed a gaussian distribution with a full width half maximum (FWHM) of about 10 mm around the focus location (half pressure length). Accordingly, the radial pressure profile at the estimated focal distance of 7.5 cm also followed a gaussian distribution around the central axis, which is characterized by a FWHM of about 4 mm (half pressure width). These measurements provide good indication of the focal spot size.

12.3.2 Motion accuracy assessment

The motion error decreased with increasing motion step, with a maximum mean positioning error of 0.08 ± 0.03 mm for both versions of the robot. For the first version, the speed of motion was estimated at 9.90 ± 0.12 mm/s and 11.07 ± 0.17 mm/s in the X and Y directions, respectively. Regarding the second version of the robot, the Z-stage was found to move with a speed of 8.65 ± 0.08 mm/s.

12.3.3 MRI compatibility assessment

The bar charts of **Figure 95** and **Figure 96** reveal how the SNR of SPGR images of the phantom is affected by changing the activation status of the system. The bar chart of **Figure 95** shows the SNR estimations with the positioning mechanism being at different activation states. The greatest SNR reduction occurred when the ultrasonic motor was moving during image acquisition.

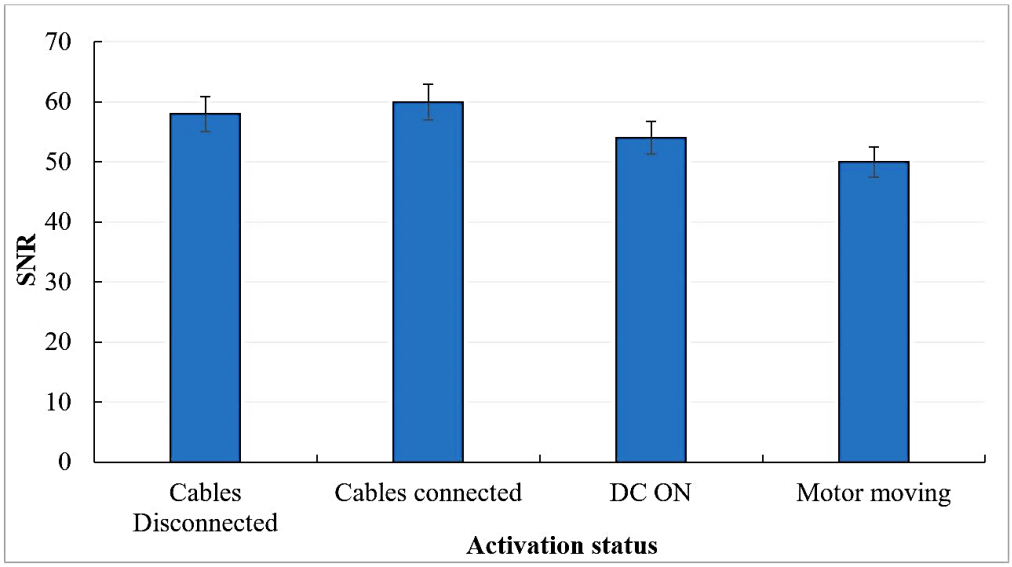

Figure 95: Bar chart of the SNR of SPGR images of an agar phantom acquired for different activation states of the robotic device. Error bars represent the standard deviation of mean.

The corresponding results for the FUS transducer are shown in **Figure 96**, which shows a gradual SNR reduction with increasing electric power from 50 to 200 W, most probably owing to the increasing target vibration. The MR compatibility was tested for version 1, which represents the worst case since it accommodates two motors.

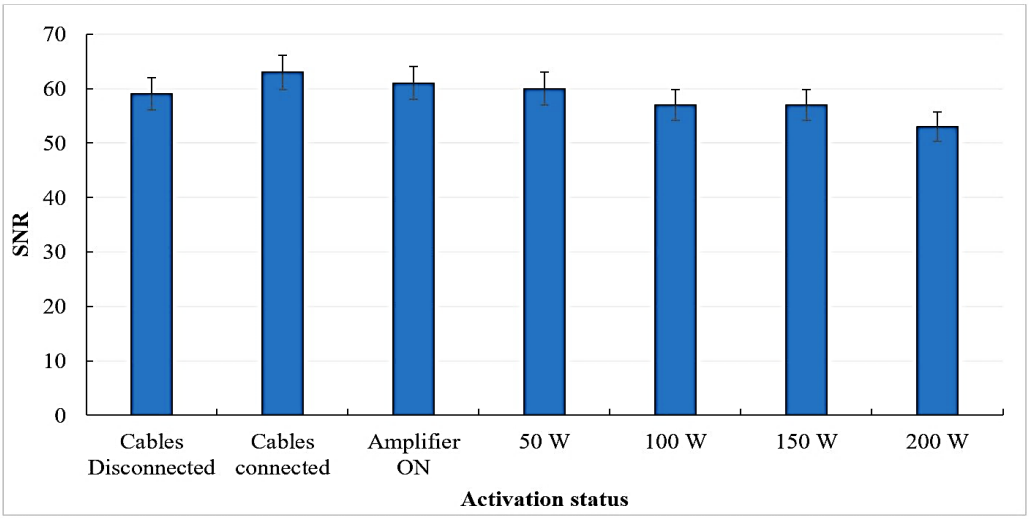

Figure 96: Bar chart of the SNR of SPGR images of an agar phantom acquired for different activation states of the FUS transducer. Error bars represent the standard deviation of mean.

12.3.4 Feasibility study in mice

BBB opening was evidenced in all cases (4/4). Representative microscopy photos of EB extravasation in the brain parenchyma adjacent to the lateral ventricles are shown in **Figure 97**. No leakage was observed in the brain parenchyma of the control mouse (**Figure 97A**) and the mouse injected with EB only (**Figure 97B**). EB leakage is clearly visible in red colour in mice treated with FUS in synergy with MBs (**Figure 97C** and **Figure 97D**). Note that the mouse treated with higher acoustic power showed higher levels of EB dye in the brain tissue covering a larger area.

The BBB permeability was also characterized using Fibrinogen and Fibronectin immunofluorescent staining. The mice treated with FUS plus MBs showed higher levels of the protein in all examined brain areas compared to the control mice. Images of fluorescence microscopy from the corpus callosum are presented in **Figure 98**, where the fibronectin is stained green, and the cell nuclei are stained blue.

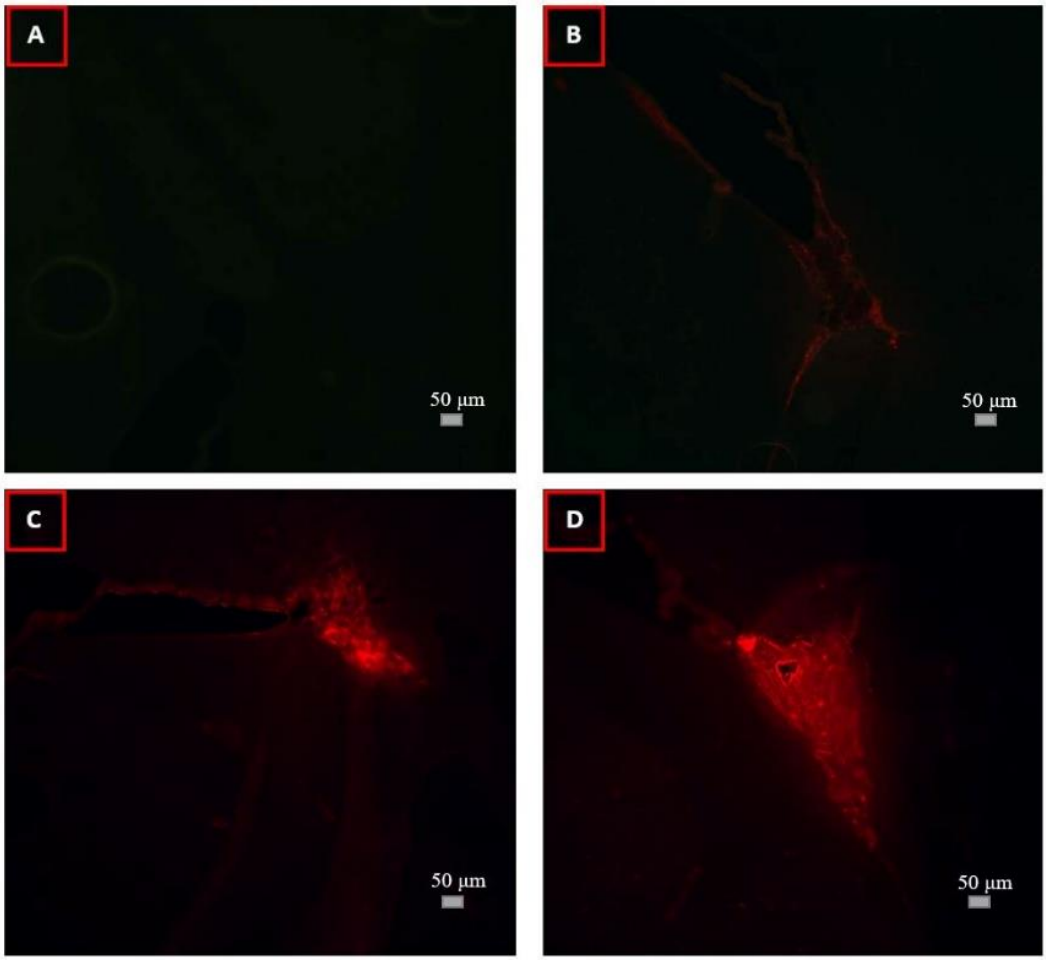

Figure 97: Fluorescence images of unstained brain sections at the level of the lateral ventricles taken from **(A)** a control mouse, **(B)** a mouse injected with EB only, and mice treated using **(C)** 20 W and 10 µl MBs, and **(D)** 30 W and 10 µl MBs (Scale bar: 50µm).

It seems that for the control mouse (**Figure 98A**) and the mouse that received EB only (**Figure 98B**) the protein remained in the perivascular extracellular matrix. On the contrary, in the case of the mouse treated using electrical power of 30 W and 20 µl MBs (**Figure 98C**), the fibronectin leakage is clearly visualized as a diffused green dye in the brain tissue.

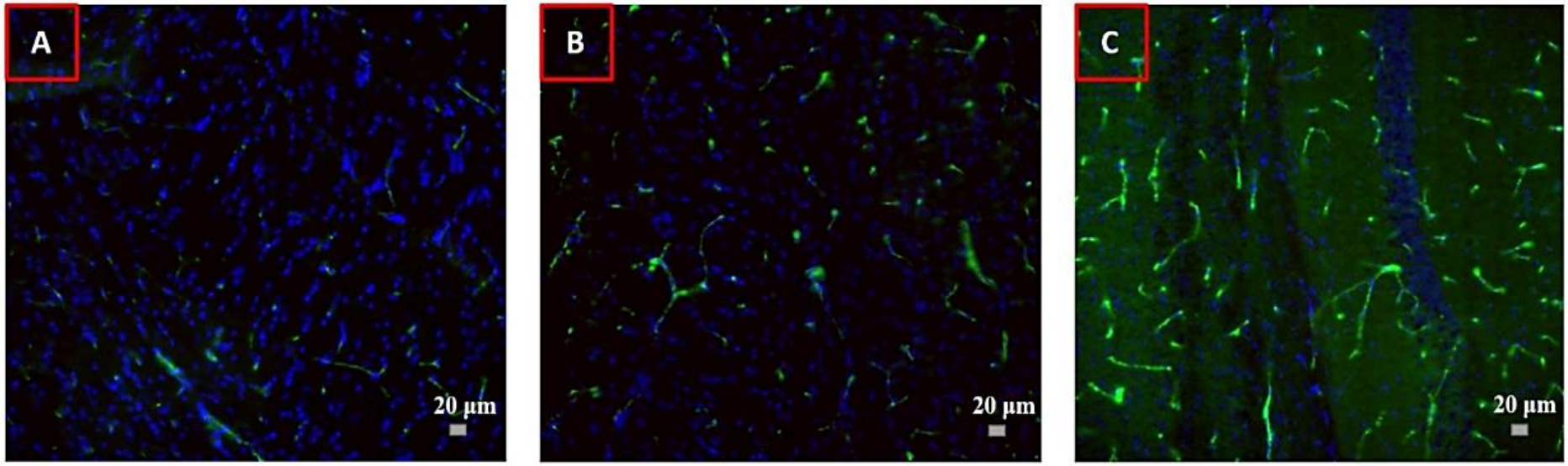

Figure 98: Fluorescence images of immunostained brain sections at the level of the corpus callosum for a **(A)** control mouse, **(B)** a mouse injected with EB only, and **(C)** a mouse treated with 30 W plus 20 µl MBs. The Fibronectin protein is stained green, and the cell nuclei are counterstained blue with DAPI (Scale bar: 20µm).

12.4 Discussion

The current section presents two robotic devices intended to facilitate preclinical research on transcranial applications of FUS in small animal models, such as mice. The specific application of the system is the FUS-mediated BBB opening for the delivery of therapeutic drugs that are normally hampered by the BBB into the brain parenchyma.

The first version of the robotic system was developed with two piezoelectric-actuated motion axes. The mechanical parts and FUS transducer were arranged in a single water enclosure. The rotational motion of the motors located outside the container is converted into linear motion of the respective stages inside the enclosure by jack screw mechanisms. The system incorporates a custom made single element FUS transducer operating at a frequency of 1 MHz. A specialized platform featuring four moving plates with locking levers was designed and fitted in the acoustic opening to safely immobilize rodents of different size and type above the transducer. During operation, the enclosure is filled with degassed water that serves as the coupling medium for proper beam propagation from the transducer to the mouse head.

The FUS transducer was also manufactured in-house using a purchased piezoelectric element that was housed in a plastic case and covered by an epoxy encapsulant. The acoustic efficiency of the transducer was experimentally determined at 33 % by the radiation force balance method. The produced FUS field was scanned using a hydrophone. The collected sound pressure signals were displayed on a digital oscilloscope, thus allowing assessment of the pressure field distribution. The obtained results revealed an actual location of the focal spot shifted at 7.5 cm, compared to the focal distance of 8 cm reported by the manufacturer for the element. This method also provided good indication of the size of the focal spot.

The most parts of the device were developed on a rapid prototyping machine using plastic to avoid interference with the scanner. The MRI compatibility of the developed system was assessed in a 1.5 T MRI scanner by comparing the SNR of SPGR images of an agar-based MRI phantom obtained under different activations of the system. Regarding the positioning mechanism, noticeable SNR reduction was observed when the motion command was initiated (motor moving). Regarding activation of the FUS transducer, the image quality was getting degraded as the output power was increasing, thus resulting in some loss of detail. However, the induced SNR reductions were not considered significant. In other words, all tested activations resulted in SNR values sufficiently high for proper imaging, suggesting that the efficacy of anatomical targeting and MR thermometry is not compromised. It should be though noted that since activation of the various components requires the use of electricity, the system is classified as MR conditional (ASTM standards).

The feasibility of the system in opening the BBB of small animal models using pulsed FUS in synergy with MBs was examined in WT mice. The mouse platform provided proper immobilization of the mouse in the supine position. Targeting was though proven challenging due to the inability to directly visualize the exact location of the transducer relative to the mouse brain. However, promising results were obtained indicating successful opening of the BBB. Specifically, EB leakage in the brain parenchyma was clearly evidenced in microscopy images of brain cryosections only in the case of mice treated with FUS in synergy with MBs. It is interesting to note that the mouse treated with higher acoustic power showed higher levels of EB dye diffusing through a larger brain area. The BBB permeability was also confirmed by Fibronectin and Fibrinogen immunofluorescent staining. Again, the FUS treated mice showed higher levels of the protein in all examined brain areas, whereas for the control mouse the protein remained in the extracellular matrix.

Some issues identified during these preliminary experiments led to the development of a second improved version of the system. The first system comprises a relatively large water container that has to be filled up to the top so that the animal's head is in direct contact with the water and efficient ultrasonic propagation is achieved. However, the large water volume needed to achieve acoustic coupling makes the device heavy and less ergonomic. It was also observed that this design is prone to water leakage from the acoustic opening. Additionally, targeting the animal's brain in the laboratory setting was proven challenging due to the inability to directly visualize the transducer's location. Another identified limitation relates to the intravenous injections and administration of anesthesia, which cannot be performed properly without removing the mouse from the device.

The second version was designed to address these issues, thus facilitating mice experiments even more. This device uses a top to bottom approach and features motion only in the vertical direction. To be more specific, the FUS transducer was integrated in a coupling cone that can be moved vertically and tightly fit the mouse head. Accordingly, the dimensions of the system were reduced considerably making the device even more compact, lightweight, and ergonomic in its use. A silicone membrane was used to seal to bottom opening of the coupling cone. The membrane unavoidably reduces the efficacy of acoustic coupling. For this reason, it was selected to be thin (0.2 mm) to minimize ultrasonic attenuation. Also, ultrasound gel was applied to displace air and maximize ultrasonic transmission. It is noted that this is a simplified device suitable for single-shot FUS applications. A more advanced device could be developed in the future with the addition of horizontal motion stages, thus enabling sequential placement of the transducer at multiple brain locations, but at the cost of increasing size and complexity.

Additionally, in the second version, the top to bottom approach allows the placement of the animal in the prone position that is much more stable, simultaneously offering better immobilization of the mouse and visual confirmation

of proper acoustic coupling. Furthermore, there is no possibility for water leakage from the cone. Finally, since the animal lies in a flat platform, there is direct access for the administration of anesthesia, MBs and contrast agents through needles. An absorbent material was incorporated into the animal platform, thus reducing ultrasound reflections.

It is important to ensure that no air bubbles obstruct the beam path. In this regard, the manual rotational mechanism of the transducer incorporated in the second version of the system is extremely useful. A simple method to remove air bubbles is to rotate the transducer at 90º, and then, once the coupling cone is filled with degassed water, rotate it back in its horizontal position. An elastic band was included in the mechanism to stabilize the transducer.

The motion accuracy of both systems was assessed following a caliper-based methodology as previously detailed in the literature [144]. The obtained results demonstrate that the motion error is decreasing with increasing motion step in all axes, with a maximum positioning error of about 0.1 mm for the 1-mm step.

The single-element spherically focused transducer of 1 MHz that was developed in-house was proven suitable for the specific trans-skull application of FUS-induced BBBD in mice, most probably due to their small skull thickness. Although very promising results were obtained, further experiments should be performed using the second version of the device, which is expected to address all the difficulties faced during the feasibility studies of the first version.

Despite the fact that the systems are mostly intended to be used in the laboratory setting, their MRI compatibility constitutes a great benefit since it allows for treatment planning and accurate targeting based on high resolution anatomical images, as well as confirmation of BBB opening by contrast agent enhanced imaging directly after treatment without moving the device from the scanner. Therefore, subsequent experiments may be benefited by treatment planning and post-treatment BBBD assessment in the MRI setting. Note that MRI has been

already employed in numerous studies mostly for assessing whether the BBB was successfully disrupted [133], [276], [278], [416], and less often for focus positioning and targeting [133], [416].

The *in-vivo* feasibility study described in this section was performed to obtain proof of concept for the developed systems in a small number of mice. Therefore, a dedicated targeting method such as the use of a stereotactic frame was not adapted. Instead, a global approach was followed, where the transducer's location was adjusted so that the FUS beam targets the skull centrally roughly focusing at the level of the hippocampus. This approach was efficient to obtain proof of successful ultrasonic coupling and disruption of the BBB. Follow up studies with the second version of the system will allow more precise targeting and will focus on optimizing the protocol for safe and efficient BBBD, as well as assessing the ability of delivering chemotherapeutic drugs through the opened BBB.

13 FUS-mediated Anti-Aβ antibodies delivery in 5XFAD AD mice

13.1 State of the art

The main role of the BBB, as previously explained, is to protect the CNS from drugs and toxins. It is composed of microvascular endothelial cells. TJs are formed between these cells, with several transporters regulating the influx and efflux of compounds, such as nutrients and small peptides [417]. There are several modes of BBB transportation. Hydrophilic molecules transport via the paracellular pathway. Glucose and small metabolites pass the BBB via specific transport proteins, whereas larger molecules enter the brain via receptor mediated or adsorptive transcytosis. Efflux systems have a protective role due to their ability to remove xenobiotics from the brain back into the blood stream [417].

The highly selective nature of BBB is the main obstacle against the application of potential disease-modifying therapies for diseases of the CNS, including brain tumors and neurodegenerative diseases such as AD and PD [418], [419]. Accordingly, drug delivery into the brain tissue has been a major challenge for researchers over a long period. Among the drug-based methods employed in the clinical setting for BBBD, the most commonly used one involves administration of the osmotic agent mannitol [420], [421]. It is typically administered via a catheter causing the endothelial cells to shrink, thus opening the BBB TJs. The most clinically studied non-drug method is the MRgFUS, followed by MRI-guided laser ablation and cranial implantable US [420].

Pulsed FUS in synergy with MBs can induce temporal BBBD by causing alterations in the cell-to-cell interactions and endothelial cell cytoskeleton. In fact, MBs-enhanced FUS was shown to loosen the endothelial cell TJs through a mechanism known as cavitation [394], [395]. The junctions' disruption is mainly attributed to changes in the level of related trans- and peripheral membrane proteins [422]. In addition, FUS treatment was found to cause stimulation of transcytosis,

sonoporation of the vascular endothelium, and increase in the paracellular diffusion due to the TJs disruption [422]. FUS can further cause disruption of drug efflux by temporally suppressing the expression of the permeability-glycoprotein (Pgp) [423]. Notably, at sufficiently high acoustic pressure, MBs begin to oscillate stably causing transient increase of permeability in the targeted area while above a threshold of pressure inertial cavitation occurs where MBs collapse violently [396], [424]. In the former case, the endothelial ligaments recover completely within a few hours post-sonication [356]. Inertial cavitation is responsible for the majority of adverse effects observed with this strategy, such as micro-hemorrhages [424].

BBBD by pulsed FUS in the presence of gaseous MBs has emerged as a feasible method of delivering large molecules normally hampered by the BBB to the brain. An indicative example is a study by Choi et al. [120], who showed that substances with high molecular weight of up to 70 kDa can reach the brain tissue through diffusion mechanisms following FUS plus MBs-mediated BBBD in the hippocampus of WT mice. This finding was particularly important in that the size of diffused substances was similar to that of drugs for key CNS diseases [120]. This strategy has been later confirmed by numerous preclinical studies to enhance the penetration of therapeutic agents, such as therapeutic peptides, genes, and antibodies into the CNS of non-transgenic and transgenic mouse models of neurological diseases, with an increasing number of clinical trials exploring clinical utility [393], [425]–[427].

Neurodegenerative disorders, such as AD and PD, are characterized by progressive neuronal dysfunction and there is currently no established method of treatment that can stop or reduce their progression. AD is the prevalent neurodegenerative disorder and cause of dementia and is characterized by the presence of intracellular neurofibrillary tangles and extracellular amyloid plaques owing to Amyloid β peptides (Aβ) aggregation [37], [38]. Available treatments are not curative but may slow disease progression and alleviate symptoms.

Given the urgent demand for disease-modifying therapies, the development of FUS therapeutics for AD receives remarkable research interest. Transgenic mouse models of AD constitute the main research tool in such studies since they are inexpensive, reproducible, and exhibit abundant plaque load. The ability of MBs-enhanced FUS without exogenous agents to reduce the Aβ pathology has been well demonstrated [127], [130], [428]. A single trans-skull MRgFUS treatment was shown to increase the levels of endogenous immunoglobulins (IgM and IgG) in the cortex of the TgCRND8 mouse model [127]. FUS-mediated endogenous antibody delivery and glia cells activation were considered as the mechanisms responsible for the observed plaque burden reduction [127]. Later, Shen et al. [130] reported that FUS in synergy with MBs applied twice a week for 6 weeks triggered behavioral changes and improved the spatial memory of triple transgenic AD mice. These changes were associated with reduced Aβ pathology and tau phosphorylation, as well as improved neuronal health of the sonicated hippocampus compared to the sham group. The findings of Poon et al. [428] support that the therapeutic effects of a single FUS treatment last for at least two weeks, and also that multiple two-week interval treatments may be a practical method to reduce the Aβ plaque load in advanced AD patients.

The positive effects of FUS in the mitigation of AD pathological features can be enhanced by administrating exogenous therapeutic agents. According to a study by Hsu et al. [429], the effects of FUS on plaque reduction were enhanced using a specific inhibitor of the glycogen synthase kinase-3 (GSK-3); a key molecule in the onset of AD. Administration of this inhibitor in APPswe/PSEN1-dE9 transgenic mice prior to MBs-enhanced FUS reduced the Aβ plaque synthesis by suppressing the GSK-3 protein activity. Therefore, a higher plaque reduction was achieved compared to when the inhibitor or FUS were applied alone [429]. Another study targeted an Aβ peptide species deposited in AD brain termed Pyroglutamate-3 Aβ (pGlu-3 Aβ) [430]. The FUS-mediated administration of an anti-pGlu-3 Aβ vaccine was found to promote plaque clearance and partial protection from cognitive

decline in APPswe/PS1ΔE9 mice [430]. Others attempted to support neuronal health as a measure for disease mitigation [431]. The repeated MRgFUS-mediated delivery of a pharmacological agent termed D3 (TrkA agonist) that promotes neuronal function was found to impart positive cognitive effects in TgCRND8 AD mice [431]. Expect from decreasing Aβ pathology, the combination of FUS and D3 induced numerous additional effects, including functional recovery, reduction of dystrophic neurites around the plaques, and enhanced hippocampal neurogenesis [431].

Several studies aimed to investigate the efficiency of FUS-mediated BBBD to facilitate the supply of large disease-specific antibodies in the brain and the resultant therapeutic effects. The feasibility of delivering an anti-Ab antibody called BAM-10 into the brain of the TgCRND8 mouse model using transcranial MRgFUS has been investigated by Jordao et al. [126]. Immunofluorescent staining revealed binding of the antibody to the plaques in the targeted brain areas that was accompanied by reduction of plaque pathology a few days later. FUS-induced BBBD was also shown to facilitate the supply of an anti-pyroglutamate-3 Aβ monoclonal antibody (mAb) called 07/2a in the brain of aged APP/PS1dE9 transgenic mice [432]. A more than 5-fold increase in the mAb levels was observed in the brain of mice treated with FUS plus antibody at 4 and 72 h post-treatment compared to those treated with antibody alone [432]. Sun et al. [433] further demonstrated that three successive weekly treatments with the 07/2a mAb combined with FUS resulted in a faster improvement of spatial learning and memory of a higher percentage of aged APP/PS1dE9 mice compared to the mice group receiving only antibody.

Recently, Bajracharya et al. [434], developed a tau-specific mAb termed RNF5 and evaluated its ability to reduce tau aggregates in K369I tau transgenic K3 mice. RNF5 was administered alone or in combination with low-intensity scanning ultrasound (SUS) plus MBs once a week for 3 months. Immunohistochemical

results revealed that the combined approach did not result in further decrease of tau levels despite the increased antibody levels observed in the brain. A possible explanation given by the authors is that accumulation of the RNF5 mAb in a specific p-tau-negative hippocampal layer reduced the RNF5 concentration available to attach to tau aggregates. Thereby, this study underlined the need to examine the post-sonication localization of antibodies in a cellular level since this seems to affect the therapeutic efficacy.

Another anti-Aβ antibody tested for its efficacy to improve cognition in AD mice is the Aducanumab. While this antibody administered alone was proved to reduce the Aβ pathology, it seems that higher doses of the antibody should reach the brain to produce clear positive cognitive effects [435]. Leinenga et al. [435] compared the effects of this antibody when administered alone or in synergy with MBs-enhanced SUS-in APP23 AD mice. The superiority of the combined approach in terms of plaque reduction over the antibody and SUS groups was controversial and dependent on the examined brain area. However, only the mice that received the combined treatment showed significant improvement in spatial memory. Specifically, the combined approach resulted in a 5-fold increase in the antibody amount compared to the non-sonicated mice a few days post-treatment and significant improvement in spatial memory. Notably, Aducanumab is the first therapeutic agent to be tested in combination with FUS in AD patients in a phase I ongoing clinical trial [436].

The Aβ (1-40) antibody targets the amyloid peptides Aβ(1-40) that represent the most abundant Aβ isoform in the AD brain [437]. The FUS-mediated delivery of the specific antibody was previously tested in a very small mice population (n=3) [129]. A 3-fold increase in fluorescence intensity of the antibody staining was observed in the brain regions treated with MBs-enhanced MRgFUS in comparison with the non-sonicated regions, with haematoxylin and eosin (H&E) staining providing evidence of hemorrhages in the sonicated brain tissue [129]. While this

study provides promising results on FUS-mediated enhanced Aβ (1-40) antibody delivery, further experiments in a larger mouse population are needed to confirm these early findings and optimize the therapeutic protocol for safe and efficient Aβ (1-40) antibody delivery.

In this study, it was examined whether the application of FUS in synergy with MBs using the previously presented manual positioning device comprising a single element FUS transducer of 1 MHz can facilitate the penetration of the Aβ (1-40) antibody into the brain of 5XFAD transgenic mice. We initially attempted to define the sonication protocol for safe and efficient BBBD. The success and extent of BBBD was assessed by EB extravasation while brain damage was assessed by H&E staining. We then examined the capability of the Aβ (1-40) antibody to consistently enter the brain parenchyma when administered alone and prior to MBs-enhanced FUS using the optimized protocol in a large 5XFAD mice group. Finally, the effect of the antibody on plaque clearance was investigated.

13.2 Materials and methods

13.2.1 FUS system

FUS was delivered using the dedicated positioning system described in section 12, which comprised a single element, spherically focused, ultrasound transducer (Piezo Hannas, 1 MHz central frequency, 80 mm radius of curvature, 50 mm diameter, and 32.5 % acoustic efficiency) tuned to an RF amplifier (AG 1016, T&G Power conversion). This system was specially designed to facilitate transcranial FUS studies in rodents. The transducer is hosted in a conical water tank whose bottom opening is sealed with a silicone membrane and which can be moved vertically via a manual positioning mechanism coupled to the mouse platform to attach to the mouse head via a top to bottom approach. A laser pointer accessory was implemented into the system to facilitate consistent targeting among

experiments. The positioning device and photo of the experimental setup can be seen in **Figure 99**.

13.2.2 Protocol optimization for efficient and safe BBB disruption

Thirty-two (32) WT B6/SJL mice were used for protocol calibration/optimization. Intraperitoneal injection of Avertin (Sigma Aldrich, St. Louis, Missouri, United States) was used to cause rapid and deep anesthesia in mice and ensure no suffering. The dose of Avertin was weight-dependent for each animal (20 μL/g). The hair was removed from the mouse head using a commercial hair removal cream (Veet Hair Removal cream). Retro-orbital injection was then used to deliver a mixture of 5 μL of SonoVue® MBs (Bracco Imaging, Turin, Italy, 2 x 10^8 microbubbles/ mL suspension) along with 5 mL/kg of 3 % w/v EB solution (Sigma, St. Louis, MO, USA). Anesthetized animals were positioned in prone position on the platform as shown in **Figure 99**.

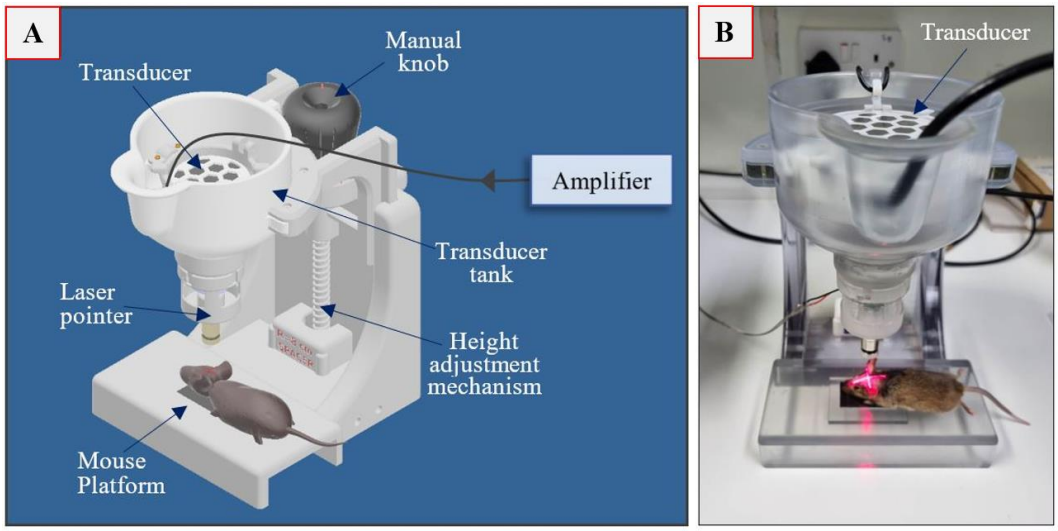

Figure 99: **(A)** CAD drawing of the 1-DOF positoning device comprising a FUS transducer of 1 MHz with a mouse positioned on the dedicated platform. **(B)** Indicative photo from mice experiments.

The tank was filled with degassed, deionized water and US coupling gel (Quick-Eco Gel, AB Medica group S.A., Barcelona, Spain) was applied on the mouse head to achieve efficient acoustic coupling. The position of the mouse was adjusted so that the FUS beam was targeted on the left hemisphere centrally with the assistance of the laser system. All mice received a single sonication within 3-4 minutes following the injection of MBs and EB using 1 MHz pulsed FUS of 10 ms bursts at a DF of 1% for a total duration of 100 s.

For protocol calibration purposes, electric power values of 20 to 70 W were tested (10 W step; 6 groups of 5 mice each). The relevant acoustic power ranged from 6.5 to 22.8 W, corresponding to *in situ* focal acoustic pressure in the range of 0.3 to 0.6 MPa. The output acoustic power was estimated based on the acoustic efficiency of the transducer of 32.5%. The respective focal pressures were initially determined in water using a needle hydrophone (HNC, ONDA, Sunnyvale, CA, USA) placed at the focal distance of the transducer. *In-situ* pressures were then calculated accounting for the transmission loss through the mouse skull. The transmission coefficient of a skull sample was measured according to the well-established through-transmission immersion technique [438] at the operating frequency of the transducer of 1 MHz. One mouse received only EB and one neither EB nor FUS, thus serving as the control mice.

Mice were sacrificed by transcardial perfusion with saline followed by 4% paraformaldehyde (PFA) 40 minutes post-treatment. This time period is well within the 4-hour window that the BBB was found to maintain open after FUS. Therefore it was considered sufficient for successful entry of EB into the brain, but also to allow for acute FUS-induced physiological responses to be resolved [439]. The brain tissue was then collected and preserved in paraformaldehyde (4%) and then sucrose (20%) diluted in Phosphate Buffer (0.1%) according to our protocol. Brain sections were prepared for fluorescence imaging. Slides containing brain sections

were visualized using a Nikon eclipse-Ni (Tokyo, Japan) fluorescence microscope to visualize EB extravasation and determine the BBB-opened region.

13.2.3 Trans-BBB Aβ (1-40) antibody delivery in a mouse model of AD

13.2.3.1 Animals

5XFAD transgenic mice recapitulating major features of AD were utilized. 5XFAD mice were bred as single transgenics. Male 5XFAD mice were crossed with female SJL/B6 F1 mice to give hemizygous or WT offspring's, which were used for the purpose of the study. The pathologic phenotype of this mouse model consists of gliosis, amyloid plaques, neurodegeneration, memory deficits (at 4-5 months), as well as intraneuronal Aβ and neuron loss. Beginning at 8 weeks of age, amyloid deposition and gliosis become increasingly widespread, especially in the deep cortical layers and subiculum.

13.2.3.2 Experimental design

5XFAD transgenic mice of 5-months of age (n=20) were used to test the feasibility and efficacy of FUS-mediated delivery of the Aβ (1-40) antibody (150 kDa, Anti-β-Amyloid Protein (1-40) antibody produced in rabbit whole antiserum, A8326, Sigma Aldrich, 3050 Spruce Street, Saint Louis, MO 63103, USA) into the brain. The ability of the antibody to pass through the BBB and bind to the Aβ plaques when administered alone and in combination with FUS was investigated using a constant antibody amount of 50 μL.

Twenty (20) mice were divided into 3 sub-groups: A. Saline (50 μL) administration followed by FUS+MB-induced BBB opening (referred to as control; n=5), B. Aβ (1-40) antibody (50 μL) administration alone (referred to as antibody, n=5), and C. Aβ (1-40) antibody (50 μL) administration followed by FUS+MB-induced BBB opening (referred to as FUS+MB plus Ab; n=10). The brain sections of mice from group A were used as negative controls and they were compared with the coronal

brain sections of mice from groups B and C, which were injected with the Aβ (1-40) antibody.

The anesthesia protocol and treatment timeline were similar to that used for the calibration study. The Aβ (1-40) antibody was delivered instead of the EB dye via retro-orbital injection along with the MBs. Based on the data gathered from the protocol optimization study, an acoustic power of 16 W (*in situ* focal acoustic pressure of 0.5 MPa) was considered optimum and used in this experimental part while the rest sonication parameters remained the same. The treatment protocol is summarized in the diagram of **Figure 100**. Note that following FUS, a time window of 4 hours was left before scarification.

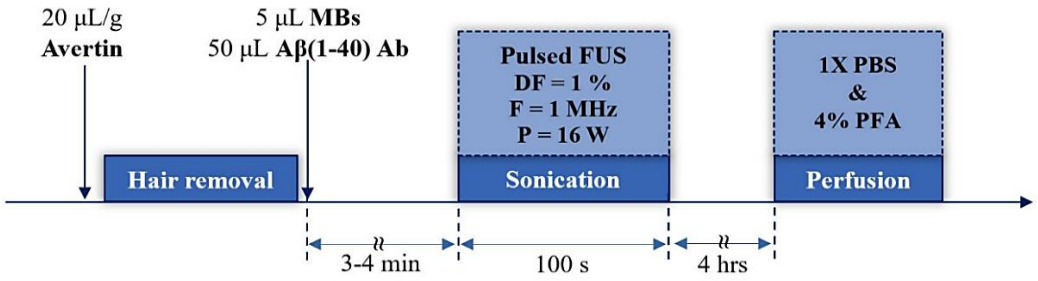

Figure 100: Protocol timeline for FUS-mediated antibody delivery in 5XFAD mice.

13.2.3.3 Mouse sacrification and tissue preparation

Transcardiac perfusion was used to clear blood and preserve the brain for immunostaining analysis. Following perfusion, the mouse head was dissected, and the skull was carefully removed using scissors and forceps, exposing the brain. The brain was washed in Phosphate Buffer Saline (PBS) and then placed for 2 hours in 4% Paraformaldehyde (PFA) solution. Then, it was again washed with PBS and placed into 20% sucrose solution (diluted in Phosphate Buffer 0.1M) overnight at 4 °C for cryoprotection prior to embedding and freezing. For tissue embedding, the cryomould containing the brain tissues, was filled with OCT, and placed into acetone-dry ice bath. Finally, the frozen OCT containing the brain tissue was removed from the cryomould and stored in a -80°C freezer.

13.2.3.4 Immunohistochemistry

Double immunostaining of coronal brain sections was performed to determine whether the injected Aβ (1-40) antibody passed the BBB and bound to Aβ plaques. Staining with Aβ (1-16) antibody (6E10, green colour) was used to identify the amyloid plaques. The tissue was permeabilized by immersing the frozen sections in acetone for 10 minutes at -20°C. It was then washed three times with 1X PBS and blocking solution (5% Bovine Serum Albumin + 0.5% Triton X-100) was applied for 1 hour on the sections at room temperature in a humidified chamber. The blocking solution was then removed and the primary antibody; anti-β-amyloid primary monoclonal 6E10 (diluted in blocking solution) was applied to the tissue sections and incubated overnight at 4°C. The following day, the primary antibody was removed, and the tissue sections were washed three times with 1X PBS. The secondary antibodies; Fluorescein (FITC) goat anti-mouse, 1:100 and Alexa Fluor® 594 goat anti-rabbit, 1:500 (diluted in blocking solution) were next applied for 1 hour at room temperature for the detection of the injected antibody in the examined brain tissue, followed by three washes with 1X PBS and incubation for 30 seconds with 4',6-diamidino-2-phenylindole (DAPI, Sigma-Aldrich) for nuclear staining. The tissues were washed two times for 5 minutes with 1X PBS, dried and mounted with mounting media in order to prepare them for microscopy.

13.2.3.5 H&E staining

We also checked the tissue integrity and the lack of hemorrhage with H&E staining for the tested acoustic pressures ranging from 0.3 to 0.6 MPa. Tissue sections in OCT were stained with Harris's haematoxylin (freshly filtered) for 3 minutes, and then washed with distilled water and stained with aqueous eosin for 6 minutes. Next, they were dehydrated in ascending concentrations of alcohol and cleared in xylene (70 %, 95 %, 100 % x 2 and xylene x 3). Finally, the tissue slides were mounted with Dibutylphthalate Polystyrene Xylene (DPX).

13.2.4 Long term assessment of amyloid plaque reduction

This experimental part investigated the effects of the antibody delivery on plaque reduction in 5XFAD mice. The following conditions were tested: (a) only antibody, (b) only FUS, and (c) combined treatment with antibody and FUS. As shown in **Figure 101**, mice were treated twice leaving a two-week interval between treatment sessions, and then perfused two weeks after the second session. Following sacrification, the amyloid plaque burden was assessed using immunofluorescence to quantify the amount of remaining amyloid plaques in the brain.

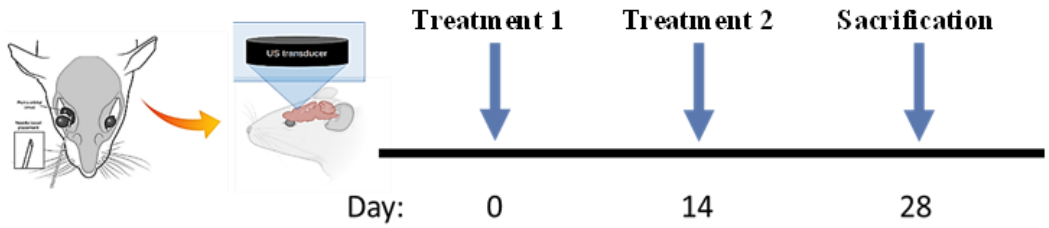

Figure 101: The treatment protocol used to assess the effect of antibody delivery on plaque reduction in 5XFAD mice.

13.3 Results

13.3.1 Protocol calibration for efficient and safe BBB disruption

According to fluorescence microscopy all tested power levels in the range of 6.5 to 22.8 W (0.3−0.6 MPa *in situ* pressure) combined with 5 μL of MBs (for the specific sonication parameters employed) caused BBBD since increased fluorescence intensity of EB was observed compared to the control mouse (receiving only EB). Indicative fluorescence images for the various acoustic powers tested are presented in **Figure 102**, revealing the power effect on the extent of EB extravasation. Note that a gradual increase of fluorescence intensity (indicating increase in the extent of BBBD) occurred as the power in the tested range was increased.

The optimal power was selected as the one resulting in the highest EB leakage (ideally spread throughout the sonicated region) without causing any adverse effects on tissue and having consistent behavior among subjects. The power value of 16 W (0.5 MPa *in situ* pressure) showed consistent EB leakage in all examined brain regions and no evidence of damage and was thus selected for follow-up experiments in the AD mouse model.

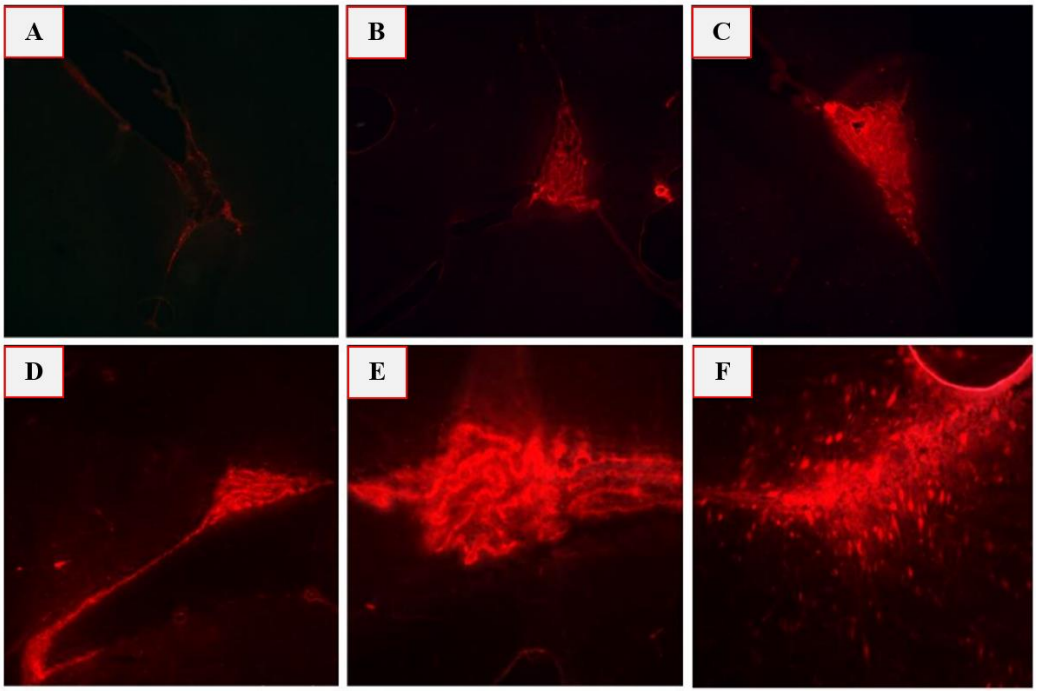

Figure 102: Fluorescence images (10x magnification) of unstained brain sections at the level of the lateral ventricles of mice injected with EB: **(A)** No FUS, **(B)** FUS at 6.5 W, **(C)** FUS at 9.7 W, **(D)** FUS at 13 W, **(E)** FUS at 16 W, and **(F)** FUS at 19.5 W (acoustic power).

Indicative histological slides from H&E examination for the selected acoustic power (16 W) from two different brain areas can be seen in **Figure 103**. No difference between the FUS treated and control cases in terms of tissue integrity was observed and there was no evidence of hemorrhage in none of the tested brain regions.

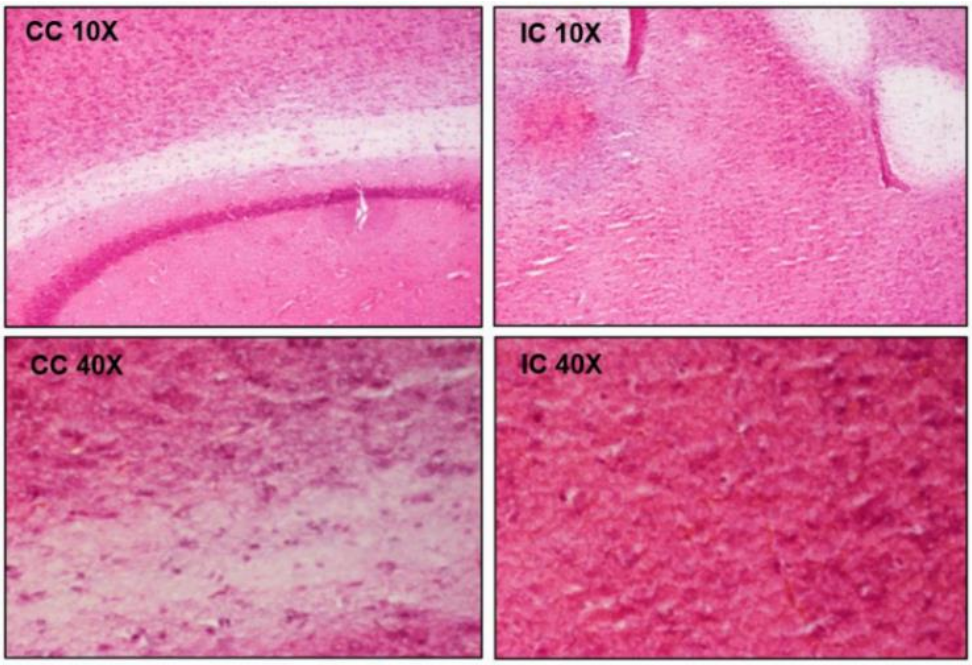

Figure 103: Representative photos (10x magnification) of H&E staining from mice treated with MBs-enhanced pulsed FUS at 16 W for two different brain areas; corpus callosum (CC) and inferior colliculus (IC).

Figure 104 shows representative fluorescence microscopy images for the selected power taken from to cortex region. Photos of the freshly perfused excised brain of a mouse treated with the selected protocol and a brain section after fixation in OCT can be seen in **Figure 104B and Figure 104C**, respectively. Note that the EB dye was diffused throughout the entire left hemisphere that was sonicated. **Figure 104D and Figure 104E** compare magnified fluorescence images of unstained brain sections at the level of the cortex between a non-sonicated mouse and a sonicated mouse (pulsed FUS with 10 ms burst length and 1 % DF at 16 W for 100 s duration & 5 μL MBs) both injected with equal amount of EB solution (5 mL/kg of 3 % w/v). Note that no leakage was observed in the brain of the control mouse (EB only), whereas FUS-induced BBBD resulted in high levels of EB dye covering the examined cortex area.

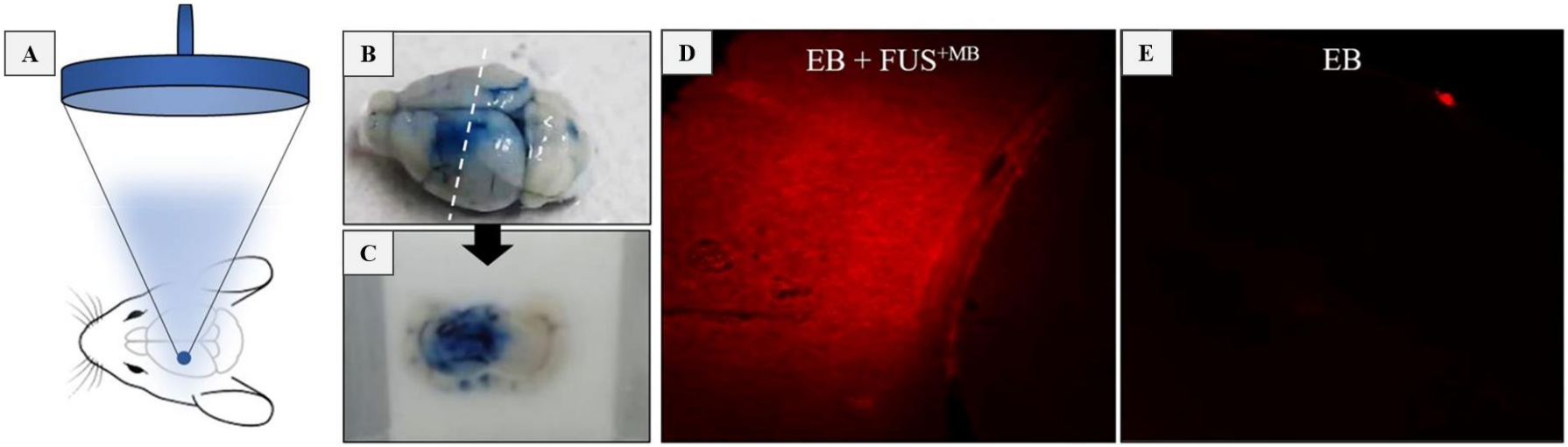

Figure 104: **(A)** FUS beam targeting centrally at the left hemisphere. **(B)** Freshly perfused excised mouse brain treated with the selected protocol (5 μL MBs and 16 W acoustic power). **(C)** Brain section after fixation in OCT revealing the distribution pattern of EB extravasation. **(D)-(E)** Fluorescence images (5x magnification) of unstained brain sections at the level of the cortex taken from perfused mice; the one injected with EB and 5 μL MBs followed by sonication at 16 W (EB + FUS^{+MB}) and the other one injected with EB only (control).

13.3.2 Trans-BBB Aβ antibody delivery in a mouse model of AD

Indicative results of immunohistochemistry analysis of brain tissue sections are presented by **Figure 105** and **Figure 106**. Co-localization of red (injected Aβ (1-40) antibody) and green (Aβ 1-16 antibody) fluorescence in multiple brain regions of the sonicated hemisphere confirmed successful BBBD, as well as entry and binding of the injected Aβ (1-40) antibody to Aβ plaques. Indicative fluorescence images of brain sections at the level of the cortex showing Aβ (1-16) staining (column A), Aβ (1-40) staining (column B) and their combination (column C) for the various mice groups are shown in **Figure 105**.

As expected, the 5XFAD mice that were injected with saline following FUS+MBs (control group) did not have any signs of the Aβ (1-40) antibody in their brain. Similarly, the antibody was not present in any of the brain sections of the mice injected only with the Aβ (1-40) antibody (antibody group), confirming the inability of the specific therapeutic agent to normally pass through the BBB. On the contrary, immunohistochemistry analysis of brain sections from the FUS+MBs plus Ab group showed entry of the Aβ 1-40 antibody in the brain parenchyma. These findings qualify the selected treatment protocol (50 μL antibody & 1 MHz pulsed FUS with 10 ms burst length and 1 % DF at 16 W for 100 s) as an efficient BBBD method for the delivery of the specific anti-Aβ antibody into the mouse brain. The repeatability of obtained results was investigated in 10 mice, which all showed successful antibody entry and specific binding to plaques. Indicative brain sections from 6 mice are shown in **Figure 106** revealing co-localization of antibodies (white circles) in the cortex.

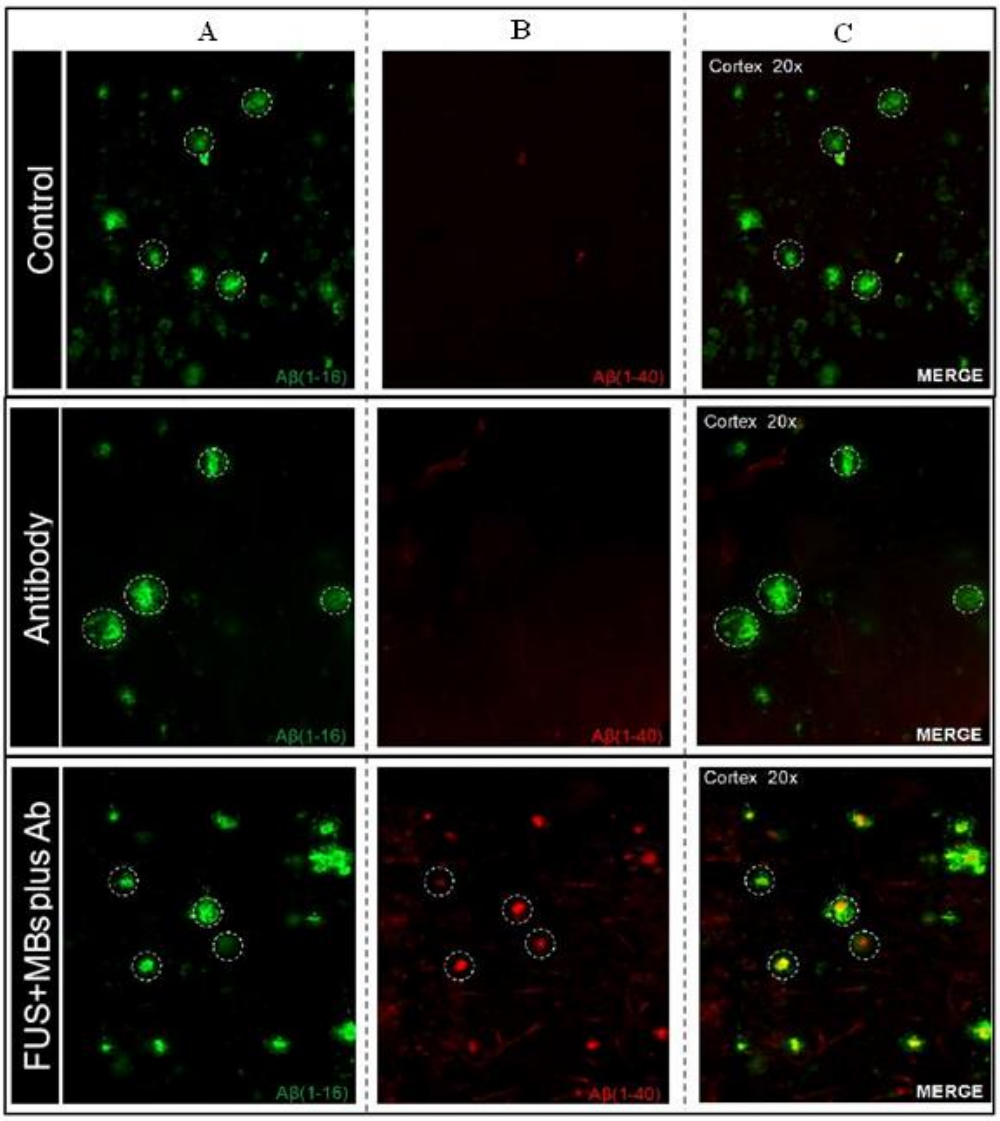

Figure 105: Immunohistochemistry analysis of brain tissue sections of 5XFAD mice. Column A: Aβ (1-16) staining confirmed the presence of amyloid plaques (green) in the cortex, Column B: Aβ (1-40) antibody staining in red colour, Column C: Merged images of antibody and plaques staining, for the three mice groups: saline followed by FUS+MBs (labeled as control), 50 µL of Aβ (1-40) antibody alone (labeled as antibody), and 50 µL of Aβ (1-40) antibody followed by FUS+MBs (labeled as FUS+MBs plus Ab). Co-localization of antibodies (white circles) in the cortex of the FUS+MBs plus Ab group (MERGE) confirmed successful binding of the Aβ (1-40) with amyloid plaques (Sonication parameters: f = 1 MHz, burst length = 10 ms, DF = 1 %, acoustic power = 16 W, and sonication duration = 100 s).

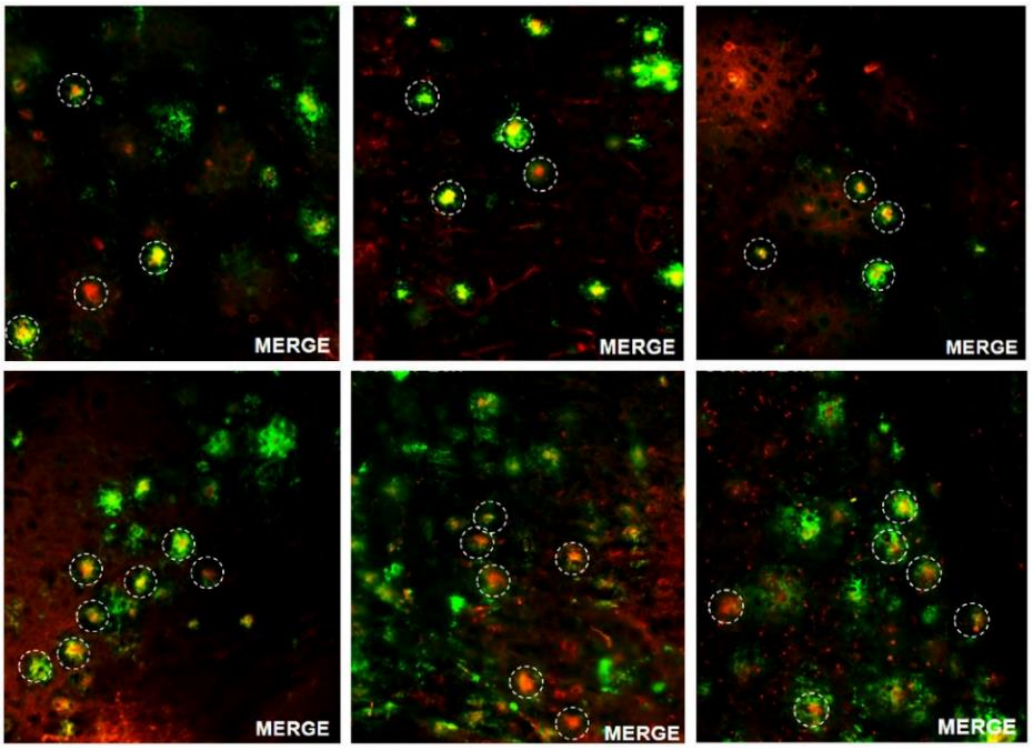

Figure 106: Immunohistochemistry analysis of brain tissue sections of 5XFAD mice injected with 50 μL of Aβ (1-40) and 5 μL MBs followed by pulsed FUS. Fluorescence images from different mice at the cortex level where plaques are stained green and the antibody red (20x magnification). Co-localization of antibodies (white circles) in the cortex confirmed the successful entry and specific binding of the Aβ (1-40) antibody.

13.3.3 Long term assessment of amyloid plaque reduction

The results revealed that the brain regions of mice that received the combined treatment (antibody and FUS) exhibited lower number of amyloid plaques in comparison to the non-sonicated regions (only antibody). On the contrary, the mice that were only injected with the Aβ (1-40) did not show any signs of amyloid clearance. Indicative results are shown in **Figure 107**. This difference was statistically significant ($p \leq 0.05$) when compared to the region that did not undergo FUS treatment. It is also important that Iba1+/CD68+ microglia were found colocalized with the amyloid plaques in the FUS+antibody treated brain regions.

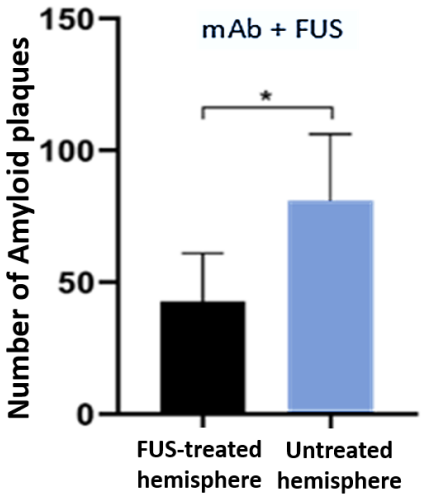

Figure 107: Number of amyloid plaques found in the hemisphere treated with FUS+antibody compared to the hemisphere that was not sonicated (only antibody).

13.4 Discussion

FUS-mediated BBBD for the enhanced delivery of brain therapeutics is currently receiving tremendous research interest. FUS in combination with MBs has been confirmed by numerous studies [27], [425], [440], as an effective method for overcoming the BBB to deliver exogenous therapeutic agents at present. AD is the first cause of dementia [38] with Aβ immunotherapy belonging to the most promising therapeutics to alter its course [437]. This study aimed to investigate whether FUS-mediated BBB opening with an optimized protocol can be used to safely and efficiently deliver a specific anti-Aβ antibody; Aβ (1-40) into the brain of 5XFAD AD mice using a custom-made FUS positioning device. The specific antibody is directed against the amyloid peptides Aβ (1-40) that represent the most abundant Aβ isoform in the AD brain [437], thus promoting plaque clearance. Unfortunately, its entrance in the brain is prohibited by the BBB due to its large molecular weight (150 KDa).

To our knowledge, this is the second study to report the use of this antibody. In fact, there is a previous study that examined the feasibility of delivering this antibody into 3 mice by FUS-mediated BBBD. Authors report a 3-fold increase in fluorescence intensity of the antibody staining in brain regions treated with MRgFUS in comparison to non-sonicated regions, with H&E staining revealing hemorrhages in the sonicated brain tissue [129]. We have verified these preliminary findings in a large mice population showing that FUS-mediated BBBD facilitates antibody penetration into the brain. However, contrary to the findings of Raymond et al. [129], non-sonicated mice showed zero fluorescence intensity indicating complete absence of the exogenous antibody in the examined brain tissue. The current results go beyond this, further demonstrating that the use of an optimized protocol allows for efficient BBBD without any tissue damage and probably the use of a smaller antibody dose (half compared to the dose used previously [129]); however further investigation is required on this matter.

The first experimental part was carried out in WT mice (n=32) and was devoted to selecting the sonication protocol for optimized BBBD. The FUS+MBs treated mice showed higher levels of EB dye in all examined brain areas, whereas for the control mouse (EB only) the dye remained in the extracellular matrix. The *in situ* peak pressure amplitude of 0.5 MPa (16 W acoustic power) applied at a frequency of 1 MHz in the presence of MBs (5 μL) was selected as offering safe and efficient BBBD and employed in follow-up studies involving the antibody. The results of H&E histology revealed no structural damage and no signs of hemorrhage in none of the sonicated hemispheres.

These results are consistent with what has been found in previous state-of-the-art studies. In fact, pressure levels of up to 0.5 MPa have been previously proposed by Hynynen et al. [356] as suitable for consistent and safe BBBD in rabbits, where the observed side effects were mostly limited to few tiny extravasations of red blood cells while above that value and up to 1.4 MPa more severe effects such as

hemorrhages and mild damage to the brain parenchyma were observed. Herein, none of the tested focal pressures ranging from 0.3 to 0.6 MPa (*in situ)* showed evidence of FUS-related effects on tissue integrity. The efficiency of the selected pressure level (0.5 MPa) to disrupt the BBB with negligible effects on brain tissue has been confirmed by other studies as well [441], [442], with McDannold et al. reporting an estimated threshold of 0.36 MPa for BBB opening. When comparing results, it must be pointed out that similar pulsed FUS parameters (10 ms burst length at 1 Hz repetition frequency) but a quite smaller frequency of 0.7 MHz were utilized in these studies.

5XFAD mice were bred for the antibody study. This mouse model was selected since it recapitulates major features of the AD amyloid pathology and is a useful model of intraneuronal Aβ42 induced neurodegeneration and amyloid plaque formation. The combined treatment involved injection with 50 μL of Aβ (1-40) antibody and 5 μL of MBs followed by pulsed FUS (16 W) at 1 MHz. Following FUS treatment, the mouse was left 4 hours before it was sacrificed, which is considered the reliable post-treatment time window during which the BBB remains open [443], [444] to allow the maximum amount of antibody to enter the brain. Immunohistochemistry analysis of brain tissue sections confirmed that the antibody cannot normally enter the brain parenchyma since no fluorescent was observed in the microscope indicating absence of the antibody when administered alone owing to its prohibitively large molecular weight of 150 kDa. FUS-mediated BBB with the selected sonication protocol (1 MHz pulsed FUS with 10 ms burst length, 1 % DF, 16 W power, and 100 s duration) allowed the injected Aβ (1-40) antibody to enter the brain. Aβ (1-40) immunofluorescent staining confirmed delivery of the antibody in the FUS+MBs plus Ab group only. In merged images, co-localization of both antibodies confirmed the presence of cortical plaques, successful trans-BBB entry of the injected anti-Aβ antibody in the brain by trans-skull pulsed FUS+MBs, as well as the specificity of the Aβ (1-40) antibodies to bind to the amyloid plaques. The results showed excellent consistency and reproducibility of BBBD and FUS-

mediated antibody delivery by single sonication in the treated hemispheres of all mice (n=10, FUS+MBs plus Ab group).

This section further examined the potential of FUS-induced Aβ (1-40) antibody delivery in the treatment of Alzheimer's disease by inducing amyloid plaque clearance. The combined treatment (FUS+antibody) caused partial clearance of amyloid plaques, whereas mice receiving only antibody did not show any signs of amyloid clearance. However, it should be clarified that this was a preliminary study that was focused on the feasibility of safely and efficiently delivering the Aβ (1-40) antibody into the mouse brain following BBB opening by FUS. Although the antibody was widely distributed through the sonicated brain and bound to Aβ plaques promoting plaque clearance, it remains unclear to which degree the selected antibody amount promotes positive cognitive effects nor whether the antibody amount can be further decreased. Accordingly, longer-term studies are required to assess the effects of the antibody and dose on suppressing AD pathological symptoms.

The positioning device employed in the study was proven an ergonomic tool for transcranial FUS applications in mice. The special design of the system allowed attaching the water-filled cone to the mouse head with visual confirmation of proper coupling following easy targeting with the assistance of the laser system. The suitability of the single element FUS transducer of 1 MHz for the particular application of transcranial BBBD in rodents was demonstrated, being in agreement with other field studies where 1 MHz burst FUS was predominantly selected for similar applications [120], [276]–[278]. Since this was a feasibility study, we did not attempt targeting a specific brain region. A global targeting approach was instead used where the beam was focused in the center of the left hemisphere. Due to the small size of the mouse brain, FUS of 1 MHz applied with the specific transducer and proposed sonication parameters affected the entire targeted hemisphere as evidenced by the extend of EB dye extravasation. Follow up studies

may account for parameters affecting ultrasonic focusing (e.g., transducer characteristics), thus enabling a more specific delivery of the antibody in brain regions of interest.

Overall, the study findings revealed that the Aβ (1-40) antibody that is normally hampered by the BBB can consistently enter the brain parenchyma and bind to Aβ plaques of the 5XFAD mouse model of AD by FUS+MBs-mediated BBB opening without any brain damage using the proposed optimized protocol. Follow-up studies will examine whether repeated treatments can impart significant positive effects on cognition. These results hold promise for the development of a disease modifying therapy via non-invasive anti-Aβ antibody delivery for AD patients in future clinical applications.

14 FUS-mediated BBBD for AAV9 delivery into the CNS

14.1 State of the art

Hypomyelinating leukodystrophies represent a specific group of genetic neurological conditions that impact the white matter in the brain [40]. Hypomyelinating leukodystrophy type-2 (HLD2) causes a gradual degeneration of the white matter in the brain and spinal cord due to specific genetic mutations, and is typically diagnosed during infancy and childhood [40], [41]. Children with HLD2 usually experience various symptoms, including developmental delay, motor impairment, muscle weakness, and intellectual disabilities. MRI is the method of choice for the diagnosis and evaluation of the disease progression. Despite that the understanding of the disease pathology was enhanced significantly over the last decade, there are currently no curative treatments available [40].

Herein, the feasibility of cell-targeted AAV vector-mediated delivery of the EGFP reporter gene in the brain of P30 WT mice through the intravenous route after FUS-mediated BBBD was tested. The specific objective was to examine the efficacy of FUS-induced transient BBBD to enhance the biodistribution of AAV9 vectors into the CNS as a potential therapeutic solution for HLD2.

14.2 Materials and methods

This section was dedicated to testing the feasibility of FUS induced transient BBBD to facilitate the penetration of the AAV9.MBP.EGFP vector (AAV9 vector driving EGFP reporter gene expression, simplified as AAV9) into the CNS using the previously established protocol for BBBD (1 MHz pulsed FUS with 10 ms burst length and 1 % DF applied for 100 s). The vector was initially tested in 4 WT P30 mice of 1 month-old, which received 50 µL of the vector. 5 µL/g of body weight of AAV9 vector was injected intravenously into each mouse. Four (4) mice were treated with FUS following tail vein injection of the AAV9 vector; 2 mice were

injected with 50 μL of the vector and the other 2 with the half dose. The mice were sacrificed with PFA after 4 weeks.

Table 11 lists the treatment parameters used in each group. Note that 1 mouse was used as the control and did not receive either FUS or vector. The relevant timeline used for AAV9 vector delivery is shown in **Figure 108.**

Table 11: AAV9 vector dose and sonication parameters used in each mice group.

Group	El. power (W)	MBs (μL)	Vector (μL)
A (n=4)	-	-	50
B (n=2)	60	5	50 ($2x10^{12}$ vg)
C (n=2)	60	5	25+25 μL H_20 ($1x10^{12}$ vg)

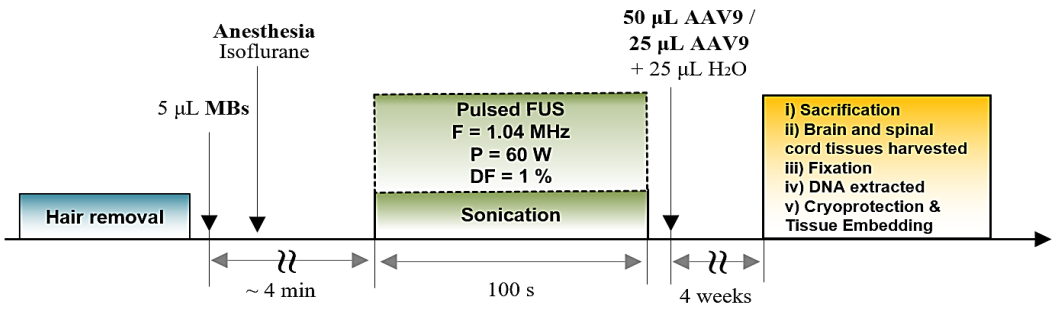

Figure 108: Timeline and experimental parameters used for AAV9 vector delivery through the FUS mediated opened BBB in P30 WT mice.

The biodistribution of the vector in the CNS was examined by measuring oligodendrocyte enhanced green fluorescent protein (EGFP) expression rates in different CNS areas, as well as vector genome copy numbers (VGCNs) in DNA extracted from different CNS regions. Therefore, following sacrification, cryosections from brain were immunostained for EGFP (Invitrogen, 1:1000) and DNA was extracted from brain, cerebellum, brainstem, and spinal cord for VGCNs determination. Slides containing brain sections were directly visualized using a fluorescence microscope (Nikon eclipse-Ni).

14.3 Results

Representative photos of EGFP immunofluorescence are shown in **Figure 109**. All CNS tissues showed high rates of EGFP compared to the non-injected mouse (control). Furthermore, the sonicated mice receiving 50 μL vector had a tendency for higher levels of EGFP in many brain areas compared to the non-sonicated mice (receiving only the vector); however, this was not consistent. Notably, the mice receiving the half amount of vector showed the lower expression. **Figure 110** shows graphs of the VGCN calculated for the brain and spinal cord areas for each tested treatment protocol. According to the estimated VGCN levels, the mice that were injected with 50 μL of the AAV9 vector following FUS-mediated BBBD had the highest transduction rates, but this should be confirmed in a larger mice population.

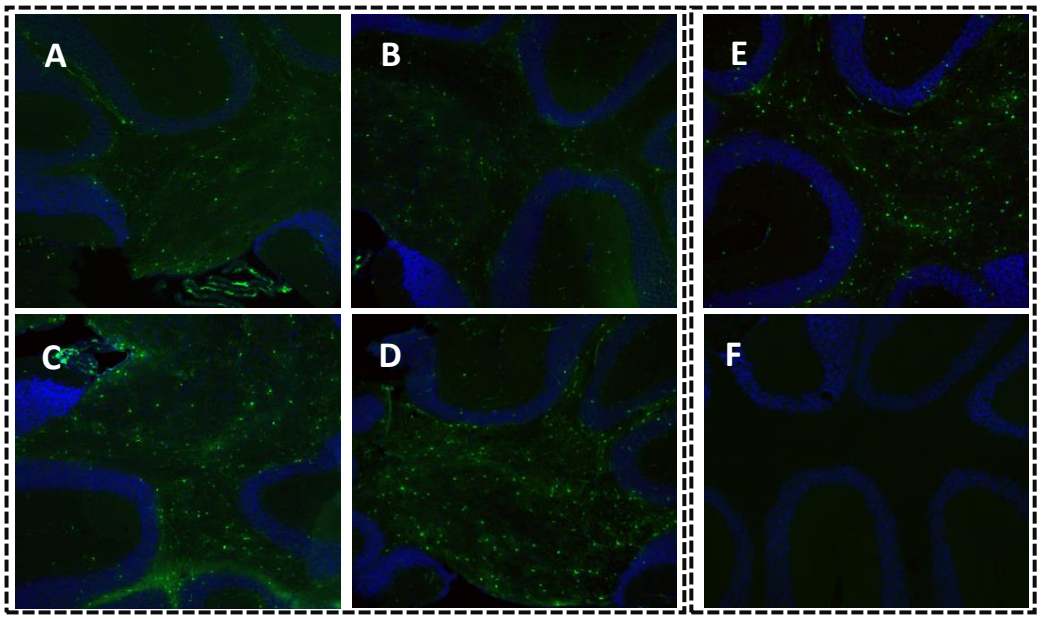

Figure 109: Representative photos (10x) of EGFP immunofluorescence staining in cerebellum: **(A)-(B)**: sonicated mice injected with 25 μL of vector, **(C)-(D)** sonicated mice injected with 50 μL of vector, **(E)** mouse injected with 50 μL of vector, and **(F)** non-injected mouse.

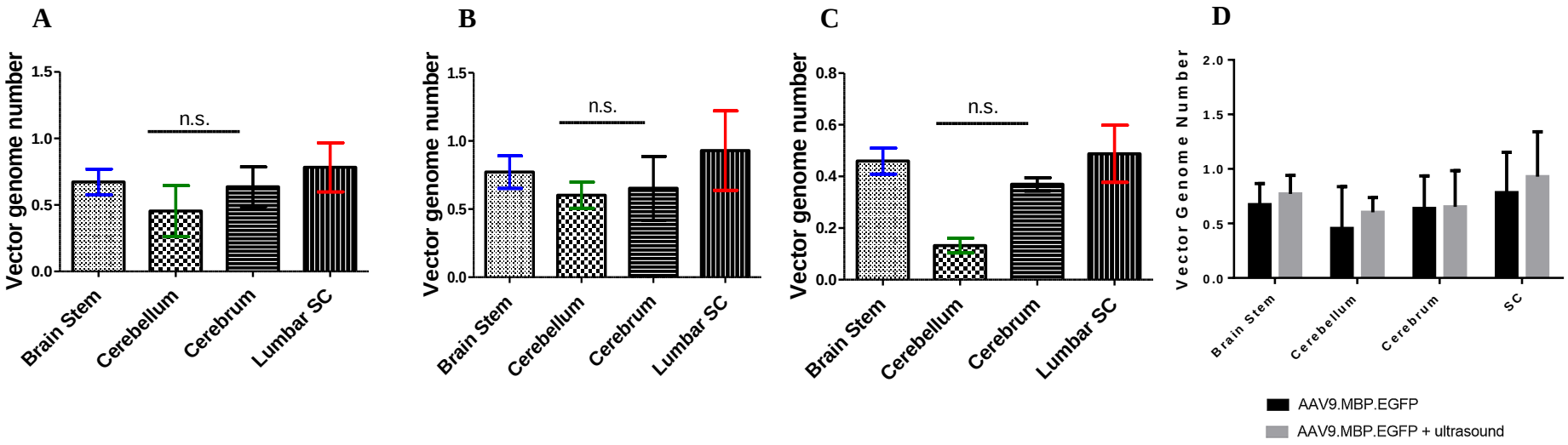

Figure 110: VGCN estimated for **(A)** mice injected with AAV9 only, **(B)** sonicated mice injected with 50 µL AAV9, and **(C)** sonicated mice injected with 25 µL of AAV9. **(D)** Comparison of VGCN between sonicated and not sonicated mice that received 50 µL AAV9.

14.4 Discussion

In these experiments, FUS-induced BBBD was performed prior to intravenously injecting different doses of the AAV9 vector driving EGFP reporter gene expression to transduce the brain of P30 WT mice, which were sacrificed 4 weeks later. Both single and double doses ($1x10^{12}$ and $2x10^{12}$ vg) were tested to assess the effect of the vector dose on brain transduction. VGCNs in extracted DNA and the rates of oligodendrocyte EGFP expression in different regions of the CNS served as the metrics for evaluating the vector distribution in the CNS.

The mice receiving 50 μl of the AAV9 vector following FUS sonication had a tendency for higher levels of EGFP and higher transduction rates compared to the non-sonicated mice in many brain areas, but mostly in the Cerebellum. However, further experiments with a larger mice population are needed to confirm this observation and obtain sufficient evidence. Furthermore, future studies may give insights on the quantity of vectors required to transduce the CNS sufficiently and compare the VGCN biodistribution with and without FUS for the lower tested vector dose of 25 μL.

15 Overall Discussion and Summary of Findings

The present thesis covers several topics in the field of preclinical MRgFUS with special emphasis on brain applications, from the development of anthropomorphic TMPs and *ex-vivo* assessment of MRI-compatible FUS robotic devices to *in-vivo* transcranial FUS application in mouse models of neurological diseases using dedicated FUS positioning devices.

TMPs are becoming more and more common for the performance characterization of therapeutic systems and emerging applications in the context of oncology. Given that MRgFUS is continuously gaining popularity as a beneficial method for tumor destruction, the development of high-quality realistic TMPs dedicated for MRgFUS studies is of significant importance. In an effort to contribute in this regard, this study aimed to develop realistic phantoms mimicking all the critical properties of human tissues and evaluate their performance under realistic conditions.

Following a comprehensive literature search on TMPs, the MR relaxation times of various agar-based phantoms were investigated. This investigation was prompted by the identification of a notable gap in the literature on this topic, and particularly on specific trends between added ingredients and resultant MR properties of TMPs. The findings suggest that the transverse relaxation time (T2) can be predominantly tailored by varying the agar concentration. The inclusion of silicon dioxide lowers both relaxation times, whereas increasing evaporated milk concentration results in a gradual reduction of the longitudinal time (T1). Accordingly, the T1 and T2 relaxation parameters of several body tissues can be accurately matched by using a proper concentration of these inclusions. It was thus concluded that the proposed phantom type has a great potential for use with the continuously emerging MRgFUS technology, also given its previously demonstrated feasibility to emulate all critical thermal and acoustical properties of human tissues.

The thesis next presents the development and evaluation of a tumor-bearing phantom model for testing MRgFUS ablation protocols based on MR thermometry. Normal tissue

was mimicked by a pure agar gel while the tumor simulator was differentiated from the surrounding material by including silicon dioxide. The inclusion of silicon dioxide in the tumor material offered the required contrast for excellent tumor visualization in US, MRI, and CT. The phantom was also capable of generating realistic response to FUS thermal heating, with MR thermometry revealing temperature elevations to ablation levels and clear evidence of larger heat accumulation within the tumor owing to the inclusion of silica. The proposed tumor phantom model constitutes a simple and inexpensive tool for preclinical MRgFUS ablation studies, and potentially other image-guided thermal applications in the context of oncology upon minimal modifications.

Taking into consideration the widespread use of mice in the assessment of emerging transcranial FUS applications, such as the FUS-mediated BBBD, an anatomically accurate mouse phantom was developed as well. The mouse model consists of skeletal and soft tissue mimics, whose design was based on the CT scans data of a live mouse. The bone part was manufactured by 3D printing using thermoplastic material, whereas the soft-tissue mimic was created by molding an agar-based silica-doped gel into a dedicated 3D-printed mold. The mouse phantom accurately matched the size and reproduced the body surface of the imaged mouse. In addition, the phantom demonstrated excellent MRI visibility and good radiological contrast between the skeletal and soft-tissue models and was also able to reproduce realistic behavior during trans-skull sonication as proved by thermocouple measurements. Therefore, it could constitute a powerful tool in small animal studies enabling the testing and optimization of FUS systems and protocols (including transcranial applications) before performing experiments in live mice, thereby avoiding the unnecessary use of live mice.

Overall, the proposed agar-based phantoms are inexpensive, accessible, realistic, and do not require ethical approval. They can be manufactured in house following a relatively easy and cost-effective process to accelerate biomedical research, also given that commercial phantoms are offered at very high cost. Agar gels can be formed in any configuration through a simple manufacturing process while maintaining sufficient

mechanical strength upon solidification. Their lifetime can easily be extended with the addition of preservatives. Cheap and easy to obtain ingredients can be added as modifiers of the acoustical, thermal, and MRI properties of this phantom type to accurately match those of human tissues. Through a series of experiments in laboratory and MRI settings, the proposed phantoms were proven very promising for MRgFUS studies. The outcomes of these experiments are expected to facilitate other researchers in the selection of appropriate materials for the construction of high-quality MRgFUS phantoms.

The subsequent sections of the thesis covered critical topics of the preclinical assessment of newly developed systems and emerging applications in the context of MRgFUS. Notably, the proposed TMPs have an essential role in this process. Firstly, a few simple methods to test the accuracy of MRgFUS robotic devices using both laboratory and MRI-based techniques were presented. Several challenges that may researchers encounter in the process of integrating robotic devices in the MRI were next discussed, and simple measures to overcome them were proposed. Insights on the topic of FUS lesion progression monitoring by T1-W and T2-W FSE imaging were also provided through a series of ablation experiments in *ex-vivo* porcine tissue. The study findings confirmed that proper lesion discrimination on T1-W and T2-W FSE images highly depends on the selected MRI parameters. Accordingly, specific imaging parameters for optimizing the CNR between FUS lesions and surrounding tissue in FSE imaging were suggested, also considering the importance of minimizing the acquisition time in the context of intraprocedural lesion monitoring. It was also demonstrated that multiple images should be acquired at varying depth in tissue to avoid non-detectability of shifted lesions, which constitutes a common phenomenon attributing to tissue inhomogeneities and/or the presence of bubbles that disturb the propagation of ultrasonic waves.

The study further aimed to provide insights on the practicality of using single-element transducers for trans-skull FUS thermal applications. FUS sonications were performed through skull phantoms embedding agar-based tissue mimicking gels using single-element spherically focused transducers with a nominal frequency close to 1 MHz. The

skull phantoms were 3D printed with thermoplastics having the exact skull bone geometry of a healthy volunteer. The temperature field distribution during and after heating was successfully monitored in a 3T MRI scanner using MR thermometry. The ABS skull demonstrated poorer performance in terms of tFUS delivery compared to the Resin skull owing to its higher ultrasonic attenuation and porosity. The thin Resin phantom of 1 mm thickness provided an efficient acoustic window for delivering tFUS and heating up deep phantom areas.

So far, tFUS applications using single-element FUS transducers have been successfully performed mostly in the preclinical setting. The wider adoption and clinical translation of this modality is limited by challenges related to inefficient trans-skull ultrasonic transmission and relevant safety concerns. Although further research is needed to fully exploit the potential of this modality, the preclinical investigation of transcranial ultrasonic propagation from single-element transducers was limited to numerical studies in the context of low intensity tFUS neuromodulation. Therefore, experimental studies involving anthropomorphic phantoms such those described in this thesis could be a valuable tool for accelerating the establishment of a wider range of tFUS applications, including tFUS ablation, potentially working supplementary to the most common numerical studies.

Furthermore, two compact devices for transcranial FUS applications in small animal models have been developed. The second version was shown to provide a cost-effective and ergonomic solution for FUS-mediated non-invasive and reversible disruption of the BBB in small animal models, such as mice and rats, through a top to bottom delivery of pulsed FUS. It should be though noted that the device could also be used for other brain or body applications in various types of rodents, provided that their size is appropriate. The preparation of the experimental setup can be completed within a few minutes taking up minimal space. Such ergonomic devices are expected to facilitate research in the relevant field, thus potentially accelerating clinical translation of the technology, with the ultimate goal to establish alternative therapeutic solutions for neurological diseases.

The last research part of the thesis was dedicated to evaluating the *in-vivo* performance of the developed FUS system (version II) in mouse models together with experts from CING. Primarily, preliminary experiments were carried out in WT mice to obtain evidence of successful BBBD and optimize the relevant protocol in terms of safety and efficiency. Electric power values of 20 to 70 W were tested (corresponding to acoustic power of 6.5 to 22.8 W and in-situ focal pressures of 0.3 to 0.6 MPa). None of the tested power levels resulted in any observed brain damage, and there was no evidence of hemorrhage associated with the procedure. As expected, the success of BBBD relied greatly on achieving efficient ultrasound coupling with the mouse head. Pulsed FUS (10 ms bursts, 1% DF) with an *in-situ* peak pressure amplitude close to 0.5 MPa applied at a frequency of 1 MHz for 100 s in the presence of MBs (5 μL) was selected as offering safe and efficient BBBD and employed in follow-up studies involving antibodies. It should be emphasized that the small skull thickness of mice allowed for efficient transcranial applications with the employed single element transducer, whereas this was not feasible in the case of the thermoplastic phantoms with the human's skull geometry.

The 5XFAD mouse model of AD was developed and used to examine the potential of FUS-mediated delivery of the Aβ (1-40) antibody; an antibody that is targeted against the amyloid plaques found in the AD brain, in the management of AD. High antibody levels were observed in the brain of mice that underwent sonication, whereas non-sonicated mice (receiving the antibody alone) did not show any signs of the antibody. It was thus confirmed that the specific antibody cannot normally enter the brain parenchyma as expected due to its high molecular weight. A single treatment with MBs-enhanced pulsed FUS using the optimized protocol transiently disrupted the BBB allowing for the non-invasive antibody delivery to amyloid plaques within the sonicated brain regions. This was consistently reproduced in ten mice. Some preliminary experiments were carried out to assess the long-term effects of the combined treatment (FUS+antibody), where two treatment sessions were performed at a two-week interval. The combined treatment caused partial clearance of amyloid plaques, whereas mice

receiving only antibody did not show any signs of amyloid clearance. These findings should be confirmed by longer-term studies further examining potential treatment-related cognitive benefit to hold promise for developing disease modifying anti-Aβ therapeutics for clinical use.

Finally, the feasibility of FUS-induced transient BBBD to enhance the biodistribution of AAV9 vectors into the CNS as a potential therapeutic solution for HLD2 was investigated. Specifically, it was tested whether the cell-targeted AAV vector-mediated delivery of the EGFP reporter gene in the brain of P30 WT mice is enhanced after FUS-mediated BBBD. The mice group that was treated with FUS and injected with 50 μL of the AAV9 vector showed a trend towards higher levels of EGFP in multiple brain regions when compared to the non-sonicated mice, further exhibiting higher transduction rates. Nevertheless, further experimentation involving a larger population of mice is required to validate these preliminary findings.

CONCLUSIONS

The ultimate goal of this thesis was to provide insights on the challenges faced in the emerging field of MRgFUS and its potential in the management of brain diseases, through a series of preclinical *ex-vivo* and *in-vivo* experiments. A substantial part of the study was devoted to the development of anthropomorphic TMPs dedicated to the study and validation of MRgFUS systems and protocols, especially for transcranial applications. The relevant outcomes are expected to contribute in the construction of high-quality MRgFUS phantoms by other researchers in the field. In the effort to accelerate the establishment of a wider range of tFUS applications, the study delved into the challenges of non-invasively delivering ultrasonic energy to the brain tissue to impart therapeutic effects in a safe and efficient manner. In this context, the practicality of using single-element transducers for tFUS thermal applications was investigated. Additionally, ergonomic FUS positioning systems dedicated for transcranial applications in small animal models have been presented through a comprehensive technical description and detailed figures, which may be useful for other engineers in the field. Such systems are likely to facilitate research on FUS-mediated BBBD; a topic that receives significant interest in the last few decades. The mice experiments demonstrated the feasibility of delivering specific anti-Aβ antibodies by FUS-mediated BBBD to target the amyloid plaques and promote plaque clearance in AD mice. Additional research is essential to investigate potential cognitive benefits and whether specific AD pathological symptoms are suppressed, and their correlation with the antibody dose. This will help establish the potential of the suggested therapeutic approach in the management of AD, potentially paving the way for clinical translation. FUS-induced transient BBBD was also proven promising as a potential therapeutic solution for HLD2 by enhancing the cell-targeted AAV vector-mediated delivery of the EGFP reporter gene into the CNS. Again, further experimentation involving a larger mice population is required to initially validate these preliminary findings and then to investigate the effect of the administered vector dose on the CNS transduction and is left for future studies.

ETHICS

Mice experiments were approved by the Veterinary services of Cyprus (License number: CY/EXP/PR.L05/2021) and carried out as part of the SOUNDPET project (INTEGRATED/0918/0008) activities in collaboration with experts from the Cyprus Institute of Neurology and Genetics. Appropriate animal handling and procedures were followed according to the Animal health and welfare committee for the project in order to ensure maximum animal wellbeing. Animals were euthanized while under the effect of deep anesthesia.

APPENDIX I: Literature search on preclinical/clinical studies on FUS-mediated BBBD

Table I: Summary of studies reporting FUS-mediated BBBD in animal models and patients. The experimental parameters, main results and adverse events are listed. SD: Sonication duration, AP: Acoustic pressure, PRF: Pulse repetition frequency, PL: Pulse length, DF: Duty factor.

Ref.	Subject	BBBD Protocol	US contrast agent	MRI contrast agent	AP (MPa) / Power (W) / MI	PL (ms) / PRF (Hz) / DF (%)	SD (s)	Molecules Leakage	Main Results	Adverse Events
[445] **2001**	Male New Zealand Rabbits (n=18)	FUS (1.63 MHz 16-sector transducer) 2x2 cm surgical window & MBs	0.05 mL/kg Optison MBs	0.125 mmol/kg GdD Magnevist®	0.2 - 11.5 W (TPAP)	10 or 100 ms/ 1Hz	20	**GdD** (928 Da)	The lowest power levels used (< 0.55 W/ < 1 MPa) produced BBB opening without damage to the surrounding neurons.	70% neurological damage occurred at 11.5 W (5 MPa)
[446] **2002**	Male volunteers (n=7)	Trans-skull diagnostic colour-coded sonography (2-3.5 MHz phased array transducer) & MBs	10 ml Levovist MBs or 3 ml of Optison MBs	0.3 mmol/kg Gd-based contrast agent Magnevist	< 2.69 MPa (PNAP) < 0.54 MPa due to skull	- / 3.5 KHz	N/A	No MRI-detectable leakage of Gd (900 Da)	Ultrasonic destruction of Levovist and Optison MB by diagnostic transcranial colour-coded sonography was shown to be safe.	N/A

[396] **2004**	Adult male New Zealand white rabbits (n=10)	FUS (1.63 MHz 16-channel phased-array transducer) 2x2 cm surgical window & MBs	0.05 ml/kg Optison PFC gas MBs	0.05 ml/kg GdD Magnevist	0.55 /3 W (SPPA)	100 ms/ 1Hz	20	**-Trypan Blue** (1.5 mL/kg, 2 % in saline) **-GdD** (938 Da) **-IgG antibody** leakage at 3 W	Mechanisms of transcapillary macromolecules passage to BBB were identified.	Vasculature damage occurred at 3 W.
[356] **2005**	New Zealand white rabbits (n=22)	Trans-skull FUS (0.69 MHz single element FUS transducer) & MBs	0.05 ml/kg Optison albumin coated MBs	0.125 mmol/kg GdD Magnevist	≤ 3.1 MPa (PRAP)	10 ms/ 1 Hz	20	**GdD** **Trypan Blue** (1.5 mL/kg) **HRP** (40 kDa, 300 mg/kg)	BBB disruption is possible (0.4 MPa-50 %, 0.8 MPa - 90% 1.4 MPa - 100% of the sonicated areas) at a frequency of 0.69 MHz with minimal damage to the exposed brain parenchyma cells.	70-80% of the sonicated areas showed tissue necrosis (H&E) at PRAP ≥ 2.3 MPa.
[447] **2005**	New Zealand white rabbits (n=24)	FUS (1.63 MHz curved 16-element phased array transducer) 2x2 cm surgical window & MBs	0.05 mL/kg Optison MBs	0.125 mmol/Kg Magnevist	0.7-1 MPa	100ms/ 1Hz	20	**MRI contrast agent**	US-induced BBBD is possible without inducing substantial vascular damage that could result in ischemic or apoptotic death to neurons.	Small extravasations and few apoptotic cells occurred. No delayed neurological effects were observed.

[448] **2007**	Male Wistar rats (n=16)	FUS (1 MHz single element FUS Transducer) 10 x 10 mm surgical window & MBs	0-90 µL/kg SonoVue MBs	N/A	0.9/ 1.2 MPa (PNPA)	10ms/ 1Hz	30	**Evans Blue** (100 mg/kg)	The amount of EB extravasation increased monotonically with the quantity of UCA used.	No neurological damage at the UCA dose of 30 µL/kg. Many cells appeared apoptotic at 1.2 MPa with 60 µL/kg UCA.
[441] **2007**	New Zealand white rabbits (n=15)	FUS (0.690 MHz Spherically curved transducer) 2 x 2 cm surgical window & MBs	- 10 µl/kg Definity Lipid-PFC gas MBs - 50 µl/kg Optison albumin - PFC gas MBs	0.125 mmol/kg Magnevist	0.2-1.5 MPa	10ms/ 1Hz	20	**MRI contrast agent**	A 50% probability of BBBD was observed at 0.4 MPa, which was increased to 100% for pressures > 0.8 MPa. Optison® produced a larger effect for the same acoustic pressure amplitude.	Tiny regions of damaged brain parenchyma at pressures > 0.8 MPa.

[276] **2007**	Brown CB57-b16 type mice (n=9)	Trans-skull FUS (1.525 MHz Single element FUS transducer) & MBs	10 µL (0.4 mL/kg) or 25 µL Optison MBs	0.5 mL Gd Omniscan	0.8 - 2.7 MPa	20 ms/ 10Hz	5 x 30 s with 30 s delay	**Gd**	For UCA injection of 10 µL, 15 min before FUS, the threshold of BBB opening was about 2.5 MPa, while for injection of 25 µL, 1 min before FUS, opening occurred at the lowest pressure of 0.8 MPa.	No visible damage was detected on T1 MRI scans
[442] **2008**	New Zealand white rabbits (n=26)	FUS (0.69 MHz focused transducer) 2 x 2 cm surgical window & MBs	50, 100, 250 µl/kg Optison albumin - PFC gas MBs	0.125 mmol/kg Magnevist	0.1 -1.5 MPa	0.1, 1, 10 ms/ 0.5, 1, 2, 5 Hz	20	**MRI contrast agent**	BBBD is not affected by PRF or UCA dose. Both the BBBD magnitude and its threshold depend on the burst length.	Tiny damaged regions of brain parenchyma in ~ 6% of tested locations.
[403] **2008**	Male Sprague-Dawley rats (n=25)	Transcranial FUS (1.5 MHz spherically curved transducer) & MBs	0.05 - 0.07 ml/Kg Optison MBs	.03 mmol/kg GdD Magnevist	1.1 MPa /0.6 W (PNPA)	10ms / 1Hz	-	-**Trypan Blue** (0.6 ml, 4% in saline) **-GdD** -**HRP** (40 KDa, 300 mg/kg) - **La^{3+}**(139 Da, 10 mM)	Tests at several time periods after sonication showed that leakage of agents was accomplished. At 6 and 24 h after sonication function was fully restored and no leakage was observed.	-

[399] **2008**	Male New Zealand white rabbits (n=11)	FUS (0.69 MHz spherically curved transducer) 2 x 2 cm surgical window & MBs	50 µl/Kg Optison MBs	0.125 mmol/kg Magnevist	0.3 - 2.3 MPa	10ms / 1Hz	20	**MRI contrast agent**	BBBD threshold expressed in PNPA increased as a function of the frequency. It appeared to be constant, however, when the exposures were expressed as a function of the mechanical index.	Minor vascular damage, tiny clumps of extravasated erythrocytes &extravasated red blood cells.
[120] **2010**	Wild-type male C57BL/6 mice (n=13)	Trans-skull FUS (1.525 MHz single element transducer) & MBs	25 µl SonoVue MBs	N/A	0.57 MPa (APRP)	20 ms / 10 Hz	2 x 30 s with 30 s delay	fluorescent tagged **Dextrans** (3 and 70 kDa)	Pharmacological molecules of 3 and 70 KDa can pass through the BBB while molecules of 2000 KDa can't.	N/A
[397] **2010**	New Zealand rabbits (n=12) & Male Wistar rats (n=25)	Trans-skull FUS (1.08 MHz Spherically curved Transducer) & MBs	10 µL/kg Definity MBs	0.1 mmol/kg Omniscan	3.9 W/ 0.38 MPa (PNPA) 0.2- 0.8 W/ 0.27-0.54 MPa (PNPA)	10ms / 1Hz	30-1200 // 300	**MRI contrast agent**	Lower power for longer time gives higher permeability, than shorter sonications of increased power. Exposure durations < 180 s (at 0.38 MPa) are linked with a low probability of irreversible damage.	Exposure > 600 s (for 0.38 MPa) & pressure amplitudes > 0.47 MPa (for 300 s) resulted in ≥ 50% localized lesions.

[361] **2011**	Male rhesus macaques (n=2)	Trans-skull FUS (0.5 MHz Single element Transducer) & MBs	500µl In-house MBs & Definity MBs	0.2 mL/kg Gadodiamide Omniscan	0.3, 0.45 and 0.6MPa (focal maximum pressure)	10 ms / 2 Hz	120	**Gadodiamide** (573.66 Da)	Transcranial HIFU induced BBBD in non-human primates with different pressures and microbubbles type. BBBD was induced at all tested pressures (larger BBBD at 0.6 MPa).	An edematous region was detected using custom made microbubbles at 0.6 MPa.
[449] **2011**	Male Wistar rats (n=20)	US (1.15-1.2 MHz single element planar transducer) 5 x 5 mm surgical window & MBs	0.02 mL/kg Definity MBs	N/A	0.071 - 0.25 MPa (PNPA) / 0.26 -1.45 W (input electric power)	10 ms / 1 Hz	120	**Dextran-conjugated Texas Red** (10 kDa)	Different types of leakage can be attained by controlling the acoustic pressure. Smaller vessels are easier to disrupt.	Haemorrhagic damages were observed at higher powers (significant extravasation at 0.173 MPa).
[450] **2011**	Wistar rats (n=28)	Trans-skull FUS (8 sector spherically focused array 1.18 MHz) & MBs	0.02 ml/kg Definity MBs	0.2 mL/kg Gd Omniscan	0.54 MPa	10 ms (3 µs cycles with 6 - 600 µs delay) / 1 Hz PRF OR 6 µs delay/ 0.2, 1, 2 Hz	120 OR 300	**Gd** (T1-w images)	Use of short burst lengths has the potential to decrease treatment times. PRF of 2 Hz may increase enhancement over a 1-Hz PRF when used with infusion MB delivery.	The shortest delay (6 µs) provided the highest percentage of cases (42.5%) resulted in edema (T2w images)

[451] **2011**	Male Fischer rats (n=8)	Trans-skull FUS (1-MHz single element transducer) & MBs	450 µL/kg SonoVue MBs (phosphor-lipid-coated MBs)	1 mmol/kg Gd Omniscan	0.5 MPa (PNPA) / 1.43 W	50 ms/ 1Hz	60	**Gd** **Evans Blue** (100 mg/kg)	Pulsed HIFU enhances the relative permeability of the BTB in glioma rats. The tumor-to-contralateral brain ratio of EB were highest after pulsed HIFU exposure.	N/A
[277] **2011**	C57Bl6 male mice (n=99)	Transcranial FUS (1.525 MHz single element focused) & MBs	0.01, 0.05, 0.25 µL/g Definity MBs	N/A	0.46 MPa (PRPA)	0.03- 30 ms/ 0.1 to 25Hz	30	**Texas Red-tagged dextrans** (3 kDa, 60 µg/g)	The lowest values for consistent disruption and dextran delivery were: 0.2 ms PL and 5 Hz PRF. As PL increases, the delivered dextran concentration increases.	N/A
[452] **2012**	Male F98 glioma-bearing Fischer rats (n=27)	Trans-skull FUS (1-MHz single element transducer) & MBs	300 µL/kg SonoVue MBs	1 mmol/kg Gd Omniscan	5.72 W	50 ms/ 1 Hz	60	**Evans Blue** (100 mg/kg) **Gd**	Pulsed HIFU significantly elevated the tumor: brain drug ratio in the focal region, and led to a widening of intercellular gaps of tumors (H&E)	Increased extravasation of red blood cells in the sonicated tumor tissues.

[363] **2013**	Swine (n=29)	Trans-skull FUS (0.4 MHz single element transducer) & MBs	0.3 mL/kg/min SonoVue MBs	0.1 mmol/kg **Gd-DTPA** Magnevist	0.26, 0.43, 0.56 MPa	10ms/ 1Hz	30	**Gd-DTPA Evans Blue**	The threshold pressure for BBBD in swine was 0.43 MPa. Neuronavigation allows monitoring of BBBD during FUS. MR relaxometry and ICP-OES assay demonstrated high correlation, suggesting that Gd-DTPA deposition can be directly measured by imaging.	9.5% of animals appeared erythrocyte extravasations (H&E). Multipoint exposure (3 x 3 grid) showed a higher incidence of extravasations.
[453] **2013**	Male Sprague-Dawley rats (18 normal, 16 tumor animals)	Trans-skull FUS (0.4 MHz single element transducer) & MBs	2.4 μL/kg SonoVue SF6-coated MBs	0.3 mL/kg Gd-DTPA Magnevist®	0.4 MPa (PNPA; free field)	10 ms/ 1 Hz	90	**Evans Blue** (960 Da, 2 mg/kg, 2% in saline) **Gd-DTPA** (938 Da)	The AUC values of Gd-DTPA measured by MRI were well correlated with EB delivery, suggesting that Gd-DTPA is a good indicator of total small-molecule delivery. Permeability -enhancing effect may be more significant on tumor peripheral.	Structure did not change significantly. Hemorrhagic regions remained similar to those in the unexposed tumor (T2-w MRI, H&E of tumors).

Ref.	Subject	BBBD Protocol	US contrast agent	MRI contrast agent	AP (MPa) / Power (W) / MI	PL (ms) / PRF (Hz) / DF (%)	SD (s)	Molecules Leakage	Main Results	Adverse Events
[454] **2014**	Swine (n=10)	Trans-skull FUS (256-Channel Dual-freq. Phased-Array System) & MBs	0.3 mL/kg/min SonoVue MBs	N/A	0.52/ 0.78 MPa	10 ms/ 1 Hz	30	**Evans blue** (2 mg/kg, 3% in saline; 960 Da ⇒ 60-70 kDa when bounds to serum albumin)	Dual-frequency exposure can potentially enhance the BBBD effect. Dual-frequency FUS exposure did not further increase erythrocyte extravasation above the level obtained with traditional single-frequency exposures. The pressure level in multiple exposures should be reoptimized when intending to induce a large BBB-opened region.	Extravasations for single-point exposures occurred in 15.3% at 400 kHz 10.0% at 600 kHz (0.52 MPa) 66.7% at 400 kHz (0.78 MPa). For 3 × 3 multiple exposures occurred in 76.7% at 400 kHz (0.52 MPa). (H&E)

[278] **2014**	C57BL/6 mice (n=18)	Trans-skull FUS (1.5 MHz single element transducer) & MBs	1 µl/g in-house polydisperse (IHP) MBs or Definity MBs	0.3 mL GD-DTPA Omniscan	0.3, 0.45, 0.6 MPa	20ms/ 10Hz	60	**GD-DTPA**	The MB type and distribution could have significant effects on the FUS-induced BBBD mostly at higher pressure levels (0.45/ 0.6 MPa). IHP MBs showed significantly higher permeability and volume of opening at 0.3 MPa.	There were no damage in the Definity® injected groups. Several dark neurons were detected in one mouse (0.45 MPa) injected with IHP MBs. (H&E).
[455] **2015**	Rats (n=3: FUS & drug, n=4: FUS only)	FUS (690 kHz single element FUS transducer) & MBs & Lipo-DOX (5.67 mg/kg) - three weekly sessions	10 µl/kg Definity MBs	0.25 ml/kg of GdDTPA (Magnevist)	0.55 – 0.81 MPa	10 ms / 1 Hz	60	**GdDTPA** **Lipo-DOX** (doxorubicin: 580 Da)	Clinically-relevant concentrations (4.8 ± 0.5 µg/g) of DOX were delivered to the brain. The concentration of Lipo-DOX was reduced by 32% when injected 10 min after the last sonication compared to pre-sonication injection.	In histology, some rats who received FUS & drug had regions with evidence of prior damage (scar or cyst).

[393] **2015**	Balb/c male mice	Pulsed FUS (500-kHz single-element FUS) & MBs & LpDNA solution (dose: 3, 9, and 27 μg, 1 μg /μL)	4 μL/kg SonoVue SF6 MBs ($2–5 \times 10^8$ bubbles /mL)	N/A	0.3, 0.5, 0.8 MPa	10 ms / 1 Hz / 1% DC	60	**Evans Blue** (30 mg/kg) **Gene transduction by LpDNA**	Successful BBBD was achieved at 0.5 MPa, but not 0.3 MPa. Concurrent FUS-BBBD and LpDNA induced luciferase proteins and increase GDNF protein levels. Transduction after BBBD had a relative intensity 5-fold greater than that of the LpDNA only. The transfection efficiency was found to be LpDNA dose dependent (5 MPa).	At 0.8 Mpa, a broad flux area with hemorrhage damage presented in the exposure regions.
[456] **2016**	Adult male rats (n=12)	Transcranial Burst-Mode FUS (1.5-MHz FUS transducer) & MBs	30 μg/kg SonoVue SF6-coated US MBs	N/A	0.11– 0.705 MPa (PNP after skull penetration)	10 ms/ 1 Hz	60	**Evans Blue** (2 mg/kg)	Backscattered US acoustic wave reconstruction provides a feasible way to to guide FUS-BBB opening.	Erythrocyte extravasations were observed at 0.705 MPa, but not at 0.467 MPa.

[416] **2016**	adult C57BL/6 mice (n=16)	Transcranial FUS (1.68 MHz custom-built FUS transducer) with/without MBs	0.02 ml/kg Definity MBs (prior to FUS)	0.2 ml/kg Gd-based MCA (Gadovist)	0.39 and 0.78 MPa (with MBs) 1.56 and 3.0 MPa (without MBs)	10ms/ 1Hz	120	**MCA** (T1-w images)	US-Induced Neurogenesis Requires increased BBB Permeability. Only FUS at ~0.78 MPa with MBs promoted hippocampal neurogenesis associated with an increase in BBB permeability.	N/A
[457] **2016**	Nude rats with HER2-positive cells (n=30)	FUS (690 kHz single-element sph. focused transducer) & 2/4 mg/kg trastuzumab and pertuzumab (first/ next wks.)	100 µl/kg Optison MBs (prior to FUS; diluted 10 times with saline)	0.25 ml/kg Gd-DTPA (Magnevist)	0.40 - 0.70 W => 0.46 - 0.62 MPa (PNP)	10-ms / 1 Hz	60 (each son.)	**Gd-DTPA** (T1-w images; 938 Da)	The median survival of the FUS+antibody animals was longer compared to the control group. 4/10 animals in the FUS+antibody group showed an average tumor growth constant of 0.010 ± 0.007 mm^3/day, compared to 0.033 ± 0.009 mm3 /day for antibody-only animals.	In most animals, showed that cystic and necrotic areas started to develop at weeks 13–15 (T2-w imaging).

[458] **2016**	Female Sprague Dawley rats	MRgFUS (589.636 KHz single- element sph. focused transducer) & MB	100 μL Optison MBs at a rate of 1 μL/s	200 μL Gadofosveset (Ablavar)	0.3 MPa	10-ms/ 1% DC	120; per 9 spots	**Gadofosveset** (T1-w images)	Within 5 min posttreatment, BBBD and increased expression of DAMPs leading to a SIR (compatible with ischemia or mild traumatic brain injury) that lasted ~24 h were observed.	Early injuries were evidenced by TUNEL staining. DAMP response included elevations in heat-shock proteins and TNFα indicative of SIR in parenchyma.
[459] **2016**	healthy Sprague-Dawley rats (n=15)	MRgFUS (690 kHz Single element, focused transducer) & MBs 6 weekly sessions	10 μL/kg Definity MBs - before each sonication	0.25 mL/kg Gd-DTPA (Magnevist)	0.66, 0.73 and 0.80 MPa (PNP)	10 ms/ 1 Hz	60	**Gd** (T1-w images; 938 Da)	Positive relationship found between pressure and SI change in post-sonication T1-w images. Process of repeatable BBBD does not produce additional significant side effects. T2-w imaging agreed with histopathology.	The most extensive damage was observed at 0.8 MPa (e.g., multiple hemorrhages & hemorrhagic infarct)

[460] **2016**	healthy and tumor-bearing mice (U87 glioma animal model) (n=35)	Transcranial FUS (400 kHz transducer) & MBs & Bevacizumab (50 mg/kg per week for 5 weeks)	10 µL SonoVue SF6–filled US MBs (prior to FUS)	Gd-DTPA (Magnevist)	0.4–0.8 MPa (PNP)	10 ms/ 1 Hz	60	**Gd-DTPA** **Bevacizumab** (150 kDa)	FUS significantly enhanced bevacizumab penetration into the CNS by 5.7 to 56.7 fold compared to nonexposed brain. Drug delivery retarded glioma progression, with a significantly increased median survival (135% in the drug + FUS group vs 48% in the drug-alone group.	Erythrocyte extravasation was caused by 0.53-MPa exposure (H&E)
[461] **2017**	Female Fischer 344 rats inoculated with F98 glioma cells	MRgFUS (1.14 MHz single element FUS transducer) 9-spot square grid & MBs & Nanoparticles; CDDP-BPN	$1x10^5$ MBs/g albumin-shelled MBs	0.25 µl/g MRI contrast agent	0.6/ 0.8 MPa (PNP)	0.5 % DC	120	**MRI contrast agent** **CDDP-BPN** (2.5 mg/kg, composed of PAA/PAA-PEG: **27 kDa PAA**)	MRgFUS is capable of enhancing the delivery of ~60 nm fluorescent tracer BPN in F98 glioma models. CDDP-BPN were delivered to gliomas using MRgFUS, eliciting a significant reduction in tumor growth and improved animal survival.	N/A

[462] **2017**	Female adult Sprague-Dawley rats	Transcranial MRgFUS & (1.5 MHz FUS transducer) & hNPCs; ($1.5x10^6$ cells in 0.5 mL of PBS, after FUS)	250 mL monodisperse MBs; ($2.27x10^9$ MBs per mL, prior to FUS)	0.2 mL/kg Gadodiamide (Omniscan)	0.45 MPa	5 ms/ 10 Hz/ 5% DC	60	**Evans Blue** (150 mL at 2%) **Gadodiamide** (T1-w MRI) **hNPCs**	Magnetic attraction can substantially enhance the retention of stem cells (SPION-loaded hNPCs) after FUS-mediated BBBD. Greater numbers of SPIONs-loaded cells retained in the brain at the site of BBBD as compared to noniron loaded cells.	No evidence of FUS-induced damage to the tissue. (H&E)
[423] **2017**	Male Sprague-Dawley rats (n=31)	Transcranial MRgFUS (690 kHz single element FUS transducer; 5 overlapping sonications) & MBs	10 µl/kg Definity MBs	0.25 mL/kg Gd-DTPA (Magnevist)	0.55 - 0.81 MPa.	10 ms/ 1 Hz	60 (each son.)	**DTPA** (T1-w images)	For BBBD at 0.55 MPa, Pgp was suppressed up to 48 hours and restored by 72 hours. At 0.81 MPa, suppression can last 72 hours or longer. These findings support that MB-enhanced FUS disrupts the functional components of the BBB through suppression of drug efflux.	T2*WI images revealed vessel damage and extravasated erythrocytes at 0.81 MPa. H&E revealed tiny clusters of extravasated erythrocytes at 0.55 MPa.

[362] **2017**	Male NHPs (n=5); rhesus macaques (n=4) & marmoset (n=1)	Transcranial FUS (0.5 MHz single-element spherical-segment FUS transducer) & MBs	In-house manufactured lipid-shell, MBs (2×10^5 Bubbles /mL)	0.2 ml/kg Gadodiamide	0.25 - 0.6 MPa (PNP)	10 ms/ 2 Hz	120	**Gadodiamide** (T1-w images)	Results prove linear relationship of the incidence angle with the volume of BBB opening and the PNP, and monotonic increase of the opening volume with close to normal incidence angles.	No evidence of damage (on T2-weighted and SWI image).
[463] **2017**	Adult male Sprague Dawley Rats (n=33) Target: striatum	Transcranial FUS (1 MHz focused annular piezoelectric array) & MBs & dsAAV1-CMV-eGFP	4 mL/kg EB+MB cocktail; 4×10^8/ 2×10^9/ 4×10^9 MB/kg of 2-µm MB or 4×10^7/ 2×10^8/ 4×10^8 MB/kg of 6-µm MB	1 MPa (PNP)	N/A	100 Hz/ 10% DC	300	**Evans Blue** (4 mL/kg of 1, 2, 4 wt%) **Biologically relevant agent Virus: dsAAV1-CMV-eGFP (**50 µL**)**	Regarding the effect of gas volume doses, a linear dose-response of Evans Blue extravasation was found, suggesting that MB gas volume dose, not size, determines the extent of BBBD (1 MHz, 0.5 MPa). One wk. after BBBD, gene delivery and expression was demonstrated using a viral vector.	Evans Blue experiments showed limited hemorrhaging immediately after BBBD at the high MB volume doses but was not present a week after.

[125] **2017**	Wild-type mice Target: hippocampus and motor cortex	FUS (1.5 MHz single element FUS transducer) & MBs & AAV vectors	5 µl lipid-shelled in-house MBs (prior to FUS)	0.15 ml bolus GD-DTPA (Omniscan)	0.74 MPa (PRAP, free field)	10 ms/ 5 Hz	120	**GD-DTPA** (T1-w images) **AAV** (100 µl diluted AAV vectors)	The volume of BBBD, which also determines the volume of viral transduction, can be altered through proper selection of the US parameters.	No structural damage was observed (H&E). Microglia staining revealed no notable related inflammatory response.
[464] **2017**	Trans–human skull porcine model (n=11)	MRgFUS (230-kHz FUS array of 1024 elements; ExAblate 4000, InSightec; 3 x 3 grid, Craniotomy)	2 mL/ kg or 4 mL/kg Definity MBs	0.1 mL/kg Gd (Gadovist)	3–20 W	2 ms on/ 28 ms off bursts of 300 ms (each of 9 spots)	50 s; 2.7 s per cycle	**Gd** (FSE T1-w images) **Evans Blue** (2 mL/kg, ≈65 kDa when bounded to albumin)	With repeatable results, 5 W and 4 µL/kg MBs were considered standard parameters for this BBBD protocol. Upon optimization of cavitation thresholds only low level scattered extravasation of red blood cells were observed.	In some cases, hemorrhages larger than 500 µm were discovered at 4–10 W with 4 µL/kg MBs (H&E).

[465] **2017**	Male Sprague-Dawley rats (n=12)	MRgFUS (551.5 kHz spherically focused transducer) & MBs	20 µL/kg Definity MBs	Gd-based contrast agent (Gadovist)	0.128 MPa increased by 0.008MPa every sec.	10 ms/ 1Hz	120	**Gd** (T1-w images) **Evans Blue** (4% in saline)	There is an acute inflammatory response in hippocampal microvessels following sonication and increased transcription of proinflammatory cytokine genes, largely returning to baseline by 24 hrs.	N/A
[466] **2017**	Male Sprague-Dawley Rats (n=24)	Continuous FUS (1 MHz single-element focused transducer) & nanoscale droplets	10 mg/kg PEG-PLGA-PFP nano-droplets	N/A	0.5, 1.0 or 1.5 MPa	100% DC	180 or 300	**Evans Blue** (100 mg/kg)	The nanodroplets had the capacity to realize liquid to gas phase shift under FUS. Significant EB extravasation occurred when pressure reached 1.0 MPa. Prolonged sonication could enhance the level of BBBD and broaden the time window.	Intracerebral hemorrhages and erythrocyte extravasations were observed when the pressure was increased to 1.5 MPa.

[467] **2018**	Male Sprague-Dawley rats (n=100)	FUS (400 kHz FUS transducer; multiple sessions) & MBs	0.15µl/kg or 0.4µl/kg SonoVue Lipid-shell SF6 MBs & 0.03 ml/kg of heparin	N/A	0, 0.2 – 0.3, 0.5 and 0.9 MPa (or MI 0.33–0.47, 0.8, and 1.4.	10ms/ 1Hz	120	N/A	Frequent exposure of excessive FUS (1.4 MI) produced minor and short-term behavioral changes, while frequent BBBD with below-threshold exposure (MI: 0.33–0.8) did not. Excessive doses of MBs induced a cellular apoptotic response.	Adverse effects included macrophage infiltration, parenchymal loss, and necrosis (Histological examination).
[468] **2018**	Wistar rats (n = 30) & 9L Glioma mice models (n=20)	Continuous or intermittent mCUES (US diagnostic machine; 1.7/3.3 MHz probe) & Temozolomide (prior to FUS, daily for 5 d)	1 ml/kg MB contrast suspension (8 µl sulfur hexafuoride per ml)	N/A	MI: 0.8	400-ms interval (pulsed)	600	**Evans Blue** (2%, 50 mg/kg) **Temozolomide** (100 mg/kg)	When rats were treated by mCEUS with intermittent launches + MBs, BBB permeability was increased, and drug penetration was enhanced. Induction of permeability in temozolomide-treated glioma model rats was associated with reduction in tumor volume.	N/A

[469] **2019**	Rat F98 glioma model	Transcranial MRgFUS (230 kHz phased array transducer; ExAblate Neuro, InSightec, multiple son.) & MBs	10 µl/kg Definity MBs	0.125 mmol/kg (Gadavist)	0.16 - 0.39 W	5 ms/ 1.1 Hz	75 (each son.)	**MRI contrast agent** (T1-w images) **carboplatin** delivery (50 mg/kg)	In tumor-bearing rats, concentrations of Gadavist were 1.7 and 3.3 times higher in the tumor center and margin, respectively, than non-sonicated tumors. Tissue-to-plasma ratios of carboplatin concentrations were significantly increased in brain and tumor after FUS.	No brain tissue damage occurred. Only a tiny scar in the striatum in one animal (H&E).
[470] **2018**	Female Sprague Dawley rats (n=40)	Transcranial FUS (0.5MHz transducer) & bubble-based agents	- 30 µl/kg. Optison MBs - 6 µl/kg Defnity MBs - 737 µl/kg Nano-bubbles	N/A	0.1–0.7 MPa	10 ms/ 1 Hz	100	**Evans blue**	Under similar total gas volume, nanobubbles showed a more reliable opening effect compared to Optison and Defnity.	N/A

[24] **2018**	Patients with AD (n=5)	Transcranial MRgFUS (220 kHz; ExAblate Neuro, InSightec, 2x2/ 3x3 grid) & MBs	4 µl/kg Definity MBs	Gd	4.6 W (AMSP)	2 ms on/ 28 ms off bursts of 300 ms (each spot)	50 (2.7 s RI)	**Gd**	BBB within the target volume was safely, reversibly, and repeatedly opened and completely closed within 24 h.	We observed no serious clinical or radiographic adverse events (no haemorrhages, swelling, or neurologic deficits.
[471] **2019**	Women (n=2) and men (n=2) with ALS Target: eloquent primary motor cortex	Transcranial burst-mode MRgFUS (220 kHz phased array; ExAblate Neuro 4000 system type 2.0, InSightec®) & MBs	4 µl/kg Definity perflutren MBs	Gd	4.0–10.0 W	0.88% DC & 300 ms PRP	90 (each son.)	**Gd** (T1-w images)	Gd leakage at the target site occurred immediately after FUS in all subjects and normalized 24 hours later. MRgFUS can be coupled with therapeutics to provide a targeted delivery platform in ALS.	Mild-to-moderate procedure-related adverse events included scalp pain, edema, and scalp petechial rash.

[472] **2019**	Patients with glioma (n=5)	Transcranial MRgFUS (220 KHz phased array transducer; ExAblate Neuro, InSightec) & lipo-DOX +temozolomide chemotherapy	4 µl/kg Definity MBs	Gd	4-15 W	2.6 ms on/ 30.4 ms off 300 ms bursts (at each spot)	50 (3x3 grid)	**Gd** (T1-w images)	The targeted BBB showed an immediate 15–50% increased contrast enhancement on T1-w MRI, and resolution ~20 hours after. Chemotherapy concentration was higher in the tissue where BBBD occurred.	No adverse clinical or radiologic events related to the procedure
[473] **2019**	Male rTg4510 mice with tau pathology (n=13) Target: hippocampus	Transcranial FUS (1.5 MHz single-element spherical-segment transducer) & MBs (multiple sessions)	0.1 µL/g polydisperse 'in-house' MBs	0.3 ml GD-DTPA (Omniscan)	0.45 MPa (PNAP)	6.7 ms/ 10 Hz	60	**GD-DTPA** (T1-w images)	Quantification of the opening volume across weeks suggests that repeated US application does not compromise the integrity of the barrier. FUS-induced BBB opening reduces p-tau from the hippocampus.	FUS-induced BBBD does not compromise neuronal integrity. There was no evidence of edematous incidences.

[474] **2019**	Male Sprague Dawley rats (n=19) Target: striatum	MRgFUS (spherically focused transducer) & cocktail of rAAV and MBs	0.4 - 0.64 × 10^8 MBs/kg Optison MBs	0.4 ml/kg Gd-DTPA (Magnevist)	0.97 MPa (PRAP)	10 ms/ 1 Hz	200	**Gd-DTPA** (T1-w images)	BBBD allowed efficient delivery of the AAV1/2 vector to the targeted rodent striatum, with 50%–75% of striatal neurons transduced and GFP transgene expression. The method is promising for gene therapy of neurological disorders.	Transient inflammation from BBBD alone was noted for the first few days, but there was no evidence of brain inflammation from 2 weeks to 6 months.
[475] **2019**	Female C57BL/6 mouse (n=1)	Transcranial FUS (1-MHz transducer) & MBs	1 μL/g Lipid-coated MBs solution (8 × 10^8 MBs/mL)	0.2 mL gadodiamide (Omniscan)	280 kPa (PNP)	4 μs	N/A	**Gadodiamide** (T1-w 2D FLASH images)	Power cavitation-guided BBBD with FUS could constitute a standalone system that may not require MRI guidance during the procedure.	N/A

[364] **2019**	Female Sheep (n=7)	Transcranial pulsed sinusoidal FUS waves (250 kHz single-element FUS transducer) & MBs	0.01 mL/kg Definity® MBs	0.2 mL/kg Magnevist	0.39 - 0.58 MPa (in situ)	10 ms/ 1 Hz	60 or 120	**Gd**	Localized enhancement in BBB permeability was observed at acoustic pressure of 0.48 Mpa, whereas sonication at 0.58 MPa resulted in localized minor cerebral hemorrhage.	The sheep exposed to the highest pressure of 0.58 MPa exhibited evidence of hemorrhage around the targeted region.
[476] **2019**	Male R6/2 HD mice and the wild-type littermates Target: striatum	Transcranial pulsed FUS (500 kHz single-element FUS transducer) & MBs & Gene delivery into the CNS (weekly sessions)	0.1 mg/kg SonoVue phospholipid-coated MBs (prior to FUS)	0.012 mmol/kg Gd-DTPA (Magnevist)	0.33 MPa	10-ms/ 1-Hz/ 1% DC	30 or 60	**Gd-DTPA** (T1-w images; 938 Da) **Evans Blue** (67 kDa when conjugated with albumin in plasma **GDNF-gene** delivery	US-BBBD facilitates CNS GDNF-gene delivery into the R6/2 HD mice. FUS & MBs-enhanced GDNF transduction was shown to be capable of reversing motor deficits, brain rostral atrophy, and neuronal dysfunction and loss.	The HE-stained brain sections confirmed no potential capillary/brain tissue damage.

[477] **2019**	Female Sprague Dawley rats (n = 40)	Transcranial FUS & nanobubbles (0.5 MHz single element focused transducer)	737, 73.7 and 7.37 mL/kg Lipid-shelled nano-bubbles (dilutions: 1:1, 1:10, 1:100)	-	0.14 - 0.76 MPa	10 ms/ 1 Hz	120	**Evans blue** (3.33 mL/kg)	With all three tested dilutions (1:1, 1:10 and 1:100), successful BBBD was achieved under real-time feedback control. The pressure required to achieve a target level of acoustic emissions was independent of the nanobubble concentration (at 0.5 MHz).	-
[478] **2020**	Patients with early AD (n=6) Target: Hippocampus & entorhinal cortex	MR-guided, low-intensity FUS (220 KHz phased array; ExAblate Neuro Type 2; InSightec) & MBs	Definity MBs	0.1 mmol/kg gadobutrol	N/A	N/A	N/A	**MRI contrast agent** (T1-w SPGR images)	Post-FUS MR images revealed immediate and sizable hippocampal parenchymal contrast enhancement of 95 ± 4% of the FUS targeted volume, indicating BBBD followed by BBB closure within 24 h.	There were no treatment-related adverse effects or neurological changes (up to 15 months post-FUS).

[479] **2020**	Male Sprague Dawley rats	FUS (1.1 MHz single element transducer, double FUS exposure; 5 min apart)	30 µL/kg Definity MBs (0.2 mL/2 mins)	0.1 mL/ kg Gadovist	0.30 MPa	10 ms/ 1 Hz	120	**Gadovist** **Evans blue** (1 mL/kg) **MRI visible NCs** (100 - 200 nm, 2 mg/mL)	IV injected NCs were able to penetrate the BBB after FUS delivered at the low power of 0.3MPa. NC load was sufficient to cause localized changes in neural activity.	No damage was detected in T2-weighted MR images.
[480] **2021**	Patients with PDD (n=5)	Transcranial MRgFUS (220 kHz; ExAblate Neuro, InSightec, 2 sessions 2–3 weeks apart)	4 µl/kg Luminity MBs	Gd (Gadovist)	17 W (AMSP, session.1) 19.4 W (AMSP, session.2)	N/A	85.8 ses.1 80.4 ses.2	**Gd**	BBBD in the parieto-occipitotemporal junction occurred in 8/10 of treatments. Gd enhancement disappeared within 24 h of BBBD in 5/10 procedures.	MRI showed no evidence of swelling or hemorrhage. Minor effects included local phlebitis and needle site redness
[481] **2021**	Rhesus macaques (n=2)	RaSP or LP US (300 kHz single-element, spherical focused transducer)	0.2 µL/g SonoVue TM MBs	0.15–0.17 mL/kg Gd-DTPA	0.56 MPa (PNP)	300 µs, 600 µs, 10 ms/ 1 Hz	180	**Gd-DTPA** (T1w FSE images)	The relative signal enhancement in RaSP reached more than 60% of that with LP, while the energy deposition was only 6% of LP.	No edema or hemorrhage was found on MR images after RaSP.

[482] **2021**	Patients with rGBM (n=6)	Transcranial FUS (500 kHz transducer; NaviFUS system 3x3 grid spots) & MBs	0.1 ml/kg SonoVue MBs	0.2 ml/kg Gd-DTPA (Magnevist; infusion rate of 4 ml/s)	0.48, 0.58, and 0.68 MI	10 ms/ 9 Hz **(**nine-spot steering switch for every second**)**	120	**Gd**	A dose-dependent BBBD was observed, which reverted to baseline within 24 hours after treatment. No immunological response was observed under the applied FUS level in humans.	36 adverse events in five patients during the post-1-month follow-up period. No AEs were determined to be related to FUS treatment or MB.
[483] **2021**	GL261 gliomas in C57BL/6 mice & EGFRvIII-U87 gliomas in NSG mice & chemokine CXCL10 in GL261 mice	LIPU preclinical platform (1-MHz transducer)	200-mL Lumason MBs	N/A	0.3 MPa (in situ)	1 Hz/ 2.5% DC	120	**Evans Blue** (100 mg/kg)	LIPU increases immune therapeutic delivery to the tumor microenvironment with an associated increase in survival; Mice treated with anti–PD-1 and LIPU had a median survival duration of 58 days compared with 39 days for mice treated with anti–PD only.	Repeated dual IV treatments rarely led to tail necrosis, leading to partial amputation. EGFRvIII-CAR T cells lead to mild, short-term signs of systemic toxicity.

[484] **2021**	PDGFB-driven high-grade syngeneic pontine glioma model (n=40)	Transcranial FUS (1.5 MHz single-element, spherical-segment US transducer, 2x2 grid) & MBs	100 µl **SonoVue** MBs	0.2 ml GD-DTPA (Omniscan)	0.7 MPa	10 ms/ 5 Hz	120 for 600 pul-ses	**Gd** (T1-w 2D FLASH images) **Evans blue** **Etoposide** delivery (20 mg/kg)	Repeated FUS was demonstrated to be safe and feasible to open BBB and enhance drug delivery in a mouse pontine glioma. FUS increased intra-tumoral etoposide concentration by more than fivefold. There was no difference in survival between the groups.	Tumor margins in both groups showed regions of micro-hemorrhage. The degree of intra-tumoral hemorrhage and inflammation on H&E in control and treated mice was similar.

APPENDIX II: Literature search on MR relaxation times of TMPs

Table II1: T1 and T2 relaxation times of agar-based phantoms, along with the MR technique used for relaxometry mapping and the temperature at which measurements were conducted (if provided by the relevant study).[1]

Agar-based phantoms				
Recipe	**T1 rel. time (ms)**	**T2 rel. time (ms)**	**Purpose**	**Ref.**
3% agarose in water **3 % fibrous cellulose** **7% glycerol** **0.05 % methylene blue**	1679 ± 15 3T MR scanner *IR* seq. TI: 50 – 5000 ms	41 ± 1 3T MR scanner *ME SE* seq. -	Tumor mimic for MRgFUS studies	[174]
0.5 % agar in water **5 – 30 µl gadopentetate acid meglumine**	735-1667 3T MR scanner *IR SE* seq. TI: 100-2100 ms	236-311 3T MR scanner *ME SE* seq. TE: 8-56 ms	Phantom for testing fast T1 mapping method	[167]
2 % w/v agar **4 % w/v wood powder**	844 1.5 T MR scanner *T1-w IR FSE* seq. TI: 200 – 1600 ms	66 1.5 T MR scanner *T2-w FSE* seq. TE: 23 – 101 ms	TMP for MRgFUS applications	[110]

[1] IR = Inversion Recovery; ME = Multi-Echo; SE = Spin-Echo; FSE = Fast SE; T2-w = T2-weighted; T1-w = T1-weighted; TSE = Turbo SE; CPMG = Carr-Purcell-Meiboom-Gill; TIRSE = Turbo Inversion Recovery SE; SR = Saturation Recovery; DESPOT = Driven Equilibrium Single Pulse Observation of T1/T2.

0.6 % agar solution **0 – 0.15 mM $MnCl_2$**	700 – 1800 3T MR scanner *2D IR TSE* seq. TI: 30 – 2000 ms	-	Brain MRI phantom	[170]
4% agarose gel	1207 ± 168 1.5 T MR scanner *IR* seq.	66 ± 9 1.5 T MR scanner *ME* seq.	CT/MRI prostate phantom	[171]
2 % w/v agar **25% v/v evaporated milk** **1.2% w/v silica**	852 1.5 T MR scanner *IR SE* seq. TIs: 66 – 750 ms	66 1.5 T MR scanner *T2-w FSE* seq. ETs: 18 – 99 ms	Brain TMP for US surgery	[93]
1 liter of distilled water **35 g high gel strength agar** **80 mL glycerol.** **30 g cellulose particles (size: 50 µm)** **20 mL of formaldehyde (2 wt. %)**	1090 ± 140 (0.5 T) 1150 ± 162 (1.5 T)	42 ± 3 (0.5 T) 50 ± 6 (1.5 T)	Carotid Phantom for MRI applications	[161]
82.97 wt. % distilled water **3.0 wt. % agar, 11.21 wt. % glycerol** **0.53 wt. % silicon carbide (400 grain)** **0.88 wt. % aluminum oxide (0.3 µm)** **0.94 wt. % aluminum oxide (3 µm)** **0.46 wt. % benzalkoniumchloride**	1504 ± 10 3T MR scanner *IR* seq. -	40.0 ± 0.4 3T MR scanner *CPMG* SE seq. TEs: 10 – 80 ms	Multimodality renal artery phantom	[172]

0.3 % w/v agarose + 0.03mM Gd-DTPA/ **0.6 % w/v agarose + 0.10mM Gd-DTPA**	1654 ± 9/ 1134 ± 7 1.5 T MR scanner 2D *TIRSE* seq. TIs: 25 – 3970 ms 19 °C	376 ± 4/ 200 ± 7 1.5 T MR scanner 2D *CPMG ME SE* seq. TEs: 20 –640 ms 19 °C	TMP simulating T1 and T2 of neonatal brain	[173]
0.3 – 4 wt. % agarose **0.5 – 8 mM Ni^{2+}**	180 - 1400 10.7 MHz (0.25 T) MR analyzer, *SR* seq.	34 - 200 10.7 MHz (0.25 T) MR analyzer, *SE* seq.	TMP for MR imaging	[163]
agarose gel **0.0 – 2.0 mM gadolinium** **0, 10, 20, 100% peanut oil (content ratio)**	$50 < T_1 < 350$ 3T MR scanner *DESPOT* seq	-	Method for fast MR mapping	[168]
0.5 – 4.0 % w/v agarose	1000 (± 92) - 1481 (± 151) 5 MHz NMR spectrometer 1390 (± 84) − 2743 (± 71) 60 MHz NMR spectrometer *IR* seq.	23 (± 9) - 240 (± 15) 5 MHz NMR spectrometer 27 (± 3) − 278 (± 43) 60 MHz NMR spectrometer *CPMG SE* seq.	TMP for NMR imaging	[155]

agarose & varying concentration of $MnCl_2$	397 (± 12) – 759 (± 19) 3T MR scanner *UTE-MRF* seq.	37 (± 3) – 85 (± 7) 3T MR scanner *UTE-MRF* seq.		
agarose & varying concentration of $NICl_2$	200 < T1 < 1500 1.5 T MR scanner *IR SE* seq. TI: 50 – 3000 ms	41 - 80 (1.5 T) 1.5 T MR scanner *ME SE* seq.	Evaluation of methods for MR parameter mapping	[164][165] [166]
agarose & varying concentration of GdCl3	200 - 1600 (1.5/3 T) *2D IR single echo SE seq.* TI: 50 – 3800 ms or *Look-Locker* seq.	-		
2 % w/v agar **2 % w/v silicon dioxide** **40 % v/v evaporated milk**	776 1.5 T MR scanner *IR SE* seq. TIs: 50 –800 ms	66 1.5 T MR scanner *T2-w FSE* seq. TEs: 10.8 – 150.8 ms	MRI bone phantom for thermal exposures	[95]
1.3% w/v agar **0 – 26.7 % w/v granulated sugar**	921 (± 16) − 2239 (± 55) 3 T MR scanner *IR* seq.	68 ± 2 − 73 ± 3 3 T MR scanner *ME* seq.	Evaluation of methods for breast diffusion-weighted MRI	[169]

0.24 – 2.38 % Agarose **0.18 – 5.55 mM $NiCl_2$**	256 - 1870 1.4 T Minispec relaxometer, 22 °C/ 250 – 1872 3T MR scanner *IR* seq. 21 ± 2 °C	50 - 288 1.4 T Minispec relaxometer, 22 °C/ 42 – 231 3T MR scanner *SE* seq. 21 ± 2 °C	Phantom for global T1 mapping quality assurance	[162]
<u>Prostate</u> **50 % v/v agarose solution (2% dry w/v)** **50 % v/v condensed milk** **7.9 % v/v n-propyl alcohol (per agarose)** **0.06 w/v % CuCl2 salt (per total vol.)** **0.103 w/v % Ethylenediamine tetra acetic acid (EDTA) (per total vol.)** **1 g/l of 45-53 µm diameter glass beads** **thimerosal**	937 ± 13 40 MHz Minispec relaxometer *IR* seq. 21 °C	88 ± 3.8 40 MHz Minispec relaxometer *CPMG SE* seq. 21 °C	TMP multi-imaging modality	[178]
<u>Muscle</u> **50 % v/v agarose solution (6% dry w/v)** **50 % v/v condensed milk** **7.9 % v/v n-propyl alcohol (per agarose)** **0.048 % w/v CuCl2 salt (per total vol.)** **0.082 % w/v EDTA (per total volume)** **5 % w/v glass beads, thimerosal**	686 ± 9 40 MHz Minispec relaxometer *IR* sequence 21 °C	36.7 ± 1.9 40 MHz Minispec relaxometer *CPMG SE* seq. 21 °C		

Table II2: T1 and T2 relaxation times of gelatin-based phantoms, along with the technique used for relaxometry mapping and the temperature at which measurements were conducted (if provided by the relevant study).[2]

Gelatin-based phantoms					
Recipe	**T1 rel. time (ms)**		**T2 rel. time (ms)**	**Purpose**	**Ref.**
Tumor **225 bloom gelatin in saline water** **5 % oil-in-gelatin dispersion** **Muscle** **225 bloom gelatin in saline water** **10 % oil-in-gelatin dispersion**	1034.7 1084.9 1.5 T MR scanner T1-w *SPGR* seq. TR: 50 – 3000	T2*	113.1 64.5 1.5 T MR scanner T2*-w *SPGR* seq. TE: 7.5 – 160.7	TMP for RF heating and MRI thermal monitoring	[98]
13.3 wt. % gelatin **1 g/L thimerosal** **0.35 g/L formaldehyde** **50 % safflower oil** **4 g/L glass beads** **<u>OR</u> 20 g/L glass beads**	560 **OR** 1610 40 MHz Bruker relaxometer *IR* seq. 22 ºC		230 **OR** 416 40 MHz Bruker relaxometer *CPMG* seq. 22 ºC	Tissue-Mimicking Heterogeneous Elastography Phantoms	[181]

[2] T2-w = T2-weighted; T1-w = T1-weighted; SPGR = Spoiled gradient recalled echo; IR = Inversion Recovery; CPMG = Carr-Purcell-Meiboom-Gill; STIR = Short T1 Inversion Recovery; ME = Multi-Echo; GRE = Gradient Recalled Echo; TSE = Turbo Spin Echo; MPME = Multi-Pathway Multi-Echo.

11.1 % w/v porcine gelatin powders (125/ 175/ 250 bloom) 50 % v/v water – 50 % v/v evaporated milk vyse defoamer solution	970 ± 3 (125 bloom) 853 ± 3 (175 bloom) 1093 ± 5 (250 bloom) 3T MR scanner *STIR* seq., TI: 50 – 2500 ms	T2* 58 ± 7 (125 bloom) 55 ± 7 (175 bloom) 67 ± 12 (250 bloom) 3T MR scanner *ME GRE* seq., TE: 2.83 - 80 ms	TMPs for use with MRgFUS	[99]
50 vol. % water – 50 vol. % evap.milk 111 g/L 250-bloom gelatin powder 3.33 g/L DOWACIL 75 0.5 – 16 g/L psyllium Husk 0.17 vol. % defoamer	974–1038 3T MR scanner 2D *IR TSE* seq. TI: 50 – 2500 ms 21 °C	T2: 97-108 3T MR scanner 2D *TSE* seq. TE: 13.1 – 262 ms 21 °C	Phantom for US and MRI imaging	[180]
gelatin & varying concentration of gadolinium	$150 < T1 < 500$ 3T MR scanner *MPME* seq.	$100 < T2 < 220$ 3T MR scanner *MPME* seq.	New method to quantitatively map MR parameters	[182]
Gelatin/ Agar phantoms				
1.11 – 3.64 wt. % agar 3.60 – 5.70 wt. % 200 bloom gelatin 0.113 – 0.116 wt. % $CuCl_2$-$2H_20$ 0.33 – 0.34 wt. % EDTA tetra-Na hydrate 0.77 – 0.80 wt. % NaCl 0.24 – 0.33 wt. % formaldehyde 1.45 – 1.50 wt. % German plus 0 – 5.6 wt. % glass bead	369 – 498 60 MHz Bruker relaxometer *IR* seq. 22 ºC	28 – 63 60 MHz Bruker relaxometer *CPMG* seq. 22 ºC	Heterogeneous elastography phantoms	[143]

<u>Thalamus</u> **2.3 wt. % agar & 7.5 wt. % gelatin** **0.028 wt. % CuCl2** **0.13 wt. % EDTA-tetra Na** **0.1 wt. % NaCl, 0.24 wt. % HCHO** **0.1 wt. % thimerosal**	T1 of water in phantom: 1065 ± 30	T2 of water in phantom: 98.06 ± 0.20		
<u>Tumor</u> **2 wt. % agar & 7.5 wt. % gelatin** **0.0223 wt. % CuCl2, 0.1 wt. % NaCl** **0.101 wt. % EDTA-tetra Na** **0.24 wt. % formaldehyde** **0.1 wt. % thimerosal**	1215 ± 1 1.9 T Bruker spectrometer *IR* seq. 22 °C	149.6 ± 0.2 1.9 T Bruker spectrometer *CPMG* sequence 22 °C	Anthropomorphic MRS head phantom	[179]
0 – 50 vol % (of liquid components) glycerol **40 vol. % animal hide gel – 60 vol. % agar** **8.3 vol. % n-propyl alcohol** **0.0065 mass ratio of p-methylbenzoic acid /animal hide gel** **0.017 mass ratio of formaldehyde**	$200 < T1 < 1100$ 10 MHz spectrometer *IR* seq. 22 ºC	$50 < T2 < 80$ 10 MHz spectrometer *CPMG SE* seq. 22 ºC	TMPs for MRI phantoms	[188]

Table II3: T1 and T2 relaxation times of PAA-based phantoms, along with the technique used for relaxometry mapping and the temperature at which measurements were conducted (if provided by the relevant study).[3]

PAA-based phantoms				
Recipe	**T1 rel. time (ms)**	**T2 rel. time (ms)**	**Purpose**	**Ref.**
70.0 % v/v deionized water **7.0 % v/v 40% acrylamide/bis-acrylamide** **5.0 % v/v Magenta (thermochromic ink)** **3.0 % w/v BSA** **1.1% w/v Silicon dioxide,** **0.9 % w/v NaCl** **0.15 % w/v APS** **0.15 % v/v TEMED**	-	225 ± 14 1.5 T MR scanner 152 ± 8 3 T MR scanner *2D ME TSE* seq. TE: 50 – 450 ms	TMP for HIFU applications	[92]
37.9 vol. % distilled water **30 vol. % Rotiphorese® acrylamide** **16 wt. % BSA** **10 vol. % PVA microsphere** **0.04 vol. % Magnevist®** **3.3 vol. % Lumirem®** **0.08 vol. % TEMED, 1.75 vol. % APS** **0.9 wt. % NaCl, 0.03 wt. % NaN3**	$275 < T1 < 500$ for 25 – 75˚C 1.5 T MR scanner *IRTF* seq. TI: 100 – 2500 ms	$46 < T2 < 52$ for 25 – 75˚C 1.5 T MR scanner *MCSE* seq. TE: 10.6 – 339.2 ms	Liver-mimicking MRI phantom	[193]

[3] ME = Multi-Echo; TSE = Turbo Spin Echo; IRTF = Inversion Recovery Turbo Flash; MCSE = Multi-Contrast Spin Echo.

60 vol. % distilled water **30 vol. % Rotiphorese® acrylamide** **5 vol. % PVA microsphere** **3.92 ± 0.42 vol. % bovine hemoglobin** **0.098 ± 0.023 vol. % Magnevist®** **2.980 ± 0.067 vol. % Lumirem®** **0.084 vol. % TEMED, 1.5 vol. % APS** **0.9 wt. % NaCl, 0.03 wt. % NaN3**	246.6 – 597.2 for 25 – 75 ºC 1.5 T MR scanner *IRTF* seq. TI: 120 – 1000 ms	40.8 – 67.1 for 25 – 75 ºC 1.5 T MR scanner *MCSE* seq. TE: 10.6 – 339.2 ms	A liver mimicking MRI phantom for thermal therapy studies	[91]

Table II4: T1 and T2 relaxation times of carrageenan-based phantoms, along with the technique used for relaxometry mapping and the temperature at which measurements were conducted (if provided by the relevant study).[4]

Recipe	T1 rel. time (ms)	T2 rel. time (ms)	Purpose	Ref.
Carrageenan phantom				
5 wt. % carrageenan **0.2 mM $MnCL_2$** **0.19 wt. % NaCl, 0.1 wt. % NaN_3**	429 (1.5 T)	84.9 (1.5 T)	MRI phantom	[485]
Carrageenan/ Agarose phantoms				
3 % carrageenan in distilled water **0 – 1.6 % agarose** **0 – 140 µmol/kg $GdCl_3$** **0 – 0.7 % NaCl, 0.03 % NaN3**	$100 < T1 < 2100$ 1.5 T MR scanner *SR* seq. TR: 140 – 16 474 ms 25 ± 1°C	$20 < T2 < 420$ 1.5 T MR scanner *SE* seq. TE: 15 – 300 ms 25 ± 1°C	Phantom compatible for MRI and hyperthermia	[177]
3 wt. % carrageenan in distilled water **0 – 1.6 wt. % agarose** **0 – 140 µmol/kg $GdCl_3$** **0.03 wt. % NaN_3**	202 – 1904 1.5 T MR scanner *SR* seq. TR: 140 – 16 474 ms 25 ± 1°C	38 – 423 1.5 T MR scanner *SE* seq. TE: 15 – 300 ms 25 ± 1°C	Tissue mimicking MRI phantom	[175]

[4] SR = Saturation Recovery; SE = Spin-Echo; T2-w = T2-weighted; T1-w = T1-weighted; IR = Inversion Recovery; TSE = Turbo Spin Echo.

3 % carrageenan in distilled water **1.3 % agarose** **2.37 ppm gadoterate meglumine** **20 mM Na^+**	790 ± 28 3 T MR scanner *T1-w IR TSE* seq. TI: 250 – 5000 ms	65 ± 1 3 T MR scanner *T2-w TSE* seq. TE: 15 – 240 ms	MR/ CT liver phantom	[176]

Table II5: T1 and T2 relaxation times of other tissue-mimicking materials, along with the technique used for relaxometry mapping and the temperature at which measurements were conducted (if provided by the relevant study).[5]

Recipe	T1 rel. time (ms)	T2 rel. time (ms)	Purpose	Ref.
PVA phantoms				
10 % PVA cryogel, 90 % water **10 % PVA cryogel** **50 µl/ml gadolinium solution**	1317 ± 23 106 ± 16 3T MR scanner *3D fast-field ME* seq. TI: 20 – 2000 ms	T2: 98 ± 8 T2*: 191 ± 36 T2: 122 ± 30 T2* 4.5 ± 0.56 3T MR scanner T2*: *3D fast-field ME* seq. T2: *TSE* seq.	MRI phantom	[100]
10 wt. % PVA in water solution **1 – 4 freeze–thaw cycles**	718 – 1034 1.5 T MR scanner *2D FSE-IR* seq. TI: 50 – 3200 ms	108 – 175 1.5 T MR scanner *2D FSE* seq. TE: 15 – 195 ms	TMP for MR and US imaging	[102]
6 % PVA, 1 freeze-thaw cycle (FTC) **2 % BaSO4, 0.025 % CuSO4,** **1 % talcum** **or 4 % PVA with 3 FTCs**	1004 –1213 or 1900–2600 3T MR scanner *T1-w SE* seq.	163 – 182 or 1100–1665 3T MR scanner *T2-w GE* seq.	Brain phantom for multimodal imaging	[101]

[5] ME = Multi-Echo; FSE = Fast Spin Echo; IR = Inversion Recovery; T1-w = T1-weighted; T2-w = T2-weighted, GE = Gradient Echo; TSE = Turbo SE.

PVC phantoms				
12.3 ×10^{-2} g/mL PVC powder/softener	206.81 ± 17.50 (3 T)	20.22 ± 5.74 (3 T)	Multi-purpose breast TMP	[103]
mass ratio PVC /plasticizer: 40 – 70%. 0.6, 0.8, and 1% concentrated cellulose	258 – 223 1.5 T MR scanner *TSE* seq. TI: 23 – 2,970 ms	50 – 44 1.5 T MR scanner *SE* seq. TE: 3.5 – 200 ms	TMP for MR and US elastography	[104]
0-1 ratio of softener to PVC polymer, 0/5 % mass fraction of mineral oil 0/1 % mass fraction of Glass beads	426.3 – 450.2 7 T RF volume coil *SE* seq. TI: 50 – 2500 ms	21.5 – 28.4 7 T RF volume coil *SE* seq. TE: 11 – 80 ms	TMP for multimodal imaging	[105]
Silicone phantoms				
-	410 – 765 (1.4 T)	50 – 165 (1.4 T)	Multimodality imaging Phantom	[106]
-	1002 ± 8 3 T MR scanner *Look-Locker IR* seq. TI: 30 - 400 ms	58 ± 1 3 T MR scanner *ME SE seq.* TE: 40 – 400 ms	MR compatible cardiac left ventricle model	[107]
TX-150/ TX-151 phantoms				
3 – 18 wt. % TX-150 in degassed water	586 ± 30 – 2211 ± 37 20.9 MHz (0.5 T) NMR pulsed spectrometer *IR* seq., 20 ºC	57 – 287 0.5 T MR scanner *SE* seq., 20 ºC	Lesion phantom for MRI	[109]

7.00 wt. % TX-151 polysaccharide material **83.50 wt. % water** **0.303 wt. % NaCl** **9.20 wt. % Al powder** **0.0 – 0.8 mM Gd-DTPA**	174 (± 10) − 1405 (± 59) 1 T MR scanner 447 (± 15) − 2949 (± 213) 1.5 T MR scanner	30.4 (± 0.2) − 36.3 (±0.1) 1 T MR scanner 19.6 (± 0.1) − 24.8 (± 0.6) 1.5 T MR scanner	Tissue mimicking MRI phantom	[108]
0.08 mM GdDTPA **41.75 g water** **0.1515 g NaCl** **3.5 g TX-151** **0 – 14.2 wt. % Al**	746 ± 13 − 803 ± 28 (1 T) 1523 ± 147 − 1567 ± 77 (1.5 T) *SE* seq., TR: 50 – 3000 ms 18 ºC	25.4 ± 0.1 − 162.4 ± 10.2 (1 T) 18.8 ± 0.0 − 72.8 ± 3.2 (1.5 T) *SE* seq., TE: 20 – 160 ms 18 ºC		

APPENDIX III: List of Journal Publications and Conference Presentations

Journal Publications:

1. **Antoniou A**, Evripidou N, Giannakou M, Constantinides G, Damianou C, Acoustical properties of 3D printed thermoplastics, *Journal of Acoustical Society of America* (2021), doi:10.1121/10.0004772.
2. **Antoniou A**, Drakos T, Giannakou M, Evripidou N, Georgiou L, Christodoulou T, Panayiotou N, Ioannides C, Zamboglou N, Damianou C, Simple methods to test the accuracy of MRgFUS robotic systems, *International Journal of Medical Robotics and Computer Assisted Surgery* (2021), doi: 10.1002/rcs.2287.
3. **Antoniou A**, Giannakou M, Evripidou N, Evripidou G, Spanoudes K, Menikou G, Damianou C, Robotic system for magnetic resonance guided focused ultrasound ablation of abdominal cancer, *International Journal of Medical Robotics and Computer Assisted Surgery* (2021), doi: 10.1002/rcs.2299.
4. Drakos T, **Antoniou A**, Evripidou N, Alecou T, Giannakou M, Menikou G, Constantinides G, Damianou C, Ultrasonic attenuation of an agar, silicon dioxide, and evaporated milk gel phantom, *Journal of Medical Ultrasound* (2021), doi: 10.4103/JMU.JMU_145_20.
5. **Antoniou A**, Georgiou L, Christodoulocu T, Panayiotou N, Ioannides C, Zamboglou N, Damianou C, "MR relaxation times of agar-based tissue mimicking phantoms", *Journal of Applied Clinical Medical Physics* (2021), doi: 10.1002/acm2.13533.
6. **Antoniou A**, Damianou C, Review of MR relaxation properties of tissue-mimicking phantoms, Ultrasonics (2022), doi: 10.1016/j.ultras.2021.106600.
7. **Antoniou A**, Giannakou M, Evripidou N, Stratis S, Pichardo S, Damianou C, Robotic system for top to bottom MRgFUS therapy of multiple cancer types, *International Journal of Medical Robotics and Computer Assisted Surgery* (2022), doi: 10.1002/rcs.2364.

8. **Antoniou A**, Georgiou A, Evripidou N, Damianou C. “Full coverage path planning algorithm for MRgFUS therapy”, *International Journal of Medical Robotics and Computer Assisted Surgery* (2022), doi: 10.1002/rcs.2389.
9. **Antoniou A**, Panayiotou S, Spanoudes K, Damianou C, "Treatment of canine and feline sarcoma using MR-guided focused ultrasound system", *Journal of Ultrasound* (2022), doi: 10.1007/s40477-022-00672-5.
10. **Antoniou A**, Damianou C, “Simple, inexpensive, and ergonomic phantom for quality assurance control of MRI guided Focused Ultrasound systems”, *Journal of Ultrasound* (2022), doi: 10.1007/s40477-022-00740-w.
11. Giannakou M, **Antoniou A**, Damianou C, “Preclinical robotic device for magnetic resonance imaging guided focused ultrasound”, *International Journal of Medical Robotics and Computer Assisted Surgery* (2022), doi: 10.1002/rcs.2466.
12. **Antoniou A**, Giannakou M, Georgiou E, Kleopa K, Damianou C, “Robotic device for transcranial FUS applications in small animal models”, *International Journal of Medical Robotics and Computer Assisted Surgery* (2022), doi: 10.1002/rcs.2447.
13. **Antoniou A**, Georgiou L, Evripidou N, Panayiotou N, Ioannides C, Damianou C, “Challenges regarding MR compatibility of an MRgFUS robotic system”, *Journal of Magnetic Resonance* (2022), doi: 10.1016/j.jmr.2022.107317.
14. **Antoniou A**, Nikolaou A, Georgiou A, Evripidou N, Damianou C, “Development of an US, MRI, and CT imaging compatible realistic mouse phantom for thermal ablation and focused ultrasound evaluation”, *Ultrasonics* (2023), doi: 10.1016/j.ultras.2023.106955.
15. **Antoniou A**, Spanoudes K, Damianou C, “Treatment of mammary cancer with Focused Ultrasound: A pilot study in canine and feline patients”, *Ultrasonics* (2023), doi: 10.1016/j.ultras.2023.106974.
16. **Antoniou A**, Evripidou N., Georgiou L., Chrysanthou A., Ioannides C., and Damianou C., “Tumor phantom model for MRI guided Focused Ultrasound ablation studies,” *Medical Physics* (2023), doi: 10.1002/mp.16480.

17. **Antoniou A**, Nikolaou A, Evripidou N, Georgiou A, Filippou A, Zinonos V, Giannakou M, Chrysanthou A, Ioannides C, Damianou C, "Phantom-based assessment of motion and needle targeting accuracy of robotic devices for MRI-guided needle biopsy", *International Journal of Medical Robotics and Computer Assisted Surgery* (2023), doi: 10.1002/rcs.2526.
18. **Antoniou A**, Evripidou N, and Damianou C, "Focused ultrasound heating in brain tissue/skull phantoms with 1-MHz single-element transducer," *Journal of Ultrasound* (2023), doi: 10.1007/s40477-023-00810-7.
19. **Antoniou A**, Stavrou M, Evripidou N, Georgiou E, Kousiappa I, Koupparis A, Papacostas S, Kleopa K, and Damianou C, "FUS-mediated Blood-brain barrier disruption for delivering anti-Aβ antibodies in 5XFAD Alzheimer's disease mice," *Journal of Ultrasound* (2023), doi: 10.1007/s40477-023-00805-4.
20. **Antoniou A**, Damianou C, "Feasibility of ultrasonic heating through skull phantom using single-element transducer", *Journal of Medical Ultrasound* (2023).

Submitted papers under review:

1. **Antoniou A**, Evripidou N, Nikolaou A, Georgiou A, Giannakou M, Chrysanthou A, Georgiou L, Ioannides C, and Damianou C, "MRI monitoring of thermal lesions produced by focused ultrasound," *Medical Physics* (2023).
2. Evripidou N, **Antoniou A**, Georgiou L, Ioannides C, and Damianou C, "MRI compatibility testing of commercial HIFU transducers," *Physica Medica* (2023).
3. Evripidou N, **Antoniou A**, Lazarou G, Georgiou L, Chrysanthou A, Ioannides C, and Damianou C, "Workflow of a preclinical robotic MRI-guided FUS body system," *Ultrasonics* (2023).
4. Ioannides C, **Antoniou A**, Zinonos V, and Damianou C, "Development and evaluation of a robotic device for MRI-guided needle breast biopsy," *Int J Med Robot.* (2023).

5. **Antoniou A**, Evripidou N, Chrysanthou A , Georgiou L, Ioannides C, Spanoudes K, Damianou C, "Effect of MRI on the motion accuracy of MRI-compatible Focused Ultrasound robotic system," *CMPB* (2023)

Conference presentations:

1. Giannakou M , Drakos T, Evripidou N, Evripidou G, **Antoniou A**, and Damianou C, "MRI-guided Focused Ultrasound Robotic System for Preclinical Use of Small and Large Animals". 20th Annual International Symposium for Therapeutic Ultrasound (ISTU 2021), HICO, Gyeongju, Korea, 6-9 June 2021.
2. Giannakou M, Evripidou N, **Antoniou A**, and Damianou C, Robotic Device for MRgFUS Applications in Veterinary Medicine, 2021 International Conference on Medical Imaging Science and Technology (MIST), 1-3 December 2021.
3. Giannakou M, Evripidou N, **Antoniou A**, and Damianou C, "MRI compatible robotic device for FUS therapy of canine and feline mammary tumours". *2021 VI International Scientific Conference – INDUSTRY 4.0*, Borovets, Bulgaria, 8-11 December 2021.
4. Giannakou M, Evripidou N, **Antoniou A**, and Damianou C, "Robotic device for veterinary applications of MRgFUS". *2021 VI International Scientific Conference – INDUSTRY 4.0*, Borovets, Bulgaria, 8-11 December 2021.
5. Giannakou M, Evripidou N, **Antoniou A**, and Damianou C, "Robotic device for preclinical and veterinary trials of magnetic resonance guided focused ultrasound", *Annual Integrative Ultrasound Meeting 2022 (AIUM)*, San Diego, CA, USA, 12-16 March 2022.
6. Georgiou A, Evripidou N, **Antoniou A**, Demetriades I, Messios C, and Damianou C, "Algorithm for path planning in MRgFUS therapy", *21st Annual International Symposium for Therapeutic Ultrasound (ISTU 2022)*, Toronto, Canada, USA, 07-10 June 2022.

7. **Antoniou A**, Giannakou M, and Damianou C, "A simple MRI-guided robotic system for breast biopsy", 13th International MRI Symposium 2022, Leipzig, Germany, 14-15 October 2022.
8. Filippou A, Giannakou M, Evripidou N, **Antoniou A**, and Damianou C, "Agar/Wood-powder Breast Phantom for Focused Ultrasound Applications", *21st Annual International Symposium for Therapeutic Ultrasound (ISTU)*, Toronto, Canada, 07-10 June 2022.
9. Giannakou M, Evripidou N, **Antoniou A**, and Damianou C, "Robotic Device For Preclinical and Veterinary Trials Of Focused Ultrasound", *21st Annual International Symposium for Therapeutic Ultrasound (ISTU)*, Toronto, Canada, 07-10 June 2022.
10. **Antoniou A**, Giannakou M, and Damianou C, "Two simple 3D printed robotic systems for opening the blood brain barrier of small animals", *8th International symposium on Focused ultrasound*, Bethesda, USA, 23-25 October 2022.
11. **Antoniou A**, Evripidou N, and Damianou C, "Challenges regarding MR compatibility of an MRGFUS robotic system" *13th Interventional MRI Symposium,* Leipzig, Germany, 14-15 October 2022.
12. **Antoniou A**, Evripidou N, and Damianou C, "Focused Ultrasound Ablation Of Canine Mammary Cancer", *UltraCon Annual Meeting 2023*, Orlando, Florida, USA, 25-29 March 2023.
13. Damianou C, **Antoniou A**, and Evripidou N, "Focused Ultrasound Phantom With Inclusion Of Tumour", *UltraCon Annual Meeting 2023*, Orlando, Florida, USA, 25-29 March 2023.
14. **Antoniou A**, Evripidou N, Stavrou M, Kousiappa I, Georgiou E, Kleopa K, and Damianou C, "Opening of the Blood-brain barrier using focused ultrasound with simultaneous delivery of anti-Aβ antibodies in a 5XFAD amyloid beta mouse model", *6th International Caparica Conference on Ultrasonic-based applications from analysis to synthesis*, Caparica, Portugal, 26–29 June 2023.
15. Evripidou N, **Antoniou A**, and Damianou C, "Ultrasound and MRI guided focused ultrasound system for veterinary applications", *The 29th annual international*

conference of the Australian sonographers association, Brisbane, Australia, 26-28 May 2023.

16. **Antoniou A**, Evripidou N, Spanoudes K, and Damianou C, "Treatment of cancer with focused Ultrasound in cats and dogs", *The 22nd Annual International Symposium on Therapeutic Ultrasound (ISTU),* Lyon, France, 17-20 April 2023.

REFERENCES

[1] N. M. Duc and B. Keserci, “Emerging clinical applications of high-intensity focused ultrasound,” *Diagnostic Interv. Radiol.*, vol. 25, no. 5, pp. 398–409, 2019, doi: 10.5152/dir.2019.18556.

[2] Z. Izadifar, Z. Izadifar, D. Chapman, and P. Babyn, “An Introduction to High Intensity Focused Ultrasound: Systematic Review on Principles, Devices, and Clinical Applications,” *J. Clin. Med.*, vol. 9, no. 2, p. 460, 2020, doi: 10.3390/jcm9020460.

[3] M. R. Bailey, V. . Khokhlova, O. A. Sapozhnikov, S. G. Kargl, and L. A. Crum, “Physical Mechanisms of the Therapeuctic Effect of Ultrasound,” *Acoust. Phys.*, vol. 49, no. 4, pp. 369–388, 2003, doi: 1063-7710/03/4904-0369.

[4] C. R. Hill and G. R. ter Haar, “High intensity focused ultrasound—potential for cancer treatment,” *Br. J. Radiol.*, vol. 68, no. 816, pp. 1296–1303, 1995, doi: 10.1259/0007-1285-68-816-1296.

[5] W. S. Chen, C. Lafon, T. J. Matula, S. Vaezy, and L. A. Crum, “Mechanisms of lesion formation in high intensity focused ultrasound therapy,” *Acoust. Res. Lett. Online*, vol. 4, no. 2003, pp. 41–46, 2003, doi: 10.1121/1.1559911.

[6] I. A. S. Elhelf, H. Albahar, U. Shah, A. Oto, E. Cressman, and M. Almekkawy, “High intensity focused ultrasound: The fundamentals, clinical applications and research trends,” *Diagn. Interv. Imaging*, vol. 99, no. 6, pp. 349–359, 2018, doi: 10.1016/j.diii.2018.03.001.

[7] S. A. Quadri *et al.*, “High-intensity focused ultrasound: Past, present, and future in neurosurgery,” *Neurosurg. Focus*, vol. 44, no. 2, 2018, doi: 10.3171/2017.11.FOCUS17610.

[8] C. G. Hernando, L. Esteban, T. Cañas, E. Van Den Brule, and M. Pastrana, “The role of magnetic resonance imaging in oncology,” *Clin. Transl. Oncol.*, vol. 12,

no. 9, pp. 606–613, 2010, doi: 10.1007/s12094-010-0565-x.

[9] V. Rieke and K. B. Pauly, “MR Thermometry,” *J Magn Reson Imaging*, vol. 27, no. 2, pp. 376–390, 2008, doi: 10.1002/jmri.21265.MR.

[10] B. Zhu, J. Li, L. Diao, K. Ma, Y. Fan, and W. Yang, “High-intensity focused ultrasound ablation for advanced pancreatic cancer,” *J. Cancer Res. Ther.*, vol. 15, pp. 831–835, 2019, doi: 10.4103/jcrt.JCRT_408_18.

[11] B. D. et al. de Senneville, “MRI-Guided HIFU Methods for the Ablation of Liver and Renal Cancers.,” *Adv. Exp. Med. Biol.*, vol. 880, pp. 43–63, 2016, doi: 10.1007/978-3-319-22536-4_3.

[12] R. Scipione, M. Anzidei, A. Bazzocchi, C. Gagliardo, C. Catalano, and A. Napoli, “HIFU for Bone Metastases and other Musculoskeletal Applications,” *Semin. Intervent. Radiol.*, vol. 35, no. 4, pp. 261–267, 2018, doi: 10.1055/s-0038-1673363.

[13] A. Napoli *et al.*, “Real-time magnetic resonance-guided high-intensity focused ultrasound focal therapy for localised prostate cancer: Preliminary experience,” *Eur. Urol.*, vol. 63, no. 2, pp. 395–398, 2013, doi: 10.1016/j.eururo.2012.11.002.

[14] F. Pediconi, F. Marzocca, B. Cavallo Marincola, and A. Napoli, “MRI-guided treatment in the breast,” *J. Magn. Reson. Imaging*, vol. 48, no. 6, pp. 1479–1488, 2018, doi: 10.1002/jmri.26282.

[15] A. Roberts, “Magnetic Resonance-Guided focused ultrasound for uterine fibroids,” *Semin. Intervent. Radiol.*, vol. 25, no. 4, pp. 394–405, 2008, doi: 10.1055/s-0028-1102999.

[16] T. R. Wang *et al.*, “Transcranial magnetic resonance imaging-guided focused ultrasound thalamotomy for tremor: Technical note,” *Neurosurg. Focus*, vol. 44, no. 2, pp. 1–7, 2018, doi: 10.3171/2017.10.FOCUS17609.

[17] J. G. Lynn, R. L. Zwemer, A. J. Chick, and A. E. Miller, “A new method for the

generation and use of focused ultrasound in experimental biology," *J. Gen. Physiol.*, vol. 26, no. 2, pp. 179–193, 1942, doi: 10.1085/jgp.26.2.179.

[18] J. Jagannathan *et al.*, "High Intensity Focused Ultrasound surgery of the brain: Historical Perspective , With Modern Applications," *Phys. Med. Biol.*, vol. 55, no. 7, pp. 201–211, 2014, doi: 10.1227/01.NEU.0000336766.18197.8E.High.

[19] K. Hynynen *et al.*, "500-Element ultrasound phased array system for noninvasive focal surgery of the brain: A preliminary rabbit study with ex vivo human skulls," *Magn. Reson. Med.*, vol. 52, no. 1, pp. 100–107, 2004, doi: 10.1002/mrm.20118.

[20] F. A. Jolesz and K. Hynynen, "Magnetic resonance image-guided focused ultrasound surgery.," *Cancer J.*, vol. 8, 2002.

[21] N. Mylonas and C. Damianou, "MR compatible positioning device for guiding a focused ultrasound system for the treatment of brain deseases," *Int. J. Med. Robot. ComIputer Assist. Surg.*, vol. 10, pp. 1–10, 2014, doi: 10.1002/rcs.1501.

[22] N. Y. Jung, C. K. Park, M. Kim, P. H. Lee, Y. H. Sohn, and J. W. Chang, "The efficacy and limits of magnetic resonance–guided focused ultrasound pallidotomy for Parkinson's disease: A Phase I clinical trial," *J. Neurosurg.*, vol. 1306, no. 6, pp. 1853–1861, 2019, doi: 10.3171/2018.2.JNS172514.

[23] S. J. Kim, D. Roh, H. H. Jung, W. S. Chang, C. H. Kim, and J. W. Chang, "A study of novel bilateral thermal capsulotomy with focused ultrasound for treatment-refractory obsessive– compulsive disorder: 2-year follow-up," *J. Psychiatry Neurosci.*, vol. 43, no. 5, pp. 327–337, 2018, doi: 10.1503/jpn.170188.

[24] N. Lipsman *et al.*, "Blood–brain barrier opening in Alzheimer's disease using MR-guided focused ultrasound," *Nat. Commun.*, vol. 9, no. 1, pp. 1–8, 2018, doi: 10.1038/s41467-018-04529-6.

[25] C. E. Parker, W. E., Weidman, E. K., Chazen, J., Niogi, S. N., Uribe-Cardenas, R., Kaplitt, M. G., and Hoffman, "Magnetic resonance–guided focused ultrasound for ablation of mesial temporal epilepsy circuits: modeling and theoretical feasibility

of a novel noninvasive approach.," *J. Neurosurg. JNS*, pp. 1–8, 2019.

[26] J. MacDonell *et al.*, "Magnetic resonance-guided interstitial high-intensity focused ultrasound for brain tumor ablation," *Neurosurg. Focus*, vol. 44, no. 2, pp. 1–6, 2018, doi: 10.3171/2017.11.FOCUS17613.

[27] K. Gandhi, A. Barzegar-Fallah, A. Banstola, S. B. Rizwan, and J. N. J. Reynolds, "Ultrasound-Mediated Blood–Brain Barrier Disruption for Drug Delivery: A Systematic Review of Protocols, Efficacy, and Safety Outcomes from Preclinical and Clinical Studies," *Pharmaceutics*, vol. 14, no. 4, 2022, doi: 10.3390/pharmaceutics14040833.

[28] "Exablate Neuro," *Insightec*. [Online]. Available: https://www.insightec.com/media/1364/exablate-neuro-product-brochure-digital-et-tdpd_pub41003030-na-rev-3-digital-low-res.pdf. [Accessed: 16-Mar-2021].

[29] "Essential Tremor," *Focused Ultrasound Foundation*. [Online]. Available: https://www.fusfoundation.org/diseases-and-conditions/neurological/essential-tremor. [Accessed: 16-Mar-2021].

[30] R. Pandit, L. Chen, and J. Götz, "The blood-brain barrier: Physiology and strategies for drug delivery," *Adv. Drug Deliv. Rev.*, vol. 165–166, pp. 1–14, 2020, doi: 10.1016/j.addr.2019.11.009.

[31] A. Burgess and K. Hynynen, "Noninvasive and Targeted Drug Delivery to the Brain Using Focused Ultrasound," *ACS Chem. Neurosci.*, vol. 4, no. 4, p. 519−526, 2013, doi: 10.1021/cn300191b.

[32] D. Sohel, T. Sultana, and M. H. Kawsar, "Largest Obstacle of Drug Delivery to the Blood Brain Barrier and Current Approach to Solve this Problem: Recent Comprehensive Review," *Glob J Nano.*, vol. 4, no. 2, 2018, doi: 10.19080/GJN.2018.04.555633.

[33] Y. Meng *et al.*, "Safety and efficacy of focused ultrasound induced blood-brain barrier opening, an integrative review of animal and human studies," *J. Control.*

Release, vol. 309, pp. 25–36, 2019, doi: 10.1016/j.jconrel.2019.07.023.

[34] K. Hynynen, N. McDannold, N. Vykhodtseva, and F. A. Jolesz, "Noninvasive MR Imaging guided Focal Opening of the Blood-Brain Barrier in Rabbits," *Radiology*, vol. 220, no. 3, pp. 640–646, 2001, doi: 10.1148/radiol.2202001804.

[35] T. A. Arsiwala *et al.*, "Ultrasound-mediated disruption of the blood tumor barrier for improved therapeutic delivery," *Neoplasia (United States)*, vol. 23, no. 7, pp. 676–691, 2021, doi: 10.1016/j.neo.2021.04.005.

[36] D. Rajib, "Central nervous system diseases associated with blood brain barrier breakdown - A Comprehensive update of existing literatures," *J. Neurosci. Neurol. Disord.*, vol. 4, no. 2, pp. 053–062, 2020, doi: 10.29328/journal.jnnd.1001035.

[37] J. J. Choi, S. Wang, T. R. Brown, S. A. Small, K. E. K. Duff, and E. E. Konofagou, "Noninvasive and Transient Blood-Brain Barrier Opening in the Hippocampus of Alzheimer ' s Double Transgenic Mice Using Focused Ultrasound," *Ultrason. Imaging*, vol. 30, no. 3, pp. 189–200, 2008.

[38] "Alzheimer's disease," *Alzheimer's Disease International*. [Online]. Available: https://www.alzint.org/about/dementia-facts-figures/types-of-dementia/alzheimers-disease/. [Accessed: 16-Jan-2023].

[39] K. G. Yiannopoulou and S. G. Papageorgiou, "Current and Future Treatments in Alzheimer Disease: An Update," *J. Cent. Nerv. Syst. Dis.*, vol. 12, pp. 1–12, 2020, doi: 10.1177/1179573520907397.

[40] N. I. Wolf, C. ffrench-Constant, and M. S. van der Knaap, "Hypomyelinating leukodystrophies — unravelling myelin biology," *Nat. Rev. Neurol.*, vol. 17, no. 2, pp. 88–103, 2021, doi: 10.1038/s41582-020-00432-1.

[41] C. K. Abrams *et al.*, "A new mutation in GJC2 associated with subclinical leukodystrophy," *J Neurol*, vol. 261, pp. 1929–1938, 2014, doi: 10.1007/s00415-014-7429-1.

[42] B. S. Peters, P. R. Armijo, C. Krause, S. A. Choudhury, and D. Oleynikov, “Review of emerging surgical robotic technology,” *Surg. Endosc.*, vol. 32, no. 4, pp. 1636–1655, 2018, doi: 10.1007/s00464-018-6079-2.

[43] “Insightec.com.” [Online]. Available: https://www.insightec.com/products/exablate-body-system/overview. [Accessed: 01-Mar-2021].

[44] P. Medical, “Sonalleve.” [Online]. Available: https://profoundmedical.com/sonalleve/. [Accessed: 24-May-2023].

[45] “2020 State of the field,” *Focused Ultrasound Foundation*. [Online]. Available: http://www.fusfoundation.org/images/pdf/Focused_Ultrasound_Foundation_2020_State_of_the Field Report.pdf. [Accessed: 01-Mar-2021].

[46] “Fusinstruments.com.” [Online]. Available: https://www.fusinstruments.com/. [Accessed: 08-Apr-2021].

[47] “Image Guided Therapy - Image Guided Therapy,” *Imageguidedtherapy.com*. [Online]. Available: http://www.imageguidedtherapy.com/.

[48] Alpinion.com, “ALPINION-ALPIUS900.” [Online]. Available: http://www.alpinion.com/en/product/product_view_alpius900.do?productKey=KEY.1505083248000000219. [Accessed: 30-Nov-2021].

[49] Alpinion.com, “ALPINION-VIFU 2000.” [Online]. Available: http://www.alpinion.com/en/product/product_view_vifu2000.do?productKey=KEY.1606034801000003466.

[50] “SONOVEIN - Theraclion.” [Online]. Available: https://www.theraclion.com/products/sonovein/. [Accessed: 30-Nov-2021].

[51] “ECHOPULSE - Theraclion.” [Online]. Available: https://www.theraclion.com/products/echopulse/. [Accessed: 30-Nov-2021].

[52] “Ultrasonic Therapy Equipment | HIFU Ablation System,”

Aishen.allbiomedical.com. [Online]. Available: http://aishen.allbiomedical.com/company/product_detail-HIFU-Ablation-System-134.html. [Accessed: 06-Dec-2021].

[53] M. Yiannakou, G. Menikou, C. Yiallouras, and C. Damianou, "MRI-guided coupling for a focused ultrasound system using a top-to-bottom propagation," *J. Ther. Ultrasound*, vol. 5, no. 1, pp. 1–8, 2017, doi: 10.1186/s40349-017-0087-x.

[54] S. Tognarelli, G. Ciuti, A. Diodato, and P. Miloro, "The FUTURA platform: a new approach merging non-invasive ultrasound therapy with surgical robotics," in *36th Annual International Conference of the IEEE Engineering in Medicine and Biology Society*, 2014.

[55] K. D. Price *et al.*, "Design and validation of an MR-conditional robot for transcranial focused ultrasound surgery in infants," *Med. Phys.*, vol. 43, no. 9, pp. 4983–4995, 2016, doi: 10.1118/1.4955174.

[56] A. J. Loeve *et al.*, "Workflow and intervention times of MR-guided focused ultrasound-Predicing the impact of new techniques," *J. Biomed. Inform.*, vol. 60, pp. 38–48, 2016, doi: 10.1016/j.jbi.2016.01.001.

[57] Z. Izadifar, Z. Izadifar, D. Chapman, and P. Babyn, "An Introduction to High Intensity Focused Ultrasound: Systematic Review on Principles, Devices, and Clinical Applications," *J Clin Med*, vol. 9, no. 2, p. 460, 2020, doi: 10.3390/jcm9020460.

[58] G. Ning, X. Zhang, Q. Zhang, Z. Wang, and H. Liao, "Real time and multimodality image-guided intelligent HIFU therapy for uterine fibroid," *Theranostics*, vol. 10, no. 10, pp. 4676–4693, 2020, doi: 10.7150/thno.42830.

[59] J. E. Villanueva-Meyer, M. C. Mabray, and S. Cha, "Current clinical brain tumor imaging," *Clin. Neurosurg.*, vol. 81, no. 3, pp. 397–415, 2017, doi: 10.1093/neuros/nyx103.

[60] E. J. Lee, A. Fomenko, and A. M. Lozano, "Magnetic resonance-guided focused

ultrasound: Current status and future perspectives in thermal ablation and blood-brain barrier opening," *J. Korean Neurosurg. Soc.*, vol. 62, no. 1, pp. 10–26, 2019, doi: 10.3340/jkns.2018.0180.

[61] W. Zhang, Y. Wu, B. Yang, S. Hu, L. Wu, and S. Dhelimd, "Overview of multi-modal brain tumor mr image segmentation," *Healthc.*, vol. 9, no. 8, pp. 1–20, 2021, doi: 10.3390/healthcare9081051.

[62] A. Wadhwa, A. Bhardwaj, and V. Singh Verma, "A review on brain tumor segmentation of MRI images," *Magn. Reson. Imaging*, vol. 61, pp. 247–259, 2019, doi: 10.1016/j.mri.2019.05.043.

[63] M. Xu, D. Zhang, Y. Yang, Y. Liu, Z. Yuan, and Q. Qin, "A split-and-merge-based uterine fibroid ultrasound image segmentation method in HIFU therapy," *PLoS One*, vol. 10, no. 5, pp. 1–24, 2015, doi: 10.1371/journal.pone.0125738.

[64] A. Vargas-Olivares, O. Navarro-Hinojosa, S. Pichardo, L. Curiel, M. Alencastre-Miranda, and J. E. Chong-Quero, "Image Segmentation for the Treatment Planning of Magnetic Resonance-Guided High-Intensity Focused Ultrasound (MRgFUS) Therapy: A Parametric Study," *Appl. Sci.*, vol. 9, no. 24, pp. 1–23, 2019, doi: 10.3390/app9245296.

[65] Y. Zhou, S. G. Kargl, and J. H. Hwang, "The Effect of the Scanning Pathway in High-Intensity Focused Ultrasound Therapy on Lesion Production," *Ultrasound Med. Biol.*, vol. 37, no. 9, pp. 1457–1468, 2011, doi: 10.1016/j.ultrasmedbio.2011.05.848.

[66] L. Curiel, F. Chavrier, B. Gignoux, S. Pichardo, S. Chesnais, and J. Y. Chapelon, "Experimental evaluation of lesion prediction modelling in the presence of cavitation bubbles: Intended for high-intensity focused ultrasound prostate treatment," *Med Biol Eng Comput*, vol. 42, no. 1, pp. 44–54, 2004, doi: 10.1007/BF02351010.

[67] Y. Zhou, S. G. Kargl, and J. H. Hwang, "Producing uniform lesion pattern in HIFU

ablation," in *AIP Conference Proceedings*, 2009, vol. 1113, pp. 91–95, doi: 10.1063/1.3131478.

[68] A. Filippou, T. Drakos, M. Giannakou, N. Evripidou, and C. Damianou, "Experimental evaluation of the near-field and far-field heating of focused ultrasound using the thermal dose concept," *Ultrasonics*, vol. 116, p. 106513, 2021, doi: 10.1016/j.ultras.2021.106513.

[69] K. Qian, C. Li, Z. Ni, J. Tu, X. Guo, and D. Zhang, "Uniform tissue lesion formation induced by high-intensity focused ultrasound along a spiral pathway," *Ultrasonics*, vol. 77, pp. 38–46, 2017, doi: 10.1016/j.ultras.2017.01.018.

[70] D. Li, G. Shen, H. Luo, J. Bai, and Y. Chen, "A Study of Heating Duration and Scanning Path in Focused Ultrasound Surgery," *J. Med. Syst.*, vol. 35, pp. 779–786, 2011, doi: 10.1007/s10916-010-9463-6.

[71] N. I. Vykhodtseva, K. Hynynen, and C. Damianou, "Pulse duration and peak intensity during focused ultrasound surgery: Theoretical and experimental effects in rabbit brain in vivo," *Ultrasound Med. Biol.*, vol. 20, no. 9, pp. 987–1000, 1994, doi: 10.1016/0301-5629(94)90058-2.

[72] C. Damianou and K. Hynynen, "The effect of various physical parameters on the size and shape of necrosed tissue volume during ultrasound surgery," *J. Acoust. Soc. Am.*, vol. 95, no. 3, pp. 1641–1649, 1994, doi: 10.1121/1.408550.

[73] P. Shokrollahi, J. M. Drake, and A. A. Goldenberg, "Signal-to-noise ratio evaluation of magnetic resonance images in the presence of an ultrasonic motor," *Biomed. Eng. Online*, vol. 16, no. 1, pp. 1–12, 2017, doi: 10.1186/s12938-017-0331-1.

[74] K. G. Chan, T. Fielding, and M. Anvari, "An image-guided automated robot for MRI breast biopsy," *Int. J. Med. Robot. Comput. Assist. Surg.*, vol. 12, no. 3, pp. 461–477, 2016, doi: 10.1002/rcs.

[75] A. Patriciu, D. Petrisor, M. Muntener, D. Mazilu, M. Schär, and D. Stoianovici,

"Automatic Brachytherapy Seed Placement Under MRI Guidance," *IEEE Trans Biomed Eng*, vol. 54, no. 8, pp. 1499–1506, 2007, doi: 10.1109/TBME.2007.900816.Automatic.

[76] N. Patel, J. Yan, R. Monfaredi, K. Sharma, K. Cleary, and I. Iordachita, "Preclinical evaluation of an integrated robotic system for magnetic resonance imaging guided shoulder arthrography," *Med. Imaging*, vol. 6, no. 2, 2019, doi: 10.1117/1.JMI.6.2.025006.

[77] H. Dou, S. Jiang, Z. Yang, L. Sun, X. Ma, and B. Huo, "Design and validation of a CT-guided robotic system for lung cancer brachytherapy:," *Med. Phys.*, vol. 44, no. 9, pp. 4828–4837, 2017, doi: 10.1002/mp.12435.

[78] M. A. Tavallaei, P. M. Johnson, J. Liu, and M. Drangova, "Design and evaluation of an MRI-compatible linear motion stage," *Med. Phys.*, vol. 43, no. 1, pp. 62–71, 2016, doi: 10.1118/1.4937780.

[79] Y. Koseki, T. Washio, K. Chinzei, and H. Iseki, "Endoscope Manipulator for Trans-nasal Neurosurgery, Optimized for and Compatible to Vertical Field Open MRI," *Med. Image Comput. Comput. Interv. — MICCAI 2002. MICCAI 2002. Lect. Notes Comput. Sci. Springer, Berlin, Heidelberg.*, vol. 2488, pp. 114–121, 2002.

[80] V. Groenhuis, F. J. Siepel, J. Veltman, J. K. van Zandwijk, and S. Stramigioli, "Stormram 4: An MR Safe Robotic System for Breast Biopsy," *Ann. Biomed. Eng.*, vol. 46, no. 10, pp. 1686–1696, 2018, doi: 10.1007/s10439-018-2051-5.

[81] C. Yiallouras, N. Mylonas, and C. Damianou, "MRI-compatible positioning device for guiding a focused ultrasound system for transrectal treatment of prostate cancer," *Int. J. Comput. Assist. Radiol. Surg.*, vol. 9, no. 4, pp. 745–753, 2014, doi: 10.1007/s11548-013-0964-x.

[82] C. Yiallouras, K. Ioannides, T. Dadakova, M. Pavlina, M. Bock, and C. Damianou, "Three-axis MR-conditional robot for high-intensity focused ultrasound for

treating prostate diseases transrectally," *J. Ther. Ultrasound*, vol. 3, no. 1, pp. 1–10, 2015, doi: 10.1186/s40349-014-0023-2.

[83] C. Yiallouras and C. Damianou, "Review of MRI positioning devices for guiding focused ultrasound systems," *Int. J. Med. Robot. Comput. Assist. Surg.*, vol. 11, pp. 247–255, 2015, doi: 10.1002/rcs.1601.

[84] T. Wu, "A quality control program for MR-guided focused ultrasound ablation therapy," *J. Appl. Clin. Med. Phys.*, vol. 3, no. 2, p. 162, 2002, doi: 10.1120/1.1459262.

[85] N. A. Patel *et al.*, "An Integrated Robotic System for MRI-Guided Neuroablation: Preclinical Evaluation," *IEEE Trans Biomed Eng*, vol. 67, no. 10, pp. 2990–2999, 2020.

[86] A. Krieger *et al.*, "Development and Evaluation of an Actuated MRI-Compatible Robotic System for MRI-Guided Prostate Intervention," *IEEE ASME Trans Mechatron*, vol. 18, no. 1, pp. 273–284, 2013, doi: 10.1109/TMECH.2011.2163523.Development.

[87] J. G. A. Moreau-gaudry, N. Hungr, and A. Moreau-gaudry, "Evaluation of the Needle Positioning Accuracy of a Light Puncture Robot Under MRI Guidance: Results of a Clinical Trial on Healthy Volunteers," *Cardiovasc Interv. Radiol*, vol. 41, no. 9, pp. 1428–1435, 2018, doi: 10.1007/s00270-018-2001-5.

[88] G. Sagias, C. Yiallouras, K. Ioannides, and C. Damianou, "An MRI-conditional motion phantom for the evaluation of high-intensity focused ultrasound protocols," *Int. J. Med. Robot. Comput. Assist. SURGER*, vol. 12, pp. 431–441, 2016.

[89] C. Y. An, J. H. Syu, C. S. Tseng, and C. J. Chang, "An ultrasound imaging-guided robotic HIFU ablation experimental system and accuracy evaluations," *Appl. Bionics Biomech.*, vol. 2017, 2017, doi: 10.1155/2017/5868695.

[90] C. K. McGarry *et al.*, "Tissue mimicking materials for imaging and therapy phantoms: A review," *Phys. Med. Biol.*, vol. 65, no. 23, pp. 1–43, 2020, doi:

10.1088/1361-6560/abbd17.

[91] B. Bazrafshan, F. Hubner, P. Farshid, M. C. Larson, V. Vogel, and W. Mantele, “A liver-mimicking MRI phantom for thermal ablation experiments,” *Med Phys*, vol. 38, no. 5, pp. 2674–2684, 2011, doi: 10.1118/1.3570577.

[92] A. Eranki, A. S. Mikhail, A. H. Negussie, P. S. Katti, B. J. Wood, and A. Partanen, “Tissue-mimicking thermochromic phantom for characterization of HIFU devices and applications,” *Int J Hyperthermia.*, vol. 36, no. 1, pp. 518–529, 2019, doi: 10.1080/02656736.2019.1605458.

[93] G. Menikou, T. Dadakova, M. Pavlina, M. Bock, and C. Damianou, “MRI compatible head phantom for ultrasound surgery,” *Ultrasonics*, vol. 57, pp. 144–152, 2015, doi: 10.1016/j.ultras.2014.11.004.

[94] G. Menikou, M. Yiannakou, C. Yiallouras, C. Ioannides, and C. Damianou, “MRI-compatible breast/rib phantom for evaluating ultrasonic thermal exposures,” *Int. J. Med. Robot. Comput. Assist. Surg.*, vol. 14, no. 1, pp. 1–12, 2018, doi: 10.1002/rcs.1849.

[95] G. Menikou, M. Yiannakou, C. Yiallouras, C. Ioannides, and C. Damianou, “MRI-compatible bone phantom for evaluating ultrasonic thermal exposures,” *Ultrasonics*, vol. 71, pp. 12–19, 2016, doi: 10.1016/j.ultras.2016.05.020.

[96] G. Menikou and C. Damianou, “Acoustic and thermal characterization of agar based phantoms used for evaluating focused ultrasound exposures,” *J. Ther. Ultrasound*, vol. 5, 2017, doi: 10.1186/s40349-017-0093-z.

[97] A. Dabbagh, B. J. J. Abdullah, C. Ramasindarum, and N. H. Abu Kasim, “Tissue-mimicking gel phantoms for thermal therapy studies,” *Ultrason. Imaging*, vol. 36, no. 4, pp. 291–316, 2014, doi: 10.1177/0161734614526372.

[98] Y. Yuan *et al.*, “A heterogeneous human tissue mimicking phantom for RF heating and MRI thermal monitoring verification,” *Phys Med Biol*, vol. 57, no. 7, pp. 2021–2037, 2013, doi: 10.1088/0031-9155/57/7/2021.

[99] A. I. Farrer *et al.*, “Characterization and evaluation of tissue-mimicking gelatin phantoms for use with MRgFUS,” *J. Ther. Ultrasound*, vol. 3, no. 1, pp. 1–11, 2015, doi: 10.1186/s40349-015-0030-y.

[100] G. M. Soultanidis, J. E. MacKewn, C. Tsoumpas, and P. K. Marsden, “PVA cryogel for construction of deformable PET-MR visible phantoms,” *IEEE Trans. Nucl. Sci.*, vol. 60, no. 1, pp. 95–102, 2013, doi: 10.1109/TNS.2013.2238952.

[101] S. J. Chen *et al.*, “An anthropomorphic polyvinyl alcohol brain phantom based on Colin27 for use in multimodal imaging,” *Am Assoc Phys Med*, vol. 39, no. 1, pp. 554–561, 2012, doi: 10.1118/1.3673069.

[102] K. J. M. Surry, H. J. B. Austin, A. Fenster, and T. M. Peters, “Poly(vinyl alcohol) cryogel phantoms for use in ultrasound and MR imaging,” *Phys. Med. Biol.*, vol. 49, no. 24, pp. 5529–5546, 2004, doi: 10.1088/0031-9155/49/24/009.

[103] Y. He *et al.*, “3D-printed breast phantom for multi-purpose and multi-modality imaging,” *Quant. Imaging Med. Surg.*, vol. 9, no. 1, pp. 63–74, 2019, doi: 10.21037/qims.2019.01.05.

[104] S. Chatelin *et al.*, “Investigation of PolyVinyl Chloride Plastisol Tissue-Mimicking Phantoms for MR- and Ultrasound-Elastography,” *Front. Phys.*, vol. 8, pp. 1–12, 2020, doi: 10.3389/fphy.2020.577358.

[105] W. Li *et al.*, “Polyvinyl chloride as a multimodal tissue-mimicking material with tuned mechanical and medical imaging properties,” *Med. Phys.*, vol. 43, no. 10, pp. 5577–5592, 2016, doi: 10.1118/1.4962649.

[106] D. Goldstein, H. Kundel, M. Daube-Witherspoon, L. Thibault, and E. Goldstein, “A silicone gel phantom suitable for multimodality imaging,” *Invest Radiol.*, vol. 22, no. 2, pp. 153–157, 1987, doi: 10.1097/00004424-198702000-00013.

[107] M. A. Dieringer *et al.*, “Design, construction, and evaluation of a dynamic MR compatible cardiac left ventricle model,” *Med. Phys.*, vol. 39, no. 8, pp. 4800–4806, 2012, doi: 10.1118/1.4736954.

[108] G. P. Mazzara, R. W. Briggs, Z. Wu, and B. G. Steinbach, “Use of a modified polysaccharide gel in developing a realistic breast phantom for MRI,” *Magn. Reson. Imaging*, vol. 14, no. 6, pp. 639–648, 1996, doi: 10.1016/0730-725X(96)00054-9.

[109] M. W. Groch, J. A. Urbon, W. D. Erwin, and S. Al-Doohan, “An MRI tissue equivalent lesion phantom using a novel polysaccharide material,” *Magn. Reson. Imaging*, vol. 9, no. 3, pp. 417–421, 1991, doi: 10.1016/0730-725X(91)90430-T.

[110] T. Drakos, M. Giannakou, G. Menikou, G. Constantinides, and C. Damianou, “Characterization of a soft tissue-mimicking agar/wood powder material for MRgFUS applications,” *Ultrasonics*, vol. 113: 10635, 2021, doi: 10.1016/j.ultras.2021.106357.

[111] R. L. King, B. A. Herman, S. Maruvada, K. A. Wear, and G. Harris, “Development of a HIFU phantom,” *AIP Conf. Proc.*, vol. 911, pp. 351–356, 2007, doi: 10.1063/1.2744296.

[112] V. Hadjisavvas, K. Ioannides, M. Komodromos, N. Mylonas, and C. Damianou, “Evaluation of the contrast between tissues and thermal lesions in rabbit in vivo produced by high intensity focused ultrasound using fast spin echo MRI sequences,” *J Biomed. Sci. Eng.*, vol. 4, no. 1, pp. 51–61, 2010, doi: 10.4236/jbise.2011.41007.

[113] A. Eranki *et al.*, “Mechanical Fractionation of Tissues using Microsecond-Long HIFU Pulses on a Clinical MR-HIFU System,” *Int J Hyperth.*, vol. 34, no. 8, pp. 1213–1224, 2019, doi: 10.1080/02656736.2018.1438672.

[114] E. Kholmovski, R. Ranjan, N. Angel, and N. F. Marrouche, “T2* -weighted MRI technique for visualization of RF ablation lesions,” *J. Cardiovasc. Magn. Reson.*, vol. 18, no. Suppl 1, pp. 2–4, 2016, doi: 10.1186/1532-429X-18-S1-O128.

[115] E. C. Mackle *et al.*, “Patient-specific polyvinyl alcohol phantom fabrication with ultrasound and x-ray contrast for brain tumor surgery planning,” *J. Vis. Exp.*, no.

161, p. e61344, 2020, doi: 10.3791/61344.

[116] E. T. W. Tan, J. M. Ling, and S. K. Dinesh, “The feasibility of producing patient-specific acrylic cranioplasty implants with a low-cost 3D printer,” *J. Neurosurg.*, vol. 124, no. 5, pp. 1531–1537, 2016, doi: 10.3171/2015.5.JNS15119.

[117] V. Hadjisavvas, N. Mylonas, K. Ioannides, and C. Damianou, “An MR-compatible phantom for evaluating the propagation of high intensity focused ultrasound through the skull,” *AIP Conf. Proc.*, vol. 1481, pp. 119–124, 2012, doi: 10.1063/1.4757321.

[118] F. Sohet and R. Daneman, “Genetic mouse models to study blood-brain barrier development and function,” *Fluids Barriers CNS*, vol. 10, no. 1, pp. 1–18, 2013, doi: 10.1186/2045-8118-10-3.

[119] W. A. Banks, “Mouse Models of Neurological Disorders: A View From the Blood-brain Barrier,” *Biochim Biophys Acta*, vol. 1802, no. 10, pp. 881–888, 2010, doi: 10.1016/j.bbadis.2009.10.011.

[120] J. J. Choi, S. Wang, Y.-S. Tung, B. Morrison, and E. E. Konofagou, “Molecules of various pharmacologically-relevant sizes can cross the ultrasound-induced blood-brain barrier opening in vivo,” *Ultrasound Med Biol*, vol. 36, no. 1, pp. 58–67, 2010, doi: 10.1016/j.ultrasmedbio.2009.08.006.

[121] J. J. Choi, K. Selert, Z. Gao, G. Samiotaki, B. Baseri, and E. E. Konofagou, “Noninvasive and localized blood-brain barrier disruption using focused ultrasound can be achieved at short pulse lengths and low pulse repetition frequencies,” *J. Cereb. Blood Flow Metab.*, vol. 31, no. 2, pp. 725–737, 2011, doi: 10.1038/jcbfm.2010.155.

[122] S. Wang, G. Samiotaki, O. Olumolade, J. A. Feshitan, and E. E. Konofagou, “Microbubble Type and Distribution Dependence of Focused Ultrasound Induced Blood Brain Barrier Opening,” *Bone*, vol. 23, no. 1, pp. 1–7, 2008, doi: 10.1016/j.ultrasmedbio.2013.09.015.

[123] N. A. Lapin, K. Gill, B. R. Shah, and R. Chopra, “Consistent opening of the blood brain barrier using focused ultrasound with constant intravenous infusion of microbubble agent,” *Sci. Rep.*, vol. 10, no. 1, pp. 1–11, 2020, doi: 10.1038/s41598-020-73312-9.

[124] C. D. Arvanitis *et al.*, “Mechanisms of enhanced drug delivery in brain metastases with focused ultrasound-induced blood–tumor barrier disruption,” *Proc. Natl. Acad. Sci. U. S. A.*, vol. 115, no. 37, pp. E8717–E8726, 2018, doi: 10.1073/pnas.1807105115.

[125] S. Wang *et al.*, “Non-invasive , Focused Ultrasound- Facilitated Gene Delivery for Optogenetics,” *Sci. Rep.*, pp. 1–7, 2017, doi: 10.1038/srep39955.

[126] J. F. Jordão *et al.*, “Antibodies targeted to the brain with image-guided focused ultrasound reduces amyloid-β plaque load in the TgCRND8 mouse model of Alzheimer’s disease,” *PLoS One*, vol. 5, no. 5, pp. 4–11, 2010, doi: 10.1371/journal.pone.0010549.

[127] J. F. Jordão *et al.*, “Amyloid-β plaque reduction, endogenous antibody delivery and glial activation by brain-targeted, transcranial focused ultrasound,” *Exp Neurol*, vol. 248, pp. 16–29, 2013, doi: 10.1016/j.expneurol.2013.05.008.

[128] A. Burgess *et al.*, “Alzheimer disease in a mouse model: Mr imaging-guided focused ultrasound targeted to the hippocampus opens the blood-brain barrier and improves pathologic abnormalities and behavior,” *Radiology*, vol. 273, no. 3, pp. 736–745, 2014, doi: 10.1148/radiol.14140245.

[129] S. B. Raymond, L. H. Treat, J. D. Dewey, N. J. Mcdannold, K. Hynynen, and B. J. Bacskai, “Ultrasound Enhanced Delivery of Molecular Imaging and Therapeutic Agents in Alzheimer ’ s Disease Mouse Models,” *PLoS One*, vol. 3, no. 5, pp. 1–7, 2008, doi: 10.1371/journal.pone.0002175.

[130] Y. Shen, L. Hua, C. Yeh, L. Shen, M. Ying, and Z. Zhang, “Ultrasound with microbubbles improves memory, ameliorates pathology and modulates

hippocampal proteomic changes in a triple transgenic mouse model of Alzheimer' s disease," *Theranostics*, vol. 10, no. 25, pp. 11794–11819, 2020, doi: 10.7150/thno.44152.

[131] R. Haumann, J. C. Videira, G. J. L. Kaspers, and D. G. Van Vuurden, "Overview of Current Drug Delivery Methods Across the Blood – Brain Barrier for the Treatment of Primary Brain Tumors," *CNS Drugs*, vol. 34, no. 11, pp. 1121–1131, 2020, doi: 10.1007/s40263-020-00766-w.

[132] A. Dréan *et al.*, "Temporary blood-brain barrier disruption by low intensity pulsed ultrasound increases carboplatin delivery and efficacy in preclinical models of glioblastoma," *J Neurooncol*, vol. 144, no. 1, pp. 33–41, 2019, doi: 10.1007/s11060-019-03204-0.

[133] J. Ishida *et al.*, "MRI-guided focused ultrasound enhances drug delivery in experimental diffuse intrinsic pontine glioma," *J Control ReleaseJ Control Release*, vol. 330, pp. 1034–1045, 2021, doi: 10.1016/j.jconrel.2020.11.010.

[134] K. Abe and T. Taira, "Focused ultrasound treatment, present and future," *Neurol. Med. Chir. (Tokyo).*, vol. 57, no. 8, pp. 386–391, 2017, doi: 10.2176/nmc.ra.2017-0024.

[135] C. Damianou, M. Giannakou, G. Menikou, and L. Ioannou, "Magnetic resonance imaging-guided focused ultrasound robotic system with the subject placed in the prone position," *Digit. Med.*, vol. 6, no. 1, pp. 24–31, 2020, doi: 10.4103/digm.digm_2_20.

[136] T. Drakos *et al.*, "MRI-Guided Focused Ultrasound Robotic System for Preclinical use," *J. Vet. Med. Anim. Sci.*, vol. 4, no. 1, pp. 1–11, 2021.

[137] A. Antoniou, M. Giannakou, N. Evripidou, S. Stratis, S. Pichardo, and C. Damianou, "Robotic system for top to bottom MRgFUS therapy of multiple cancer types," *Int. J. Med. Robot. Comput. Assist. Surg.*, 2022, doi: 10.1002/rcs.2364.

[138] A. Antoniou *et al.*, "Robotic system for magnetic resonance guided focused

ultrasound ablation of abdominal cancer," *Int. J. Med. Robot. Comput. Assist. Surg.*, vol. 17, no. 5, 2021, doi: 10.1002/rcs.2299.

[139] M. Giannakou *et al.*, "MRI-guided focused ultrasound robotic system for transrectal prostate cancer therapy," *Int. J. Med. Robot. Comput. Assist. Surg.*, pp. 1–15, 2021, doi: 10.1002/rcs.2237.

[140] A. Antoniou and C. Damianou, "MR relaxation properties of tissue-mimicking phantoms," *Ultrasonics*, vol. 119, 2022, doi: 10.1016/j.ultras.2021.106600.

[141] K. Takegami, Y. Kaneko, T. Watanabe, T. Maruyama, Y. Matsumoto, and H. Nagawa, "Polyacrylamide gel containing egg white as new model for irradiation experiments using focused ultrasound," *Ultrasound Med Biol*, vol. 30, no. 10, pp. 1419–1422, 2004, doi: 10.1016/j.ultrasmedbio.2004.07.016.

[142] A. Antoniou *et al.*, "MR relaxation times of agar-based tissue-mimicking phantoms," *J. Appl. Clin. Med. Phys.*, p. 213533, 2022, doi: 10.1002/acm2.13533.

[143] E. L. Madsen, M. A. Hobson, H. Shi, T. Varghese, and G. R. Frank, "Tissue-mimicking agar/gelatin materials for use in heterogeneous elastography phantoms," *Phys. Med. Biol.*, vol. 50, no. 23, pp. 5597–5618, 2005, doi: 10.1088/0031-9155/50/23/013.

[144] A. Antoniou *et al.*, "Simple methods to test the accuracy of MRgFUS robotic systems," *Int. J. Med. Robot. Comput. Assist. Surg.*, vol. 17, no. 4, 2021, doi: 10.1002/rcs.2287.

[145] L. Chen, C. Ma, and J. Meyer, "Quality Assurance for MR Guided Focused Ultrasound Treatment of Bone Metastasis: A Clinical Experience," *Int. J. Radiat. Oncol.*, vol. 90, no. 1, p. S703, 2014, doi: 10.1016/j.ijrobp.2014.05.2059.

[146] N. Mcdannold and K. Hynynen, "Quality assurance and system stability of a clinical MRI-guided focused ultrasound system: Four-year experience," *Med. Phys.*, vol. 33, no. 11, pp. 4307–4313, 2006, doi: 10.1118/1.2352853.

[147] K. R. Gorny, N. J. Hangiandreou, G. K. Hesley, B. S. Gostout, K. P. McGee, and J. P. Felmlee, “MR guided focused ultrasound: Technical acceptance measures for a clinical system,” *Phys. Med. Biol.*, vol. 51, no. 12, pp. 3155–3173, 2006, doi: 10.1088/0031-9155/51/12/011.

[148] F. Vicari *et al.*, “A daily quality assurance routine for ultrasounds in vitro experiments,” *Transl. Cancer Res.*, vol. 3, no. 5, pp. 421–429, 2014, doi: 10.3978/j.issn.2218-676X.2014.09.02.

[149] U. Schätzle, T. Reuner, J. Jenne, and A. Heilingbrunner, “Quality assurance tools for therapeutic ultrasound,” *Ultrasonics*, vol. 36, no. 1–5, pp. 679–682, 1998, doi: 10.1016/S0041-624X(97)00138-8.

[150] G. Acri *et al.*, “A ‘user-friendly’ phantom to conduct Quality Controls on MRgFUS device,” in *Journal of Physics: Conference Series*, 2022, vol. 2162, no. 1, p. 012004, doi: 10.1088/1742-6596/2162/1/012004.

[151] S. Ambrogio *et al.*, “A standard test phantom for the performance assessment of magnetic resonance guided high intensity focused ultrasound (MRgHIFU) thermal therapy devices,” *Int. J. Hyperth.*, vol. 39, no. 1, pp. 57–68, 2022, doi: 10.1080/02656736.2021.2017023.

[152] A. Antoniou, N. Evripidou, M. Giannakou, G. Constantinides, and C. Damianou, “Acoustical properties of 3D printed thermoplastics,” *J. Acoust. Soc. Am.*, vol. 149, no. 4, pp. 2854–2864, 2021, doi: 10.1121/10.0004772.

[153] T. Drakos *et al.*, “Ultrasonic Attenuation of an Agar, Silicon Dioxide, and Evaporated Milk Gel Phantom,” *J. Med. Ultrasound*, vol. 29, no. 4, pp. 239–249, 2021, doi: 10.4103/JMU.JMU.

[154] R. Ortega, A. Téllez, L. Leija, and A. Vera, “Measurement of Ultrasonic Properties of Muscle and Blood Biological Phantoms,” *Phys. Procedia*, vol. 3, no. 1, pp. 627–634, 2010, doi: 10.1016/j.phpro.2010.01.079.

[155] M. D. Mitchell, H. L. Kundel, L. Axel, and P. M. Joseph, “Agarose as a tissue

equivalent phantom material for NMR imaging," *Magn. Reson. Imaging*, vol. 4, no. 3, pp. 263–266, 1986, doi: 10.1016/0730-725X(86)91068-4.

[156] A. Partanen, C. Mougenot, and T. Vaara, "Feasibility of agar-silica phantoms in quality assurance of MRgHIFU," *AIP Conf. Proc.*, vol. 1113, pp. 296–300, 2009, doi: 10.1063/1.3131434.

[157] D. Johnson and V. Zderic, "Design and construction of a flow phantom for HIFU research," *Proc. - IEEE Ultrason. Symp.*, pp. 1294–1296, 2007, doi: 10.1109/ULTSYM.2007.325.

[158] D. W. Rickey, P. A. Picot, D. A. Christopher, and A. Fenster, "A wall-less vessel phantom for Doppler ultrasound studies," *Ultrasound Med. Biol.*, vol. 21, no. 9, pp. 1163–1176, 1995, doi: 10.1016/0301-5629(95)00044-5.

[159] E. L. Madsen, G. R. Frank, and F. Dong, "Liquid or solid ultrasonically tissue-mimicking materials with very low scatter," *Ultrasound Med. Biol.*, vol. 24, no. 4, pp. 535–542, 1998, doi: 10.1016/S0301-5629(98)00013-1.

[160] H. Kato, M. Hiraoka, and T. Ishida, "An agar phantom for hyperthermia," *Int. J. Med. Phys. Res. Pract.*, vol. 13, no. 3, pp. 396–398, 1986, doi: 10.1118/1.595882.

[161] R. F. Smith, B. K. Rutt, and D. W. Holdsworth, "Anthropomorphic Carotid Bifurcation Phantom for MRI Applications," *J. Magn. Reson. Imaging*, vol. 10, no. 4, pp. 533–544, 1999, doi: 10.1002/(sici)1522-2586(199910)10:4<533::aid-jmri6>3.0.co;2-z.

[162] G. Captur *et al.*, "A medical device-grade T1 and ECV phantom for global T1 mapping quality assurance — the T 1 Mapping and ECV Standardization in cardiovascular magnetic resonance (T1MES) program," *J. Cardiovasc. Magn. Reson.*, vol. 18: 58, pp. 1–20, 2016, doi: 10.1186/s12968-016-0280-z.

[163] J. O. Christoffersson, L. E. Olsson, and S. Sjöberg, "Nickel-doped agarose gel phantoms in MR imaging," *Acta radiol.*, vol. 32, no. 5, pp. 426–431, 1991, doi: 10.3109/02841859109177599.

[164] Y. Chen *et al.*, “Rapid Volumetric T1 Mapping of the Abdomen Using 3D Through-Time Spiral GRAPPA,” *Magn Reson Med*, vol. 75, no. 4, pp. 1457–1465, 2017, doi: 10.1002/mrm.25693.

[165] Q. Li, X. Cao, H. Ye, C. Liao, H. He, and J. Zhong, “Ultrashort echo time magnetic resonance fingerprinting (UTE - MRF) for simultaneous quantification of long and ultrashort T 2 tissues,” *Magn. Reson. Med.*, vol. 82, pp. 1359–1372, 2019, doi: 10.1002/mrm.27812.

[166] M. Nezafat and M. Botnar, “Imaging sequence for joint myocardial T1 mapping and fat/water separation,” *Magn. Reson. Med.*, vol. 81, no. 1, pp. 486–494, 2019, doi: 10.1002/mrm.27390.

[167] K. Jiang, Y. Zhu, S. Jia, Y. Wu, X. Liu, and Y. Chung, “Fast T1 mapping of the brain at high fi eld using Look-Locker and fast imaging,” *Magn. Reson. Imaging*, vol. 36, pp. 49–55, 2017, doi: 10.1016/j.mri.2016.10.022.

[168] D. Tamada, T. Wakayama, H. Onishi, and U. Motosugi, “Multiparameter estimation using multi-echo spoiled gradient echo with variable flip angles and multicontrast compressed sensing,” *Magn. Reson. Med.*, vol. 80, no. 4, pp. 1546–1555, 2018, doi: 10.1002/mrm.27151.

[169] T. Yoshida, A. Urikura, K. Shirata, Y. Nakaya, M. Endo, and S. Terashima, “Short tau inversion recovery in breast diffusion - weighted imaging : signal - to - noise ratio and apparent diffusion coefficients using a breast phantom in comparison with spectral attenuated inversion recovery,” *Radiol. Med.*, vol. 123, no. 4, pp. 296–304, 2018, doi: 10.1007/s11547-017-0840-9.

[170] A. Altermatt *et al.*, “Design and construction of an innovative brain phantom prototype for MRI,” *Magn. Reson. Med.*, vol. 81, no. 2, pp. 1165–1171, 2019, doi: 10.1002/mrm.27464.

[171] M. De Brabandere, C. Kirisits, R. Peeters, K. Haustermans, and F. Van den Heuvel, “Accuracy of seed reconstruction in prostate postplanning studied with a CT- and

MRI-compatible phantom," *Radiother. Oncol.*, vol. 79, no. 2, pp. 190–197, 2006, doi: 10.1016/j.radonc.2006.04.009.

[172] D. M. King, A. J. Fagan, C. M. Moran, and J. E. Browne, "Comparative imaging study in ultrasound, MRI, CT, and DSA using a multimodality renal artery phantom," *Med. Phys.*, vol. 38, no. 2, pp. 565–573, 2011, doi: 10.1118/1.3533674.

[173] A. Kozana, T. Boursianis, G. Kalaitzakis, M. Raissaki, and T. G. Maris, "Neonatal brain: Fabrication of a tissue-mimicking phantom and optimization of clinical T1w and T2w MRI sequences at 1.5 T," *Phys. Medica*, vol. 55, pp. 88–97, 2018, doi: 10.1016/j.ejmp.2018.10.022.

[174] S. Pichardo, D. Melodelima, L. Curiel, and J. Kivinen, "Suitability of a tumour-mimicking material for the evaluation of high-intensity focused ultrasound ablation under magnetic resonance guidance," *Phys. Med. Biol.*, vol. 58, no. 7, pp. 2163–2183, 2013, doi: 10.1088/0031-9155/58/7/2163.

[175] K. Yoshimura *et al.*, "Development of a Tissue-Equivalent MRI Phantom Using Carrageenan Gel," *Magn. Reson. Med.*, vol. 50, pp. 1011–1017, 2003, doi: 10.1002/mrm.10619.

[176] W. Neumann, F. Lietzmann, L. R. Schad, and F. G. Zöllner, "Design of a multimodal (MR/CT) anthropomorphic thorax phantom," *Z Med Phys*, vol. 27, no. 2, pp. 124–131, 2017, doi: 10.1016/j.zemedi.2016.07.004.

[177] A. Yoshida *et al.*, "Development of a phantom compatible for MRI and hyperthermia using carrageenan gel — relationship between T 1 and T 2 values and NaCl concentration," *Int. J. Hyperth.*, vol. 20, no. 8, pp. 803–814, 2009, doi: 10.1080/02656730420002 00268.

[178] W. D. D'Souza, E. L. Madsen, O. Unal, K. K. Vigen, G. R. Frank, and B. R. Thomadsen, "Tissue mimicking materials for a multi-imaging modality prostate phantom," *Am Assoc Phys Med*, vol. 28, no. 4, pp. 688–700, 2001, doi: 10.1118/1.1354998.

[179] J. R. Rice, R. H. Milbrandt, E. L. Madsen, G. R. Frank, E. J. Boote, and J. C. Blechinger, “Anthropomorphic 1H MRS head phantom,” *Med Phys*, vol. 25, no. 7, pp. 1145–1156, 1998, doi: 10.1118/1.598306.

[180] L. W. Hofstetter *et al.*, “Development and Characterization of a Tissue Mimicking Psyllium Husk Gelatin Phantom for Ultrasound and Magnetic Resonance Imaging,” *Int J Hyperth.*, vol. 37, no. 1, pp. 283–290, 2020, doi: 10.1080/02656736.2020.1739345.

[181] E. L. Madsen, G. R. Frank, T. A. Krouskop, T. Varghese, F. Kallel, and J. Ophir, “Tissue-mimicking oil-in-gelatin dispersions for use in heterogeneous elastography phantoms,” *Ultrason. Imaging*, vol. 25, no. 1, pp. 17–38, 2003, doi: 10.1177/016173460302500102.

[182] C. Cheng, F. Preiswerk, W. S. Hoge, T. Kuo, and P. Healthcare, “Multi-Pathway Multi-Echo (MPME) imaging: all main MR parameters mapped based on a single 3D scan,” *Magn Reson Med*, vol. 81, no. 3, pp. 1699–1713, 2020, doi: 10.1002/mrm.27525.

[183] P. G. Anderson, N. C. Rouze, and M. L. Palmeri, “Effect of Graphite Concentration on Shear-Wave Speed in Gelatin-Based Tissue-Mimicking Phantoms,” *Ultrason Imaging*, vol. 33, no. 2, pp. 134–142, 2011, doi: 10.1177/016173461103300204.

[184] M. P. Robinson, M. J. Richardson, J. L. Green, and A. W. Preece, “New materials for dielectric simulation of tissues,” *Phys. Med. Biol.*, vol. 36, no. 12, pp. 1565–1571, 1991, doi: 10.1088/0031-9155/36/12/002.

[185] A. Bigi, G. Cojazzi, S. Panzavolta, N. Roveri, and K. Rubini, “Stabilization of gelatin films by crosslinking with genipin,” *Biomaterials*, vol. 23, no. 24, pp. 4827–4832, 2002, doi: 10.1016/S0142-9612(02)00235-1.

[186] R. . De Carvalho and C. R. F. Grosso, “Characterization of Gelatin Based Films Modified with Transglutaminase, Glyoxal and Formaldehyde,” *Food Hydrocoll.*, vol. 18, pp. 717–726, 2004, doi: 10.1016/j.foodhyd.2003.10.005.

[187] A. Bigi, G. Cojazzi, S. Panzavolta, K. Rubini, and N. Roveri, “Mechanical and thermal properties of gelatin films at different degrees of glutaraldehyde crosslinking,” *Biomaterials*, vol. 22, no. 8, pp. 763–768, 2001, doi: 10.1016/s0142-9612(00)00236-2.

[188] J. C. Blechinger, E. L. Madsen, and G. R. Frank, “Tissue mimicking gelatin–agar gels for use in magnetic resonance imaging phantoms,” *Med. Phys.*, vol. 15, no. 4, pp. 629–636, 1988, doi: 10.1118/1.596219.

[189] A. K. Siddiqi and S. H. Cho, “Agar-based heat-sensitive gel with linear thermal response over 65–80 °C,” *J Therm Anal Calorim*, vol. 111, pp. 1805–1809, 2013, doi: 10.1007/s10973-012-2491-3.

[190] M. Lazebnik, E. L. Madsen, G. R. Frank, and S. C. Hagness, “Tissue-mimicking phantom materials for narrowband and ultrawideband microwave applications,” *Phys Med Biol*, vol. 50, no. 18, pp. 4245–4258, 2005, doi: 10.1088/0031-9155/50/18/001.

[191] C. Lafon *et al.*, “Gel phantom for use in high-intensity focused ultrasound dosimetry,” *Ultrasound Med. Biol.*, vol. 31, no. 10, pp. 1383–1389, 2005, doi: 10.1016/j.ultrasmedbio.2005.06.004.

[192] N. P. Brodin, A. Partanen, P. Asp, C. A. Branch, C. Guha, and W. A. Tomé, “A simple method for determining the coagulation threshold temperature of transparent tissue-mimicking thermal therapy gel phantoms: Validated by magnetic resonance imaging thermometry,” *Med Phys*, vol. 43, no. 3, pp. 1167–1174, 2016, doi: 10.1118/1.4941361.

[193] B. Bazrafshan *et al.*, “Temperature imaging of laser-induced thermotherapy (LITT) by MRI: Evaluation of different sequences in phantom,” *Lasers Med. Sci.*, vol. 29, no. 1, pp. 173–183, 2014, doi: 10.1007/s10103-013-1306-5.

[194] M. McDonald, S. Lochhead, R. Chopra, and M. J. Bronskill, “Multi-modality tissue-mimicking phantom for thermal therapy,” *Phys. Med. Biol.*, vol. 49, no. 13,

pp. 2767–2778, 2004, doi: 10.1088/0031-9155/49/13/001.

[195] M. J. Choi, S. R. Guntur, K. IL Lee, D. G. Paeng, and A. Coleman, "A Tissue Mimicking Polyacrylamide Hydrogel Phantom for Visualizing Thermal Lesions Generated by High Intensity Focused Ultrasound," *Ultrasound Med. Biol.*, vol. 39, no. 3, pp. 439–448, 2013, doi: 10.1016/j.ultrasmedbio.2012.10.002.

[196] F. De Luca, B. Maraviglia, and A. Mercurio, "Biological tissue simulation and standard testing material for MRI," *Magn Reson Med*, 1987, doi: 10.1002/mrm.1910040213.

[197] K. Zell, J. I. Sperl, M. W. Vogel, R. Niessner, and C. Haisch, "Acoustical properties of selected tissue phantom materials for ultrasound imaging," *Phys. Med. Biol.*, vol. 52, no. 20, pp. N475–N484, 2007, doi: 10.1088/0031-9155/52/20/N02.

[198] J. S. Huber, Q. Peng, and W. W. Moses, "Multi-modality phantom development," *IEEE Trans. Nucl. Sci.*, vol. 56, no. 5, pp. 2722–2727, 2009, doi: 10.1109/TNS.2009.2028073.

[199] A. C. Waspe *et al.*, "Dynamic T 2 -mapping during magnetic resonance guided high intensity focused ultrasound ablation of bone marrow," in *AIP Conference Proceedings*, 2012, vol. 1503, no. 1, pp. 222–226, doi: 10.1063/1.4769948.

[200] J. Z. Bojorquez, S. Bricq, C. Acquitter, F. Brunotte, P. M. Walker, and A. Lalande, "What are normal relaxation times of tissues at 3 T?," *Magn. Reson. Imaging*, vol. 35, no. 2017, pp. 69–80, 2017, doi: 10.1016/j.mri.2016.08.021.

[201] T. Drakos, M. Giannakou, G. Menikou, C. Ioannides, and C. Damianou, "An improved method to estimate ultrasonic absorption in agar-based gel phantom using thermocouples and MR thermometry," *Ultrasonics*, vol. 103, 2020, doi: 10.1016/j.ultras.2020.106089.

[202] P. A. Bottomley, T. H. Foster, R. E. Argersinger, and L. M. Pfeifer, "A review of normal tissue hydrogen NMR relaxation times and relaxation mechanisms from 1–

100 MHz: Dependence on tissue type, NMR frequency, temperature, species, excision, and age," *Int. J. Med. Phys. Res. Pract.*, vol. 11, no. 4, pp. 425–448, 1984, doi: 10.1118/1.595535.

[203] G. J. Stanisz *et al.*, "T1, T2 relaxation and magnetization transfer in tissue at 3T," *Magn. Reson. Med.*, vol. 54, no. 3, pp. 507–512, 2005, doi: 10.1002/mrm.20605.

[204] M. S. Ahmad *et al.*, "Dynamic Hepatocellular Carcinoma Model Within a Liver Phantom for Multimodality Imaging," *Eur. J. Radiol. Open*, vol. 7, p. 100257, 2020, doi: 10.1016/j.ejro.2020.100257.

[205] Q. Gan *et al.*, "Benchtop and Animal Validation of a Projective Imaging System for Potential Use in Intraoperative Surgical Guidance," *PLoS One*, vol. 11, no. 7, p. e0157794, 2016, doi: 10.1371/journal.pone.0157794.

[206] D. J. McHugh *et al.*, "A biomimetic tumor tissue phantom for validating diffusion-weighted MRI measurements," *Magn. Reson. Med.*, vol. 80, no. 1, pp. 147–158, 2018, doi: 10.1002/mrm.27016.

[207] E. P. M. LaRochelle, S. S. Streeter, E. A. Littler, and A. J. Ruiz, "3D-Printed Tumor Phantoms for Assessment of In Vivo Fluorescence Imaging Analysis Methods," *Mol. Imaging Biol.*, 2022, doi: 10.1007/s11307-022-01783-5.

[208] S. Hatamikia *et al.*, "Realistic 3D printed imaging tumor phantoms for validation of image processing algorithms," *Med Phys*, pp. 1–17, 2022, doi: 10.48550/arXiv.2211.14861.

[209] A. Valladares, T. Beyer, and I. Rausch, "Physical imaging phantoms for simulation of tumor heterogeneity in PET, CT, and MRI: An overview of existing designs," *Med. Phys.*, vol. 47, no. 4, pp. 2023–2037, 2020, doi: 10.1002/mp.14045.

[210] L. Presotto *et al.*, "PET textural features stability and pattern discrimination power for radiomics analysis: An 'ad-hoc' phantoms study," *Phys. Medica*, vol. 50, pp. 66–74, 2018, doi: 10.1016/j.ejmp.2018.05.024.

[211] S. A. Waugh, R. A. Lerski, L. Bidaut, and A. M. Thompson, “The influence of field strength and different clinical breast MRI protocols on the outcome of texture analysis using foam phantoms,” *Med. Phys.*, vol. 38, no. 9, pp. 5058–5066, 2011, doi: 10.1118/1.3622605.

[212] M. T. Sramek *et al.*, “Development of a novel tumor phantom model for head and neck squamous cell carcinoma and its applications,” in *Image-Guided Procedures, Robotic Interventions, and Modeling*, 2020, p. 99, doi: 10.1117/12.2550597.

[213] S. Y. Ng and C. Lin, “Low-cost and easily fabricated ultrasound-guided breast phantom for breast biopsy training,” *Prepr. (Version 1) available Res. Sq.*, pp. 1–22, 2020, doi: 10.21203/rs.2.19957/v1.

[214] B. L. Daniel, R. L. Birdwell, J. W. Black, D. M. Ikeda, G. H. Glover, and R. J. Herfkens, “Interactive MR-guided, 14-gauge core-needle biopsy of enhancing lesions in a breast phantom model,” *Acad. Radiol.*, vol. 4, no. 7, pp. 508–512, 1997, doi: 10.1016/S1076-6332(97)80238-3.

[215] H. Webb, M. G. Lubner, and J. L. Hinshaw, “Thermal Ablation,” *Semin. Roentgenol.*, vol. 46, no. 2, pp. 133–141, 2011, doi: 10.1053/j.ro.2010.08.002.

[216] M. B. Glassberg *et al.*, “Microwave ablation compared with radiofrequency ablation for treatment of hepatocellular carcinoma and liver metastases: A systematic review and metaanalysis,” *Onco. Targets. Ther.*, vol. 12, pp. 6407–6438, 2019, doi: 10.2147/OTT.S204340.

[217] Y. Zhou *et al.*, “A thermochromic tissue-mimicking phantom model for verification of ablation plans in thermal ablation,” *Ann Transl Med*, vol. 9, no. 4, p. 354, 2021, doi: 10.21037/atm-21-523.

[218] W. J. Chen, Q. Wang, and C. Y. Kim, “Gel Phantom Models for Radiofrequency and Microwave Ablation of the Liver,” *Dig Dis Interv*, vol. 4, no. 3, pp. 303–310, 2020, doi: 10.1055/s-0040-1716737.

[219] Z. Liu, M. Ahmed, Y. Weinstein, M. Yi, R. L. Mahajan, and S. N. Goldberg,

"Characterization of the RF ablation-induced 'oven effect': the importance of background tissue thermal conductivity on tissue heating," *Int J Hyperth.*, vol. 22, no. 4, pp. 327–342, 2006, doi: 10.1080/02656730600609122.

[220] D. Haemmerich and D. J. Schutt, "RF ablation at low frequencies for targeted tumor heating: In vitro and computational modeling results," *IEEE Trans. Biomed. Eng.*, vol. 58, no. 2, pp. 404–410, 2011, doi: 10.1109/TBME.2010.2085081.

[221] R. Ortega-Palacios, C. J. Trujillo-Romero, M. F. J. Cepeda-Rubio, L. Leija, and A. V. Hernández, "Heat transfer study in breast tumor phantom during microwave ablation: Modeling and experimental results for three different antennas," *Electronics*, vol. 9, no. 3, p. 535, 2020, doi: 10.3390/electronics9030535.

[222] X. Zhong, P. Zhou, Y. Zhao, W. Liu, and X. Zhang, "A novel tissue-mimicking phantom for US/CT/MR-guided tumor puncture and thermal ablation," *Int. J. Hyperth.*, vol. 39, no. 1, pp. 557–563, 2022, doi: 10.1080/02656736.2022.2056249.

[223] K. S. Kim and S. Y. Lee, "Nanoparticle-mediated radiofrequency capacitive hyperthermia: A phantom study with magnetic resonance thermometry," *Int. J. Hyperth.*, vol. 31, no. 8, pp. 831–839, 2015, doi: 10.3109/02656736.2015.1096968.

[224] K. Li, Z. Su, E. Xu, Q. Huang, Q. Zeng, and R. Zheng, "Evaluation of the ablation margin of hepatocellular carcinoma using CEUS-CT/MR image fusion in a phantom model and in patients," *BMC Cancer*, vol. 17, no. 1, pp. 1–10, 2017, doi: 10.1186/s12885-017-3061-7.

[225] A. Hassanuddin *et al.*, "Factors affecting tumor ablation during high intensity focused ultrasound treatment," *Gut Liver*, vol. 8, no. 4, pp. 433–437, 2014, doi: 10.5009/gnl.2014.8.4.433.

[226] C. Y. An, Y. L. Hsu, and C. S. Tseng, "An Ultrasound-Guided Robotic HIFU Ablation System with Respiration Induced Displacement and Time Delay

Compensation," *J. Med. Biol. Eng.*, vol. 39, no. 5, pp. 796–805, 2019, doi: 10.1007/s40846-019-00463-0.

[227] K. Kaczmarek, T. Hornowski, I. Antal, M. Rajnak, M. Timko, and A. Józefczak, "Sono-magnetic heating in tumor phantom," *J. Magn. Magn. Mater.*, vol. 500, p. 166396, 2020, doi: 10.1016/j.jmmm.2020.166396.

[228] C. Damianou, "The role of phantoms in magnetic resonance imaging-guided focused ultrasound surgery," *Digit. Med.*, vol. 5, no. 2, pp. 52–55, 2019, doi: 10.4103/digm.digm_13_19.

[229] M. Zeece, "Food additives," in *Introduction to the Chemistry of Food*, 2020, pp. 251–311.

[230] A. Filippou and C. Damianou, "Evaluation of ultrasonic scattering in agar-based phantoms using 3D printed scattering molds," *J. Ultrasound*, vol. 25, no. 3, pp. 597–609, 2022, doi: 10.1007/s40477-021-00630-7.

[231] A. Filippou, I. Louca, and C. Damianou, "Characterization of a fat tissue mimicking material for high intensity focused ultrasound applications," *J. Ultrasound*, 2022, doi: 10.1007/s40477-022-00746-4.

[232] R. D. Peters, R. S. Hinks, and R. M. Henkelman, "Heat-source orientation and geometry dependence in proton-resonance frequency shift magnetic resonance thermometry," *Magn. Reson. Med.*, vol. 41, no. 5, pp. 909–918, 1999, doi: 10.1002/(SICI)1522-2594(199905)41:5<909::AID-MRM9>3.0.CO;2-N.

[233] C. Bing *et al.*, "Drift correction for accurate PRF shift MR thermometry during mild hyperthermia treatments with MR-HIFU," *Int J Hyperth.*, vol. 32, no. 6, pp. 673–687, 2017, doi: 10.1080/02656736.2016.1179799.

[234] J. A. De Zwart, F. C. Vimeux, C. Delalande, P. Canioni, and C. T. W. Moonen, "Fast lipid-suppressed MR temperature mapping with echo-shifted gradient- echo imaging and spectral-spatial excitation," *Magn. Reson. Med.*, vol. 42, no. 1, pp. 53–59, 1999, doi: 10.1002/(SICI)1522-2594(199907)42:1<53::AID-

MRM9>3.0.CO;2-S.

[235] T. D. Mast, “Empirical relationships between acoustic parametersin human soft tissues,” *Acoust. Res. Lett. Online*, 2000, doi: 10.1121/1.1336896.

[236] S. A. Goss, L. A. Frizzell, and F. Dunn, “ULTRASONIC ABSORPTION AND ATTENUATION IN MAMMALIAN TISSUES,” *Ultrasound Med. Biol.*, vol. 5, no. 2, pp. 181–186, 1979, doi: 10.1016/0301-5629(79)90086-3.

[237] V. Chan and A. Perlas, “Basics of Ultrasound Imaging,” in *Atlas of Ultrasound-Guided Procedures in Interventional Pain Management*, 2011, pp. 13–19.

[238] K. Giering, O. Minet, I. Lamprecht, and G. Müller, “Review of Thermal Properties of Biological Tissues,” in *Proceedings of SPIE - The International Society for Optical Engineering*, 1995, pp. 45–65.

[239] A. Antoniou, A. Nikolaou, A. Georgiou, N. Evripidou, and C. Damianou, “Development of an US, MRI, and CT imaging compatible realistic mouse phantom for thermal ablation and focused ultrasound evaluation,” *Ultrasonics*, vol. 131, 2023, doi: 10.1016/j.ultras.2023.106955.

[240] A. Kalra and K.-H. Yang, “Developing FE Human Models From Medical Images,” in *Basic Finite Element Method as Applied to Injury Biomechanics*, Academic Press, 2018, pp. 389–415.

[241] C. Damianou and K. Hynynen, “The effect of various physical parameters on the size and shape of necrosed tissue volumeuring ultrasound surgery,” *J. Acoust. Soc. Am.*, vol. 95, no. 3, pp. 1641–1649, 1994, doi: 10.1121/1.408550.

[242] J. E. Kennedy, G. R. TER Haar, and D. Cranston, “High intensity focused ultrasound: surgery of the future?,” *Br. J. Radiol.*, vol. 76, pp. 590–599, 2003, doi: 10.1259/bjr/17150274.

[243] S. Y. Ng and C.-L. Lin, “A Multilayered, Lesion-Embedded Ultrasound Breast Phantom with Realistic Visual and Haptic Feedback for Needle Biopsy,”

Ultrasound Med. Biol., vol. 48, no. 8, pp. 1468–1483, 2022, doi: 10.1016/j.ultrasmedbio.2022.03.009.

[244] A. Antoniou, M. Giannakou, E. Georgiou, K. A. Kleopa, and C. Damianou, "Robotic device for transcranial focussed ultrasound applications in small animal models," *Int. J. Med. Robot. Comput. Assist. Surg.*, pp. 1–11, 2022, doi: 10.1002/rcs.2447.

[245] J. Bini, J. M. David Izquierdo-Garcia, J. Machac, J. Narula, V. Fuster, and Z. A. Fayad, "Preclinical evaluation of MR-attenuation correction versus CT-attenuation correction on a sequential whole-body MR/PET scanner," *Invest Radiol.*, vol. 48, no. 5, pp. 313–322, 2013, doi: 10.1097/RLI.0b013e31827a49ba.

[246] A. N. Pouliopoulos, S. Y. Wu, M. T. Burgess, M. E. Karakatsani, H. A. S. Kamimura, and E. E. Konofagou, "A Clinical System for Non-invasive Blood–Brain Barrier Opening Using a Neuronavigation-Guided Single-Element Focused Ultrasound Transducer," *Ultrasound Med. Biol.*, vol. 46, no. 1, pp. 73–89, 2020, doi: 10.1016/j.ultrasmedbio.2019.09.010.

[247] C. K. McGarry *et al.*, "Tissue mimicking materials for imaging and therapy phantoms: A review," *Phys. Med. Biol.*, vol. 65, no. 23, 2020, doi: 10.1088/1361-6560/abbd17.

[248] L. A. Dewerd and M. Kissick, *Biological and Medical Physics, Biomedical Engineering - The Phantoms of Medical and Health Physics: Devices for Research and Development*. New York: Springer, 2014.

[249] C. Bai, M. Ji, A. Bouakaz, Y. Zong, and M. Wan, "Design and Characterization of an Acoustically and Structurally Matched 3-D-Printed Model for Transcranial Ultrasound Imaging," *IEEE Trans. Ultrason. Ferroelectr. Freq. Control*, vol. 65, no. 5, pp. 741–748, 2018, doi: 10.1109/TUFFC.2018.2811756.

[250] Technical Committee EPL/87, "IEC 61685:2001," *Ultrasonics - Flow measurement systems - Flow test object*, 2001. [Online]. Available:

https://webstore.iec.ch/publication/5721. [Accessed: 07-Nov-2022].

[251] Technical Committee EPL/87, "IEC TS 62791:2022," *Ultrasonics - Pulse-echo scanners - Low-echo sphere phantoms and method for performance testing of grey-scale medical ultrasound scanners applicable to a broad range of transducer types*, 2022. [Online]. Available: https://webstore.iec.ch/publication/68146. [Accessed: 07-Nov-2022].

[252] S. Rajagopal, N. Sadhoo, and B. Zeqiri, "Reference Characterisation of Sound Speed and Attenuation of the IEC Agar-Based Tissue-Mimicking Material Up to a Frequency of 60 MHz," *Ultrasound Med. Biol.*, vol. 41, no. 1, pp. 317–333, 2015, doi: 10.1016/j.ultrasmedbio.2014.04.018.

[253] E. Doney *et al.*, "3D printing of preclinical X-ray computed tomographic data sets," *J. Vis. Exp.*, no. 73, pp. 1–6, 2013, doi: 10.3791/50250.

[254] H. Zhang *et al.*, "Fabrication of an anthropomorphic heterogeneous mouse phantom for multimodality medical imaging," *Phys. Med. Biol.*, vol. 63, no. 19, 2018, doi: 10.1088/1361-6560/aadf2b.

[255] T. Dann *et al.*, "Anatase titanium dioxide imparts photoluminescent properties to PA2200 commercial 3D printing material to generate complex optical imaging phantoms," *Materials (Basel).*, vol. 14, no. 7, pp. 1–9, 2021, doi: 10.3390/ma14071813.

[256] D. Welch, A. D. Harken, G. Randers-Pehrson, and D. J. Brenner, "Construction of mouse phantoms from segmented CT scan data for radiation dosimetry studies," *Phys. Med. Biol.*, vol. 60, no. 9, pp. 3589–3598, 2015, doi: 10.1088/0031-9155/60/9/3589.

[257] N. Esplen, E. Alyaqoub, and M. Bazalova-Carter, "Technical Note: Manufacturing of a realistic mouse phantom for dosimetry of radiobiology experiments," *Med. Phys.*, vol. 46, no. 2, pp. 1030–1036, 2019, doi: 10.1002/mp.13310.

[258] G. Price *et al.*, "An open source heterogeneous 3D printed mouse phantom utilising

a novel bone representative thermoplastic," *Phys. Med. Biol.*, vol. 65, no. 10, 2020, doi: 10.1088/1361-6560/ab8078.

[259] M. Bainier, A. Su, and R. L. Redondo, "3D printed rodent skin-skull-brain model: A novel animal-free approach for neurosurgical training," *PLoS One*, vol. 16, no. 6 June, pp. 1–12, 2021, doi: 10.1371/journal.pone.0253477.

[260] Z. Cheng and P. Liang, "Advances in ultrasound-guided thermal ablation for symptomatic benign thyroid nodules," *Adv Clin Exp Med*, vol. 29, no. 9, pp. 1123–1129, 2020, doi: 10.17219/acem/125433.

[261] M. Zhu, Z. Sun, and C. K. Ng, "Image-guided thermal ablation with MR-based thermometry," *Quant Imaging Med Surg.*, vol. 7, no. 3, pp. 356–368, 2017, doi: 10.21037/qims.2017.06.06.

[262] E. Botsa, S. Mylona, I. Koutsogiannis, A. Koundouraki, and L. Thanos, "CT image guided thermal ablation techniques for palliation of painful bone metastases," *Ann Palliat Med*, vol. 3, no. 2, pp. 47–53, 2014, doi: 10.3978/j.issn.2224-5820.2014.04.02.

[263] N. Esplen, F. Therriault-Proulx, L. Beaulieu, and M. Bazalova-Carter, "Preclinical dose verification using a 3D printed mouse phantom for radiobiology experiments," *Med. Phys.*, vol. 46, no. 11, pp. 5294–5303, 2019, doi: 10.1002/mp.13790.

[264] T. E. Reeves, P. Mah, and W. D. McDavid, "Deriving Hounsfield units using grey levels in cone beam CT: A clinical application," *Dentomaxillofacial Radiol.*, vol. 41, no. 6, pp. 500–508, 2012, doi: 10.1259/dmfr/31640433.

[265] A. Fedorov *et al.*, "3D Slicer as an Image Computing Platform for the Quantitative Imaging Network," *Magn. Reson. Imaging*, vol. 30, no. 9, pp. 1323–1341, 2012, doi: 10.1016/j.mri.2012.05.001.

[266] W. Schneider, T. Bortfeld, and W. Schlegel, "Correlation between CT numbers and tissue parameters needed for Monte Carlo simulations of clinical dose

distributions," *Phys. Med. Biol.*, vol. 45, no. 2, pp. 459–478, 2000, doi: 10.1088/0031-9155/45/2/314.

[267] S. V G, M. K, and B.-F. P, "Electrical properties of phantoms for mimicking breast tissue," in *39th Annual International Conference of the IEEE Engineering in Medicine and Biology Society*, 2017, pp. 157–160.

[268] A. A. Konstas, G. V. Goldmakher, T.-Y. Lee, and M. H. Lev, "Theoretic basis and technical implementations of CT perfusion in acute ischemic stroke, Part 2: Technical implementations," *Am. J. Neuroradiol.*, vol. 30, no. 5, pp. 885–892, 2009, doi: 10.3174/ajnr.A1492.

[269] D. N. Makris *et al.*, "Characterization of a novel 3D printed patient specific phantom for quality assurance in cranial stereotactic radiosurgery applications," *Phys. Med. Biol.*, vol. 64, no. 10, 2019, doi: 10.1088/1361-6560/ab1758.

[270] F. Fischer, "FDM and Polyjet 3D Printing," *Pop. Plast. Packag.*, vol. 60, no. 6, p. 7, 2015.

[271] F. J. Fry and J. E. Barger, "Acoustical properties of the human skull," *J. Acoust. Soc. Am.*, vol. 63, no. 5, pp. 1576–1590, 1978, doi: 10.1121/1.381852.

[272] J. Huang, R. G. Holt, R. O. Cleveland, and R. A. Roy, "Experimental validation of a tractable numerical model for focused ultrasound heating in flow-through tissue phantoms," *J. Acoust. Soc. Am.*, vol. 116, 2004, doi: 10.1121/1.1787124.

[273] J. Crezee and J. J. W. Lagendijk, "Temperature uniformity during hyperthermia: the impact of large vessels," *Phys. Med. Biol.*, vol. 37, no. 6, 1992.

[274] S. Patrick, N. P. Birur, K. Gurushanth, A. S. Raghavan, and S. Gurudath, "Comparison of gray values of cone-beam computed tomography with hounsfield units of multislice computed tomography: An in vitro study," *Indian J. Dent. Res.*, vol. 28, no. 1, pp. 66–70, 2017, doi: 10.4103/ijdr.IJDR_415_16.

[275] J. Foley, J. Snell, A. Hananel, N. Kassell, and J. Aubry, "Image-guided focused

ultrasound: state of the technology and the challenges that lie ahead," *Imaging Med.*, vol. 5, pp. 357–370, 2013, doi: 10.2217/IIM.13.38.

[276] J. J. Choi, M. Pernot, S. A. Small, and E. E. Konofagou, "Noninvasive, transcranial and localized opening of the blood-brain barrier using focused ultrasound in mice," *Ultrasound Med. Biol.*, vol. 33, no. 1, pp. 95–104, 2007, doi: 10.1016/j.ultrasmedbio.2006.07.018.

[277] J. J. Choi, K. Selert, Z. Gao, G. Samiotaki, B. Baseri, and E. E. Konofagou, "Noninvasive and Localized Blood—Brain Barrier Disruption using Focused Ultrasound can be Achieved at Short Pulse Lengths and Low Pulse Repetition Frequencies," *J. Cereb. Blood Flow Metab.*, vol. 31, no. 2, pp. 725–737, 2011, doi: 10.1038/jcbfm.2010.155.

[278] S. Wang, G. Samiotaki, O. Olumolade, J. A. Feshitan, and E. E. Konofagou, "Microbubble type and distribution dependence of focused ultrasound-induced blood-brain barrier opening," *Ultrasound Med. Biol.*, vol. 40, no. 1, pp. 130–137, 2014, doi: 10.1016/j.ultrasmedbio.2013.09.015.

[279] C. Damianou, K. Ioannides, and N. Milonas, "Positioning device for MRI-guided high intensity focused ultrasound system," *Int. J. Comput. Assist. Radiol. Surg.*, vol. 2, no. 6, pp. 335–345, 2008, doi: 10.1007/s11548-007-0145-x.

[280] E. Epaminonda, T. Drakos, C. Kalogirou, M. Theodoulou, C. Yiallouras, and C. Damianou, "MRI guided focused ultrasound robotic system for the treatment of gynaecological tumors," *Int. J. Med. Robot. Comput. Assist. Surg.*, vol. 12, pp. 46–52, 2016, doi: 10.1002/rcs.1653.

[281] M. Yiannakou, G. Menikou, C. Yiallouras, C. Ioannides, and C. Damianou, "MRI guided focused ultrasound robotic system for animal experiments," *Int. J. Med. Robot. Comput. Assist. Surg.*, vol. 13, no. 4, p. e1804, 2017, doi: 10.1002/rcs.1804.

[282] J. J. Li, M. F. Gu, G. Y. Luo, L. Z. Liu, R. Zhang, and G. L. Xu, "Complications of high intensity focused ultrasound for patients with hepatocellular carcinoma,"

Technol. Cancer Res. Treat., vol. 8, no. 3, pp. 217–224, 2009, doi: 10.1177/153303460900800306.

[283] J. G. Lynn, R. L. Zwemer, and A. J. Chick, "The biological application of focused ultrasonic waves," *Science (80-.).*, vol. 96, pp. 119–120, 1942, doi: 10.1126/science.96.2483.119.

[284] W. J. FRY, "Intense ultrasound in investigations of the central nervous system," *Adv. Biol. Med. Phys.*, vol. 6, pp. 281–348, 1958, doi: 10.1016/b978-1-4832-3112-9.50012-8.

[285] W. J. Fry and F. J. Fry, "Fundamental Neurological Research and Human Neurosurgery Using Intense Ultrasound," *IRE Trans. Med. Electron.*, vol. ME-7, no. 3, pp. 166–181, 1960, doi: 10.1109/IRET-ME.1960.5008041.

[286] B. R. Shah *et al.*, "Advanced MRI techniques for transcranial high intensity focused ultrasound targeting," *Brain*, vol. 143, no. 9, pp. 2664–2672, 2020, doi: 10.1093/brain/awaa107.

[287] Y. Ishihara *et al.*, "A precise and fast temperature mapping using water proton chemical shift," *Magn. Reson. Imaging*, vol. 34, no. 6, pp. 814–823, 1995, doi: 10.1002/mrm.1910340606.

[288] K. Hynynen, "MRIgHIFU: A Tool for Image-Guided Therapeutics," *J. Magn. Reson. Imaging*, vol. 34, pp. 482–493, 2011, doi: 10.1002/jmri.22649.

[289] L. Winter *et al.*, "Magnetic resonance thermometry: Methodology, pitfalls and practical solutions," *Int. J. Hyperth.*, vol. 32, no. 1, pp. 63–75, 2015, doi: 10.3109/02656736.2015.1108462.

[290] J. Corea, P. Ye, D. Seo, K. Butts-Pauly, A. C. Arias, and M. Lustig, "Printed Receive Coils with High Acoustic Transparency for Magnetic Resonance Guided Focused Ultrasound," *Sci. Rep.*, vol. 8, no. 1, pp. 1–10, 2018, doi: 10.1038/s41598-018-21687-1.

[291] S. M. Wright and L. L. Wald, “Theory and application of array coils in MR spectroscopy,” *NMR Biomed.*, vol. 10, no. 8, pp. 394–410, 1998, doi: 10.1002/(SICI)1099-1492(199712)10:8<394::AID-NBM494>3.0.CO;2-0.

[292] P. B. Roemer, W. A. Edelstein, C. E. Hayes, S. P. Souza, and O. M. Mueller, “The NMR phased array,” *Magn. Reson. Med.*, vol. 16, no. 2, pp. 192–225, 1990, doi: 10.1002/mrm.1910160203.

[293] K. N. Kim *et al.*, “Quantitative assessment of phased array coils with different numbers of receiving channels in terms of signal-to-noise ratio and spatial noise variation in magnetic resonance imaging,” *PLoS One*, vol. 14, no. 7, pp. 1–13, 2019, doi: 10.1371/journal.pone.0219407.

[294] O. Dietrich, J. G. Raya, S. B. Reeder, M. F. Reiser, and S. O. Schoenberg, “Measurement of signal-to-noise ratios in MR images: Influence of multichannel coils, parallel imaging, and reconstruction filters,” *J. Magn. Reson. Imaging*, vol. 26, no. 2, pp. 375–385, 2007, doi: 10.1002/jmri.20969.

[295] B. Werner, E. Martin, R. Bauer, and R. O’Gorman, “Optimizing MR imaging-guided navigation for focused ultrasound interventions in the brain,” in *AIP Conference Proceedings*, 2017, vol. 1821, pp. 120001–1–120001–5, doi: 10.1063/1.4977641.

[296] B. Gruber, R. Rehner, E. Laistler, and S. Zink, “Anatomically Adaptive Coils for MRI—A 6-Channel Array for Knee Imaging at 1.5 Tesla,” *Front. Phys.*, vol. 8, no. April, pp. 1–17, 2020, doi: 10.3389/fphy.2020.00080.

[297] W. C. G. Peh and J. H. M. Chan, “Artifacts in musculoskeletal magnetic resonance imaging: identification and correction,” *Skelet. Radiol*, vol. 30, pp. 179–191, 2001, doi: 10.1007/s002560100341.

[298] K. Krupa and M. Bekiesińska-Figatowska, “Artifacts in magnetic resonance imaging,” *Polish J. Radiol.*, vol. 80, no. 1, pp. 93–106, 2015, doi: 10.12659/PJR.892628.

[299] “ASTM F2503–13: Standard Practice for Marking Medical Devices and Other Items for Safety in the Magnetic Resonance Environment.” [Online]. Available: http://compass.astm.org/EDIT/html_annot.cgi?%0AF2503+13.

[300] N. V Tsekos, E. Christoforou, and A. Ozcan, “A general-purpose MR-compatible robotic system: implementation and image guidance for performing minimally invasive interventions,” *IEEE Eng. Med. Biol. Mag.*, vol. 27, no. 3, pp. 51–8, 2008, doi: 10.1109/EMB.2007.910270.A.

[301] D. Stoianovici *et al.*, “Multi-Imager Compatible, MR Safe, Remote Center of Motion Needle-Guide Robot,” *IEEE Trans Biomed Eng*, vol. 65, no. 1, pp. 165–177, 2018, doi: 10.1109/TBME.2017.2697766.

[302] D. Stoianovici, “Multi-imager compatible actuation principles in surgical robotics,” *Int. J. Med. Robot.*, vol. 1, no. 2, pp. 86–100, 2005, doi: 10.1002/rcs.19.

[303] S. S. Cheng, “Challenges on the Development of MRI-Compatible Neurosurgical Robotic Systems,” *Int. J. Robot. Res. Appl. Autom.*, vol. 1, no. 1, pp. 2–5, 2019, doi: 10.18689/ijra-1000102.

[304] G. Menikou, C. Yiallouras, M. Yiannakou, and C. Damianou, “MRI-guided focused ultrasound robotic system for the treatment of bone cancer,” *Int. J. Med. Robot. Comput. Assist. Surg.*, vol. 13, no. 1, pp. 1–11, 2017, doi: 10.1002/rcs.1753.

[305] H. Elhawary, Z. T. H. Tse, A. Hamed, M. Rea, B. L. Davies, and M. U. Lamperth, “The case for MR-compatible robotics: a review of the state of the art,” *Int. J. Med. Robot. Comput. Assist. Surg.*, vol. 4, no. 2, pp. 105–113, 2008, doi: 10.1002/rcs.192.

[306] B. Hargreaves, P. W. Worters, K. B. Pauly, J. M. Pauly, K. M. Koch, and G. E. Gold, “Metal Induced Artifacts in MRI,” *Am J Roentgenol.*, vol. 197, no. 3, pp. 547–555, 2011, doi: 10.2214/AJR.

[307] C. Damianou, M. Giannakou, N. Evripidou, S. Kegel, P. Huber, and J. Jenne, “Focused ultrasound robotic system for very small bore magnetic resonance

imaging," *Int. J. Med. Robot. Comput. Assist. Surg.*, vol. 16, no. 6, pp. 1–9, 2020, doi: 10.1002/rcs.2165.

[308] B. T. Larson, A. G. Erdman, N. V. Tsekos, E. Yacoub, P. V. Tsekos, and I. G. Koutlas, "Design of an MRI-Compatible Robotic Stereotactic Device for Minimally Invasive Interventions in the Breast.," *J Biomech Eng.*, vol. 126, no. 4, pp. 458–465, 2004.

[309] F. Tajima *et al.*, "An MR-compatible master–slave manipulator with interchangeable surgical tools," *Int. Congr. Ser.*, vol. 1256, pp. 529–537, 2003, doi: 10.1016/S0531-5131(03)00212-7.

[310] H. Elhawary *et al.*, "A Modular Approach to MRI-Compatible Robotics," *IEEE Eng. Med. Biol. Mag.*, vol. 27, no. 3, pp. 35–41, 2008, doi: 10.1109/EMB.2007.910260.

[311] D. Speicher *et al.*, "MRI compatible ultrasound transducers for simultaneous acquisition of coregistered ultrasound to MRI data," *Phys. Procedia*, vol. 70, pp. 1002–1006, 2015, doi: 10.1016/j.phpro.2015.08.209.

[312] B. Gerold, S. Reynolds, A. Melzer, and S. Cochran, "Early exploration of MRI-compatible diagnostic ultrasound transducers," in *Proceedings - IEEE Ultrasonics Symposium*, 2010, pp. 2404–2407, doi: 10.1109/ULTSYM.2010.5935882.

[313] S. M. Lechner-Greite, N. Hehn, B. Werner, E. Zadicario, M. Tarasek, and D. Yeo, "Minimizing eddy currents induced in the ground plane of a large phased-array ultrasound applicator for echo-planar imaging-based MR thermometry," *J. Ther. Ultrasound*, vol. 4, no. 1, pp. 1–14, 2016, doi: 10.1186/s40349-016-0047-x.

[314] J. Wang, X. Xiao, Z. Huang, and A. Melzer, "3D-printing based Transducer Holder for Robotic Assisted Ultrasound Guided HIFU," in *Procedia Manufacturing*, 2019, vol. 30, pp. 3–10, doi: 10.1016/j.promfg.2019.02.002.

[315] F. L. Goerner and G. D. Clarke, "Measuring signal-to-noise ratio in partially parallel imaging MRI," *Med. Phys.*, vol. 38, no. 9, pp. 5049–5057, 2011, doi:

10.1118/1.3618730.

[316] P. Shokrollahi, J. M. Drake, and A. A. Goldenberg, “A study on observed ultrasonic motor-induced magnetic resonance imaging (MRI)artifacts,” *Biomed. J.*, vol. 42, no. 2, pp. 116–123, 2019, doi: 10.1016/j.bj.2018.12.007.

[317] G. Li *et al.*, “Robotic system for MRI-guided stereotactic neurosurgery,” *IEEE Trans Biomed Eng*, vol. 62, no. 4, pp. 1077–1088, 2015, doi: 10.1109/TBME.2014.2367233.

[318] L. W. Hofstetter, J. R. Hadley, R. Merrill, H. Pham, G. C. Fine, and D. L. Parker, “MRI-compatible electromagnetic servomotor for image-guided medical robotics,” *Commun. Eng.*, vol. 1, no. 4, 2022, doi: 10.1038/s44172-022-00001-y.

[319] E. M. Knavel and C. L. Brace, “Tumor ablation: Common modalities and general practices,” *Tech. Vasc. Interv. Radiol.*, vol. 16, no. 4, pp. 192–200, 2013, doi: 10.1053/j.tvir.2013.08.002.

[320] I. Mellal, A. Oukaira, E. Kengene, and A. Lakhssassi, “Thermal Therapy Modalities for Cancer Treatment: A Review and Future Perspectives,” *Int. J. Appl. Sci. - Res. Rev.*, vol. 04, no. 02, pp. 1–11, 2017, doi: 10.21767/2394-9988.100064.

[321] P. Tinguely *et al.*, “Stereotactic and Robotic Minimally Invasive Thermal Ablation of Malignant Liver Tumors: A Systematic Review and Meta-Analysis,” *Front. Oncol.*, vol. 11, 2021, doi: 10.3389/fonc.2021.713685.

[322] K. J. Mortele, S. G. Silverman, V. Cantisani, K. Tuncali, S. Shankar, and E. VanSonnenberg, “Magnetic Resonance Imaging Guidance for Tumor Ablation,” in *Tumor Ablation: Principles and Practise*, E. VanSonnenberg, W. N. McMullen, L. Solbiati, T. Livraghi, P. R. MÃ¼eller, and S. G. Silverman, Eds. New York, NY: Springer, 2005, pp. 148–166.

[323] B. Z. Fite, J. Wang, P. Ghanouni, and K. W. Ferrara, “A Review of Imaging Methods to Assess Ultrasound-Mediated Ablation,” *BME Front.*, vol. 2022, pp. 1–17, 2022, doi: 10.34133/2022/9758652.

[324] H. E. Cline, J. F. Schenck, R. D. Watkins, K. Hynynen, and F. A. Jolesz, “Magnetic resonance-guided thermal surgery,” *Magn. Reson. Med.*, vol. 30, no. 1, pp. 98–106, 1993, doi: 10.1002/mrm.1910300115.

[325] K. Hynynen *et al.*, “A clinical, noninvasive, MR imaging-monitored ultrasound surgery method,” *RadioGraphics*, vol. 16, no. 1, pp. 185–195, 1996, doi: 10.1148/radiographics.16.1.185.

[326] K. Hynynen, A. Darkazanli, E. Unger, and J. Schenck, “MRI-guided noninvasive ultrasound surgery,” *Med Phys*, vol. 20, no. 1, pp. 107–115, 1993, doi: 10.1118/1.597093.

[327] J. F. Schenck, K. Hynynen, E. Unger, A. Darkazanli, and C. A. Damianou, “The Usefulness of a Contrast Agent and Gradient–Recalled Acquisition in a Steady–State Imaging Sequence for Magnetic Resonance Imaging–Guided Noninvasive Ultrasound Surgery,” *Investig. Radiol.*, vol. 29, no. 10, pp. 897–903, 1994, doi: 10.1097/00004424-199410000-00006.

[328] A. H. Chung, F. A. Jolesz, and K. Hynynen, “Thermal dosimetry of a focused ultrasound beam in vivo by magnetic resonance imaging,” *Med Phys*, vol. 26, no. 9, pp. 2017–2026, 1999, doi: 10.1118/1.598707.

[329] L. Chen, D. Bouley, E. Yuh, H. D’Arceuil, and K. Butts, “Study of focused ultrasound tissue damage using MRI and histology,” *J Magn Reson Imaging*, vol. 10, no. 2, pp. 146–153, 1999, doi: 10.1002/(sici)1522-2586(199908)10:2<146::aid-jmri6>3.0.co;2-c.

[330] K. Foldes *et al.*, “Magnetic Resonance Imaging-guided Focused Ultrasound Synovectomy,” *Scand. J. Rheumatol.*, vol. 28, no. 4, pp. 233–237, 1999, doi: 10.1080/03009749950155607.

[331] N. Vykhodtseva, V. Sorrentino, F. A. Jolesz, R. T. Bronson, and K. Hynynen, “MRI detection of the thermal effects of focused ultrasound on the brain,” *Ultrasound Med. Biol.*, vol. 26, no. 5, pp. 871–880, Jun. 2000, doi: 10.1016/S0301-

5629(00)00216-7.

[332] L. Curiel, R. Souchon, O. Rouviere, A. Gelet, and J. Chapelon, “Elastography for the follow-up of high-intensity focused ultrasound prostate cancer treatment: Initial comparison with MRI,” *Ultrasound Med Biol*, vol. 31, no. 11, pp. 1461–1468, 2005, doi: 10.1016/j.ultrasmedbio.2005.06.013.

[333] I. Rivens, A. Shaw, J. Civale, and H. Morris, “Treatment monitoring and thermometry for therapeutic focused ultrasound,” *Int. J. Hyperth.*, vol. 23, no. 2, pp. 121–139, 2007, doi: 10.1080/02656730701207842.

[334] C. Damianou *et al.*, “MRI monitoring of lesions created at temperature below the boiling point and of lesions created above the boiling point using high intensity focused ultrasound,” *J. Biomed. Sci. Eng.*, vol. 03, no. 08, pp. 763–775, 2010, doi: 10.4236/jbise.2010.38102.

[335] C. Damianou, K. Ioannides, V. Hadjisavvas, N. Mylonas, A. Couppis, and D. Iosif, “In vitro and in vivo brain ablation created by high-intensity focused ultrasound and monitored by MRI,” *IEEE Trans. Ultrason. Ferroelectr. Freq. Control*, vol. 56, no. 6, pp. 1189–1198, 2009, doi: 10.1109/TUFFC.2009.1160.

[336] C. Bremer, G. Kreft, T. Filler, and P. Reimer, “Accuracy of non-enhanced MRI to monitor histological lesion size during laser-induced interstitial thermotherapy,” *Eur. Radiol.*, vol. 12, no. 1, pp. 237–244, 2002, doi: 10.1007/s003300101118.

[337] G. R. Vergara *et al.*, “Real-time magnetic resonance imagingguided radiofrequency atrial ablation and visualization of lesion formation at 3 Tesla,” *Hear. Rhythm*, vol. 8, no. 2, pp. 295–303, 2011, doi: 10.1016/j.hrthm.2010.10.032.

[338] Z. Lin, J. Chen, Y. Yan, J. Chen, and Y. Li, “Microwave ablation of hepatic malignant tumors using 1.5T MRI guidance and monitoring: feasibility and preliminary clinical experience,” *Int. J. Hyperth.*, vol. 36, no. 1, pp. 1216–1222, 2019, doi: 10.1080/02656736.2019.1690166.

[339] A. Antoniou, L. Georgiou, N. Evripidou, C. Ioannides, and C. Damianou,

"Challenges regarding MR compatibility of an MRgFUS robotic system," *J. Magn. Reson.*, vol. 344, p. 107317, 2022, doi: 10.1016/j.jmr.2022.107317.

[340] G. Liberman, Y. Louzoun, and D. Ben Bashat, "T1 Mapping using variable flip angle SPGR data with flip angle correction," *J. Magn. Reson. Imaging*, vol. 40, no. 1, pp. 171–180, 2014, doi: 10.1002/jmri.24373.

[341] R. E. Hendrick, "Signal, Noise, Signal-to-Noise, and Contrast-to-Noise Ratios," in *Breast MRI: Fundamentals and Technical Aspects*, New York, NY: Springer New York, 2008, pp. 107–110.

[342] W. J. Fry, W. H. Mosberg Jr, J. W. Barnard, and F. J. Fry, "Production of Focal Destructive Lesions in the Central Nervous System With Ultrasound," *J. Neurosurg.*, vol. 11, no. 5, pp. 471–478, 1954.

[343] J. W. Barnard, W. J. Fry, F. J. Fry, and R. F. Krumins, "Effects of high intensity ultrasound on the central nervous system of the cat," *J. Comp. Neurol.*, vol. 103, no. 3, pp. 459–484, 1955.

[344] A. N. Guthkelch *et al.*, "Treatment of malignant brain tumors with focused ultrasound hyperthermia and radiation: results of a phase I trial," *J. Neurooncol.*, vol. 10, pp. 271–284, 1991.

[345] M. Tanter, J.-L. Thomas, and M. Fink, "Focusing and steering through absorbing and aberrating layers: Application to ultrasonic propagation through the skull," *J. Acoust. Soc. Am.*, vol. 103, no. 5, 1998, doi: 10.1121/1.422759.

[346] K. Hynynen and F. A. Jolesz, "Demonstration of Potential Noninvasive Ultrasound Brain Therapy Through an Intact Skull," *Ultrasound Med. Biol.*, vol. 24, no. 2, pp. 275–283, 1998, doi: 10.1016/S0301-5629(97)00269-X.

[347] J. Sun and K. Hynynen, "Focusing of therapeutic ultrasound through a human skull: a numerical study," *J. Acoust. Soc. Am.*, vol. 104, pp. 1705–1715, 1998, doi: 10.1121/1.424383.

[348] J.-F. Aubry, M. Tanter, M. Pernot, J.-L. Thomas, and M. Fink, “Experimental demonstration of noninvasive transskull adaptive focusing based on prior computed tomography scans,” *J. Acoust. Soc. Am.*, vol. 113, no. 1, pp. 84–93, 2003, doi: 10.1121/1.1529663.

[349] M. R. Focused and U. Neurosurgery, “Magnetic resonance-guided focused ultrasound neurosurgery for essential tremor: A health technology assessment,” *Ont. Health Technol. Assess. Ser.*, vol. 18, no. 4, pp. 1–141, 2018.

[350] G. Foffani *et al.*, “Focused Ultrasound in Parkinson’s Disease: A Twofold Path Toward Disease Modification,” *Mov Disord*, vol. 34, no. 9, pp. 1262–1273, 2019, doi: 10.1002/mds.27805.

[351] K. W. Chang, H. H. Jung, and J. W. Chang, “Magnetic Resonance-Guided Focused Ultrasound Surgery for Obsessive-Compulsive Disorders: Potential for use as a Novel Ablative Surgical Technique,” *Front. Psychiatry*, vol. 12, pp. 1–9, 2021, doi: 10.3389/fpsyt.2021.640832.

[352] K. Abe *et al.*, “Magnetic resonance-guided focused ultrasound for mesial temporal lobe epilepsy: A case report,” *BMC Neurol.*, vol. 20, no. 1, pp. 1–7, 2020, doi: 10.1186/s12883-020-01744-x.

[353] A. Idbaih *et al.*, “Safety and feasibility of repeated and transient blood-brain barrier disruption by pulsed ultrasound in patients with recurrent glioblastoma,” *Clin. Cancer Res.*, vol. 25, no. 13, pp. 3793–3801, 2019, doi: 10.1158/1078-0432.CCR-18-3643.

[354] K.-T. Chen *et al.*, “Neuronavigation-guided focused ultrasound (NaviFUS) for transcranial blood-brain barrier opening in recurrent glioblastoma patients: clinical trial protocol,” *Ann. Transl. Med.*, vol. 8, no. 11, pp. 673–673, 2020, doi: 10.21037/atm-20-344.

[355] Y. Meng *et al.*, “Technical Principles and Clinical Workflow of Transcranial MR-Guided Focused Ultrasound,” *Stereotact. Funct. Neurosurg.*, vol. 99, no. 4, pp.

329–342, 2021, doi: 10.1159/000512111.

[356] K. Hynynen, N. Mcdannold, N. A. Sheikov, F. A. Jolesz, and N. Vykhodtseva, “Local and reversible blood – brain barrier disruption by noninvasive focused ultrasound at frequencies suitable for trans-skull sonications,” *Neuroimage*, vol. 24, pp. 12–20, 2005, doi: 10.1016/j.neuroimage.2004.06.046.

[357] S. Y. Wu *et al.*, “Transcranial cavitation detection in primates during blood-brain barrier opening-a performance assessment study,” *IEEE Trans. Ultrason. Ferroelectr. Freq. Control*, vol. 61, no. 6, pp. 966–978, 2014, doi: 10.1109/TUFFC.2014.2992.

[358] G. Samiotaki *et al.*, “Pharmacokinetic analysis and drug delivery efficiency of the focused ultrasound-induced blood-brain barrier opening in non-human primates,” *Magn. Reson. Imaging*, vol. 37, pp. 273–281, 2017, doi: 10.1016/j.mri.2016.11.023.

[359] S. Y. Wu *et al.*, “Efficient blood-brain barrier opening in primates with neuronavigation-guided ultrasound and real-time acoustic mapping,” *Sci. Rep.*, vol. 8, no. 1, pp. 1–11, 2018, doi: 10.1038/s41598-018-25904-9.

[360] F. Marquet *et al.*, “Real-time, transcranial monitoring of safe blood-brain barrier opening in non-human primates,” *PLoS One*, vol. 9, no. 2, pp. 1–11, 2014, doi: 10.1371/journal.pone.0084310.

[361] F. Marquet, Y. Tung, T. Teichert, V. P. Ferrera, and E. E. Konofagou, “Noninvasive , Transient and Selective Blood-Brain Barrier Opening in Non-Human Primates In Vivo,” vol. 6, no. 7, pp. 1–7, 2011, doi: 10.1371/journal.pone.0022598.

[362] M. E. Karakatsani, G. Samiotaki, M. E. Downs, V. P. Ferrera, and E. E. Konofagou, “Targeting Effects on the Volume of the Focused Ultrasound Induced Blood-Brain Barrier Opening in Non-Human Primates in vivo,” *IEEE Trans Ultrason Ferroelectr Freq Control*, vol. 64, no. 5, pp. 798–810, 2017, doi:

10.1109/TUFFC.

[363] K.-C. Wei *et al.*, “Neuronavigation-guided focused ultrasound-induced blood-brain barrier opening: a preliminary study in swine.,” *AJNR. Am. J. Neuroradiol.*, vol. 34, no. 1, pp. 115–20, Jan. 2013, doi: 10.3174/ajnr.A3150.

[364] K. Yoon *et al.*, “Localized blood-brain barrier opening in ovine model using image-guided transcranial focused ultrasound,” *Ultrasound Med Biol*, vol. 45, no. 9, pp. 2391–2404, 2019, doi: 10.1016/j.ultrasmedbio.2019.05.023.

[365] G. Maimbourg, A. Houdouin, T. Deffieux, and M. Tanter, “3D-printed adaptive acoustic lens as a disruptive technology for transcranial ultrasound therapy using single-element transducers,” *Phys. Med. Biol.*, vol. 63, pp. 1–14, 2018, doi: 10.1088/1361-6560/aaa037.

[366] M. Ferri, J. M. Bravo, J. Redondo, and J. V. Sanchez-Perez, “Enhanced Numerical Method for the Design of 3-D-Printed Holographic Acoustic Lenses for Aberration Correction of Single-Element Transcranial Focused Ultrasound,” *Ultrasound Med. Biol.*, vol. 45, no. 3, pp. 867–884, 2019, doi: 10.1016/j.ultrasmedbio.2018.10.022.

[367] A. R. Selfridge, “Approximate Material Properties in Isotropic Materials,” *IEEE Trans. Sonics Ultrason.*, vol. 32, no. 3, pp. 381–383, 1985, doi: 10.1109/T-SU.1985.31608.

[368] S. Pichardo, V. W. Sin, and K. Hynynen, “Multi-frequency characterization of the speed of sound and attenuation coefficient for longitudinal transmission of freshly excised human skulls,” *Phys. Med. Biol.*, vol. 56, no. 1, pp. 219–250, 2011, doi: 10.1088/0031-9155/56/1/014.

[369] A. Y. Ammi *et al.*, “Characterization of Ultrasound Propagation Through Ex-vivo Human Temporal Bone HHS Public Access Author manuscript,” *Ultrasound Med Biol*, vol. 34, no. 10, pp. 1578–1589, 2008, doi: 10.1016/j.ultrasmedbio.2008.02.012.Characterization.

[370] T. Selbekk *et al.*, “Ultrasound imaging in neurosurgery: Approaches to minimize

surgically induced image artefacts for improved resection control," *Acta Neurochir. (Wien).*, vol. 155, no. 6, pp. 973–980, 2013, doi: 10.1007/s00701-013-1647-7.

[371] Z. Shen, Y. Yao, Y. Xie, C. Guo, X. Shang, and X. Dong, "The process of 3D-printed skull models for the anatomy education," *Comput. Assist. Surg.*, vol. 24, no. 1, pp. 1–14, 2017, doi: 10.1080/24699322.2018.1560101.

[372] A. R. Arulpragasam, M. van 't Wout-Frank, J. Barredo, C. R. Faucher, B. D. Greenberg, and N. S. Philip, "Low Intensity Focused Ultrasound for Non-invasive and Reversible Deep Brain Neuromodulation—A Paradigm Shift in Psychiatric Research," *Front. Psychiatry*, vol. 13, 2022, doi: 10.3389/fpsyt.2022.825802.

[373] H. Kima, A. Chiu, S. D. Lee, K. Fischer, and S.-S. Yoo, "Focused Ultrasound-mediated Non-invasive Brain Stimulation: Examination of Sonication Parameters," *Brain Stimul.*, vol. 7, no. 5, pp. 748–756, 2014, doi: 10.1016/j.brs.2014.06.011.

[374] "Focused ultrasound modulates region-specific brain activity," *Neuroimage*, vol. 56, no. 3, pp. 1267–1275, 2011, doi: 10.1016/j.neuroimage.2011.02.058.

[375] H. Kim, M. Y. Park, S. D. Lee, W. Lee, A. Chiua, and S.-S. Yoo, "Suppression of EEG visual-evoked potentials in rats via neuromodulatory focused ultrasound," *Neuroreport*, vol. 26, no. 4, pp. 211–215, 2015, doi: 10.1097/WNR.0000000000000330.

[376] N. Wattiez *et al.*, "Transcranial ultrasonic stimulation modulates single-neuron discharge in macaques performing an antisaccade task," *Brain Stimul.*, vol. 10, no. 6, pp. 1024–1031, 2017, doi: 10.1016/j.brs.2017.07.007.

[377] W. Lee *et al.*, "Transcranial focused ultrasound stimulation of human primary visual cortex," *Sci. Rep.*, vol. 6, pp. 1–12, 2016, doi: 10.1038/srep34026.

[378] W. Lee *et al.*, "Non-invasive transmission of sensorimotor information in humans using an EEG/focused ultrasound brain-to-brain interface," *PLoS One*, vol. 12, no.

6, pp. 1–20, 2017, doi: 10.1371/journal.pone.0178476.

[379] K. Yoon, W. Lee, P. Croce, A. Cammalleri, and S.-S. Yoo, “Multi-resolution Simulation of Focused Ultrasound Propagation through Ovine Skull from a Single-element Transducer,” *Phys Med Biol*, vol. 63, no. 10, p. 105001, 2019, doi: 10.1088/1361-6560/aabe37.

[380] Y. Huang, P. Wen, B. Song, and Y. Li, “Numerical investigation of the energy distribution of Low-intensity transcranial focused ultrasound neuromodulation for hippocampus,” *Ultrasonics*, vol. 124, p. 106724, 2022, doi: 10.1016/j.ultras.2022.106724.

[381] T. Deffieux and E. E. Konofagou, “Numerical study of a simple transcranial focused ultrasound system applied to blood-brain barrier opening,” *IEEE Trans Ultrason Ferroelectr Freq Control*, vol. 57, no. 12, pp. 2637–2653, 2010, doi: 10.1109/TUFFC.2010.1738.

[382] H. Seo, H. Huh, E. H. Lee, and J. Park, “Numerical Evaluation of the Effects of Transducer Displacement on Transcranial Focused Ultrasound in the Rat Brain,” *Brain Sci.*, vol. 12, no. 2, p. 216, 2022, doi: 10.3390/brainsci12020216.

[383] M. Chen *et al.*, “Numerical and experimental evaluation of low-intensity transcranial focused ultrasound wave propagation using human skulls for brain neuromodulation,” *Med. Phys.*, vol. 50, no. 1, pp. 38–49, 2023, doi: 10.1002/mp.16090.

[384] S. T. Brinker, F. Preiswerk, N. J. McDannold, K. L. Parker, and T. Y. Mariano, “Virtual Brain Projection for Evaluating Trans-Skull Beam Behavior of Transcranial Ultrasound Devices,” *Ultrasound Med Biol*, vol. 45, no. 7, pp. 1850–1856, 2019, doi: 10.1016/j.ultrasmedbio.2019.03.009.

[385] A. Antoniou and C. Damianou, “Feasibility of ultrasonic heating through skull phantom using single-element transducer,” *J. Med. Ultrasound*, 2023, doi: 10.4103/jmu.jmu_3_23.

[386] T. Rahne, S. Svensson, H. Lagerkvist, M. Holmberg, S. K. Plontke, and C. Wenzel, "Assessment of Temporal Bone Thickness for Implantation of a New Active Bone-Conduction Transducer," *Otol. Neurotol.*, vol. 42, no. 2, pp. 278–284, 2021, doi: 10.1097/MAO.0000000000002919.

[387] G. Pinton, J. Aubry, E. Bossy, M. Muller, and M. Pernot, "Attenuation, scattering ,and absorption of ultrasound in the skull bone," vol. 39, no. October 2011, pp. 299–307, 2012, doi: 10.1118/1.3668316.

[388] N. McDannold, R. L. King, and K. Hynynen, "MRI monitoring of heating produced by ultrasound absorption in the skull: in vivo study in pigs," *Magn. Reson. Med.*, vol. 51, no. 5, pp. 1061–1065, 2004, doi: 10.1002/mrm.20043.

[389] M. Chen *et al.*, "Biosafety of low-intensity pulsed transcranial focused ultrasound brain stimulation: a human skull study," in *Health Monitoring of Structural and Biological Systems XV*, 2021, p. 34.

[390] K. Hynynen and R. M. Jones, "Image-guided ultrasound phased arrays are a disruptive technology for non-invasive therapy," *Phys Med Biol.*, vol. 61, no. 17, pp. 206–248, 2016, doi: 10.1088/0031-9155/61/17/R206.

[391] J. Sun and K. Hynynen, "The potential of transskull ultrasound therapy and surgery using the maximum available skull surface area," *J Acoust Soc Am*, vol. 105, no. 4, pp. 2519–27, 1999, doi: 10.1121/1.426863.

[392] P. Wu *et al.*, "Focused Ultrasound Thalamotomy for the Treatment of Essential Tremor: A 2-Year Outcome Study of Chinese People," *Front. Aging Neurosci.*, vol. 13, pp. 1–8, 2021, doi: 10.3389/fnagi.2021.697029.

[393] C. Y. Lin *et al.*, "Focused ultrasound-induced blood-brain barrier opening for non-viral, non-invasive, and targeted gene delivery," *J. Control. Release*, vol. 212, pp. 1–9, 2015, doi: 10.1016/j.jconrel.2015.06.010.

[394] A. H. Mesiwala *et al.*, "High-intensity focused ultrasound selectively disrupts the blood-brain barrier in vivo," *Ultrasound Med. Biol.*, vol. 28, no. 3, pp. 389–400,

2002, doi: 10.1016/S0301-5629(01)00521-X.

[395] Y. Yang *et al.*, “Cavitation dose painting for focused ultrasound-induced blood-brain barrier disruption,” *Sci. Rep.*, vol. 9, no. 1, pp. 1–10, 2019, doi: 10.1038/s41598-019-39090-9.

[396] N. Sheikov, N. McDannold, N. Vykhodtseva, F. Jolesz, and K. Hynynen, “Cellular mechanisms of the blood-brain barrier opening induced by ultrasound in presence of microbubbles,” *Ultrasound Med. Biol.*, vol. 30, no. 7, pp. 979–989, 2004, doi: 10.1016/j.ultrasmedbio.2004.04.010.

[397] R. Chopra, N. Vykhodtseva, and K. Hynynen, “Influence of Exposure Time and Pressure Amplitude on Blood - Brain-Barrier Opening Using Transcranial Ultrasound Exposures,” pp. 391–398, 2010, doi: 10.1021/cn9000445.

[398] Y.-S. Tung, F. Vlachos, J. A. Feshitan, M. A. Borden, and E. E. Konofagou, “The mechanism of interaction between focused ultrasound and microbubbles in blood-brain barrier opening in mice,” *J. Acoust. Soc. Am.*, vol. 130, no. 5, pp. 3059–3067, 2011, doi: 10.1121/1.3646905.

[399] N. McDannold, N. Vykhodtseva, and K. Hynynen, “Blood-Brain Barrier Disruption Induced by Focused Ultrasound and Circulating Preformed Microbubbles Appears to Be Characterized by the Mechanical Index,” *Ultrasound Med. Biol.*, vol. 34, no. 5, pp. 834–840, 2008, doi: 10.1016/j.ultrasmedbio.2007.10.016.

[400] E. E. Konofagou, “Optimization of the ultrasound-induced blood-brain barrier opening,” *Theranostics*, vol. 2, no. 12, pp. 1223–1237, 2012, doi: 10.7150/thno.5576.

[401] H. Chen and E. E. Konofagou, “The size of blood-brain barrier opening induced by focused ultrasound is dictated by the acoustic pressure,” *J. Cereb. Blood Flow Metab.*, vol. 34, no. 7, pp. 1197–1204, 2014, doi: 10.1038/jcbfm.2014.71.

[402] M. E. Karakatsani, J. Blesa, and E. E. Konofagou, “Blood–brain barrier opening

with focused ultrasound in experimental models of Parkinson's disease," *Mov. Disord.*, vol. 34, no. 9, pp. 1252–1261, 2019, doi: 10.1002/mds.27804.

[403] N. Sheikov, N. McDannold, S. Sharma, and K. Hynynen, "Effect of Focused Ultrasound Applied With an Ultrasound Contrast Agent on the Tight Junctional Integrity of the Brain Microvascular Endothelium," *Ultrasound Med. Biol.*, vol. 34, no. 7, pp. 1093–1104, 2008, doi: 10.1016/j.ultrasmedbio.2007.12.015.

[404] S. Jalali, Y. Huang, D. J. Dumont, and K. Hynynen, "Focused ultrasound-mediated bbb disruption is associated with an increase in activation of AKT: Experimental study in rats," *BMC Neurol.*, vol. 10, no. 1, p. 114, 2010, doi: 10.1186/1471-2377-10-114.

[405] A. Burgess, C. A. Ayala-Grosso, M. Ganguly, J. F. Jordão, I. Aubert, and K. Hynynen, "Targeted delivery of neural stem cells to the brain using MRI-guided focused ultrasound to disrupt the blood-brain barrier," *PLoS One*, vol. 6, no. 11, 2011, doi: 10.1371/journal.pone.0027877.

[406] A. B. Etame *et al.*, "Enhanced delivery of gold nanoparticles with therapeutic potential into the brain using MRI-guided focused ultrasound.," *Nanomedicine*, vol. 8, no. 7, pp. 1133–42, Oct. 2012, doi: 10.1016/j.nano.2012.02.003.

[407] "Home | FUS Instruments." [Online]. Available: https://www.fusinstruments.com/. [Accessed: 22-May-2022].

[408] "HIFUPlex Options - Verasonics." [Online]. Available: https://verasonics.com/hifuplex-options/. [Accessed: 15-May-2022].

[409] "Image Guided Therapy - TargetedFUS." [Online]. Available: http://www.imageguidedtherapy.com/Focused-ultrasounds/MR-guided-Focused-Ultrasounds-System-for-experimental-research.html. [Accessed: 15-May-2022].

[410] "Focused Ultrasound - SonoVol, Inc." .

[411] M. H. A. Groen *et al.*, "Safety and feasibility of arterial wall targeting with robot-

assisted high intensity focused ultrasound: a preclinical study," *Int. J. Hyperth.*, vol. 37, no. 1, pp. 903–912, 2020, doi: 10.1080/02656736.2020.1795278.

[412] M. Yiannakou, G. Menikou, C. Yiallouras, C. Ioannides, and C. Damianou, "MRI guided focused ultrasound robotic system for animal experiments," *Int. J. Med. Robot. Comput. Assist. Surg.*, vol. 13, no. 4, p. e1804, Dec. 2017, doi: 10.1002/rcs.1804.

[413] Ł. Fura, W. Dera, C. Dziekoński, M. Świątkiewicz, and T. Kujawska, "Experimental assessment of the impact of sonication parameters on necrotic lesions induced in tissues by HIFU ablative device for preclinical studies," *Arch. Acoust.*, vol. 46, no. 2, pp. 341–352, 2021, doi: 10.24425/aoa.2021.136573.

[414] Fura, W. Dera, C. Dziekoński, M. Świątkiewicz, and T. Kujawska, "Experimental evaluation of targeting accuracy of ultrasound imaging-guided robotic HIFU ablative system for the treatment of solid tumors in pre-clinical studies," *Appl. Acoust.*, vol. 184, 2021, doi: 10.1016/j.apacoust.2021.108367.

[415] W. Shou *et al.*, "Acoustic power measurement of high intensity focused ultrasound in medicine based on radiation force," *Ultrasonics*, vol. 44, pp. 17–20, 2006, doi: 10.1016/j.ultras.2006.06.034.

[416] S. J. Mooney, K. Shah, S. Yeung, A. Burgess, I. Aubert, and K. Hynynen, "Focused ultrasound-induced neurogenesis requires an increase in blood-brain barrier permeability," *PLoS One*, vol. 11, no. 7, pp. 1–11, 2016, doi: 10.1371/journal.pone.0159892.

[417] H. Kadry, B. Noorani, and L. Cucullo, "A blood–brain barrier overview on structure, function, impairment, and biomarkers of integrity," *Fluids Barriers CNS*, vol. 17, no. 1, pp. 1–24, 2020, doi: 10.1186/s12987-020-00230-3.

[418] Z. Ebrahimi, S. Talaei, S. Aghamiri, N. H. Goradel, A. Jafarpour, and B. Negahdari, "Overcoming the blood–brain barrier in neurodegenerative disorders and brain tumours," *IET Nanobiotechnology*, vol. 14, no. 6, pp. 441–448, 2020,

doi: 10.1049/iet-nbt.2019.0351.

[419] S. Harilal *et al.*, “Revisiting the blood-brain barrier: A hard nut to crack in the transportation of drug molecules,” *Brain Res. Bull.*, vol. 160, pp. 121–140, 2020, doi: 10.1016/j.brainresbull.2020.03.018.

[420] B. S. Karmur *et al.*, “Blood-Brain Barrier Disruption in Neuro-Oncology: Strategies, Failures, and Challenges to Overcome,” *Front. Oncol.*, vol. 10, 2020, doi: 10.3389/fonc.2020.563840.

[421] A. Rodriguez, S. B. Tatter, and W. Debinski, “Neurosurgical techniques for disruption of the blood–brain barrier for glioblastoma treatment,” *Pharmaceutics*, vol. 7, no. 3, pp. 175–187, 2015, doi: 10.3390/pharmaceutics7030175.

[422] F. Gosselet, R. A. Loiola, A. Roig, A. Rosell, and M. Culot, “Central nervous system delivery of molecules across the blood-brain barrier,” *Neurochem. Int.*, vol. 144, p. 104952, 2021, doi: 10.1016/j.neuint.2020.104952.

[423] M. Aryal, K. Fischer, C. Gentile, S. Gitto, Y. Z. Zhang, and N. McDannold, “Effects on P-glycoprotein expression after blood-brain barrier disruption using focused ultrasound and microbubbles,” *PLoS One*, vol. 12, no. 1, pp. 1–15, 2017, doi: 10.1371/journal.pone.0166061.

[424] J. M. Wasielewska and A. R. White, “‘Focused Ultrasound-mediated Drug Delivery in Humans – a Path Towards Translation in Neurodegenerative Diseases,’” *Pharm. Res.*, vol. 39, no. 3, pp. 427–439, 2022, doi: 10.1007/s11095-022-03185-2.

[425] K. Chen, K. Wei, and H. Liu, “Theranostic Strategy of Focused Ultrasound Induced Blood-Brain Barrier Opening for CNS Disease Treatment,” *Front Pharmacol*, vol. 10, no. 86, 2019, doi: 10.3389/fphar.2019.00086.

[426] M. G. Z. Ghali, V. M. Srinivasan, and P. Kan, “Focused Ultrasonography-Mediated Blood-Brain Barrier Disruption in the Enhancement of Delivery of Brain Tumor Therapies,” *World Neurosurg.*, vol. 131, pp. 65–75, 2019, doi:

10.1016/j.wneu.2019.07.096.

[427] P. S. Fishman and J. M. Fischell, “Focused Ultrasound Mediated Opening of the Blood-Brain Barrier for Neurodegenerative Diseases,” *Front. Neurol.*, vol. 12, no. November, pp. 1–5, 2021, doi: 10.3389/fneur.2021.749047.

[428] C. T. Poon *et al.*, “Time course of focused ultrasound effects on β-amyloid plaque pathology in the TgCRND8 mouse model of Alzheimer’s disease,” *Sci. Rep.*, vol. 8, no. 1, pp. 1–11, 2018, doi: 10.1038/s41598-018-32250-3.

[429] P. H. Hsu *et al.*, “Focused Ultrasound-Induced Blood-Brain Barrier Opening Enhances GSK-3 Inhibitor Delivery for Amyloid-Beta Plaque Reduction,” *Sci. Rep.*, vol. 8, no. 1, pp. 1–9, 2018, doi: 10.1038/s41598-018-31071-8.

[430] J. L. Frost *et al.*, “An anti-pyroglutamate-3 Aβ vaccine reduces plaques and improves cognition in APPswe/PS1ΔE9 mice,” *Neurobiol Aging*, vol. 36, no. 12, pp. 3187–3199, 2015, doi: 10.1016/j.neurobiolaging.2015.08.021.

[431] K. Xhima, K. Markham-Coultes, R. Hahn Kofoed, H. U. Saragovi, K. Hynynen, and I. Aubert, “Ultrasound delivery of a TrkA agonist confers neuroprotection to Alzheimer-associated pathologies,” *Brain*, vol. 145, no. 8, pp. 2806–2822, 2022, doi: 10.1093/brain/awab460.

[432] P. Bathini, T. Sun, M. Schenk, S. Schilling, N. J. Mcdannold, and C. A. Lemere, “Acute Effects of Focused Ultrasound-Induced Blood-Brain Barrier Opening on Anti-Pyroglu3 Abeta Antibody Delivery and Immune Responses,” *Biomolecules*, vol. 12, no. 7, p. 951, 2022, doi: 10.3390/biom12070951.

[433] T. Sun *et al.*, “Focused ultrasound with anti-pGlu3 Aβ enhances efficacy in Alzheimer’s disease-like mice via recruitment of peripheral immune cells,” *J. Control. Release*, vol. 336, pp. 443–456, 2021, doi: 10.1016/j.jconrel.2021.06.037.

[434] R. Bajracharya, E. Cruz, J. Götz, and R. M. Nisbet, “Ultrasound-mediated delivery of novel tau-specific monoclonal antibody enhances brain uptake but not therapeutic efficacy,” *J. Control. Release*, vol. 349, pp. 634–648, 2022, doi:

10.1016/j.jconrel.2022.07.026.

[435] G. Leinenga, W. K. Koh, and J. Götz, “A comparative study of the effects of Aducanumab and scanning ultrasound on amyloid plaques and behavior in the APP23 mouse model of Alzheimer disease,” *Alzheimer’s Res. Ther.*, vol. 13, no. 1, pp. 1–14, 2021, doi: 10.1186/s13195-021-00809-4.

[436] “Safety and Feasibility of Exablate Blood-Brain Barrier Disruption for Mild Cognitive Impairment or Mild Alzheimer’s Disease Undergoing Aduhelm Therapy,” *ClinicalTrials.gov Identifier: NCT05469009*. [Online]. Available: https://beta.clinicaltrials.gov/study/NCT05469009. [Accessed: 10-Jan-2023].

[437] H. J. Fu, B. Liu, J. L. Frost, and C. A. Lemere, “Amyloid-β Immunotherapy for Alzheimer’s Disease,” *CNS Neurol Disord Drug Targets*, vol. 9, no. 2, pp. 197–206, 2010, doi: 10.2174/187152710791012017.

[438] E. L. Madsen *et al.*, “Interlaboratory Comparison of Ultrasonic Backscatter, Attenuation, and Speed Measurements,” *J Ultrasound Med*, vol. 18, pp. 615–631, 1999, doi: 10.7863/jum.1999.18.9.615.

[439] N. Todd *et al.*, “Focused Ultrasound Induced Opening of the Blood-Brain Barrier Disrupts Inter-Hemispheric Resting State Functional Connectivity in the Rat Brain,” *Neuroimage*, vol. 178, pp. 414–422, 2018, doi: 10.1016/j.neuroimage.2018.05.063.

[440] A. Burgess and H. H. Kullervo, “Drug delivery across the blood-brain barrier using focused ultrasound,” *Expert Opin Drug Deliv.*, vol. 11, no. 5, pp. 711–721, 2014, doi: 10.1517/17425247.2014.897693.

[441] N. McDannold, N. Vykhodtseva, and K. Hynynen, “Use of ultrasound pulses combined with Definity for targeted blood-brain barrier disruption: a feasibility study.,” *Ultrasound Med. Biol.*, vol. 33, no. 4, pp. 584–90, Apr. 2007, doi: 10.1016/j.ultrasmedbio.2006.10.004.

[442] N. McDannold, N. Vykhodtseva, and K. Hynynen, “Effects of Acoustic

Parameters and Ultrasound Contrast Agent Dose on Focused-Ultrasound Induced Blood-Brain Barrier Disruption," *Ultrasound Med. Biol.*, vol. 34, no. 6, pp. 930–937, 2008, doi: 10.1016/j.ultrasmedbio.2007.11.009.

[443] N. Sheikov, N. McDannold, S. Sharma, and K. Hynynen, "Effect of focused ultrasound applied with an ultrasound contrast agent on the tight junctional integrity of the brain microvascular endothelium," *Ultrasound Med Biol*, vol. 34, no. 7, pp. 1093–1104, 2008, doi: 10.1016/j.ultrasmedbio.2007.12.015.

[444] M. E. Downs *et al.*, "Long-term safety of repeated blood-brain barrier opening via focused ultrasound with microbubbles in non-human primates performing a cognitive task," *PLoS One*, vol. 10, no. 5, pp. 1–26, 2015, doi: 10.1371/journal.pone.0125911.

[445] K. Hynynen, N. McDannold, N. Vykhodtseva, and F. A. Jolesz, "Noninvasive MR imaging-guided focal opening of the blood-brain barrier in rabbits.," *Radiology*, vol. 220, no. 4, pp. 640–646, 2001, doi: 10.1148/radiol.2202001804.

[446] F. Schlachetzki *et al.*, "Observation on the integrity of the blood-brain barrier after microbubble destruction by diagnostic transcranial color-coded sonography," *J. Ultrasound Med.*, vol. 21, no. 4, pp. 419–429, 2002, doi: 10.7863/jum.2002.21.4.419.

[447] N. McDannold, N. Vykhodtseva, S. Raymond, F. A. Jolesz, and K. Hynynen, "MRI-guided targeted Blood-brain barrier distribution with focused ultrasound: Histological Findings in Rabbits," *Ultrasound Med. Biol.*, vol. 31, no. 11, pp. 1527–1537, 2005, doi: 10.1016/j.ultrasmedbio.2005.07.010.

[448] F.-Y. Yang, W.-M. Fu, R.-S. Yang, H.-C. Liou, K.-H. Kang, and W.-L. Lin, "Quantitative Evaluation of Focused Ultrasound with a Contrast Agent on Blood-Brain Barrier Disruption," *Ultrasound Med. Biol.*, vol. 33, no. 9, pp. 1421–1427, 2007, doi: 10.1016/j.ultrasmedbio.2007.04.006.

[449] E. E. Cho, J. Drazic, M. Ganguly, B. Stefanovic, and K. Hynynen, "Two-Photon

Fluorescence Microscopy Study of Cerebrovascular Dynamics in Ultrasound-Induced Blood—Brain Barrier Opening," *J. Cereb. Blood Flow Metab.*, vol. 31, no. 9, pp. 1852–1862, 2011, doi: 10.1038/jcbfm.2011.59.

[450] M. A. O'Reilly, A. C. Waspe, M. Ganguly, and K. Hynynen, "Focused-Ultrasound Disruption of the Blood-Brain Barrier Using Closely-Timed Short Pulses: Influence of Sonication Parameters and Injection Rate," *Ultrasound Med. Biol.*, vol. 37, no. 4, pp. 587–594, 2011, doi: 10.1016/j.ultrasmedbio.2011.01.008.

[451] F. Yang *et al.*, "Pulsed High-Intensity Focused Ultrasound Enhances the Relative Permeability of the Blood – Tumor Barrier in a Glioma-Bearing Rat Model," *IEEE Trans. Ultrason. Ferroelectr. Freq. Control*, vol. 58, no. 5, pp. 964–970, 2011, doi: 10.1109/TUFFC.2011.1897.

[452] F. Y. Yang, H. E. Wang, G. L. Lin, H. H. Lin, and T. T. Wong, "Evaluation of the increase in permeability of the blood-brain barrier during tumor progression after pulsed focused ultrasound," *Int. J. Nanomedicine*, vol. 7, pp. 723–730, 2012, doi: 10.2147/IJN.S28503.

[453] P. C. Chu *et al.*, "Pharmacodynamic analysis of magnetic resonance imaging-monitored focused ultrasound-induced blood-brain barrier opening for drug delivery to brain tumors," *Biomed Res. Int.*, vol. 2013, 2013, doi: 10.1155/2013/627496.

[454] H.-L. Liu *et al.*, "Design and Experimental Evaluation of a 256 -Channel Dual-Frequency Ultrasound Phased-Array System for Transcranial Blood-Brain Barrier Opening and Brain Drug Delivery," *IEEE Trans Biomed Eng.*, vol. 61, no. 4, pp. 1350–60, 2014, doi: 10.1109/TBME.2014.2305723.

[455] M. Aryal, N. Vykhodtseva, Y. Z. Zhang, and N. McDannold, "Multiple sessions of liposomal doxorubicin delivery via focused ultrasound mediated blood-brain barrier disruption: A safety study," *J. Control. Release*, vol. 204, pp. 60–69, 2015, doi: 10.1016/j.jconrel.2015.02.033.

[456] J. Xia, P. Tsui, and H. Liu, “Low-Pressure Burst-Mode Focused Ultrasound Wave Reconstruction and Mapping for Blood-Brain Barrier Opening : A Preclinical Examination,” *Sci. Rep.*, vol. 6, no. 27939, 2016, doi: 10.1038/srep27939.

[457] T. Kobus, I. K. Zervantonakis, Y. Zhang, and N. J. McDannold, “Growth inhibition in a brain metastasis model by antibody delivery using focused ultrasound-mediated blood-brain barrier disruption,” *J. Control. Release*, vol. 238, pp. 281–288, 2016, doi: 10.1016/j.jconrel.2016.08.001.

[458] Z. I. Kovacsa *et al.*, “Disrupting the blood-brain barrier by focused ultrasound induces sterile inflammation,” *Proc. Natl. Acad. Sci. U. S. A.*, vol. 114, no. 1, pp. E75–E84, 2017, doi: 10.1073/pnas.1614777114.

[459] T. Kobus, N. Vykhodtseva, M. Pilatou, Y. Zhang, and N. McDannold, “SAFETY VALIDATION OF REPEATED BLOOD–BRAIN BARRIER DISRUPTION USING FOCUSED ULTRASOUND,” *Ultrasound Med Biol*, vol. 42, no. 2, pp. 481–492, 2016, doi: 10.1016/j.ultrasmedbio.2015.10.009.

[460] H. L. Liu *et al.*, “Focused ultrasound enhances central nervous system delivery of Bevacizumab for malignant glioma treatment,” *Radiology*, vol. 281, no. 1, pp. 99–108, 2016, doi: 10.1148/radiol.2016152444.

[461] K. F. Timbie *et al.*, “MR image-guided delivery of cisplatin-loaded brain-penetrating nanoparticles to invasive glioma with focused ultrasound,” *J. Control. Release*, vol. 263, pp. 120–131, 2017, doi: 10.1016/j.jconrel.2017.03.017.

[462] W. Bin Shen *et al.*, “Magnetic enhancement of stem cell–targeted delivery into the brain following MR-guided focused ultrasound for opening the blood–brain barrier,” *Cell Transplant.*, vol. 26, no. 7, pp. 1235–1246, 2017, doi: 10.1177/0963689717715824.

[463] K. H. Song, A. C. Fan, J. J. Hinkle, J. Newman, M. A. Borden, and B. K. Harvey, “Microbubble gas volume: A unifying dose parameter in blood-brain barrier opening by focused ultrasound,” *Theranostics*, vol. 7, no. 1, pp. 144–152, 2017,

doi: 10.7150/thno.15987.

[464] Y. Huang, R. Alkins, M. L. Schwartz, and K. Hynynen, “Opening the Blood-Brain Barrier with MR Imaging – guided Focused Ultrasound : Preclinical Testing on a Trans – Human Skull,” *Radiology*, vol. 282, no. 1, pp. 123–130, 2017, doi: 10.1148/radiol.2016152154.

[465] D. Mcmahon, R. Bendayan, and K. Hynynen, “Acute effects of focused ultrasound-induced increases in blood-brain barrier permeability on rat microvascular transcriptome,” *Sci. Rep.*, vol. 7, no. April, pp. 1–15, 2017, doi: 10.1038/srep45657.

[466] X. Zhang *et al.*, “PEGylated PLGA-based phase shift nanodroplets combined with focused ultrasound for blood brain barrier opening in rats,” *Oncotarget*, vol. 8, no. 24, pp. 38927–38936, 2017, doi: 10.18632/oncotarget.17155.

[467] H. Tsai, C. Tsai, W. Chen, C. Inserra, K. Wei, and H.-L. Liu, “Safety evaluation of frequent application of microbubble- enhanced focused ultrasound blood-brain-barrier opening,” *Sci. Rep.*, vol. 8, pp. 1–13, 2018, doi: 10.1038/s41598-018-35677-w.

[468] Q. Dong, L. He, L. Chen, and Q. Deng, “Opening the Blood-Brain Barrier and Improving the Efficacy of Temozolomide Treatments of Glioblastoma Using Pulsed , Focused Ultrasound with a Microbubble Contrast Agent,” *Biomed Res. Int.*, vol. 2018, 2018, doi: 10.1155/2018/6501508.

[469] N. McDannold *et al.*, “Acoustic feedback enables safe and reliable carboplatin delivery across the blood-brain barrier with a clinical focused ultrasound system and improves survival in a rat glioma model,” *Theranostics*, vol. 9, no. 21, pp. 6284–6299, 2019, doi: 10.7150/thno.35892.

[470] C. Bing *et al.*, “Characterization of different bubble formulations for blood-brain barrier opening using a focused ultrasound system with acoustic feedback control,” *Sci. Rep.*, vol. 8, no. 1, pp. 1–12, 2018, doi: 10.1038/s41598-018-26330-7.

[471] A. Abrahao *et al.*, “First-in-human trial of blood–brain barrier opening in amyotrophic lateral sclerosis using MR-guided focused ultrasound,” *Nat Commun*, vol. 10, 2019, doi: 10.1038/s41467-019-12426-9.

[472] T. Mainprize *et al.*, “Blood-Brain Barrier Opening in Primary Brain Tumors with Non-invasive MR-Guided Focused Ultrasound: A Clinical Safety and Feasibility Study,” *Sci. Rep.*, vol. 9, no. 1, pp. 1–7, 2019, doi: 10.1038/s41598-018-36340-0.

[473] M. E. Karakatsani *et al.*, “Unilateral Focused Ultrasound-Induced Blood-Brain Barrier Opening Reduces Phosphorylated Tau from The rTg4510 Mouse Model,” *Theranostics*, vol. 9, no. 18, pp. 5396–5411, 2019, doi: 10.7150/thno.28717.

[474] M. A. Stavarache *et al.*, “Safe and stable noninvasive focal gene delivery to the mammalian brain following focused ultrasound,” *J Neurosurg*, vol. 130, pp. 989–998, 2019, doi: 10.3171/2017.8.JNS17790.

[475] M. T. Burgess, I. Apostolakis, and E. E. Konofagou, “Power cavitation-guided blood-brain barrier opening with focused ultrasound and microbubbles,” *Phys Med Biol*, vol. 63, no. 6, 2019, doi: 10.1088/1361-6560/aab05c.

[476] C. Y. Lin *et al.*, “Focused ultrasound-induced blood brain-barrier opening enhanced vascular permeability for GDNF delivery in Huntington’s disease mouse model,” *Brain Stimul.*, vol. 12, no. 5, pp. 1143–1150, 2019, doi: 10.1016/j.brs.2019.04.011.

[477] B. Cheng, C. Bing, Y. Xi, B. Shah, A. A. Exner, and R. Chopra, “Influence of Nanobubble Concentration on Blood–Brain Barrier Opening Using Focused Ultrasound Under Real-Time Acoustic Feedback Control,” *Ultrasound Med. Biol.*, vol. 45, no. 8, pp. 2174–2187, 2019, doi: 10.1016/j.ultrasmedbio.2019.03.016.

[478] A. R. Rezai *et al.*, “Noninvasive hippocampal blood−brain barrier opening in Alzheimer’s disease with focused ultrasound,” *Proc. Natl. Acad. Sci. U. S. A.*, vol. 117, no. 17, pp. 9180–9182, 2020, doi: 10.1073/pnas.2002571117.

[479] M. C. Rich *et al.*, “Focused ultrasound blood brain barrier opening mediated

delivery of MRI-visible albumin nanoclusters to the rat brain for localized drug delivery with temporal control," *J. Control. Release*, vol. 324, pp. 172–180, 2020, doi: 10.1016/j.jconrel.2020.04.054.

[480] C. Gasca-salas *et al.*, "Blood-brain barrier opening with focused ultrasound in Parkinson's disease dementia," *Nat. Commun.*, vol. 12, no. 1, pp. 1–7, 2021, doi: 10.1038/s41467-021-21022-9.

[481] H. Zhou *et al.*, "MR-guided blood-brain barrier opening induced by rapid short-pulse ultrasound in non-human primates," *Quant. Imaging Med. Surg.*, vol. 11, pp. 2223–4306, 2021, doi: 10.21037/qims-20-1047.

[482] K. T. Chen *et al.*, "Neuronavigation-guided focused ultrasound for transcranial blood-brain barrier opening and immunostimulation in brain tumors," *Sci. Adv.*, vol. 7, no. 6, 2021, doi: 10.1126/sciadv.abd0772.

[483] A. Sabbagh *et al.*, "Opening of the Blood–Brain Barrier Using Low-Intensity Pulsed Ultrasound Enhances Responses to Immunotherapy in Preclinical Glioma Models," *Clin. Cancer Res.*, pp. 1–14, 2021, doi: 10.1158/1078-0432.ccr-20-3760.

[484] Z. K. Englander *et al.*, "Focused ultrasound mediated blood–brain barrier opening is safe and feasible in a murine pontine glioma model," *Sci. Rep.*, vol. 11, no. 1, pp. 1–10, 2021, doi: 10.1038/s41598-021-85180-y.

[485] H. Kato, M. Kuroda, K. Yoshimura, S. Kawasaki, and N. Yamamoto, "An MRI phantom using carrageenan gel," *Nippon Jiki Kyomei Igakkai Zasshi*, vol. 20, no. 8, pp. 365–373, 2000.